Deformation dependent states in cyclic disturbed sand

Sabaliauskas, Tomas

DOI (link to publication from Publisher):
10.54337/aau300036042

Publication date:
2018

Document Version
Publisher's PDF, also known as Version of record

Citation for published version (APA):
Sabaliauskas, T. (2018). *Deformation dependent states in cyclic disturbed sand*. Aalborg Universitetsforlag. https://doi.org/10.54337/aau300036042

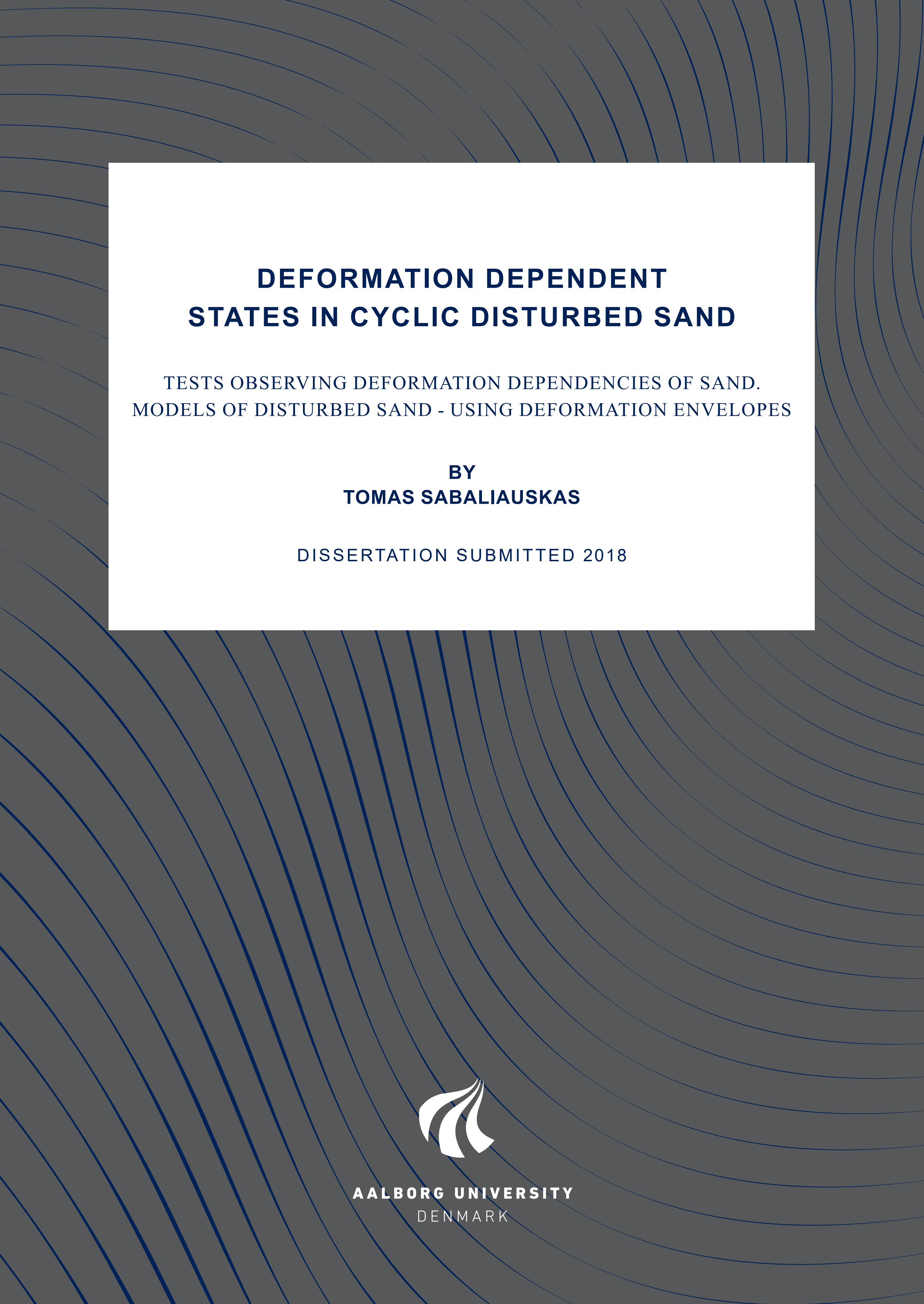

DEFORMATION DEPENDENT STATES IN CYCLIC DISTURBED SAND

TESTS OBSERVING DEFORMATION DEPENDENCIES OF SAND.
MODELS OF DISTURBED SAND - USING DEFORMATION ENVELOPES

BY
TOMAS SABALIAUSKAS

DISSERTATION SUBMITTED 2018

AALBORG UNIVERSITY
DENMARK

Deformation dependent states in cyclic disturbed sand

Tests observing deformation dependencies of sand.
Models of disturbed sand - using deformation envelopes.

Ph.D. Dissertation
Tomas Sabaliauskas

Dissertation submitted xx, 2018

Dissertation submitted: August 2018

PhD supervisor: Prof. Lars Bo Ibsen
Aalborg University

PhD committee: Professor Lars Damkilde (chairman)
Aalborg University

Professor Dr.-Ing. Martin Achmus
Leibniz University Hannover

Professor Susumu IAI
President, FLIP Consortium

PhD Series: Faculty of Engineering and Science, Aalborg University

Department: Department of Civil Engineering

ISSN (online): 2446-1636
ISBN (online): 978-87-7210-250-4

Published by:
Aalborg University Press
Langagervej 2
DK – 9220 Aalborg Ø
Phone: +45 99407140
aauf@forlag.aau.dk
forlag.aau.dk

Printed in Denmark by Rosendahls, 2018

Abstract

Offshore wind turbine are slender structures, performance of which depends on foundation stiffness. Wind turbine foundations embedded in sand episodically lose and recover stiffness due to soil being disturbed by cyclic loads. To understand and model this phenomenon, new methods of testing and modeling of disturbed sand were attempted.

To observe the phenomenon governing disturbed sand states, dynamic tests were conducted using a frictionless triaxial apparatus and a small scale mono-bucket foundation. Experimental observations were then summarized into an original model. While developing the original concept, new paradoxes and anomalies were predicted: soil states of lower stiffness at higher density. The anomalies are confirmed to exist experimentally.

The new knowledge allows to control cyclic stiffness of sand in real-life real-time testing. Methods adequate to control a phenomenon, should be adequate to model it. Because deformation allows to control cyclic stiffness in experiment, deformation envelopes were proposed for modeling. Remarkably, the final result is one set of rules which are applicable in both drained and undrained soil states, combining loss and recovery of stiffness, during irregular cyclic loads.

Contents

Preface

"within the duration of two years, I can not recall him making a single theoretical calculation. He suggested, and we attempted numerous correlations among soil properties, geometry and effects of tunnelling. And with the aid of the correlations, we began to feel that we understood the cause and effect. The understanding came about exclusively as a result of detailed observations and measurements. Near the end of the project, when all the data had been assembled, commenced into working memorandum, and described in almost daily correspondence with Terczaghi, he settled down to study all the information" – Ralph B. Peck (1993) describing research by Terczaghi.

Sand is the perfect model of itself. Much remains to be learned from it: yet to be tested; yet to be noticed; yet to be modeled; yet to be solved.

Reality is perfect, She never makes an error.
She was not made for us, She knows not we exist.
-
By measuring proportion an questioning causation,
non-falsified observables are found.

Tomas Sabaliauskas
Aalborg University, July 30, 2018

Chapter 1

Introduction

Motivation Global demand for energy is growing. The demand can be partially satisfied by harvesting offshore wind energy. In 2016, Dutch Borssele projects reached 72.7 EUR/MWh (USD 78.5), near-shore parks in Denmark: 64 EUR/MWh (USD 69.1), Kriegers Flak project: 49.9 EUR/MWh (USD 53.9). In 2017, EnBW and Dong placed bids for the first subsidy free offshore wind parks, estimated to produce electricity at less than 30.1 EUR/MWh. Thus, today, renewable energy is competitive, profitable, self sufficient, and de facto producing electricity at a prise below market average [16]. These are good news for geotechnical research. Offshore wind turbine foundations are unique structures, they must survive loading scenarios incompatible with conventional soil models. Substantial savings can be achieved if uncertainties in foundation design are reduced. Thus, the recent trends in wind industry generate funding for geotechnical research.

The problem: The worst case scenario for offshore wind turbine foundations is quite different from conventional. The loads are not static, irregular loading cycles need to be combined with impact loads. Thus, the relevant worst case scenario is very complex [9] [27]:

1. The sea-floor is disturbed during installation of a foundation (a life cycle begins in a disturbed soil state).
2. Disturbed soil states evolve during relative calm (stabilize).
3. A storm event begins:
    (a) Waves of increasing height cause disturbed soil states;
    (b) An extreme wave hits, thus the soil is disturbed further;
    (c) Storm continues, plastic deformation increments accumulate;

  (d) Storm calms down, soil gradually stabilizes;

4. Point 3 is repeated for every storm for at least 20 years. More than 1 storm per year is likely.

Contemporary geotechnical paradigm offers crude compromises for the worst case scenario. There is no consensus for the effects of cyclic preloading [10]. Furthermore, requirements imposed by design standards are very strict: the offshore foundation must remain vertical within 0.5^o inclination for at least 20 years [3]. This combination of large uncertainties and strict requirements means large safety coefficients are used. Due to high safety coefficients structures consume excess amounts of material. As our understanding of soil mechanics improves, safety coefficients will decrease, and foundations will become more affordable, profitable.

Besides offshore turbine foundation design, cyclic loaded sand is encountered in seismic zones. Alas, during earthquakes the loading cycles are faster and come in short bursts. Nevertheless, some overlap with phenomenon caused by slow, continuous loading cycles can be expected. Especially likely is overlap in near field seismic problems, as impact loads during an earthquake are comparable to those produced by a breaking wave hitting an offshore foundation.

Beyond natural hazards, disturbed sand properties can be applicable in controlled environments. For example, liquefaction if often viewed as a hazard, but it can be used to lower resistance of sand within a targeted volume of soil. This could be applicable in grout injecting (soil curing technique). If grout injection is executed with cyclic patterns, the cycles can liquefy a targeted volume of soil [46], thus improving lateral spreading of grout. Thus, it is worth to note that sand properties observed in one branch of a paradigm could be applicable in others.

Finally, there is a great deal of professional curiosity to be satisfied in geotechnics. Very little is known about disturbed soil states. Observations of disturbed soil states are limited by technical challenges: it is challenging to disturb a specimen without destroying it (causing shear rupture, irreversible distortion of geometry). Consequently, the field of geotechnics is ripe with potential for pioneering research, potential new observations, if limitations imposed by testing methodology are resolved.

The methods: Research presented in this thesis begins with practical experiment, where attempts are made to look at "the big picture" - stiffness patterns generated during complex irregular loading. The approach is fundamentally different from trying to calibrate an existing model. The loads applied on the specimen cause reactions far beyond reach of conventional solutions. Thus, generating datasets of inputs and outputs beyond the reach of conventional theory. This allows to find anomalies and paradoxes, which are then analyzed for patterns and regularities to be conceptualized into novel, original models. Very few theoretical assumptions are borrowed from convention in the process. The experimentally observed patterns and regularities are fitted using parametric curves, and further tests are designed to find where predictive power of the parametric curves is exhausted. Thus, focusing in attempt deductive value of tests which falsify both: the convention and the opinions of the authors. Consequently, converging to a set of parametric curves which describe experimentally observable phenomenon using experimentally nonfalsified set of rules [4].

The thesis begins with simple experiments which raise the initial questions: monotonic peak strength tests. And finalizes with examples of models which attempt to fit data generated during irregular dynamic loading cycles combining drained and undrained response. Two types of tests are used: First, the frictionless triaxial apparatus, later - an offshore foundation prototype. Each round of tests is followed by analysis of the results, which are conceptualized into evidence based models (parametric curves).

The two types of testing equipment (triaxial apparatus and a foundation prototype) work in synergy. The triaxial apparatus is used for testing isotropic stress states resembling a linear gauss point. Whereas the small scale foundation recreates complex non-linear deformation fields around a structure of complex geometry. This allows to analyze what features carry over from a simple to a complex system. The triaxial apparatus measures what is equivalent to one gauss point in a finite element, as used in finite element method (FEM). While the foundation response reveals behaviors which would require complex, nonlinear FEM analysis (substituted by p-y curves in this thesis).

Results: The key results are new facts. Original measurements revealed some new phenomenon: sand stiffness patterns previously undocumented in literature. conclusions derived from the new facts are summarized in evidence based conceptual models. The models have predicted anomalies and paradoxes (such as lower stiffness at higher density), which were then experimentally confirmed, understood, and controlled in testing practice. Thus, correctness of the new concepts is demonstrated in practice by both: demonstrating the very existence, and prescriptive control of the new found phenomenon.

The new descriptive, predictive and prescriptive power was obtained by confronting an inconvenient truth: some soil properties are exclusively deformation dependent. Some soil properties could be fundamentally incompatible with stress envelopes. Note, the Coulomb stress limits were not falsified, Coulomb stress limits remain valid and true, but a different way of interpolating within the Coulomb limits is proposed, implemented and tested.

Thus, the new findings introduce a new perspective which, in synergy with elements of existing convention, could help shape a more coherent picture truth.

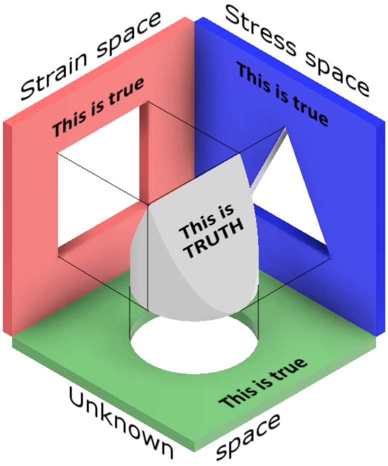

Chapter 2

State of the art

1 Brief history of geotechnics

Geotechnics is a young field of science. In medieval times castles and churches were built without measuring soil properties. Medieval engineers had few tools: ropes and compasses. These allowed to preserve linear proportion. They blueprints were engraved into flat clay floors, and "computations" of design were made by building small scale prototypes. If the small scale experiment was statically stable, the full scale structure would be attempted, by scaling the geometry linearly. The walls of a church were made using sculpted rocks without concrete or stiffeners. This allowed the rocks to move if soil under the wall started to deform. Because there was no concrete, the walls would not fracture or collapse if the soil deformed unevenly. instead, the rocks would move and gaps would gently open. If the gaps were getting too big, the structure could be disassembled top down, rocks re-sculpted, and built up again. Impressive, durable, robust and complex structures, lasting for thousands of years, were built this way even in 15'th century (Kin College Chapel [37]).

When faced with significant uncertainties we still use methods similar to those used by medieval engineers: make small scale prototypes, and measure their properties using modern precision tools. The measured proportion can then be scaled. However, unlike medieval churches, some problems cannot scaled. Offshore foundations embedded in sand, depend on a mixture of nonlinear phenomenon. Therefore, tests described in this thesis look for deeper fundamental principles, governing dynamic loaded sand response. The observations are normalized within parametric curves, which then are connected by assumed causation links. The links between cause and effect were inductively assumed from observations (observable). Then further tests were made in attempt to falsify the assumptions deductively. Thus leaving only those patterns and regularities who are both observable and non-falsifiable experimentally. During these inductive / deductive iterations, a stable set of rules has converged. The new found rules seem to question convention, they could be a precursor for a paradigm shift [4].

The paradigm of geotechnics has changed over time. Up until 18'th century retaining walls of forts were built using universal rules of thumb, without measuring soil properties. Identical slabs of wall were erected regardless of soil properties [37]. This changed after Coulomb published his famous essay in 1773 [8], where he described the principles of "application of rules of maximum and minimum to some static problems, relevant to architecture". His essay was published 244 years ago, and it is still the anchoring point in most modern day models of sand. But, as the name of the essay implies, the principles are meant for static problems. Coulomb stress limits provide reliable estimates of peak strength, but not changing stiffness problems. Coulombs essay does little to explain stiffness hysteresis loops observed in sand.

Another weak spot of Coulomb's essay was the effects pore water pressure has on effective stresses. But in 1925 Terzaghi introduced the concept of effective stresses. In his words "effective" means "stress that is effective in moving soil" [37] . As a load is applied on soil, part of the load will be pushing against the water - not the grains of soil skeleton. If pore pressure increases - more of the load is carried by water, less by the grains. If pore pressure drops - grains are pulled (locked) together. On the sea floor, the soil is always fully saturated, therefore fluctuation of pore watter is crucial to account for. It is curious, that pore water can add extra strength (the boot effect [25]) while reducing stiffness (liquefaction). These effects are especially noticeable in undrained loaded sand. For instance, if a load is applied faster than the pore pressure can dissipate (during impact loads), a structure built in dilative sand will have extra resistance to impact loads [19] [29], but at the potential cost of increased sensitivity to liquefaction after the impact (disturbed soil state).

After Terzaghi improved Coulombs concepts, the predictive power of geotechnical models improved. The paradigm could predict the ultimate strength of dams and tunnel walls. Still, those structures are static. It became plausible to predict what load (yield stress) will cause the collapse, but it remained not plausible to predict at what deformation (yield strain) the peak strength is reached. It is counter intuitive that stiffness and strength of sand are only partially correlated. Sand can become more dense (stronger), but less stiff. Undrained specimens have near constant density, near constant peak strength, but while liquefying their stiffness keeps dropping. A liquefying specimen transitions through many disturbed soil states, each soil state generating a unique stiffness curve - at the same density, and the same loading amplitude [35] [36]. Thus, Terzaghi's methods allow to predict peak strength. but does little to explain the phenomenon governing cyclic stiffness of sand - a crucial component for designing foundation of slender offshore structures, such as offshore wind turbines [27] [9].

Stiffness curves connect peak stress (force) with peak strain (deformation). Peak stress in the main focus of contemporary convention - effective stress yield envelopes. However, peak strain is important too. Very little is known about phenomenon governing peak deformation points. In 1948, Taylor made shear box tests on dense Ottawa sand, where he attempted to describe properties of peak deformation, reached at the moment of mobilizing maximum reaction force (point "maximum" by Coulomb terminology). He attempted to link dilative sand behavior to peak strength. His attempts brought forth a new perception of sand. Instead of using terms of "friction between two rigid bodies", he introduced the idea of "interlocking": sand is a granular material, made of small grains of sand, interlocking in a complex mechanism. The peak strength is the point where interlocking is overcome - the grains move inside the shear band and around it as well. This brought a shift in how sand is perceived by geotechnicians - up until then sand was a pair of perfectly rigid bodies sliding along a thin failure plane. But Taylor tests indicate the "rigid bodies" do not behave rigid. Within the "rigid bodies" the volume, arrangement of grains is changing as well. This shift in perception fixed explained some some systematic errors previous models had. Taylor brought forth awareness that, soil skeleton structure can change, dilate and contract, even outside the shear rupture zone [37]. This is important to remember when designing a test, interpreting test results, making models, and so forth.

Test results shape modeling methods, and the resulting model shape the testing equipment. In 1963, Schofield introduced the original CamClay soil model. The model describes idealized clay behavior. The model can be viewed as the beginning of critical state soil mechanics [37]. It describes over consolidated clay as dilative, and under-consolidated as contractive. The model uses stress envelope, to converge towards an equilibrium point called the critical state. It sparked a new branch of models: the critical state soil mechanics. However, in his books Schofield expresses concern that assumptions made in his model are used without enough caution. He emphasizes that the critical state is limited to clay specimens. When given enough time for pore water to dissipate, clay behaves like sand with a low friction angle. Regardless of the original authors words, the trend of the paradigm is to keep looking for more stress space variables. After many decades, this path has still failed to combine drained and undrained loading cycles, loss and recovery of stiffness - under one set of rules. Sadly, such robustness is necessary for designing offshore wind turbine foundations [27] [9], where stiffness can be lost and recovered episodically, while transitioning both drained and undrained loading conditions. At this is the point the existing convention, the state of art, is exhausted: there are models reliably predicting ultimate (static) peak strength, and methods predicting liquefaction to some degree [11]. But there is no model capturing "the full picture", the "one set of rules" which would be applicable to drained and undrained sand, combining loss and recovery of stiffness, during irregular dynamic loading cycles. Perhaps, the missing part is not yet another stress envelope. Maybe the answer can be found by observing the phonon as a function of strain, instead of stress.

Coulomb, Taylor, Terczaghi, Schofield and the medieval engineers - they all had the courage to question convention of their time. Coulomb was put in charge of designing the walls of a fort, because his superior has died. Thus allowing a young mind to test new solutions. Unavoidably, we are constrained by the theories of our time. But problems created within existing convention, could require to looks at them from a different perspective. Quoting Terzaghi: "Theory is not the starting point. Theory is the product of phenomenon observed”.

2 Putting this thesis into context

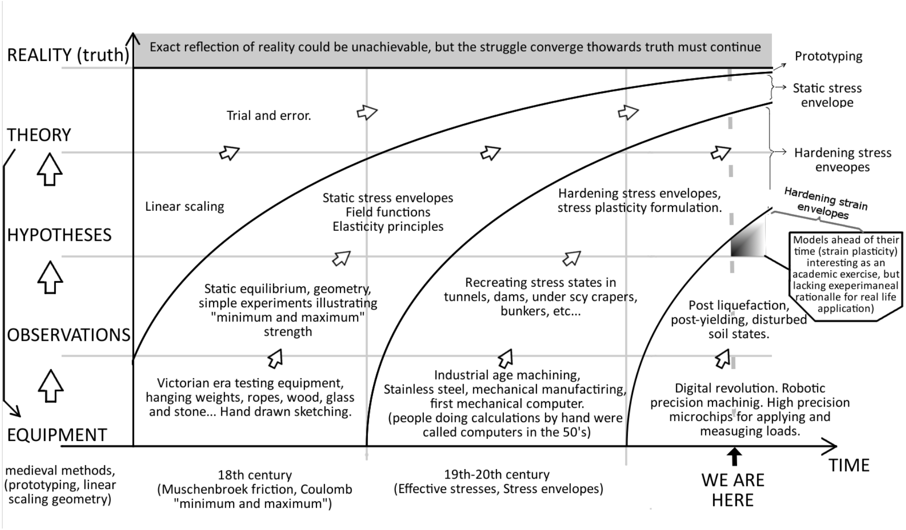

Fig. 2.1: Parallel paradigms coexist. Inductively, theory grows as new hypotheses are raised. Deductively false assumptions are removed, as testing equipment evolves.

This thesis can be put into context as indicated by "WE ARE HERE" position in Fig.2.1. It bridges the gap between "models ahead of their time" with experimental observations. It is curious that, some theoreticians managed to propose compatible formulation before the experimental observations were available. Mathematical equations have the remarkable property to preserve proportion. Alas, without experiment, it is not plausible to tell if Y is the function of X, or X is the function of Y. Mathematically speaking, both equations are equally correct. Alas, in reality, one of the equations will have superior descriptive, predictive, and prescriptive analytic power. With superior predictive power, comes superior level of control. Thus correctness of a principle can be judged by the level of control it provides. This is the key difference of work presented in this thesis from other work done in the field: instead of attempting to quantify the observed behavior, the emphasis is to learn how to control (prescribe) the phenomenon. To prescribe (control) is the highest analytic power. It requires to find ways to quantify (preserve proportion) and predict (preserve causation) correctly to a degree which allows one to chose the outcome selectively. Methods adequate to control a phenomenon in practice, should be adequate to model it in theory.

This thesis does not introduce a new constitutive formulation (results support formulation derived by P.J.Yoder [44]). Also, equipment used in testing is not a "new" or "unique". The frictionless triaxial apparatus was invented in the 60's [5]. Nevertheless, new phenomenon was observed using the old equipment. This means the conventional testing protocols can be modified, improved, changed. The old equipment was used in innovative, different ways. Instead of repeating old tests with known outcomes - tests were design to reach beyond convention - exposing new paradoxes, anomalies. Within the new testing scope, observations containing new patterns and regularities were observed. Thus, allowing to raise new (inductive) hypotheses and design new (deductive) tests. Tests with unknown outcomes - larger deformation amplitudes, irregular cycles, combining liquefaction, post-liquefaction, drained and undrained modes in one loading sequence, etc. This was the path taken in research presented in this thesis. The new observations question convention - proposing new "missing variables" (governing proportion) and false causation (logic) within convention.

Experiments contradicting convention are often celebrated as a good thing (a paradigm shift [4]). However, in real life, inconvenient truth can cause isolation, ridicule and rejection. Even when new models fit real life test results - the paradigm can be inert and blind. This can be illustrated by work of Dobry [11], who raised awareness of deformation dependent soil properties in the 80's - a bold move which failed to find the audience with adequate competence. The geotechnical paradigm appears to be suborn and inert. Similarly, work of P.J. Yoder [44] is not commonly known. He derived and implemented the constitutive formulation of strain-space plasticity for cohesionless materials. His approach is extremely computation efficient and raises new questions - deformation envelope. P.J.Yoder explicitly mentions the problem of "lack of experimental rationale" for calibrating a deformation envelope. Yet in 37 years there were few to none researchers looking for strain (deformation) envelope experimentally. It is important to notice such unusual, unconventional requests. There have to be competing hypotheses, for a paradigm to move forward. Given a dissonance, the two perspectives can compete in attempt to experimentally scrutinize each other. Thus, through inductive / deductive testing and modeling iterations converging towards the truth - a models combining experimentally observable proportion with experimentally non-falsifiable causation [4].

3 Equipment and models

Two testing methods were used during research:

1. A frictionless triaxial apparatus.
2. A foundation prototype.

Aalborg University geotechnical laboratory has a long history of making state of the art testing equipment. A team of experienced technicians assist researchers who are free to express their needs and ideas for potential equipment upgrades. Consequently, testing capabilities are kept at the edge of state of the art. In addition, supervision during testing is minimal, and personal initiative is encouraged. This combination of top grade equipment and freedom to experiment has empowered the findings published in this thesis.

3.1 The frictionless triaxial apparatus

Triaxial apparatus history in Aalborg university began in the 70's with M.Jacobsen [23]. However, the first concepts of triaxial apparatus are about as old as Coulomb's essay itself, reaching the 18th century [30]. A common mistake is to assume the new testing equipment is capable of nothing more than improved measuring precision. Modern (frictionless) triaxial apparatuses can apply larger deformations without causing fracture or bulging of specimens [42]. Therefore, tests no longer need to be stopped after measuring the peak strength. A well calibrated frictionless triaxial apparatus can liquefy a specimen, then compress it towards large deformation (test peak undrained strength), and pull the disturbed specimen back to initial length, all while sustaining isotropic stress states - preventing formation of localized shear rupture and bulging [35]. A common misconception is to assume that triaxial testing always causes shear rupture or bulging. The truth is that shear rupture and bulging can be reduced or eliminated. This can be achieved by implementing two key features:

1. Reduced friction at the end plates (lubricated end platen).

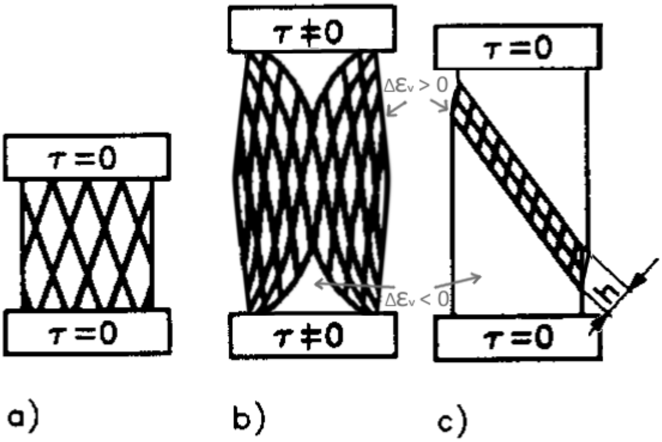

Fig. 2.2: Shear rupture is caused by high friction end plates and 2:1 specimen geometry. a) frictionless triaxial apparatus creates isotropic stress and strain states provided by 1:1 height to diameter ration and low friction end plates. [5] [30] [42]. b) classic triaxial apparatus creating nonlinear stress and strain fields even prior to shear failure. Part of the specimen is contracting while the other part is dilating. [20] [39] [15]. c) Lubricated end plates alone are not enough. If the specimen height not limited, a sliding failure plane with shear zone of thickness h can still emerge. [19]

2. Specimen height to diameter at or below 1:1 ratio (not the conventional 2:1).

It is surprising that frictionless and classic triaxial apparatuses are rarely viewed as two different categories of testing equipment. Some authors even make the misleading statement, that frictionless triaxial is a "harder to use equivalent", of conventional triaxial [30]. Such statements discourage exploration of real-life practical testing limits. It is true that the frictionless triaxial apparatus is able to do what the classical apparatus does, but the classic cannot do some tests which the frictionless apparatus can.

Both apparatus types measured similar values of friction angle (a parameter used to calibrate soil models). In both cases, peak strength estimates match within 2.5% limits [30]. However, measurement precision of all other parameters is substantially improved by frictionless end platen. Some authors overlook this fact or even argue that increased measurement precision is not relevant in geotechnics, as soil properties measured within a construction site have large uncertainties (10% errors are not uncommon and tolerated). Perhaps this is true for engineering practice, but not in research. The discipline of engineering applies known solution to known problems, while research is meant to look for new solutions and new problems: deliver new facts and reach new conclusions. To increase likelihood of observing unknown unknowns, improved precision is an important factor. Less obvious is the value of improved testing scope, which allows to execute tests with unknown outcomes, thus observing behaviors of soil which are not captured or predicted by conventional soil models. Both features (improved precision and a new testing scope) are offered by the frictionless triaxial apparatus. Thus, for research purposes, the frictionless setup is far superior.

Bishop introduced the frictionless triaxial apparatus back in the 60's [5]. He was aware that measurements obtained using the classical method are distorted due to nonlinearities imposed by bulging and rupture. Bishop recognized the problem was caused by high friction end platen [38]. In classic setup, the flat ends of a specimen cannot move, they are locked at a constant radius by friction. Thus, during axial loading, only the midsection can expand. This causes bulging and formation of shear rupture [33]. Because stress and strain become concentrated within the shear rupture zone, part of the specimen can be dilating while another part is contracting. Thus, compromising measurements of volumetric response [20] [39] [15] (See Fig.2.2,b-c).

During triaxial testing, volumetric change is estimated by measuring volume of water leaving / entering the whole specimen (see Wp in Back pressure chamber in Fig.2.3). If a localize shear zone develops, then the shear zone will start dilating before the rest of the specimen does. Meanwhile, the other parts are still contracting (See Fig.2.2,b-c) [20] [15] [39]. Dilating part will suck water in, contracting parts - squeeze it out. Therefore, while measuring total volume change, the two parts can cancel each other out, giving the false impression that no volume change is occurring. To make volume change uniform across the whole specimen (isotropic) a combination of frictionless end platen and specimen geometry of 1:1 can be used [30], as was proposed by Bishop himself [5], back in the 60's, and confirmed by numerous researchers afterwards [42] [30].

Curiously, when volumetric strain become distributed uniformly, the specimen no longer ruptures or bulges. This provides access to a new scope of testing. One can test peak strength more than once, at more than one density, using one specimen [35] [36]. Thus, the novel scope of testing has immediate practical benefits - peak strength can be measured without replacing the specimen. This can be of great benefit when specimens are hard to obtain. Also, replacing the specimen is time consuming, avoiding it can improve research productivity - more tests in less time. But the most significant benefit is the option to observe specimen behavior during complex loading sequences, which reveal limitations of conventional soil models.

If the specimen is not distorted, if the cylindrical shape is preserved, and the initial geometry can be recovered - the test can continue. Alas, too often, a test is stopped due to blindly following outdated testing protocols, inherited from old testing equipment. However, not all researchers suffer such self imposed limitations. Among the handful of experimentalist who looked for

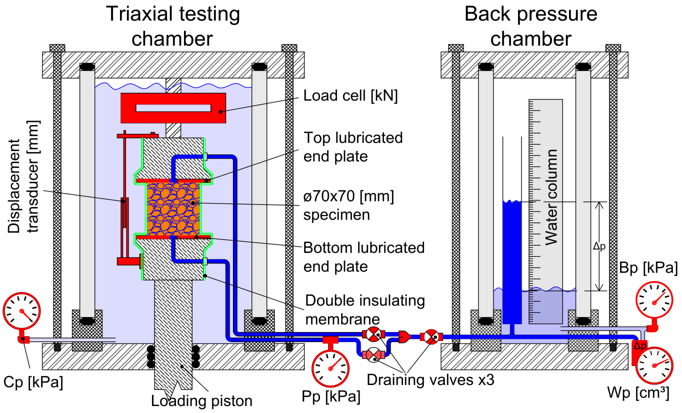

Fig. 2.3: Schematic of the Danish (frictionless) triaxial apparatus. Note the mechanical sensors are replaced with high precision digital equivalent on the real apparatus used at AAU geotechnical laboratory. [23] [18]

new testing potential in frictionless triaxial apparatus is Vardoulakis [42]. He compressed dry sand specimen to axial strains beyond 50% without forming either shear rupture or bulging. He Concluded that even larger strains could be applied if frictionless platen on his apparatus were larger in radius - his specimen radius increased beyond the radius of the end plates. That is just one of many improvements that can still be made.

It is interesting, that properties of the testing equipment are part of the measurement. Measurements representing properties of the specimen will contain some amount of equipment properties too. The effects can be significant, if the equipment is not configured correctly. For instance, stiffness of the rubber o-rings used to make a chamber watertight could become part of the measured specimen stiffness, if the load cell is attached in the wrong way. Similarly, in undrained testing, the stiffness of drainage tubes is important. Consider this thought experiment: pressure of water measured in a perfectly rigid container. Water has very high bulk pressure, near 4 GPa stiffness, therefore very small volumetric strain will cause very large pressure buildup, if the container is perfectly rigid. But if the water is injected using a soft drainage tube, the tiny volumetric strain will deform walls of the drainage tube, without causing pressure buildup within the perfectly rigid contained. Thus, effectively reducing the measured stiffness of water, down to the stiffness of the drainage tube. Such factors are crucial to consider in research applications, but are normally not required in engineering practice. In engineering, known parameters of known models are calibrated - those had been found and developed using conventional equipment with conventional settings. In research "the missing parts" are being looked for, thus it is crucial to remove all uncertainties and sources of error.

The way the equipment is constructed, can influence the outcome of tests. Consider the example of measuring Skempton B (used to estimate specimen saturation level). The confining pressure (Cp in Fig.2.3) will act not only on the specimen, but the drainage tubes as well. For sand $B = \Delta Pp/\Delta C_P$ can be used, a value near 1 means high saturation (no air bubbles within the specimen). But a substantial part of ΔPp can be caused by ΔCp acting on the drainage tubes (rather than the specimen). It is important to be aware of such sources of error. To avoid such errors, months were spent calibrating the equipment and checking sensitivities of individual components. If length of drainage tubes is increased, Skempton B measurement is distorted. If a longer tube is put inside the testing chamber - the Skempton B value goes up. If a longer part of the tube is put outside (the distance between testing chamber and draining valves), Skemptons B value goes down. Thus, for research, it is important to understand the impact of every component in touch with the quantities being measured. The drainage tubes must be stiff (made of extra stiff nylon) and as short as plausible. The best practice would be to have drainage valves installed within the end plates themselves, but this option was not available at the time Fig.2.3).

The frictionless triaxial apparatus was calibrated to the extreme of water tightness. When doing undrained tests no more than $10kPa$ pore pressure drop was allowed per day. Which is within $\approx$ 0.005% volumetric strain, or leaking $4 \cdot 10^{-8} ml/day$. This is remarkable, given stiffness of water was preserved (extra stiff nylon tubes used, near $4GPa$ bulk stiffness). Due to high stiffness of water, sub-microscopic volumetric strains become tangible. Two latex sleeves, with viscous vacuum grease in between had to be used to prevent osmosis of water molecules through the membrane. All in the effort to prevent "unknown unknowns" from evading the observer.

Because measurements are taken of quantities outside the sensory range of a human, diagnosing the problem can be complicated. Osmosis through a membrane acts like a leaking pipe, and to a well trained theoretician will look like a slowly creeping deformation. One could end-up trying to model this as a creeping behavior, rather than recognizing the pattern is caused by a sub-microscopic leak. The creep has stopped after introducing the second membrane, with vacuum grease in between the two. It is important to recognize that the laboratory coat is not meant to protect the researcher - the coat is there to protect the specimen. The researcher is a source of contamination. Both the researchers physical presence and thoughts can be a source of bias and error. Measurements taken while observing sand, have distortions caused by equipment and the researcher too.

The last aspect to be mentioned: the frictionless triaxial apparatus has many names. Bishop mentions "lubricated triaxial apparatus" [5], Vardoulakis - "improved triaxial apparatus" [42], Ibsen - "the Danish triaxial apparatus" [18]. This can cause confusion. Albeit, it is worth recognizing that each apparatus has its own unique configuration [30], therefore is likely to have its own unique testing limits and capabilities. The full name of the triaxial apparatus used for tests shown in this thesis is "the dynamic version, of the Danish triaxial apparatus". The apparatus was upgraded by L.B.Ibsen [18], [19] and students under his supervision [26] [34] [35].

3.2 Foundation prototype tested

Small scale offshore foundation tests are also developed at AAU geotechnical laboratory. Prototypes of foundations ($\approx 1 : 50$ scale) are embedded into large boxes with fully saturated sand. Loads are applied and measurements using digital sensors and actuators. This type of testing takes a lot of space, consumes a lot of time and material resources and requires a full crew of technicians in addition to the researcher himself. Thus empirical R&D is very costly, compared to the cost of numerical simulations. But until satisfactory numerical models are found, prototype testing needs to continue.

The small scale tests were conducted on mono bucket foundation: an innovative offshore foundation developed for offshore wind turbines [28]. It is meant to be a superior alternative to pile foundations. A mono bucket can be sucked onto (or pushed off of) the sea floor like a suction cup (see Fig.2.4). During installation, inclination of a full scale mono bucket is controllable using two methods - one penetrating clay soil layers, the second - sand. In clay, inclination control uses 3 smaller chambers attached along the tip of the skirt. In sand, the inclination is controlled by high pressure water nozzles, which loosen up the sand along one side of the skirt. Because installation is controlled using water pressure (no hammers) the installation process is very quiet (and fast). This reduces the cost of installation substantially, compared to a pile. A mono-bucket takes roughly 4 hours, compared to roughly 2 days per pile foundation. A monopile foundation cannot be pulled out of the sea floor either, unlike a mono bucket - which can be easily decommissioned, and potentially reused again.

A mono bucket consumes up to 25% less metal than a mono pile of equivalent strength. This is achieved due to redistributing the loads more efficiently:

1. The lid has a large area, thus vertical load is spread over a large soil surface (like a gravity foundation would).
2. The skirt has a large radius (leverage), thus overturning resistance is improved, a shorter skirt is required.
3. The water tight chamber further improves resistance to rapid (impact) loads, by holding onto a large mass of soil and water trapped within.

The idea of using a Mono Bucket for offshore foundations was proposed by Lars Bo Ibsen at AAU in year 2000. The proposal was followed with a comprehensive chain of small scale prototype testing. The low cost solution quickly caught attention of offshore industry, Universal Faundation A/S was started in cooperation with Fred Olsen. In November 2002, the first full scale prototype of the mono bucked was tested (shallow water, onshore penetration test, no wind turbine attached). In March 2009, the Mono Bucket was installed to support a meteorological mast at the Horns Rev 2 wind farm (with additional sensors to monitor performance). In October 2011, Universal Foundation was awarded a contract for installation of two meteorological masts at Forewind's Dogger Bank offshore wind farm. In September 2014, Universal Foundation completed the Trial Installation campaign across three major Round 3 offshore wind sites (Dogger Bank, Dudgeon and Hornsea) in the UK North Sea. One down scaled mono bucket was installed and removed 29 times in 24 days, in various soil profiles, encountered in open sea. Each installation achieved inclination control within 0.1 degree off perfect verticality. The constant "installation-retrieval-installation" cycle demonstrated the unique robustness of the Mono Bucket. The project was managed by Statoil and delivered by Universal Foundation, in partnership with The Carbon Trust, Statkraft, EON and DONG Energy, all in close cooperation with Aalborg University [1].

Given how well the innovative design works, one may assume prototyping is no longer relevant. However, the working principle of the foundation generates a complex array of soil response: pore pressure gradients, cyclic loads, partial liquefaction and re-stabilization of soil stiffness. This requires improved models of soil, and soil to structure interaction. Due to novelty, potential clients raise questions which cannot be answered by contemporary soil mechanics:

1. How is the soil affected during installation? While the mono-bucket is sucked onto the sea floor, pore water pressure gradients develop. They interact with confining stress (overburden pressure). In addition to soil being mechanically disturbed by the skirt, as it penetrates.

2. Dynamic stress and strain fields are created while the mono-bucket is in service. Dynamic loads cause partially drained soil behavior, which cannot be reliably modeled by existing methods.

3. Suction caissons similar to mono-bucket are normally used in anchors and jackets to carry vertical (axial) load. Therefore, traditionally minded engineers are skeptical of mono-bucket capacity to carry lateral (overturning) loads. Alas, the question is not if it is plausible, but rather "how big" a mono-bucket needs to be.

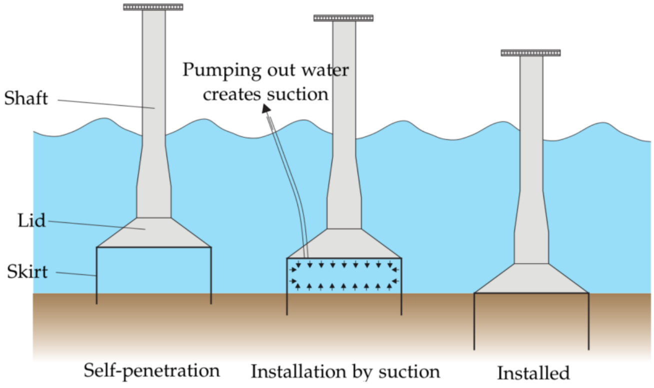

Fig. 2.4: Illustration of the Mono Bucket foundation for offshore wind turbines [25]

4. Pore water cannot escape from within the water tight chambers. In theory, this can have both positive and negative effect (additional strength through boot effect [29] [29], versus reduced stiffness by liquefaction). Alas, test results consistently show liquefaction resistance is good [25].

To answer the questions, fundamental research of disturbed sand properties has to be done. For that purpose a simplified foundation prototype (see Section 3) was tested using unorthodox loading scenarios. The original testing procedures evolved during research, as they kept re-adapting towards soil response patterns observed experimentally. By design, the research program targeted and investigated patterns and regularities not described or predicted by conventional theory. Those patters were followed down the rabbit hole, in attempt to detect fundamental properties governing them (see Appendix D).

3.3 Choosing the inputs

The frictionless triaxial apparatus and the foundation prototype testing - are not a new type of testing equipment. Alas, novel testing procedures can be applied using them. To access unconventional observations using conventional testing equipment, some software had to be upgraded. The Proportional Integral Derivative (PID) control algorithm, for instance. There are 2 default modes of PID control piston:

1. Force (F) controlled (F-PID) - calibrated to find U which generates targeted F.
2. Displacement (U) controlled, (U-PID) - calibrated to reach towards U targeted by the user (ignoring F measurement).

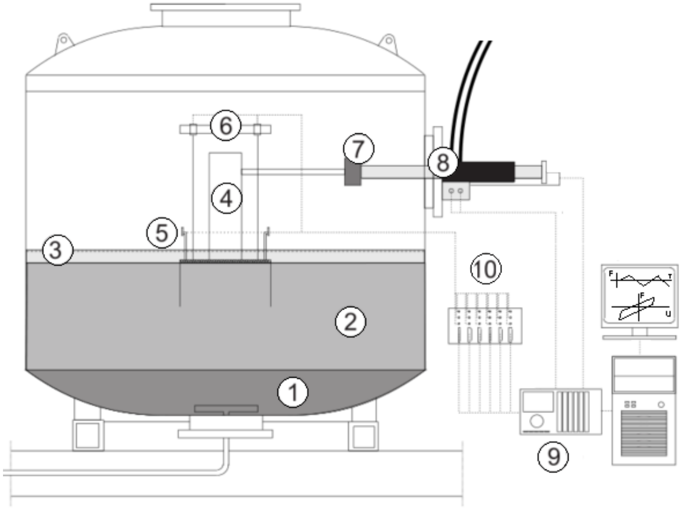

Fig. 2.5: Illustration of the testing rig used for Mono Bucket foundation prototype testing [29]. The sand box and the prototype are placed inside a pressure chamber, where the dynamic behavior of a foundation can be tested in pressures corresponding to 20m water depth. LIst of components shown in the graph: 1) drainage (coarse gravel). 2) Sand (Aalborg University sand no.1). 3) Water level. Sand is fully saturated at all times. Effects caused by higher water head can be added by increasing air pressure inside the pressure chamber. 4) shaft attached to the foundation prototype. The lateral piston pushes and pulls against the shaft. 5) Valves closing water flow at the lid of a Mono Bucket prototype. Pore pressure transducers are placed in front of some valves, with drainage channels positioned along the skirt (pore pressure development was analyzed in thesis by S.D.Nielsen [25]). 6) displacement transducers measuring vertical displacement in 2 points. 7) Load cell, measuring force applied by the hydraulic piston. 8) The hydraulic piston, controlled by a PID controller. 9) PID controller made by MOOG, and a PC allowing real time monitoring and controlling of loading. 10) Data acquisition station, converting analog reading to digital signal (MGC plus).

The standard PID controller can be incompatible compatible with sand testing, as sand extremely nonlinear stiffness curves. The specimen can become rock solid, fluid or even show negative stiffness within one loading cycle. To understand why this is problematic, behavior of the PID controller has to be understood. The PID controller makes a hydraulic piston move by injecting oil in micro steps. Oil is near incompressible, therefore U-PID is always linear - the same number of oil injections generates the same ΔU (given, oil pressure is high enough to overpower resistance). Whereas F-PID control precision depends on specimen stiffness, different number of oil injections will be required for the same ΔF, depending on specimen stiffness. This makes U-PID calibration stable, while F-PID calibration is very problematic due to specimen stiffness change. To solve the problem, the standard F-PID control had to be upgraded, but to do so, stiffness patterns had to be understood first. As new knowledge was gained during initial stages of testing, a method to apply U-PID while measuring real time F was developed (see Appendix F).

Normally, prototype tests are conducted by using F-PID as the input, while measuring U as the output. This path of causation is convenient, for it matches the way structures are normally designed - in the construction standards loads (F) are applied, and the resultant deformation (U) is predicted. Therefore, when research is conducted by engineers, there is a bias to test by apply F as input and measure U as the output. However, this path of causation can have counter intuitive consequences: by applying F, not only U is generated. Equation of motion (Eq.2.1) says F combines three effects: stiffness (K), damping (C) and inertia (M), which are triggered by deformation (u), loading rate (v) and acceleration (a). Therefore, if F is the input, then u,v and a are the outputs, which creates a complex encryption containing K, C and M components. To make it worse, in sand all components - K, C and M - behave like nonlinear, state dependent functions. The C component can be both positive and negative - it creates extra reaction force during dilative phase, and removes some reaction force during contractive phase. K of sand is not linear either, it generates curves of changing proportion, and a different curve for every loading direction. Therefore, by applying F the (for more details see Appendix D)

$$F = K \cdot u + C \cdot v + M \cdot a \tag{2.1}$$

If u is applied as the input, the operator can control the v and a components as well. By applying u increasingly slower, a point where $v \approx 0$ can be achieved. At this point quasi-static K hysteresis loops can be isolated, because C component is "switched off". After the K component becomes predictable (or, better yet, prescribe-able), it becomes plausible to isolate nonlinear C from $C \cdot v = F - K \cdot u$ (given input condition $a \approx 0$). Given the assumption based on equation of motion, most of the tests were made using U-PID, while observing the F history. This can be seen as the opposite of conventional testing. Instead of following engineering guidelines, research was conducted by following proportion and causation observed within the data itself. Inputs were selected according to their descriptive, predictive and prescriptive power.

3.4 Models

Theory is shaped by observations, generated by test results. Similarly, testing procedures are shaped by theory. Therefore the way tests are conducted (test results) are biased by existing theory. Thus, exposure to models with stress envelopes creates a bias to look for stress envelopes. It is worth noticing that "hunting for stress envelopes" has been largely inconclusive for solving cyclic loaded sand problems [10]. One school of thought emphasizes that cyclic loads cause loss of stiffness, while other emphasize that sand stabilizes. In reality, both sides are correct, both assumptions are based on test results, the existing theory merely fails to combine the two into one set of rules. This is no easy task, as stress space models face a paradoxical problem: The same stress amplitudes can cause both loss and recovery of stiffness [34] [36]. What causes stabilization in drained mode, can cause liquefaction in undrained. Also, undrained sand remain stable during stress cycles above drained strength limits [18] [35], but destabilize in partially drained. Such lack of consensus could be caused by either missing variables or a false assumptions within convention. The key assumption being - stress is the input, strain is the output. This thesis explores a opposite perspective (strain - input, stress - output, stress as a function of strain).

While cycles of deformation were input, the resulting stiffness hysteresis loops were observed for patterns and regularities proportional to deformation history. The observed patters were then fitted using Bezier curves, by hand, on top of raw data plots. This allowed to quantify causation and proportion governing the behavior of the phenomenon (changes in position and size of the stiffness hysteresis loops). In the outcome, an original, evidence based model were born. It was named as "Bezier stiffness model" (BSM) described in Appendix E.The model preserves logic and proportion observed experimentally, without deeper theoretical derivation. It allows to interpolate boundaries predicted within effective stress space, while interpolating the hysteresis loops within a deformation (strain) envelope. The new method does not contradict validity of the Coulomb stress envelope, it should be viewed as a different way of interpolating the stress history instead. To some degree, the new methodology happens to support principles used in strain-space plasticity formulation [44]. However, the conclusions to used a strain-space envelope was made without being aware of strain-space plasticity formulation. Thus, the BSM was developed based purely on experimental

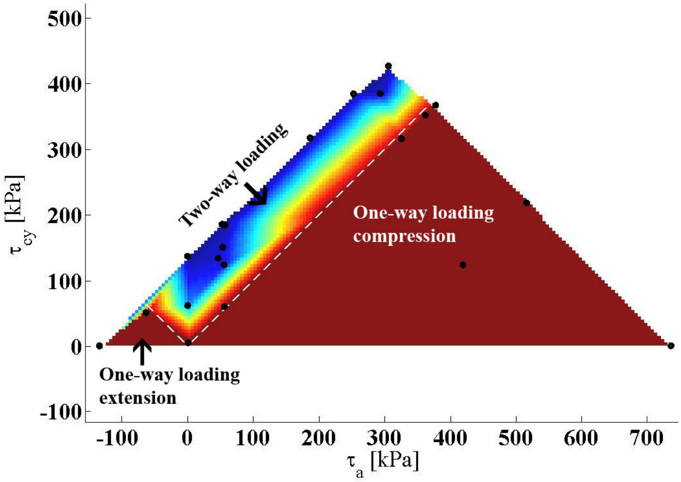

Fig. 2.6: Andersen's chart revels Aalborg university sand no.1 specimen sensitivity to liquefaction. 1000 cycles of sinusoidal loading is applied using different combinations of amplitude (τ_{cy}) and mean value (τ_a), consequent accumulated deformation is measured. Deformation beyond 10% strain considered as specimen failure, tests were stopped before applying 1000 cycles if failure was reached prematurely [34].

results, and does not follow any existing theoretical formulation. It could be described as a function made for fitting raw measurement plots. Alas, in doing so, it preserves intricate features governing the behavior of a real-life phenomenon.

It is important to note that the models using deformation (or strain) envelopes are compatible with experimental data obtained during stress cyclic loading (see Figs. 2.6, 2.7 and Appendix G). The strain based models merely add a new context: deformation controlled variables, instead of stress controlled. If a pattern behaves in proportion to deformation, modeling it as a function of strain (instead of stress) can add extra functionality. One major flaw in stress cycle diagrams is lack of ability to move from one stress amplitude to another. This means design of the structure cannot be optimized to fit changing wave heights during a storm (a threat of excessively conservative design). To make transitions between different stress amplitudes plausible, methods of quantifying and updating disturbed soil states need to be found (as illustrated in Fig.2.8). If soil states change in proportion to deformation history, the new models can open the door to achieve more efficient design.

Sand stiffness behaves like a state dependent function. Thus, some principles used in describing state-dependent systems were borrowed from the paradigm of computer science (machine learning). The borrowed concept forced the researcher to change his perspective. Instead of analyzing sand within the limits of conventional geotechnics, the analysis was done to ob-

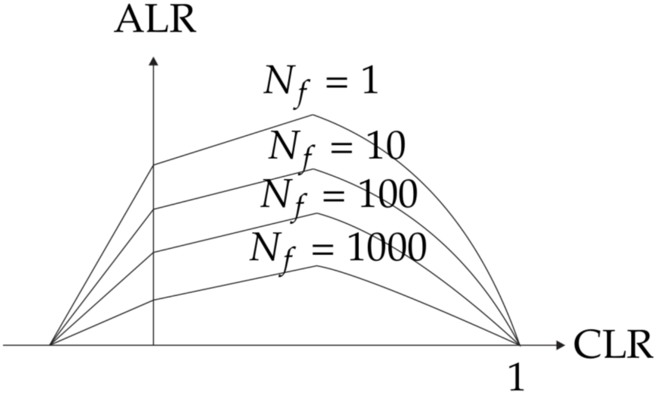

Fig. 2.7: Cyclic contour diagram of a foundation prototype [25]. Showing normalized loading amplitude (cyclic load ratio, CLR), around a mean value (average load ratio, ALR). The iso-parametric curves show how many cycles it took to reach 0.25^o inclination.

serve raw patterns and regularities within the data structure itself. Unconventional level of descriptive and predictive power was achieved in the outcome: it became plausible to recover the initial soil state, the specimen can be disturbed and reset back to initial state many times. Thus validity of the method is proved experimentally. The research has revealed the existence of a new phenomenon - stabilizing stiffness hysteresis loops. Features governing the phenomenon were then found - it became plausible to predict and control the size and position of hysteresis loops. Thus, delivering both: new facts and new conclusions.

It is worth noticing that novel findings will not be applicable in the industry instantaneously - after a phenomenon is discovered and analyzed, it can take decades to develop practical engineering tools from it. Alas, novel findings can find application in the research institution itself. Since a specimen can be reset to the initial state, testing productivity could be improved dramatically. Consider an example from real life testing procedure: a tests requires 2 days of preparation and the test itself takes up to 3 hours [25]). Time spent in preparation does not generate new data, thus time spent in preparation is wasteful. If initial soil state is reset in a few minutes, 8 tests per 24 hours could be executed. That is a 1600% increase in efficiency. More data generated in less time. Thus, new phenomenon are discovered and ways to control them are found, the new knowledge will eventually find application in unpredictable number of areas: from industrial applications, to improved research efficiency.

It is interesting, that disturbed soil states can be quantified using a state transition diagram. But it remains unclear how to best transform state tran-

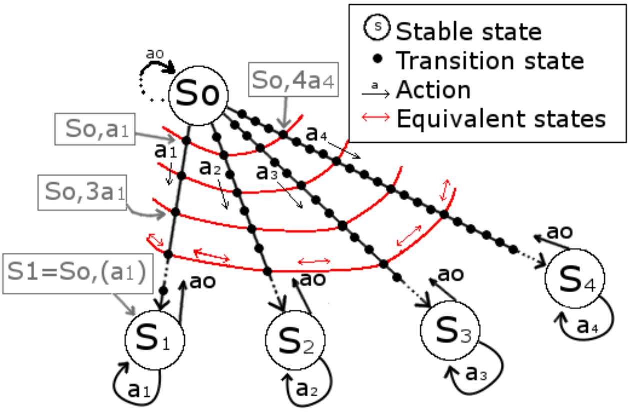

Fig. 2.8: State functions can be illustrated as a state transition function. The state (S) changes each time action (a) is executed. for instance, if $a1$ is repeated many enough times, the initial state So transitions through many "in between" soil states (($So, a1$), to ($So, 3a1$)), up until converging to a stable state $S1 = So,(a1)$. If means to quantify disturbed states are found, it becomes plausible to jump from one chain of actions to another. For instance, in this example, starting at So, executing $a1$ generates soil state ($So, a1$) which is equivalent to ($So, 4a4$), which can be continued along the path set by $a4$, all the way up to stable state ($S4,(a4)$). Notice, the ao - if this action is found, then So could be recovered.

sition diagrams into practical engineering solutions. Alas, to control - is to understand. Phenomenon controlled by deformation, should be plausible to modeled as functions of deformation. Inputs adequate to control a phenomenon, should be adequate to model the phenomenon. Thus, it is exciting that the novel models allow to de facto control:

1. Loss and recovery of stiffness in sand
2. Combine drained and undrained loading history in one sequence
3. loss and recovery of dilativity

4 Scope of the thesis

The scope of the thesis is quite wide, fundamental questions are raised: new testing options were discovered, which gave rise to discovery of a new phenomenon, which was then conceptualized into original models, which question the convention by delivering unprecedented level of predictive and prescriptive power - demonstrated experimentally. The first stage (the new scope of testing) is the root of all findings presented in this thesis. Above all, the reader is encouraged to question old testing standards. Conventional test procedures repeat what is already known (fit new values, to known coefficients, in known models), but new testing options allow to detect anomalies and paradoxes. In attempt to extract meaning from anomalies and paradoxes observed, various data analysis techniques were borrowed from different paradigms:

1. "minimum and maximum" (as used in original Coulomb essay [8], as described by Schofield [37]).
2. pattern recognition, state transition diagrams - computer science, machine learning.
3. adaptive PID control, equipment upgrading - mechanics, electrical engineering
4. principles of truth and scientific method - philosophy of science

The scope of this thesis could expand beyond geotechnical paradigm. In programming courses, sand could be used as an example of a state transition function which occurs in nature - in a programming course. It would be interesting to see what data analysis experts could discover, if they were given the test results without labels attached. If there are no labels, they would not know where the stress or where is the strain - they could only see data plots on arbitrary x and y axes. After attempting such "blind folded" analysis, the sand starts to look very different:

- Sand is no longer a brittle material. After testing peak strength, a specimen can be pulled back to initial length and re-stabilized. Therefore, perception of what is plausible in testing has changed.
- It is plausible to quantify disturbed soil states. The principles of state-space transition allows to observe disturbed soil states as a function of deformation (strain) envelope. Therefore, raising awareness of alternative modeling methods.
- It is plausible to combine drained and undrained sand, loss and recovery of stiffness, during irregular loading cycles. All while using models with fewer variables and matrix inversions.

The content on the thesis fits the definition of research quite completely - both new facts and new conclusions are present. The fact of a new phenomenon was discovered, and new conclusions were reached while deductively testing the properties of the phenomenon. The new conclusions shake roots of a branch of geotechnical paradigm, where the effective stress is viewed as the anchoring point. The outcome of this thesis concludes that the effective stresses are a functions of strain history - not the other way round. The audience in conferences and workshops had proposed to call it "a shift in paradigm". However, strain space envelopes [44] and strain normalized parameters [11] [17] had been mentioned long before this thesis. The testing equipment is not new either - old testing equipment is merely used in a different way. Thus, the content merely explores a parallel branch of geotechnical modeling, surface of which had been scratched in the past. It is unpleasant to ask why strain based models and tests are underrepresented in geotechnics. Perhaps novelty is a threat to old standards. Novelty may expose weaknesses and shortcomings in very expensive industrial projects. Also, value of novelty is hard to estimate - nobody know what the new solutions will be good for, thus research is a high risk investment. Even if fueled by blind curiosity, innovative solutions can insult insecure experts, whose prestige and life's work depend on preserving existing concepts. In theory novelty is the source of profit, but in reality it raises inconvenient questions. Perhaps, therefore, throughout history, unconventional ideas were met with fear, discontent, ridicule and rejection. Alas, it is crucial to notice when something different works in real-life practice: within a limited scope of application, a controlled laboratory environment. It is a starting point for innovative research branches - new models, new testing procedures. Properties of a new phenomenon must be observed first - before the observations can be applied for something substantial. The key to judge quality of solutions is to observe the level of control the solution gives (the highest analytic power). The more control a solution gives - the less uncertainty the solution has. Thus, the scope of this thesis goes through all steps: from observing a phenomenon for the first time, to making models which can de-facto control it. In addition, simple examples of potential application are given too (simulating a beam embedded in sand with p-y curves).

Chapter 3

Research results

1 Workflow chart

The chronological order of research is shown in the flowchart in Fig.3.1. The flowchart serves as a map for the rest of the thesis. As problems were were solved, new questions were raised, thus titter-tattering between inductive analysis / deductive testing. Hypotheses explaining the observed data patterns were raised inductively, and the next test was designed in attempt to falsify the hypothesis deductively. Therefore leaving explanations of the observable, which are which survived experimental scrutiny. Some iterators unfolded in parallel, therefore a flowchart is given, to clarify the sequence of events.

2 Frictionless triaxial - testing and modeling

2.1 Andersen's charts

Steps 1 to 3 in Fig.3.1 were attempted following procedures identical to those published in preceding M.Sc. thesis [2] [34]. Cycles of fixed stress amplitude were applied on undrained sand specimens, and the resulting deformation was measured. Results were then plotted using triangulated surfaces, creating an "Andersen's chart" (see Fig2.6 and Appendix G). such stress charts have substantial limitations - results are anchored to the initial state, therefore repeatability of the outcome depends on the initial soil state [35] [36]. As stress cycles are applied the initial state is lost, therefore it is not plausible to use this chart for applying stress cycles of different amplitude. To do so, would require to quantify disturbed soil states and follow them through the stress cycles (see Fig.2.8). Since it is not plausible to combine effects of different stress amplitudes, the use is limited to generalized decision making,

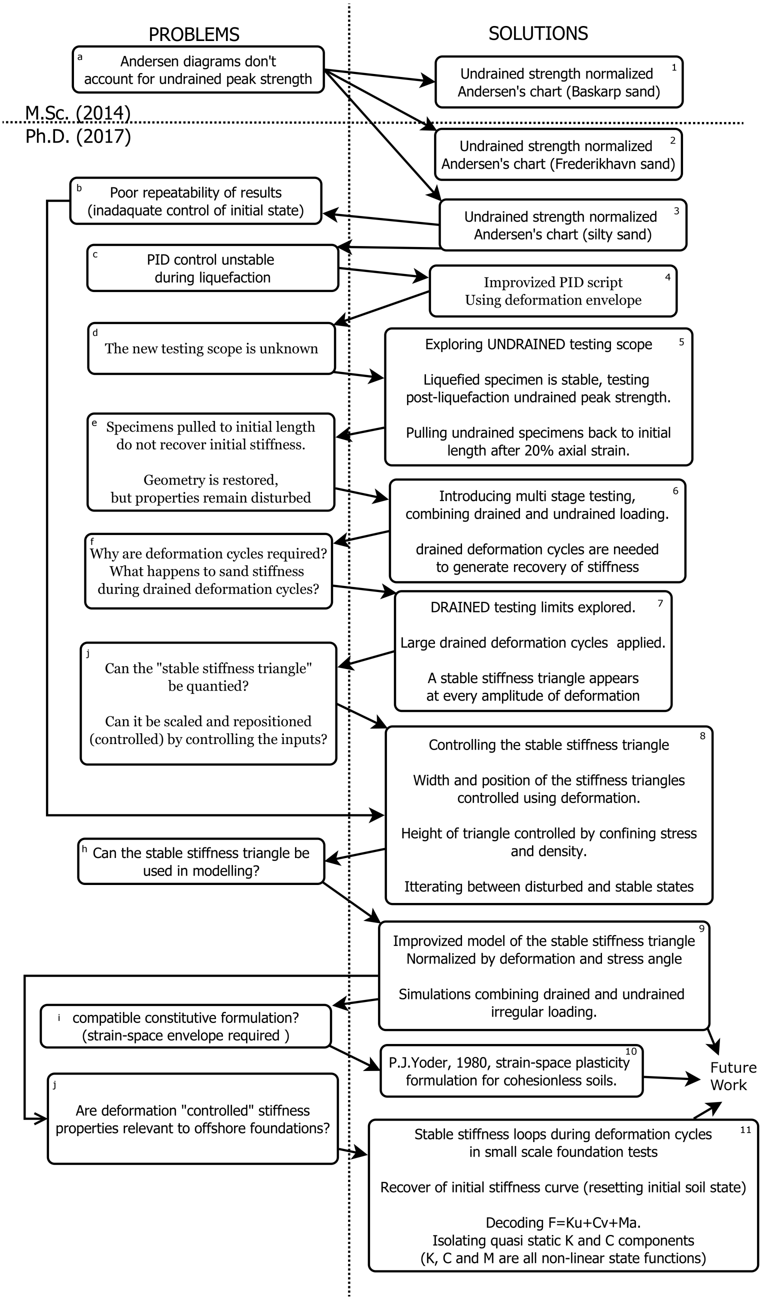

Fig 3.1: Work flowchart for the duration of Ph.D.

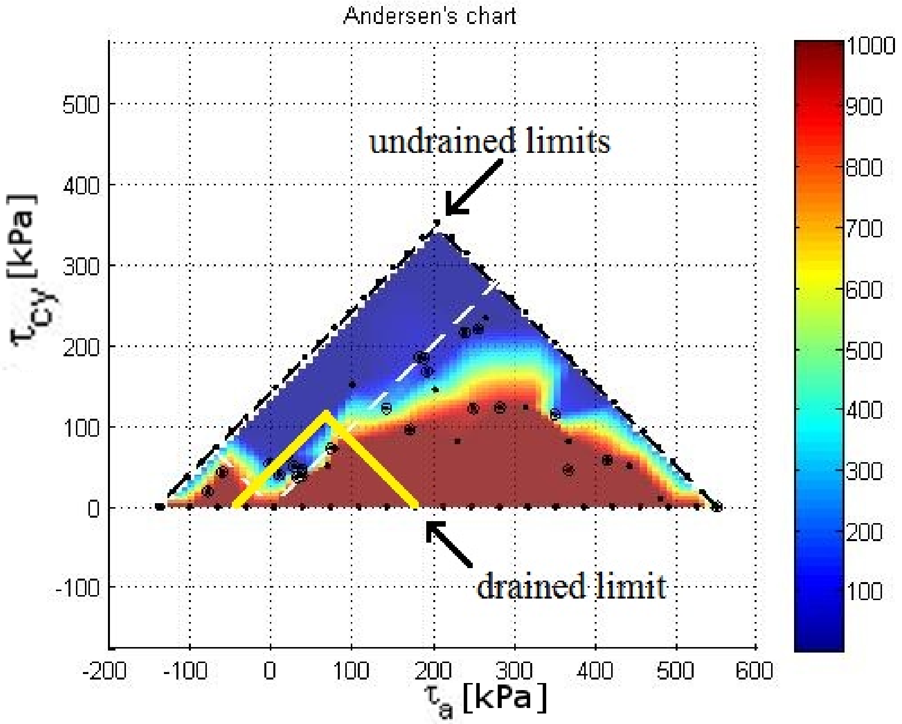

Fig. 3.2: Andersen's chart revels Frederikhavn sand specimen sensitivity to liquefaction. 1000 cycles of sinusoidal loading is applied using different combinations of amplitude (τ_{cy}) and mean value (τ_a), consequent accumulated deformation is measured. Deformation beyond 10% strain considered as specimen failure, tests were stopped before applying 1000 cycles if failure was reached prematurely [35]. Notice, specimens can liquefy below drained strength limit, yet undrained strength limit is substantially larger than the drained one.

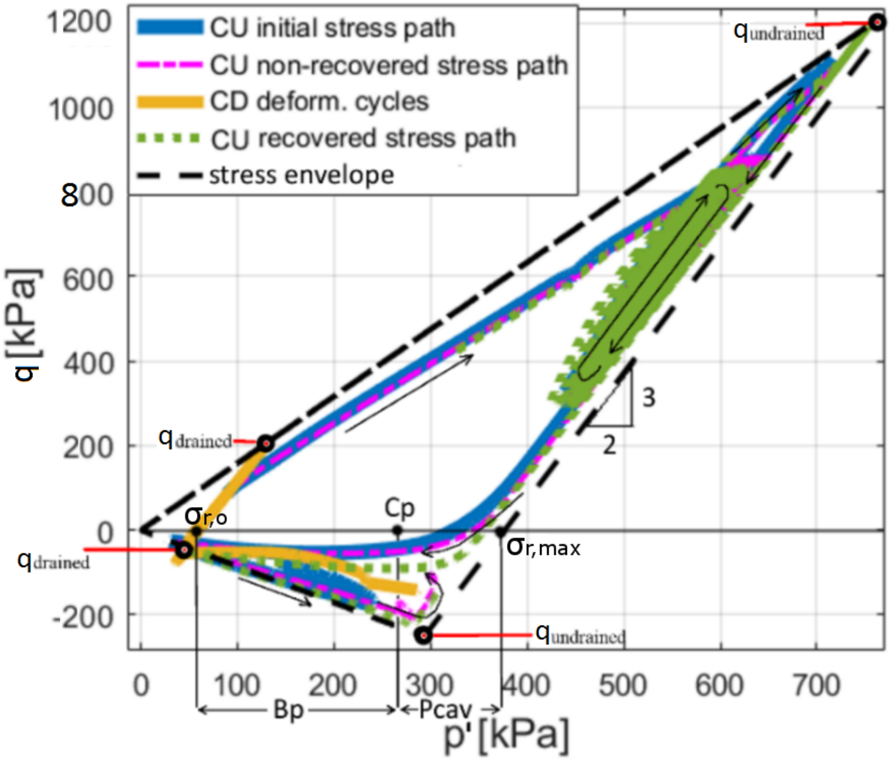

Fig. 3.3: A plot of data measured during multi stage triaxial testing. In undrained condition, dilation of sand is resisted by stiffness of pore water. As soil skeleton dilates, it pulls the water apart towards absolute vacuum. When pore pressure reaches $\approx -100kPa$ pore water cavitates, thus losing stiffness, thus setting the limit of undrained bearing capacity. Stiffness paths during which the stress histories were generated are shown in Fig.3.8.

such as avoiding the biggest wave in a storm, or discretization of the stress amplitudes into liquefying and non-liquefying regions:

1. Sand can liquefy during stress amplitudes below drained strength limits, during two way loading.
2. Sand does not liquefy during adequate one-way loading, even beyond drained limit.

In the Andersen's chart, it is visible that two-way loading is a potential trigger for liquefaction in undrained cohesionless soils. In addition, it is curious how undrained sand loses stiffness (during liquefaction), yet the strength is preserved. Notice undrained strength is much higher than drained (undrained strength is proportional to initial pore pressure (Pp) [19]). The undrained strength limit was not accounted for in the original Andersen's chart [2], thus undrained strength normalized Andersen charts were the subject of the M.Sc. thesis [34] preceding this Ph.D. thesis. The undrained sand strength limit is a very interesting for deep water foundations and anchors, as undrained strength increases proportional to overhead water pressure (compare $q_{drained}$ with $q_{undrained}$ in Fig.3.3). At $20m$ deep water, $200kPa$ additional confining pressure will be generated within voids of dilative sand, before reaching undrained peak strength. Thus, deep water conditions can increase structure strength very substantially, as is atempted by the mono bucket foundation design [29] [45]. Another interesting thing to notice in Fig.3.3 is that the stress paths are near identical despite accumulated deformation being different (to see the stiffness paths skip forward to Fig.3.8). This will be a recurring theme throughout the thesis - different deformation amplitude generate similar stress paths. If the same stress path has multiple strain paths - strain cannot be deterministically modeled as a function of strain. Alas, different strain paths converge to the same stress path, thus there is a plausibility that effective stress could be expressed as a function of strain.

It is important to recognize what "similar stress history, at different deformation amplitudes" implies for modeling practice. It is only plausible to map from the "different" towards the "common" feature. Thus, the different (strain history) must be used as input, and the common (stress) - as the output. To illustrate what this means, consider a thought experiment illustrated in Fig.3.4: two hysteresis loops (representing 2 disturbed soil states) can be seen. Attempts can be made to express the hysteresis loops as function of U or F:

- If U=f(F), then Fmob is the input. In which case a deterministic solution cannot be established, as both Umob are a plausible outcome.

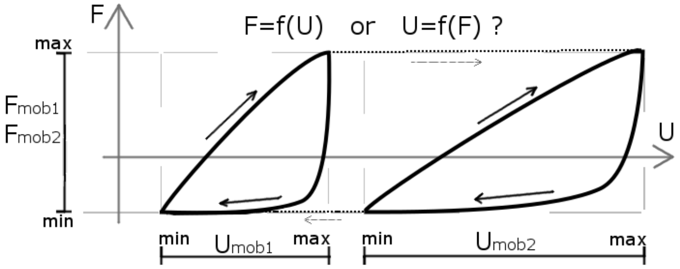

Fig. 3.4: A thought experiment introducing a mechanism, which allows to control sand stiffness. Different deformation history (Umob) generates identical force amplitudes (Fmob). Such system is best interpreted by assuming $F = f(U)$ rather than $U = f(F)$. If Fmob are applied, there is no way to know which hysteresis loop (if either) will become active. While applying Umob denotes full control over the outcome.

- If F=f(U), a deterministic solution is plausible, as all Umob provide the same Fmob. Thus, knowing U and ΔU is adequate to interpolate the entire strain space.

This is, in essence, the key conclusion reached during the thesis. The conclusion illustrated by thought experiment in Fig.3.4 is given up front, so the reader can put data plots into perspective. The final statement is simple - by apply deformation cycles on sand, the stiffness hysteresis loops appear. Then, by controlling Umob, the size and position of converging stiffness hysteresis loops can be controlled. Fmob limits remain constant, as long as confining stress does not change (thus, the Fmob amplitude can be controlled by controlling the confining stress). In triaxial testing and in foundation testing - the principle remains the same. Nevertheless, this is a non-conventional perspective of reasoning: it explains strain-space curves, as interpolate within stress-space boundaries (fmob), using strain-space envelopes (Umob).

The unconventional conclusion took three years to reach. It evolved gradually, following many iterations of solving a problem and raising new questions. The process began with making the Andersen's chart shown in Fig.3.2. It was made for Frederikhavn sand at relative density of 80%. Notice, in the chart each stress amplitude has only one point, meaning a test has accumulated a certain amount of deformation. Alas, the same amplitude can have more than one plausible outcome, thus there is some uncertainty associated with the method. Thus, repeatability of the Andersen's chart comes with some level of uncertainty. The uncertainty can be attributed to lack of control over initial soil state - only the initial density is controlled, but this is not enough to ensure reliable repetition of "initial state". Thus, some unknown variables are not accounted for. In addition, during liquefaction stiffness of sand specimens changes significantly, thus standard PID control struggles to apply required stress cycles. Thus, in the first iteration of research, two problems had to be solved:

- Changes in liquefying specimen stiffness make PID control unstable. Attempts to improve PID stability during liquefaction follow path (3) to (c) in flowchart Fig.3.1.
- Controlling density (and confining stress) is not enough to ensure repeatability of initial state, thus additional soil state dependencies are looked for by going from square (3) to (b) in the flowchart Fig.3.1).

2.2 Liquefaction compatible PID control

Proportional integral derivative (PID) controller is a very robust controlling method. It is used in a wide array of industrial control applications. However, PID controllers have their limitations - the P, I and D coefficients need to be calibrated for a specific system, with a specific stiffness. If stiffness changes, a PID controller can become unstable, thus applying forces above (over-load) or below (under-load) the targeted value. The problem is visible in Fig.3.5, where stiffness paths with localized imperfections are visible (more detail in Appendix F). The imperfections occur after stiffness temporarily drops to near 0 after crossing the $F = 0$ axis (partial liquefaction caused by two-way loading). When stiffness becomes near 0, the F-PID controller accelerates in attempt to compensate for the mismatch between real-time measured F and the targeted F. The PID controlled accelerates gradually, and de-accelerates gradually, and because the stiffness recovers rapidly the excess acceleration causes the PID controller to "bump" into the stiffness path (like a ball hitting a wall). Thus, standard PID control is not compatible with highly non-linear stiffness testing, such as liquefying specimen testing. Liquefying sand specimens can transition from near vertical, to flat horizontal stiffness, with an negative tangent stiffness phase in between. twice per each loading cycle. Therefore, to apply stress (or F) cycles on liquefying specimens standard PID is not adequate.

Unlike F-PID, the U-PID control does not depend on specimen stiffness. In its essence, the PID control algorithm is meant to predict how much oil has to be injected into the hydraulic piston. Because the piston is very stiff, the amount of oil required to move a distance ΔU is constant, regardless of how stiff the specimen is. Therefore, U-PID control is unconditionally stable. Therefore, an attempt was made to create an algorithm which uses U-PID control to apply F cycles. Resulting in an improvised peak over threshold (POT) script, development of which is explained in Appendix F). It works by applying ΔU towards $U \rightarrow +\infty$, while monitoring real-time F values. Once the Fmax is reached (see Fig.3.5), the loading direction is reversed to $U \rightarrow -\infty$. Because targeted F is used as a threshold, the method can be referred to as F-POT.

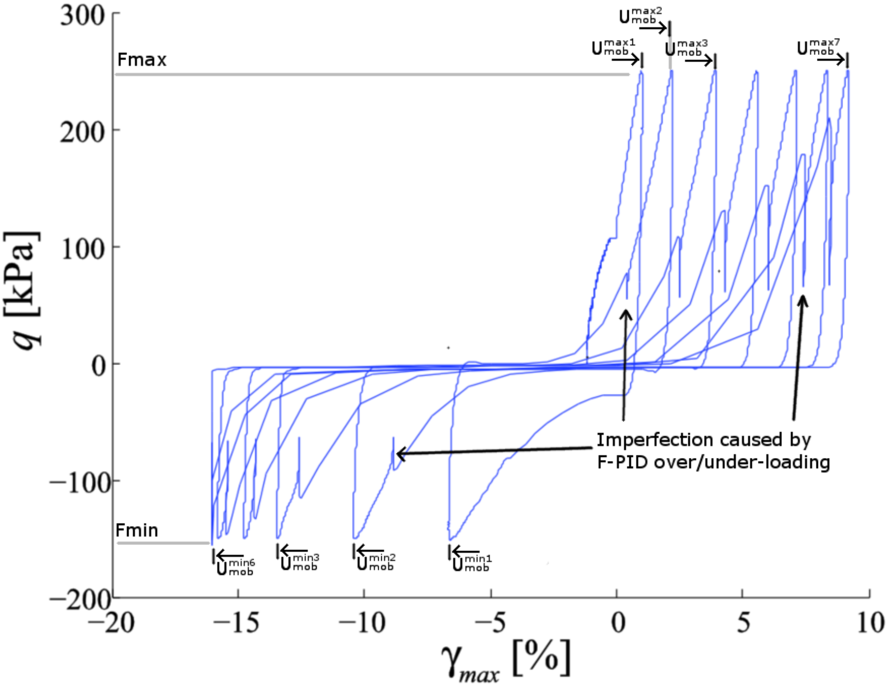

Fig. 3.5: Irregularities caused by F-PID control during liquefaction cycles [26]. While transitioning low stiffness regions PID controller can accumulate excessive velocities, and rapid recovery of stiffness at the peak of the amplitude causes overloading and under loading (collision).

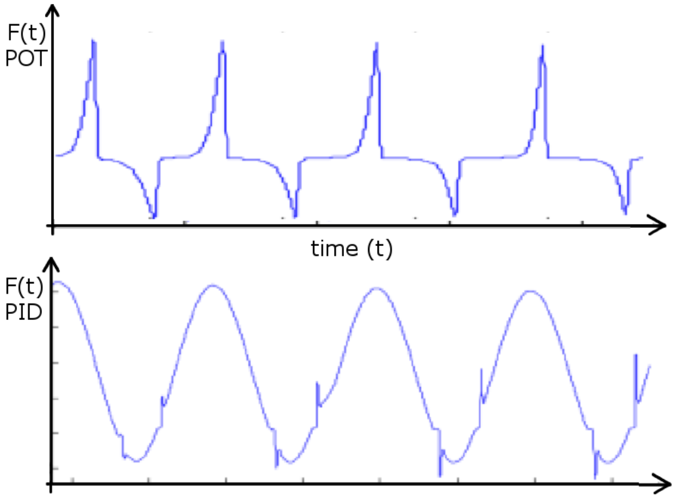

Fig. 3.6: Comparing F(t) plots produced by F-PID and F-POT with a deformation envelope.

Standard F-POT uses a constant value of ΔU loading rate. However, during liquefaction, a the specimen becomes gradually softer, thus increasing the deformation amplitudes required to transition from one F peak to the other (see Fig.3.5). Imagine a ball bouncing between two walls, where the distance between the walls is gradually increasing. This means ΔU settings have to be updated with every loading cycle, to preserve loading frequency. Thus, the improved algorithm updates ΔU value each time an F limit is crossed. Looking at Fig.3.5 it is visible, that each loading cycle increases the size of mobilized deformation $(Umob = Umax - Umin)$. Therefore, ΔU can be roughly approximated as $\Delta U \approx Umob/(2 \cdot T)$, where T is the desired load period for each cycle. Such adaptation is not perfect, but adequate to preserve most of the loading frequency (see Fig.3.6 and Appendix F).

At this point the F-POT controller is no longer "standard". ΔU is updated each time loading direction is reversed. Thus, the resulting F-POT control is custom made to account for behavior of a real sand specimen - working in synergy with the specimen being tested. Thus, a feature borrowed from a "soil model" was implemented into the PID control to make a POT controller. Note, the resulting F-POT control sacrifices sinusoidal shape of F loading history (see Fig.3.6). That can be seen as a sacrifice necessary to eliminate local imperfections. But at the same time, this allows to isolate properties proportional to ΔU rate more efficiently. The constant values of ΔU allow to control $C \cdot v$ component. Thus potentially allowing to isolate individual components within equation of motion (Eq.2.1). At this point research progresses from square 4 to square d in the flowchart in Fig.3.1.

2.3 Exploring the frictionless triaxial testing scope

Surprisingly, after introducing adaptive F-POT control, specimen durability improved. The undrained specimens became even more resistant to sher rupture and bulge formation. Specimen walls remained straight and vertical even while fully liquefied beyond amplitudes reaching 20% axial strain (see Fig.3.3). This means fully liquefied specimens remain testable, the test can continue to measure undrained peak strength after liquefaction. Such robustness of a triaxial test is a novelty, but the novelty does not stop there - after reaching undrained peak strength the specimen can be pulled back to initial length, drained, and cyclic loaded again. At this point, the testing procedure exceeds far beyond conventional testing limits. The data plots start to look chaotic, and unpredictable - beyond the scope of contemporary soil models. Thus, in order to analyze the chaotic results, a novel method of analysis was attempted (borrowed from computer science paradigm).

Notice the state transition diagram representation shown in Fig.3.3. During a test the soil state evolves, the specimen transitions through disturbed soil states, but there is no conventional method to quantify disturbed soil states yet. Alas, by using state transition diagrams a state function can be analyzed without having access to a physical model. Action (a), applied on soil state S, generates a stiffness path $\pi(S, a)$ (see Appendix D). The stiffness path $\pi(S, a)$ is unique for every combination of a and S - each stiffness path is a unique "signature". If "signatures" are similar, they can be described as equivalent. Thus, allowing to convert infinite-state transition system into a finite-state transition problem. Note, soil state can not be observed without changing it. Each time a stiffness path (the "signature") is generated, the soil state changes. Thus, by measuring what S the soil is in, the S is disturbed. In order to measure current S, the S is sacrificed.

Using the principle of state transition diagrams, the drained stiffness path in Fig.3.3 can be written as $\pi(So, ao8)$ - starting from So, action $ao8$ is applied, leaving the disturbed soil state $S8$ there after ($S8 = (So, ao8)$). Each a can be subdivided into smaller actions. Actions can also be combined, for instance $\pi(So, (ao1 + a12 + a29))$ is the undrained monotonic stiffness path starting at So ending at $S9$. Alternatively, because $S1 = (So, ao1)$, the same undrained monotonic path can be written as $\pi(So, ao1) + \pi(S1, a12) + \pi(S2, a29)$, again, leaving soil state $S9$ in the end. This is a very powerful way to illustrate state transitioning. It reveals the causation tree governing the problem.

If two signatures overlap ($\pi(Sx, aT) \approx \pi(Sy, aT)$), then $Sx\ Sy$. Thus, it is plausible to compare soil states by comparing the stiffness paths (signatures) created by action of testing (aT). aT can be any sequence of actions - the longer the sequence, the more "unique" the signature. For instance, if $ao1$ (in Fig.3.3) is used as the action of testing, all three undrained tests overlap in the region of $\pi(So, ao1)$. This overlap indicates that all three specimens had

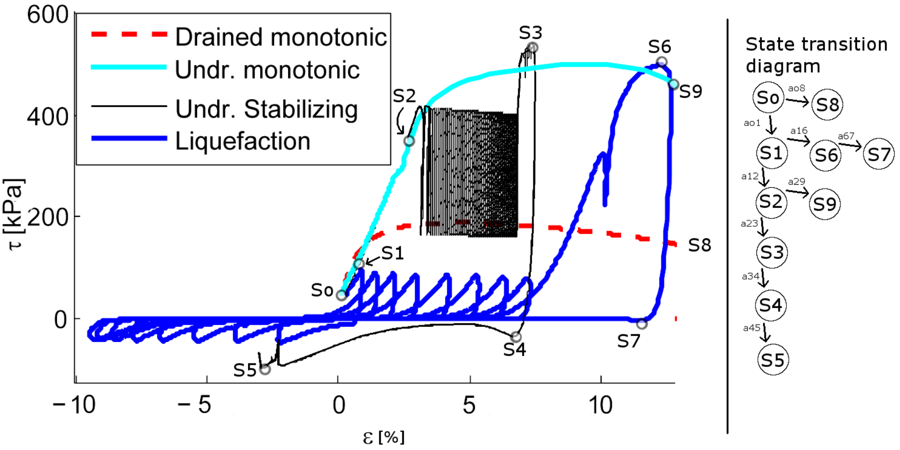

Fig. 3.7: Stiffness paths obtained using 4 specimens of Frederikhavn sand. Each specimen test starts from initial soil state So. All three undrained specimens have identical density, and common So - stiffness path $\pi(So, ao1)$ is common to all 3 tests.

similar So condition. However, $\pi(So, ao1)$ stiffness path is quite short, thus the likelihood that the overlap is not coincidental is not high. Consider the thought experiment: if aT contains 1000 loading cycles and two test $Sy = (S*, (aT))$ are show $\pi(S*_1, aT) \approx \pi(S*_2, aT)$, this means the likelihood of $Sx \approx Sy$ is very high.

Using π "signatures" to categorize soil states, the disturbed soil states can be compared to the "initial" stiffness path. After pulling an undrained specimen back to initial length, and draining it (drained consolidating) - initial stiffness path does not recover (see Fig.3.7) [35] [36]. Thus, one can deduce that, drained consolidation is inadequate for recovery of the initial state. This is unfortunate, since density and confining pressure are the only two variables controlled during preparation of a specimen. If controlling these two properties is not adequate - some unknown variables need to be found and accounted for to ensure reliable repetition of the "initial state".

First attempt to find the missing variables is shown in Fig.3.8. First two attempts failure to recover stiffness, the $3^r d$ was successful. The first attempt applies the action of testing (at) starting with the "initial" soil state. The at contains three actions (1) F-POT undrained stress cycles, (2) U-PID axial compression beyond undrained strength peak, and (3) U-PID pulling the specimen back to initial length where it is allowed to re-consolidate in drained mode. The resulting $\pi(So, at)$ stiffness path "signature" is labeled the outcome of at when $S = S_0$. Next time at is applied, the resulting stiffness path will be compared to the first one, to judge if S_0 is recovering. $\pi(S1, at)$ was generated after 10 minutes of drained consolidating - during

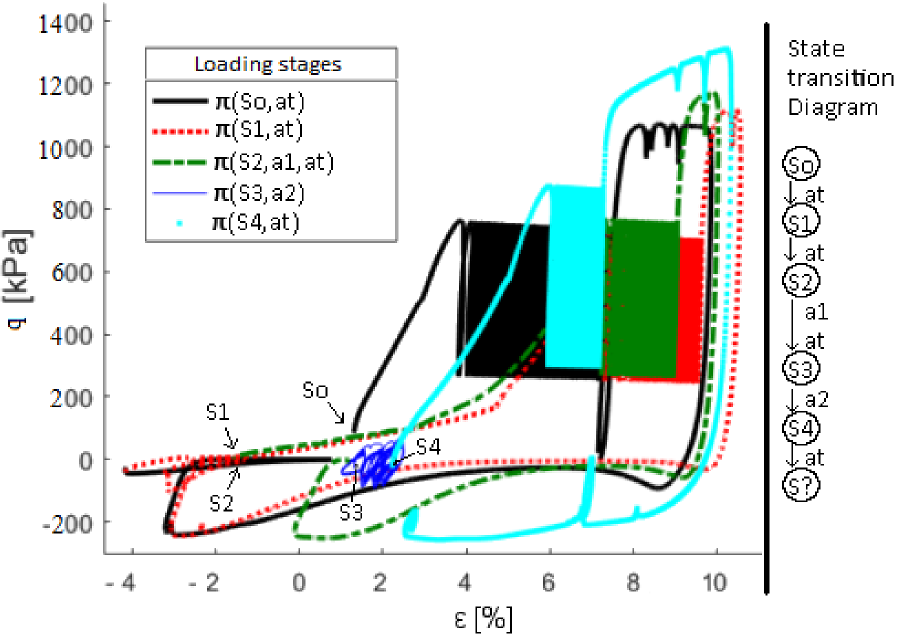

Fig. 3.8: Attempting recovery of So, in specimen disturbed by at - loading cycles used for making the Andersen's chart for Frederikhavn sand with undrained strength test in the end. $\pi(So, at)$ serves as the reference stiffness trajectory, the other paths ($\pi(s1, at)$,$\pi((s2, a1), at)$,$\pi(s4, at)$) are compared looking for signs of recovery. In the outcome, drained consolidation alone did not recover undrained stiffness, only by adding drained deformation cycles some recovery was noticed. Note, the effective stress history can be seen in Fig.3.3. [35]

which specimen density increased slightly, but (surprisingly at that time) stiffness did not recover. $\pi(S1, at)$ is much less steep than $\pi(S0, at)$. After reaching $S2 = \pi(S1, at)$, the specimen was left to drained consolidate overnight (action $a1$). However, $\pi(S2,(a1, at)) \approx \pi(S1, at) \neq \pi(So, at)$ - thus, longer exposure to dry consolidation (confining pressure $p' = 60kPa$) did not produce noticeable recovery of initial stiffness path, alas $S1$ and $S2$ seem to match well, thus repeating at did not disturb the specimen further. $S1$ was not disturbed by repeating at. Before applying at for the third time, deformation cycles were applied ($a2$). This drained procedure adds it's own stress paths to the plot $\pi(S3, a2)$. Notice, drained peak strength is substantially lower than undrained, thus the drained stiffness paths look tiny in comparison. Finally, in $\pi(S4, at)$ first signs of undrained stiffness path recovery are present - inclination of undrained stiffness path becomes substantially steeper, $\pi(So, at)$ and $\pi(S4, at)$ have similar features. Partial recovery of undrained stiffness path was detected, after drained deformation cycles were applied.

In addition to suggesting a potential factor (drained deformation cycles) governing recovery of sand stiffness, the multi stage test shown in Fig.3.8 raises uncomfortable observations, such as lower dilativity at higher density, lower stiffness at higher density, higher peak strength at lower stiffness - all looking like a paradox at that time. However, equipment was double checked, and the paradoxical patterns kept repeating. Luckily, the paradoxical phenomenon were found to follow logical patterns with recurring proportion. By the end of this study, a model which predicts the behavior was formulated. Alas, at this stage of testing, the link between cause and effect was not established conclusively. Drained deformation cycles appeared to play an important role, thus drained deformation cycles were observed further (from problem (f) to solution (7) in the flowchart, Fig.3.1).

2.4 Drained deformation cycles (the stable stiffness triangle)

Potential importance of drained deformation cycles was noticed during the test in Fig.3.8. At this point little was known about the true drained testing capabilities of the frictionless triaxial apparatus. Thus, the first task was to find the practical testing limits - how many deformation cycles of what amplitude are applicable without causing shear rupture or bulging of the specimen. The first drained deformation cycles were applied at 15% amplitude deformational (measurement given in true strain [32]). Resulting drained stiffness paths are visible in Fig.3.9. A total of 3 loading cycles were applied, before specimen failure was caused by spontaneous formation of a thin shear rupture zone during extension (alas, no bulging noticed).

Audience in conferences, and reviewers in journals had raised concerns that deformation amplitudes of 15% are not realistic - too big for practical application. Such deformations are not encountered in engineering practice. However, there are at least two reasons why such tests are interesting. Firstly - it is a real phenomenon, thus it is interesting for the very reason of its existence. Secondly - because sand can lose stiffness, a thin layer of soil can loses stiffness near the structure. In such case a tiny deformations can cause large strains (a small deformation in a thin layer). Thus, large strains can be encountered, and it should be a concern if the phenomenon is not predicted or accounted for by convention. In a layer of 7 centimeters (height of tested specimen), a deformation of just 7 millimeters will cause 10% strain. In a foundation which is 6 meters deep (a typical mono bucket), this would mean $atan(0.007/6) = 0.0668^o$ inclination, which is well within the allowable 0.5^o design limits [3]. Thus, the patterns observed at 15% could potentially be encountered within serviceability limit states of an offshore wind turbine. Alas, it is a good practice to justify research based on the first premise - this is areal phenomenon, its very existence justifies its research.

During drained deformation cycles a converging triangular stiffness path was noticed. Existence of similar hysteresis loops has already been docu-

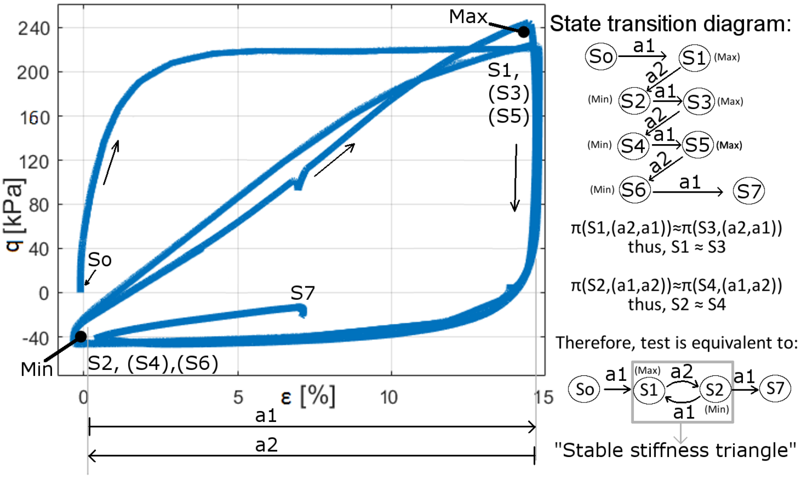

Fig. 3.9: Testing the limits of drained deformation cycles, using frictoinless triaxial apparatus. 3 cycles of 15% were plasible to apply, before specimen failure (sher rupture during extension). Overlapping stiffness paths were noticed. The cyclic stable stiffness path was assigned the name "stable stiffness triangle" [35] [36].

mented, but the factors governing this phenomenon were not explored in existing literature. Likely, because deformation cycles are normally used to investigate volumetric response of sand [22] [11], as conventional models treat only volumetric response as a function of deformation (the way we model affects how we conduct tests). Therefore, it is not uncommon to tested volumetric response using deformation as the input, but in this thesis - stiffness is observed as a function of deformation instead (while largely ignoring the volumetric response). This time the triangular stiffness pattern is assigned a name - "the stable stiffness triangles", and causality governing the behavior of the stable stiffness triangle is researched. The converging stiffness path is interesting for at least 2 reasons:

1. Features governing the stiffness triangle could reveal the missing variables required to quantify disturbed soil states.
2. The converging pattern could serve as an anchoring points for new models (such as BSM, introduced in this thesis).

Peaks of the stable stiffness triangle can be described using principles of "minimum" and "maximum", similar to how Coulomb did in his famous essay nearly 250 years ago [8]. Typically, yielding stress (q_y) limits are used in models, thus testing procedures are normally designed to look for some form of "minimum" and "maximum" in stress space only. However, the principles of "minimum and maximum" can be applied to strain as well. Yield-strain

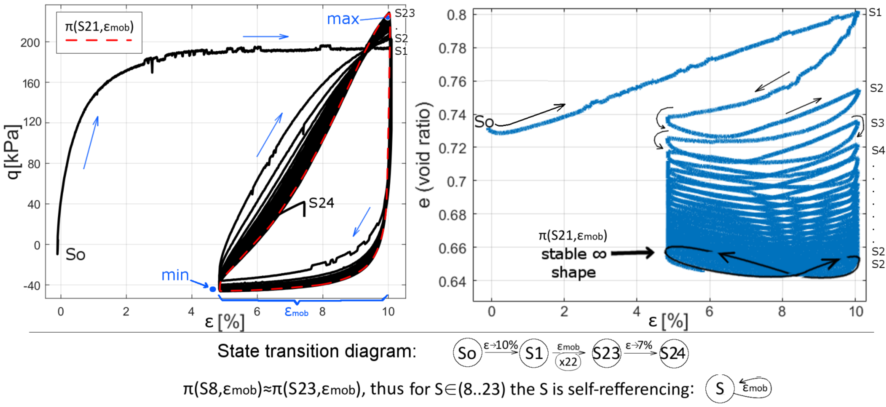

Fig. 3.10: Converging pattern - introducing self referencing loop [35] [36].

(ϵ_y) has limits ϵ_y^{max} and ϵ_y^{min}, which change their position along the ϵ axis. It takes a combination of both q_y and ϵ_y to define the limits of a stable stiffness triangle. The stiffness curve converges within a rectangle area, with two sets of boundaries (ϵ_y and q_y). The corners of the rectangle, are touched by the corners of the triangle. Therefore, the stiffness triangle cannot be modeled reliably, until rules governing both q_y and ϵ_y are established.

After choosing the boundaries governing the triangle, further tests were designed to observe behavior of the boundaries by generating triangles at different ϵ_{mob} amplitudes (See Fig's.3.11,3.10). At $\epsilon_{mob} = 5\%$ a total of 22 cycles were applicable, before reaching specimen failure. At $\epsilon_{mob} = 1\%$ a total of 44 cycles were applied and the specimen remained testable - test continued to observe peak strength limit for the 2nd and the 3rd time. Peak strength was tested 3 times on one specimen, at different densities, thus revealing further new testing scope of the equipment, as well as new observations to analyze causation governing the stable stiffness triangle.

While observing the drained stiffness paths one peculiar feature of stiffness triangle become apparent - peak strength is correlated with density, but stiffness is not. All deformation amplitudes (15%, 5% and 1%) generate triangles with very similar q_y limits, within different ϵ_y limits. Stiffness hysteresis loops behave proportional to recent deformation history. Once stabilized, the stiffness triangle geometry changes very little while the specimen density continues to change. Thus, by principle of deduction, the shape of stiffness hysteresis loop is not sensitive to absolute density. Even while transitioning from relative density of 80% towards near 100% in Fig's.3.11,3.10) ($e_{min} = 0.64$, $e_{max} = 1.05$, Frederikhavn sand). This brings an intriguing conclusion: drained sand stiffness could be modeled while ignoring absolute density, and without monitoring stress history (besides predicting the peak

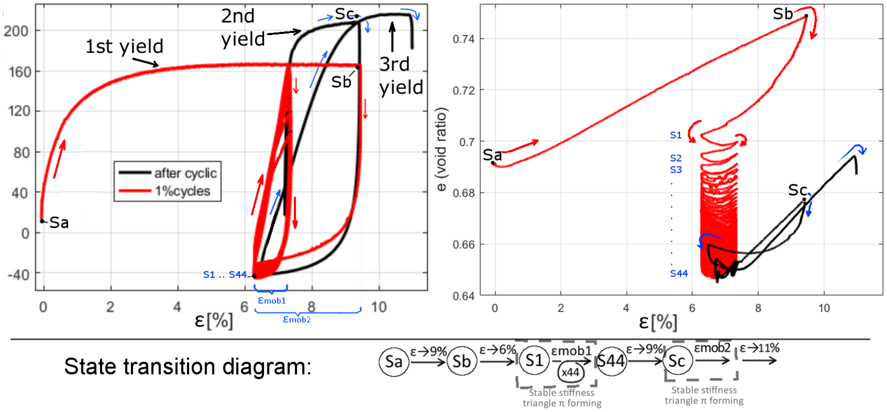

Fig. 3.11: Stable stiffness triangle generated at 1% deformation amplitude, using the frictionless triaxial apparatus. Note both "min" and "max" points are stabilizing - the test was designed to push ϵ_y limits apart, and observe the process or re-stabilizing within the middle of expanded ϵ_y envelope.

stress limits).

The absence of correlation between stiffness and density (or strength and stiffness), is observable in Fig.3.11. While comparing paths of 1^{st} and 3^{rd} yield ($\pi(Sa, \epsilon \to 9\%)$ and $\pi(Sc, \epsilon_{mob2})$ - lower stiffness at higher density is noticeable. As stiffness triangle stabilizes, the re-loading path becomes straighter (transitioning from convex to concave). It appears curved (convex) re-loading stiffness paths are a feature of disturbed soil state - a triangle which is still stabilizing. If the initial stiffness path is curved, it could indicate a freshly deposited specimen begins its life in a disturbed soil state. The new finding was published in a journal paper shown in Appendix C.

2.5 Controlling the stable stiffness triangle

By now, the stables stiffness triangle is viewed as an object, with objective properties - characteristic points "min" and "max", which have coordinates q_y and ϵ_y. Stress limits ore predictable given void ratio (e) and radial stress σ_r (or p'). The q_y limits are a function dependent on the two: $q_y = f(e, \sigma_r)$, while strain limits appear to be governed by $\epsilon_y = f(\epsilon, \Delta\epsilon)$ (as was predicted by the thought experiment in Fig.3.4). Definition of causality governing these two dependencies is still rather obscure, but enough to attempt repositioning and resizing the stable stiffness triangle - thus testing the roles of perceivable dependencies (variables adequate to model, should be adequate to control), thus research procedure continues to square 8 in Flowchart in Fig.3.1.

First, the "min" and "max" was manipulated by holding σ_r constant, while applying three groups of ϵ_{mob} cycles. This is meant to reveal ϵ dependen-

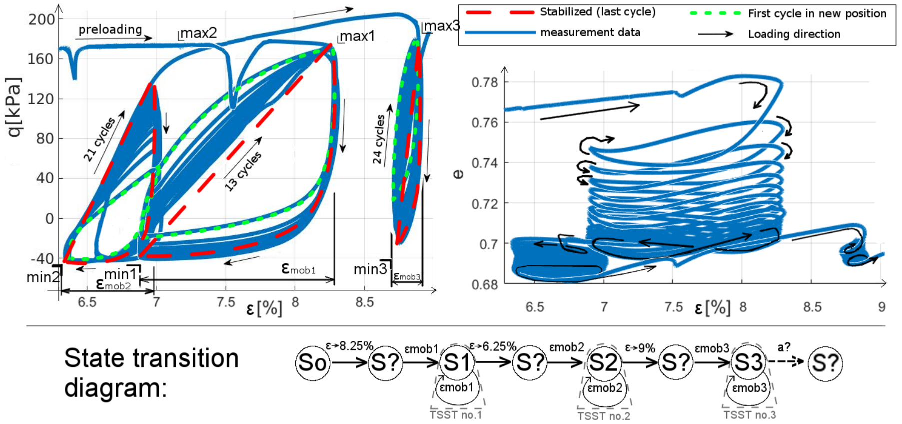

Fig. 3.12: Drained sand triaxial test, attempting 3 different ϵ_{mob} amplitudes, while holding constant σ_r. In the outcome, ϵ dependencies were explored - the stable stiffness triangles (TSST's) was repositioned and resized along the ϵ axis.

cies deductively - if σ_r is held constant, properties depending on σ_r will not change. Thus changes produced by groups of ϵ_{mob} can be considered as ϵ dependent. And the next test does the opposite: ϵ_{mob} are held constant, while σ_r is varied - thus putting stress dependencies into context (Fig.3.13).

While transitioning between groups of ϵ_{mob} cycles with different amplitudes, the "min and max" limits were noticed to adapt in two distinct patterns: (1) when crossing ϵ_y limits (yielding), the ϵ_y limits are pushed apart instantaneously, but (2) deformation increments within ϵ_y limits cause gradual shrinking of the "min" and "max" boundary. The easiest way to generalize this is to use a deformation envelope, where the edge of the envelope, where the ϵ_y coordinates expand instantly (during yielding), but shrink gradually (during stabilization). Looking at Fig.3.12 it is visible how point "max1" was pushed forward during preloading. Once "max1" was pushed into position, it staid there, as indicated by constant position of q_y (under assumption that q_y is coupled with ϵ_y). The other side of the same triangle, point "min1", was slowly catching up with each loading cycle, until the stable stiffness triangle converged. Once converged, the q_y coordinate of the "min" point was converged converged towards the ϵ_y limits. Similarly, "min2" remains constant after exiting the first triangle in extension. This time the "max2" is catching up (stabilizing). The principles of ϵ_y expanding instantly, but contracting gradually remains true for the 3'rd group of cycles as well. ϵ_{mob3}, starts with stable "max3" point, whereas "min3" is slowly catching up, thus q_y slowly converging towards "min3" point.

Notice, the frictionless triaxial apparatus has its testing limits. It was not plausible to apply enough loading cycles to fully stabilize the second

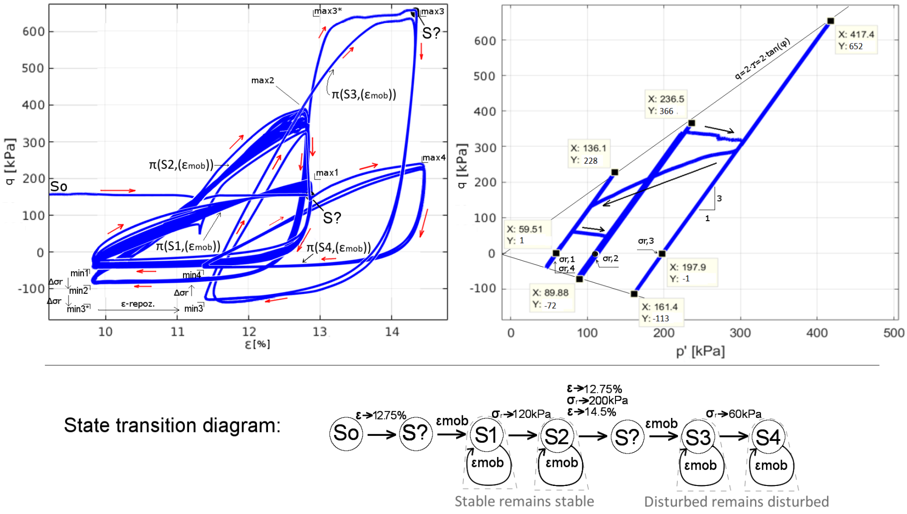

Fig. 3.13: Drained sand triaxial test using one ϵ_{mob} amplitude, at three different σ_r values. The stable stiffness triangle was resized along the q axis. Changing σ_r did not produce noticeable stabilizing or disturbing effects on the triangular stiffness path. As the "min and max" points were moved up and down, left and right - the stiffness curves were noticed to point towards the "yielding points".

triangle shown in Fig.3.12. Further loading increments were not applicable as specimen began to develop signs of separation from the end platen (small, localized bulges began to take shape). The specimen is more fragile during drained cycles, than undrained ones. In undrained specimen the pore water appears to help preserve uniform volumetric strain. Alas, if tests are done carefully, early warning signs of failure can be detected visually, as was the case during ϵ_{mob2} cycles. A tiny, small radius bulge is reversible. To prevent further development of a failure, the specimen was axially comprised towards ϵ_{mob3}, prematurely, before the stiffness triangle was fully shaped.

Once dependencies of hypothetical ϵ_y envelope were observed (instantaneous increase, gradual decrease in ϵ_y diameter), the question of stress dependencies remained. Next test was done in effort to keep ϵ cycles at constant amplitude, while applying 4 different confining pressures, thus forming four stiffness hysteresis loops of different height (along q axis), the the same length (along $/epsilon$ axis). The result is shown in Fig.3.13. Transition from triangle 1 to triangle 2 checks if changing σ_r can disturb a stable triangle. Transition from triangle 3 to triangle 4 checks if changing σ_r influences a disturbed soil state. In the outcome, variation in σ_r has little effect on overall hysteresis loop geometry. Changing σ_r merely repositions q_y limits instantaneously, and the stiffness path reaches towards the new q_y position once deformation is applied. A disturbed triangle remains disturbed, a stabilized

- remain stable (the first loading cycle creates a fully stable triangle). Thus, demonstrating how boundaries governing the stable stiffness triangle can be manipulated in real-life, real-time testing practice.

Fig.3.13 indicates points "min and max" follow very simple rules of action. They can be pushed up and down the q axis, left and right on the ϵ axis. Triangle $\pi(S1, \epsilon_{mob})$ (Fig.3.13) was stabilized within ϵ_{mob} amplitude, and the last deformation cycle was paused in the middle of a reloading phase. While pausing, max1 was raised to max2 position, by increasing σ_r. When ϵ_{mob} cycle was un-paused, the stiffness path pointed towards the new (max2) yield point instantly (no signs of gradual transitioning). Similarly, Triangle $\pi(S2, \epsilon_{mob})$ was paused at the peak position, "touching" point max2. σ_r was increased to move point max2 towards max3* position. As expected, upon applying deformation, the stiffness path $\pi(S2, [\epsilon \rightarrow 14.5\%])$ was very steep, "reaching" towards $max3*$ point (while pushing the max3* point towards max3). This indicates q_y adaptation to σ_r is near instantaneous, while ϵ_y adopts to ϵ history either gradually (during stabilization) or instantaneously (during yielding). At this point there is an experimental rationale to make conclusions for making a model:

- changes in ϵ_y coordinates of "min" and "max" are caused exclusively to strain history.
  1. ϵ_y limits are pushed apart instantaneously.
  2. otherwise, ϵ_y envelope contracts gradually.
- q_y envelope coordinates of "min and max" are caused exclusively by real time stress state.
- The stiffness paths always curve towards points "min" and "max" (depending on loading direction).

The new understanding of stress and strain dependencies improved our ability to control specimen stiffness substantially. At this point we can increase and reduce specimen stiffness, we can have the option to move back and forth between soil states of choice, by selectively prescribing deformation history. A stiffness triangle can be stretched both vertically and horizontally, or repositioned horizontally. It is interesting to note, that stiffness hysteresis loops are controlled without paying attention to volumetric response. For drained stiffness loops the effects of volume change seem to be marginal. Similar stiffness curves can be generated at different densities - the paradox of lower stiffness at higher density is no longer paradoxical. At this point the generalizations can be implemented into a model built following the causation observed experimentally. Further data plots show simulations plotted on top of further new measurements. This marks transitioning to solution stage 9, in flowchart Fig.3.1.

2.6 Modeling the stable stiffness triangle

What is enough to control a phenomenon, should be adequate to model te phenomenon. To control the stable stiffness triangle, during triaxial testing, two inputs had to be controlled: ϵ, σ_r; The two inputs were used to control two outputs: q, e. Note, e is the secondary objective. Now, the causality connecting the inputs with the outputs is assumed in a model (BSM). Very few principles are borrowed from conventional theory. Namely, the principle of "minimum and maximum" for the stress axis (q_y) will be represented by linear coulomb envelope parametrized by a friction angle ϕ [8] [43]. The novelty of this thesis is introducing the strain envelope ϵ_y, and a novel way to interpolate within the stress limits using Bezier curves (see Fig.3.4).

The ϵ_y envelope

Coordinates of the $/epsilon_y$ envelope (ϵ_y^{min} and ϵ_y^{max}) can be represented by a yield function:

$$f_\epsilon = \epsilon_R - abs(\epsilon(t) - \epsilon_o) \tag{3.1}$$

where $\epsilon(t)$ is the real time deformation, ϵ_o is the center position of the envelope, and ϵ_R is the radius. $f_\epsilon < 0$ triggers yielding (disturbing the specimen), otherwise the envelope is shrinking (stabilizing). There is no pure-elastic zone, the envelope changes its radius and/or the origin point in proportion to applied ϵ and $\Delta\epsilon$ (direction). The time variable (t) in the description is mentioned to emphasize that, in reality, the transition is continuous. Soil grains do not "teleport" from one arrangement to another. Thus, as the envelope moves, it interpolates soil states transitioned.

From observations made in previous sections, it is visible that "min" and "max" points are pushed apart instantly, but recover gradually. Thus, two sets of kinematic ($\kappa_{k,[1,2]}$) and isotropic ($\kappa_{i,[1,2]}$) hardening coefficients are required - one to be used while yielding ($f_\epsilon < 0$), the second - while stabilizing ($f_\epsilon \geq 0$), as shown in Eq's 3.2, 3.3 . When yielding, ϵ_y limits expands to contain $\epsilon(t)$ within ϵ_y limits. The $\epsilon(t)$ is not allowed to exit beyond the ϵ_y limits, thus forcing ϵ_y to adapt instantaneously during yielding. Conditions $\epsilon(t) < \epsilon_y^{max}$ and $\epsilon(t) > \epsilon_y^{min}$ must be satisfied at all times. Thus, $\kappa_{k,1} + \kappa_{i,1} \geq 1$ when yielding, which means the edge of ϵ_y either becomes equal to, or extends ahead of $\epsilon(t)$ during yielding.

$$\Delta\epsilon_R = \begin{cases} \kappa_{i,1} \cdot |\Delta\epsilon|, & \text{if } f_\epsilon < 0 \\ -\kappa_{i,2} \cdot |\Delta\epsilon|, & \text{otherwise} \end{cases} \tag{3.2}$$

$$\Delta\epsilon_o = \begin{cases} \kappa_{k,1} \cdot \Delta\epsilon, & \text{if } f_\epsilon < 0 \\ \kappa_{k,2} \cdot \Delta\epsilon, & \text{otherwise} \end{cases} \tag{3.3}$$

While stabilizing, $\kappa_{k,2} + \kappa_{i,2} < 1$, which means the envelope is shrinking in increments smaller than $\Delta\epsilon$. Therefore the envelope will gradually shrink towards $\epsilon(t)$. In simulations values $\kappa_{k,2} + \kappa_{i,2} \approx 0.15$ appear to work rather well for a wide range of tests and even among different soil profiles (reader is encouraged to experiment with different values to shape intuitive understanding of the concept). Nonetheless, selecting κ_k and κ_i as constants is not ideal. The rate of envelope shrinking changes, it is not linear, this must be emphasized. The hardening rules are incomplete, they merely illustrate the general principle of a model which is still in development.

The two pairs of κ coefficients were calibrated in drained mode. It would seem additional pairs of κ variables could be added to account for undrained response. However, while testing the algorithm, it was noticed that both drained and undrained deformations generate compatible $\Delta\epsilon_R > 0$ response. It makes little difference if yielding is caused in drained or undrained mode - the stiffness triangle shows equivalent adaptation patterns regardless of draining condition, when yielding. Thus, drained and undrained $\Delta\epsilon_R > 0$ increments are largely compatible. However, undrained mode removes specimen capability to recover - only in drained mode ϵ_y envelope is observed to shrink (stabilize). In the model, this can be emulated by removing $\Delta\epsilon_R < 0$ increments in undrained mode. Thus, ϵ_y envelope calibrated drained combine both drained to undrained response without adding extra variables. It is enough to disable drained stabilizing, to "switch off" $\Delta\epsilon_R < 0$, and the ϵ_y behaves undrained. However, given that stabilizing is rather slow to begin with ($\kappa_{k,2} + \kappa_{i,2} << 1$), an envelope calibrated for drained response keeps up with undrained loading rather well. Thus, undrained stress history can be fitted relatively well even without switching to undrained mode.

This concludes explanation of principles used to describe ϵ_y envelope. It is worth to mention that ϵ_o and ϵ_R make the ϵ_y envelope appear like a circle, laying flat on the ϵ axis. However, the two coordinates - origin and radius - are used for descriptive convenience, not because the envelope really is a circle. The frictionless triaxial apparatus generates observations along 1 axis of deformation (1D). That is inadequate to extrapolate conclusions towards 2D or 3D envelope. In 2D, the "circle" could become an ellipse or a square. In 3D it could be a more complicated shape. In the extreme case, a strain tensor has 6 degrees of freedom (3 axial, 3 shear). Each axis could need individual "min" and "max" boundaries - up to 12 deformation limits could be required. Given this uncertainty, it would be irresponsible to assume the shape of an envelope in 3D space based on 1D measurement. The 1D model is meant to fit 1D measurements - a specimen tested in a triaxial apparatus. To make observations in 3D, the true triaxial apparatus is capable of loading along all 3 principle stress axes. Thus, could be used to explore ϵ_y shape in 3D principle strain space.

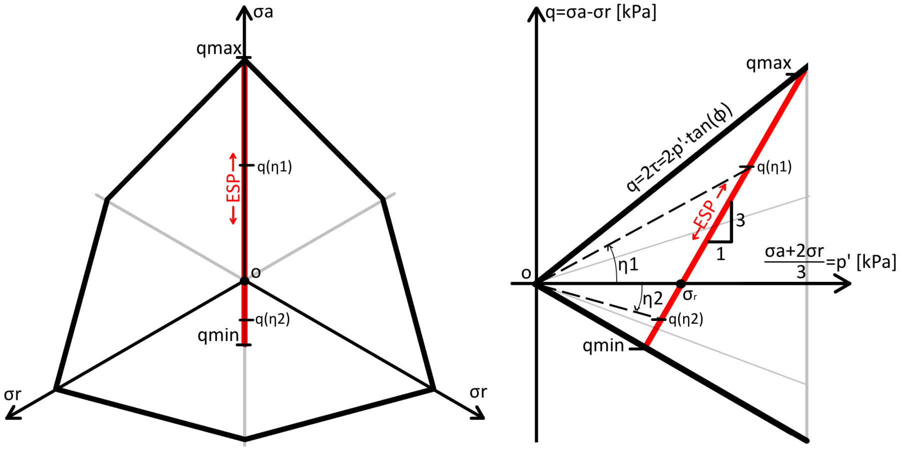

Fig. 3.14: Two 3D Coulomb envelope projections. The frictionless triaxial apparatus is limited to the ESP, thus q_{min} and q_{max} can be found as the points where ESP and Coulomb envelope cross each other. All other q values can be interpolated within the envelope by using η and σ_r.

The q_y envelope

As mentioned earlier, the effective stress limits are treated the way Coulomb described them in 1773 [8], [37], by keeping his original notation of "minumum" and "maximum", used in his original essay. The relationship with confining pressure is governed by a friction angle (ϕ). The BSM model uses a linear boundary found in effective stress space (see Fig.3.14).

It is somewhat unfortunate that a drained test executed using the frictionless triaxial apparatus (for this case study) are limited to one effective stress path (ESP, in Fig.3.14). Also, it is not plausible to vary the Lode angle - the experiment is restricted to cross through the hydrostatic axis each time $q = 0$ limit is crossed. It was noted before that two-way loading triggers liquefaction. Thus it is interesting if two-way loading would still trigger liquefaction if the effective stress path would circle around the hydrostatic axis, rather than crossing it. It is also interesting, how loading cycles offset from hydrostatic axis would affect the shapes of the stiffness curves. On the upside, being restricted to a 1D trajectory makes modeling much easier. q_{max} and q_{min} points are found at the intersection, where Coulomb envelope and the ESP line collide (See Eq's 3.4, 3.5).

$$q_{max} = -\frac{3 \cdot \sigma_r \cdot tan(\phi)}{tan(\phi) - 1} \tag{3.4}$$

$$q_{min} = -\frac{3 \cdot \sigma_r \cdot tan(\phi)}{tan(\phi) + 1} \tag{3.5}$$

Notice how the "max" point in stiffness triangle from Fig.3.10 rises along the q axis, while density is increasing - this test alone could be enough to calibrate variation in friction angle across multiple densities ($\phi = f(e)$), as the point "max" is reached at multiple densities during the test. If ϵ_y and q_y are coupled, then The test is equivalent to 22 drained peak strength tests, and it took less than one day to execute. Following the convention would take one specimen per test - 22 working days total, as it takes a day to prepare a specimen. Alas, for the purpose in mind, variation in ϕ caused by e does not have significant impact on the overall shape of the stiffness hysteresis loops. This means the general shape of the triangles can be captured by treating ϕ as a constant. Nonetheless, an attempt was made to calibrate $\phi = f(e)$ using the test shown in Fig.3.10 resulting in $\phi = 40 - (e - emin) \cdot 20.0$.

As shown during test in Fig.3.13, ESP line can be pushed up and down the p axis (see Fig.3.14) by varying $\sigma_r = Pp - Cp$, where Pp is the pore pressure inside the specimen, and Cp is the confining pressure applied by confining chamber. During drained tests Pp can be adjusted by varying either Pp or Cp vales. In drained mode Pp=Bp. Therefore, in drained simulations σ_r is constant, unless the user changes the input. However, in undrained mode Pp is fluctuating in proportion to nonlinear volumetric strain (ϵ_v) generated by the soil skeleton. The nonlinearities of volume change cannot be modeled reliably using numerical methods, yet. Therefore, for undrained simulation Pp measurements need to be borrowed from test results. This means only η is simulated in undrained mode, while σ_r is borrowed from measurement.

The principle of borrowing measurements was executed with care not to bias the simulation. Notice Eq's 3.4 and 3.5 follow polar coordinates, where σ_r serves as the radius and η acts as the angle. σ_r and η, thus, are two mutually independent variables. σ_r is the point where ESP line crosses the p axis, whereas η serves to interpolate points on the ESP line (note, η is limited within the ϕ limits). It is a longterm objective to express nonlinear $\epsilon_v = f(\epsilon_y)$ properties to adequate accuracy to simulate Pp fluctuation. But for the time being, only behavior of the η parameter is captured during undrained simulations, and the $e = f(\epsilon)$ is analyzed in parallel.

Strain-space models have the remarkable property of behaving like a parallel spring system [44]. Therefore, effects depending on ϵ can be modeled in parallel - e and η behave as two uncorrelated functions, both controlled by the same ϵ input. Thus, it is plausible to test (and model) $\eta = f(\epsilon_y)$ while by and large ignoring ϵ_v, and vice versa. Detailed examples can be found in Appendixes B, C and E.

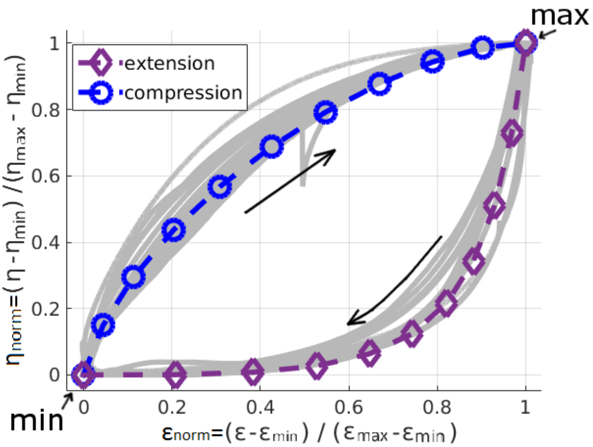

Fig. 3.15: Normalized hardening curves found by normalizing stables stiffness triangles generated at different ϵ_{mob} amplitudes.

Normalized stiffness paths

$$\eta_{norm}(x) = \begin{cases} -((9-8x)^{\frac{1}{2}}-3)^{\frac{3}{8}} & \text{, extension } (\eta_{min}) \\ \frac{3(40x+9)^{(\frac{1}{2})}}{8} - \left(\frac{5(\frac{2x}{5}+\frac{9}{100})^{\frac{1}{2}}}{2} - \frac{3}{4}\right)^{\frac{3}{2}} - \frac{9}{8} & \text{, compression } (\eta_{max}) \end{cases} \tag{3.6}$$

The methods to combine both ϵ_y and q_y limits can now be introduced. Individual stable stiffness triangles were isolated from multiple tests. Each triangle was then normalized within its own "min" and "max" limits (see Fig.3.15). Note, the stress angle $\eta = q/p$ is used to account for q_y limits. Coulomb envelope is a function where $q_y = f(\phi, \sigma_r)$, and by replacing ϕ with η (Eq's. 3.5, 3.4), the q position can be interpolated along the ESP line, within the ϕ limits. After plotting the normalized hardening curves, a distinct common pattern emerged. The common pattern was hand fitted using two Bezier curves, one curve for compressive path, and one for extension. The fit was then processed into equations 3.6.

Note the fitting is ad-hoc, and can be attempted by the reader by saving the picture and drawing brazier curves on top. Then expressing the η_{norm} as a function of ϵ_{norm}. There is no deeper meaning, the curves are obtained experimentally, and fitted by hand. This is important to note, as the stable stiffness triangle is found in specimens tested using a frictionless triaxial apparatus, where the ESP is inclined at a fixed angle (see Fig.3.14). It is not known how the shape of the normalized stiffness paths would change if the inclination of the ESP path was varied. If ESP angle was changed, the curvature of stress paths would likely change. The empirically obtained curves, therefore, should not be considered beyond simulation of a specimen tested in a triaxial apparatus. While the principle of Bezier stiffness is universally applicable, each application requires stiffness curves be generated experimentally (as will be done later, for a small scale foundation).

Once $\eta_{norm} = f(\epsilon_{norm})$ is expressed, the curve can be used to interpolate within the "min" and "max" points (see Fig.3.15). ϵ and σ_r (the inputs) can be converted to q (the output) following $[\epsilon(t), \Delta\epsilon] \rightarrow \epsilon_{norm} \rightarrow \eta_{norm} \rightarrow [\eta, \sigma_r] \rightarrow q$. Thus, for every ϵ and σ_r, a q value is generated. This is enough to predict the shape of a fully converged stiffness triangle. Alas, if the loading direction is changed the q value will "teleport" from the bottom curve to the top one and vice versa. Therefore, one final problem remains before the normalized curves can be used in simulations: a method to transition from compression curve to extension curve has to be gradual, not instantaneous. A point should not "teleport" from one curve to the other.

Bezier stiffness model

To illustrate why Bezier stiffness method is necessary, consider a thought experiment: in Fig.3.15 start at the "min" point. Then, move to the right ($\Delta\epsilon > 0$), along the compression curve, until point "max" is reached. If loading is reversed to $\Delta\epsilon < 0$, the extension line can be followed down. However, if the loading is reversed in the middle of the path, without reaching either "min" or "max" point, it is not obvious how to transition the distance between the two curves. Connecting the two paths using linear, pure elastic stiffness is not an option. A method preserving some curvature during transition needs to be found. This is attempted by using a recursive function inspired by Bezier spline - thus introducing a novel procedure with "Bezier stiffness" K_b (Eq.3.7), parametrized by a coefficient R (Eq.3.9).

The Bezier stiffness principle is illustrated in Fig.3.16. While $\Delta\epsilon < R(\epsilon)$ Bezier stiffness generates $\eta_{min}(\epsilon) < \eta(\epsilon) < \eta_{max}(\epsilon)$. This means η_{min} and η_{max} behave like hard limits - the normalized stiffness curve itself acts as the "envelope", ensuring the stress states remain within the normalized curves (which are within Coulomb stress limits). Notice the special case in η_3, shown in Fig.3.16, which illustrates what happens when $\Delta\epsilon > R(\epsilon)$: the predicted $\eta(\epsilon) > \eta_{max}(\epsilon)$, but the problem is easily corrected by setting $\eta(\epsilon) = \eta_{max}(\epsilon)$. Therefore, η_{norm} always stays within the normalized curves, which are always within the ϕ limits. Thus, Coulomb stress limit is satisfied. The method is unconditionally stable regardless of step size.

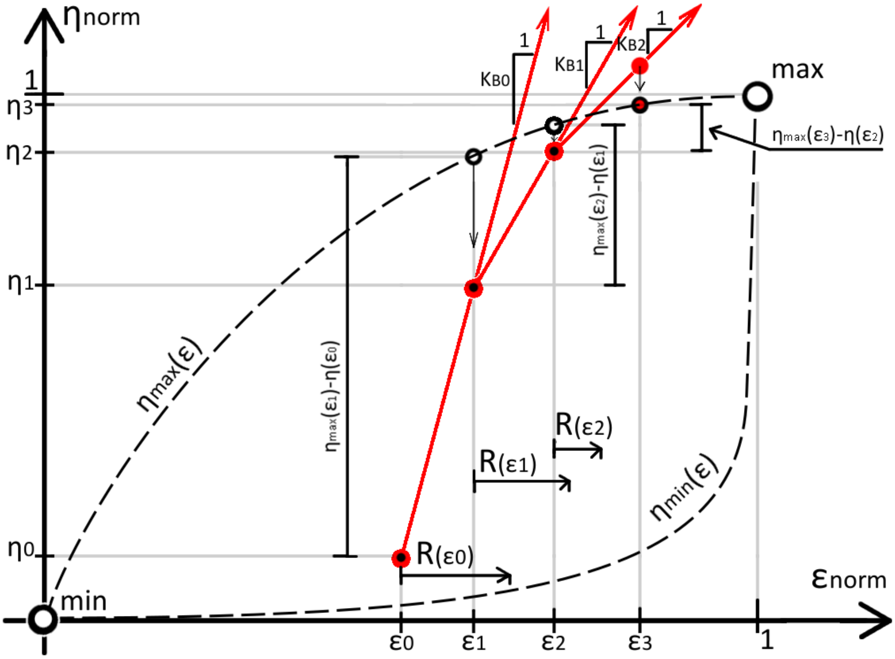

Fig. 3.16: Bezier stiffness principle illustrated.

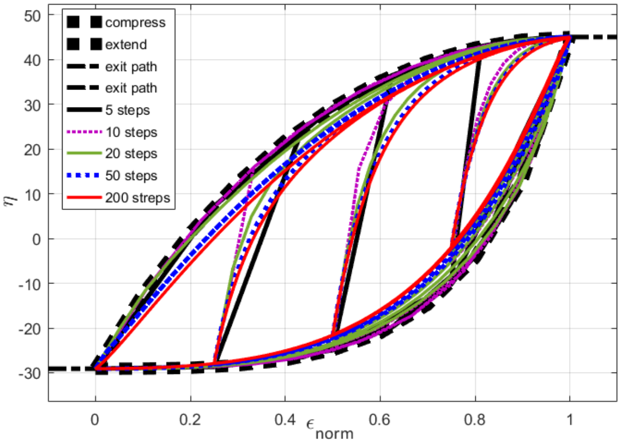

Fig. 3.17: Bezier stiffness sensitivity to steps per loading cycle. Triaxial test results were measured at 10 Hz sampling rate, while applying 10 s (or slower) deformation cycles. Thus, at least 100 step increments (50 forward, 50 backward) are available per loading cycle. Thus, ϵ measurements can be used as inputs for the model without implicit stepping along the Bezier stiffness curve.

$$K_b(i) = \frac{\eta_{max}(\epsilon(i+1)) - \eta(i)}{R(\epsilon(i))} \tag{3.7}$$

$$\eta(i+1) = \eta(i) + K_B(i)\Delta\epsilon \tag{3.8}$$

$$R(x) = \frac{1-(1-2x)^2}{10} + 10^{-4} \tag{3.9}$$

Additional steps could be taken to ensure $\Delta\epsilon < R(\epsilon)$ at all times, to ensure curvature is preserved at all times. This could be accomplished by subdividing $\Delta\epsilon$ into adequate number of implicit substeps. However, the Bezier curve is quite robust even in explicit stepping, as shown in Fig.3.17. For the purpose of simulating triaxial test results, the measurements are of high enough resolution to use explicit K_b, without adding implicit iterations (note, in section 3.2 the p-y curves using Bezier stiffness are made, and those do adopt a simple form of implicit stepping).

Addressing volumetric response behavior

It is a common practice to model ϕ as a function of e, and the new test results support it. However, absolute density (void ratio e) appears to have little correlation with stiffness. Changes in soil stiffness behave correlated with increments of Δe rather than absolute value of e. This is observed in undrained cyclic loading, where a specimen of near constant density can lose stiffness (become disturbed) but not recover (not stabilize).

Water is near incompressible, thus $\Delta e < 0$ is restricted. Given this condition, the phenomenon of stabilization (modelled by $\Delta \epsilon_R < 0$) is prevented. Sand is not observed to recover stiffness during undrained loading cycles, thus ϵ_y envelope must not shrink without increments of $\Delta e < 0$.

Stiffness can be lost in undrained mode, this is clearly visible during liquefaction (see Fig.3.7). Water is very stiff in compression, but becomes into soft gas in vacuum. Thus, pore water cannot prevent $\Delta \epsilon_R > 0$, because $\Delta e > 0$ (dilation) can't be stopped by pore water.

Water can withstand up to $70000atm$ pressure, in compression, before it transitions into a solid state (compressed into ice at room temperature), but merely $-1atm$ is enough to turn water into gas at room temperature (at which point $Pp \approx -100kPa$, and $\sigma_{r,max}$ is reached in Fig.3.3). Therefore, pore water can prevent contraction $\Delta e < 0$, but not dilation $\Delta e > 0$. Undrained specimens cannot recover stiffness, but can lose it, due small $\Delta e > 0$ increments which variating around near constant absolute e value. The observed causation is implemented in Eq's 3.10, 3.11:

$$\psi_{cont} = \begin{cases} k_{cont} \cdot (1 - \epsilon_{norm})^{\frac{(emax-e)}{(emax-emin)\cdot log(\epsilon_R \cdot k_R+1)}} & \text{, in compresion} \\ k_{cont} \cdot (\epsilon_{norm})^{\frac{(emax-e)}{(emax-emin)\cdot log(\epsilon_R \cdot k_R+1)}} & \text{, in extension} \end{cases} \tag{3.10}$$

$$\psi_{dil} = \begin{cases} k_{dil} \cdot \epsilon_{norm}^{\frac{(emax-e)}{(emax-emin)}} & \text{, in compresion} \\ k_{dil} \cdot (1 - \epsilon_{norm})^{\frac{(emax-e)}{2(emax-emin)}} & \text{, in extension} \end{cases} \tag{3.11}$$

$$\Delta \epsilon_V = |\Delta epsilon| \cdot (tan(\psi_{cont}) - tan(\psi_{dil})) \tag{3.12}$$

The volumetric change parameters were fitted to k_{cont}=1000, k_R=5000, k_{dil}=3. The same parameters is kept in all triaxial test simulations shown in this thesis. The same coefficients are used while simulating different irregular loading sequences on Frederikhaven sand and other sands (silty sand and Aalborg university sand no.1). The objective is to look at general patterns which can be predicted by one set of variables - rather than adjusting to fit individual data plots. Thus, a constant set of coefficients is made and kept through all simulations.

Because $\Delta \epsilon_R \propto \Delta e$, the strain envelope behaves proportional to incremental change in density, rather than anchoring to the absolute value ($\epsilon_R \not\propto e$). This makes BSM compatible with the experimentally observed paradox where lower stiffness (larger ϵ_R) is encountered higher density (lower e). Also, during deformation cycles, contractive volume change is observed to dominate. Cyclic loaded sand "shakes down" [10] towards a state of lowest potential - highest density. Every time the yield envelope is pushed apart, dilation takes place, but the consequent disturbed soil state super-compensates by becoming more contractive. Therefore, loading cycles are always biased towards net total of contractive behavior. In drained, this causes continuous

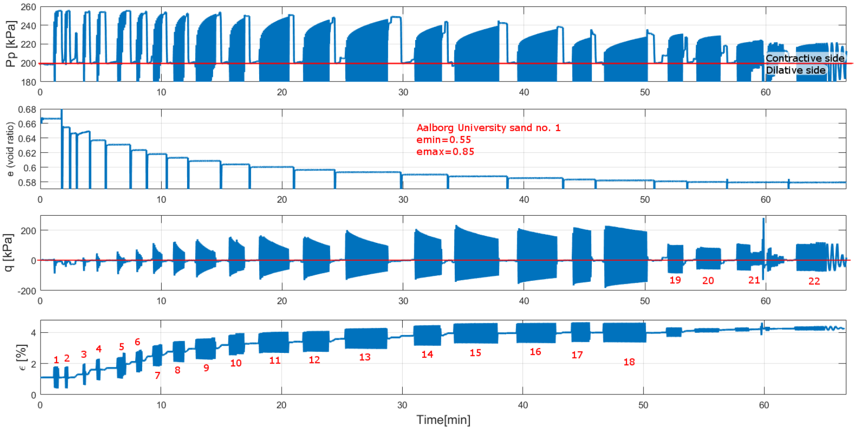

Fig. 3.18: Aalborg university sand no.1. specimen repeatedly liquefied and drained. 18 groups of ϵ cycles applied, before switching to q cycles for groups 19 to 22. Notice how increasingly more deformation cycles are necessary to generate excess pore pressure. While pure dilative state was not reached - a similar testing procedure could be used to reach soil density where no excess Pp can be generated at any phase of a loading cycle (pure dilative soil state).

increases density, reaching towards e_{min}. In undrained - this causes liquefaction.

As sand becomes denser (e_{min} limit approached), contractive increments become smaller. Specimens become harder to liquefy. At very high densities, ϵ_R size becomes limited to small deformation amplitudes [17]. Thus, a specimen cannot liquefy after reaching a certain density, as Δe increments are too small to generate the required pore pressure fluctuation. Alas, even high density sand generates small amounts of excess pore pressure, in certain phases of a loading cycle. Thus, with proper timing, a loading cycles can be paused and tiny volume of water can be allowed to escape. If this is repeated, a "purely dilative" soil state can be reached (when $e \approx e_{min}$). To prove this prediction made using the BSM model, a testing procedure to reach "pure dilative soil state" was executed (see Fig.3.18). The procedure for reaching pure dilative soil state iterates between drained and undrained loading cycles, by repeatedly disturbing the specimen in undrained mode, then pausing at a loading phase with excess pore pressure, and allowing the excess to drain. The procedure uses deformation (ϵ) dependent soil properties, at very low confining pressure, to reach $e \approx e_{min}$:

1. Undrained ϵ cycles are applied, to cause increase in density (liquefaction). Note, $Pp \leq Cp$, thus once $Pp \approx Cp \approx 260kPa$ further $\Delta e < 0$ is not plausible. But while ϵ amplitude is smaller than ϵ_R limits, the Pp in dilative side is gradually lost in the measurement.

2. Once $Pp \approx Cp$, the $\epsilon(t)$ is paused in a phase where $Pp(t) > Pp_o$. Then, while holding $\epsilon = const$, the $Pp_{excess} = Pp - Pp_o$ is stable. There is no Pp drop or increase, while $\epsilon = const$. Note, water stiffness is nearly 4GPa, thus, microscopic leaks would cause tangible changes in Pp at this point.

3. Stable Pp_{excess} can now be safely drain by opening the drainage valve. As long as $\epsilon(t)$ is locked constant - there is no danger of causing dilation. Once drained, the valve is closed again. Procedure is repeated from step 1.

By repeating steps 1 to 3, the net result is $e \rightarrow e_{min}$ (see Fig.3.18). At higher densities sand becomes increasingly less contractive, and increasingly smaller ϵ amplitudes have to be applied to prevent dilation (visible in Pp history). This means maximum ϵ_R limits are shrinking, as absolute density increases. Alas, even near pure dilative state, some excess pore pressure can still be generated. Water is so stiff ($\approx 4Gpa$), that even microscopic changes in Δe create tangible Pp fluctuations. It is not clear how many iterations it would take to reach the real "purely dilative" soil state, but at some point e history becomes flat, because microscopic volumes of water ar drained each time the drainage valves are opened. At that point microscopic ϵ amplitudes need to be applied to prevent ϵ_y envelope from yielding (causing dilating), as dilation can triger cavitation (water turns into gas at room temperature, in near vacuum pressure). When water transitions from fluid to gas state, forcing the gas to condensate back into liquid is problematic. Thus, if dilation compromised the procedure, the valves had to be opened, water allowed to flow in from the outside, and the procedure started all over. Note, this is a novel testing procedure, it's application and explanation of the processes need further research. Alas, a near dilative soil state is reached in practice, and that is an interesting physical phenomenon to observe and explore further - purely for research purposes. This is a new phenomenon, and the new model predicts / captures parts of it.

Looking at Fig.3.18 it is visible that during loading cycles 1 to 13 increasingly more deformation cycles are required to generate similar quantity of contractive Pp, and the Pp generated on dilative side of the line becomes increasingly dominant. When ϵ is paused in contractive phase, excess Pp is drained, but volume change Δe becomes gradually smaller (despite similar quantity of Pp being "released" by draining). This means bulk stiffness of the soil skeleton is increasing, as smaller volume change causes higher pore pressure buildup. Somewhat similar observations were made by R.Dobry [11], who published strain (deformation) normalized liquefaction charts, which describe volumetric response as a function of strain history, rather than being parametrized in stress space. This questions the use of critical state line for describing volumetric behavior of sand. However, Schofield (the original author of CamClay model, and thus - critical state principle) emphasizes that critical state was intended to describe only clay, and only in short term loading scenarios [37]. Schofield himself publicly criticizes blind borrowing of critical state principle when describing sand properties. The new experiment, reaching for pure dilative soil state, shows quite conclusively that cyclic loaded sand does not reach towards a critical state, but transitions towards the absolute density limit e_{min} instead. Same conclusion is given by tests executed by Vardoulakis [42], who shows sand does not stop dilating at "critical state", even at 50% strain.

When observing volumetric response of sand, care must be taken to acknowledge shortcomings of classical triaxial testing setup. Unlike frictionless end platen, the classic configuration creates non-uniform volumetric strain, part of the specimen is contracting while the shear rupture region is dilating. Thus, classical triaxial tests can measure no volume change during yielding - not because the specimen keeps constant volume, but because dilating and contracting parts cancel each other [20] [39] [15]. It is crucial to preserve isotropic volumetric strain distribution within the specimen, when measuring volumetric response. Therefore, care must be taken to differentiate between volumetric response observations made using the high friction and low friction end platen triaxial test results.

2.7 BSM in action

Finally, simulations of specimen tested using a frictionless triaxial apparatus can be attempted by following a simple algorithm:

1. INPUT $\epsilon(t)$, σ_r
2. if $f_\epsilon(\epsilon(t)) < 0$, then Update ϵ_R, ϵ_o;
3. if $f_\epsilon(\epsilon(t)) > 0$, then Update ϵ_R, ϵ_o;
4. Interpolate $\epsilon(t)$ within ϵ_y envelope
5. OUTPUT $e = f(e, \psi(\epsilon_{norm}), \Delta\epsilon)$
6. Update $\phi = f(e)$;
7. Update $\eta_{norm} = f(\eta_{norm}, \epsilon_{norm}, \Delta\epsilon_{norm})$
8. Update $\eta = \eta_{norm} \cdot ((\phi_{comp} - \phi_{ext}) - \phi_{ext})$;
9. OUTPUT $q = f(q, \epsilon, \sigma_r)$

Some clarification on the 9 steps of the algorithm: Step 1 takes $\epsilon(t)$ (and σ_r from measurement. Step 2 generates stabilization: the ϵ_y envelope contracts. Step 3 checks if $\epsilon(t)$ is still within ϵ_y limits (compensating for excess contraction in step 2 if necessary). Step 4 interpolates $\epsilon(t)$ within ϵ_y to obtain $epsilon_{norm} \in [0,1]$. Step 5 estimates volumetric response - it is not the primary objective of the model, but interesting nevertheless. Step 6 is optional for ϕ variation is relatively small. Step 7 converts $\epsilon_{norm} \rightarrow \eta_{norm}$ using Bezier stiffness principle. Step 8 scales $\eta_{norm} \in [0,1]$ up towards $\eta \in [\phi_{ext}, \phi_{comp}]$, thus simulation results are always within the coulomb limits governed by ϕ. Step 9 combines η and σ_r to find q. In summary, the inputs are: ϵ and σ_r, the output: q and e.

Simulations are presented with sequential increase in complexity. First, tests presented earlier are fitted using the BSM, to demonstrate descriptive power. Later, predictive power is demonstrated, by generating new testing histories and fitting them without re-calibrating the model. Test in Fig.**??** is the "reference test" towards which the ϵ_y envelope was calibrated, and the same calibration is then kept for all other tests.

First, tests with constant σ_r are fitted. Then, drained test with varying σ_r. Finally, tests combining drained and undrained loading are generated and fitted. Thus, tests become gradually more complex, going through irregular cycles combining drained and undrained loading in one, aggressive, complex loading sequence. For extra challenge, BSM calibrated for Frederikshaven sand is challenged to predict behavior of two other sands: Aalborg University sand no.1 and Silty sand. Calibration of the ϵ_y envelope is kept constant through all the tests, only ϵ_{min} and ϵ_{max} limits are adjusted to "scale" the plots vertically:

1. Aalborg university sand no.1: $e_{min} = 0.55$, $e_{max} = 0.854$
2. Silty sand: $e_{min} = 0.42$, $e_{max} = 1.155$
3. Frederikhaven sand: $e_{min} = 0.64$, $e_{max} = 1.05$

Triaxial test simulation results

Test data in Fig.3.19 is the same as Fig.3.12 - where formation of the stable stiffness triangle was observed at three different ϵ_{mob} amplitudes. This time the simulation result is plotted on top of the measurement data. Notice how Fig.3.19 is split into left and right: on the left $q(\epsilon)$ and $e(\epsilon)$ are plotted, to observe to stiffness and dilativity. On the right: the time series of $\epsilon(t)$, $\sigma_r(t)$, $q(t)$ and $e(t)$ are plotted. It is necessary to provide time series plots, as complex lading histories start overlapping in q-ϵ and e-ϵ plots.

While looking at the left side of simulation plots, beware the model is not intended to predict "initial" soil state. The initial $\epsilon_R = 0.1$ is assumed in

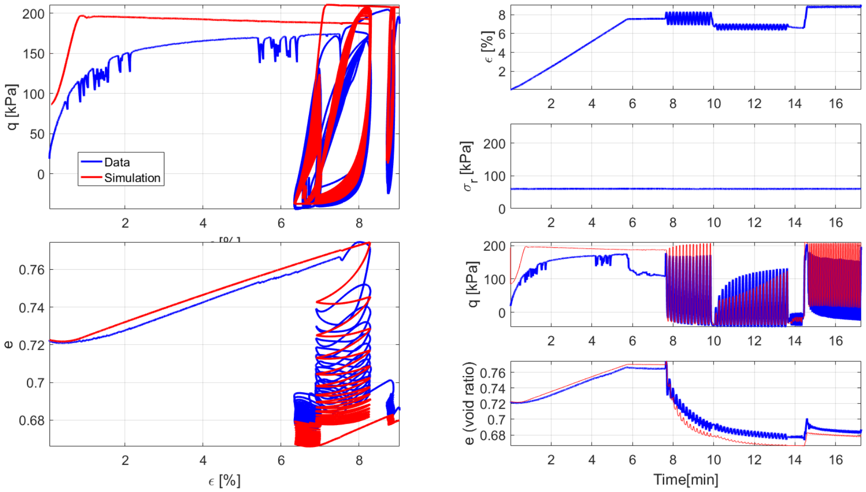

Fig. 3.19: Frederikhaven sand test. Drained, σ_r is held constant, while three groups of ϵ cycles are applied. This is the reference test towards which the model was calibrated. All the coefficients will hold constant, except for e_{max} and e_{min} - which will be change when Frederikhaven sand is replaced by silty sand, well graded gravel of Aalborg University sand no.1.

all tests. The model is intended to converge towards the correct soil states from arbitrary initial soil state. Therefore, the beginning of simulation can be ignored. Note, initial e is known when preparing a specimen, thus initial e is inserted to match starting e of each specimen. Notice how $\sigma_r(t)$ is a flat line in Fig.3.19. In drained triaxial test σ_r is a constant. Only in undrained tests σ_r varies depending on the phase of a loading cycle. Sadly, until e response is captured with higher precision, nonlinearities of Pp cannot be simulated.

Next, the model is tested by moving the σ_r value, while holding ϵ_t constant (shown in Fig.3.20. Some shortcomings of the model become apparent, as the triangles are somewhat flat at the top and, when σ_r is increased, stiffness points towards the new "max" position too steeply. It is not clear how to address this shortcoming yet. It is challenging to improve fitting of one data plot without compromising the others. It could be an option to use multiple ϵ_y envelopes, with different hardening rates. Implementation of such option in strain-space is mentioned by P.J.Yoder [44].

A noticeable distortion of $e(\epsilon)$ measurement is visible in Fig.3.20. This is likely because the loading rate was too fast, and water flow velocity generated dynamic water pressure in drainage tubes. The e sensors used in measurement was designed to measure clay, thus water seepage generated by dynamic loaded sand can exceed tolerances of the testing equipment. However, when loading is paused the measurement stabilizes, thus the mean value of measured curve is reliable. In addition, to ensure fully drained condition,

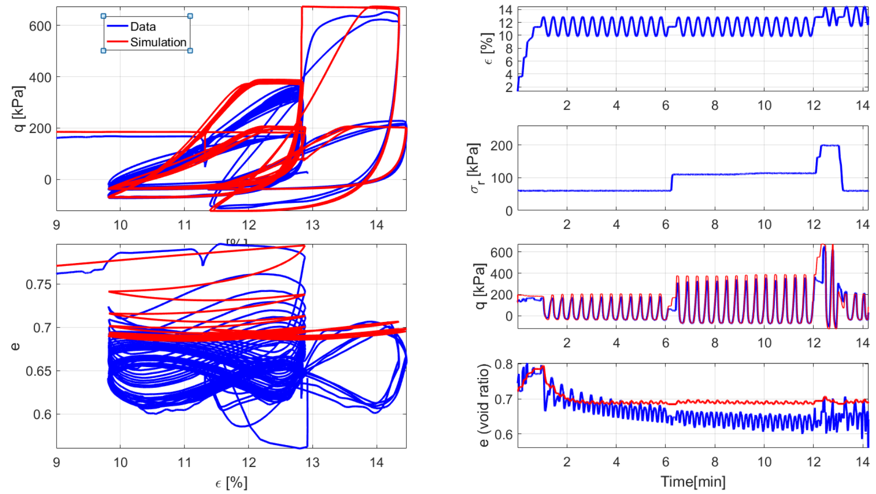

Fig. 3.20: Frederikhaven sand test. Drained, σ_r is varied, while four groups of similar ϵ cycles are applied. This illustrates how disturbed soil state is not affected by changes in p'. Also revealing some shortcomings in preliminary model (excess stiffness after increasing σ_r)

specimens were drained only through the top of the specimen, while measuring Pp at the bottom. The bottom of the specimen is the last part to be drained. Therefore if measured $Pp \approx Bp$, the loading rate is not excessive. As can be seen from $\sigma_r(t)$ plot, no Pp fluctuation was present during this test. Thus, noise in the e measurement does not affect the quality of the drained condition (the schematic of frictionless triaxial apparatus can be seen in Fig.2.3, also Appendixes A, B and C can be referred to for more details).

Next test is different from all previous tests. The test contains q cycles applied on a disturbed specimen. This is a test procedure designed using q as the input, and $epsilon$ as the output. The resulting $epsilon$ history was input into the model to see if the model will recognize what q history was applied on the specimen (see Fig.3.21. Such test is interesting because, eventually, the model is meant to be used in engineering practice where loads are obtained and applied as forces, not displacements. In the outcome, the ϵ_R appears to have shrunk faster than it should have. However, the simulation does predict the stress amplitudes rather well.

At this point it is expected that readers have developed a certain degree of intuitive understanding what material properties ϵ_y envelope captures. It should be intuitive, that the large deformation applied before loading cycles (see Fig.3.21) pushes the ϵ_y envelope apart, thus leaving a disturbed soil state, with the "max" point at $\epsilon = 10\%$ limit. Before unloading to apply the q cycles. At the end of the test both the $e(t)$ and the $q(t)$ match quite well. Thus, the model has a remarkable tendency to calibrate itself - to converge towards the

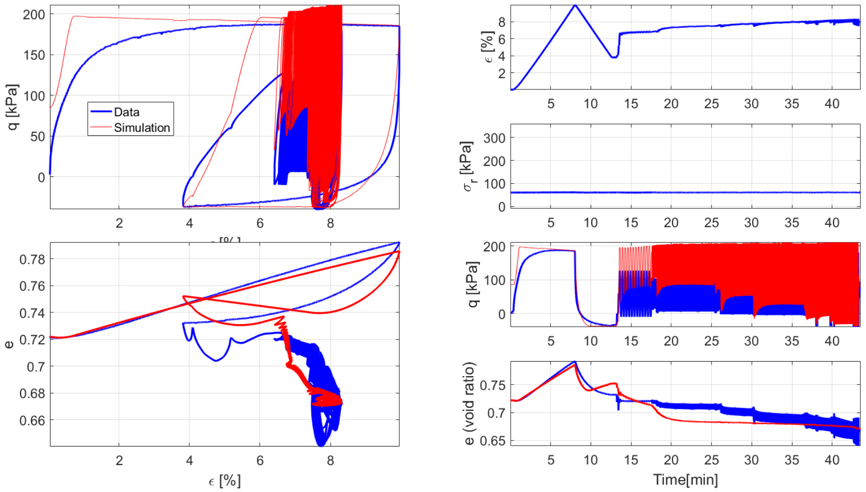

Fig. 3.21: Frederikhaven sand test. Drained, q cycles applied on the specimen (specimen left disturbed after overloading by large ϵs amplitude). The generated $\epsilon(t)$ was used as the input for simulation. The output $q(t)$ (Simulation) was compared with the input $q(t)$ (Data).

correct soil state.

Thus far simulations in Fig's.3.19, 3.20 and 3.21 were drained. Next, the model performance is evaluated in undrained mode, during liquefaction (see Fig.3.22). This test is fully undrained from start to finish, therefore increment $\Delta\epsilon_R < 0$ was disabled. This changes the model performance ever so slightly, by preventing stabilization of the stable stiffness triangle. Alas, e and ϵ_y are modeled in parallel, thus the e was allowed to behave as it would in drained mode (variation of ϕ caused by e is negligible). The choice to plot drained e on top of undrained e history was made for two reasons: (1) undrained e is constant, there is nothing to see. (2) The e cannot be converted to Pp history yet as nonlinear e response is not modeled precisely enough, in addition to the fact that water stiffness itself changes depending on water pressure (nonlinear e would have to be scaled by nonlinear water stiffness). Alas, by observing the "expected" e response the reader can make assumptions and make conclusions regarding the behavior modelled by BSM in it current version.

It is remarkable, how well the stiffness simulation overlaps in $q(\epsilon)$ plot in Fig.3.22. This level of fitting can be attributed to $\eta \approx \phi$ when ϵ_y is yielding. Because during yielding η is nearly constant ($\approx \phi$). As η is constant, the undrained stress path moves in close proximity to the Coulomb envelope, as the ESP line is pushed up by σ_r. Thus, causing q to slide along the linear Coulomb envelope. In undrained tests σ_r is borrowed from measurement, thus good fitting is not surprising, if the model predicts η behavior correctly.

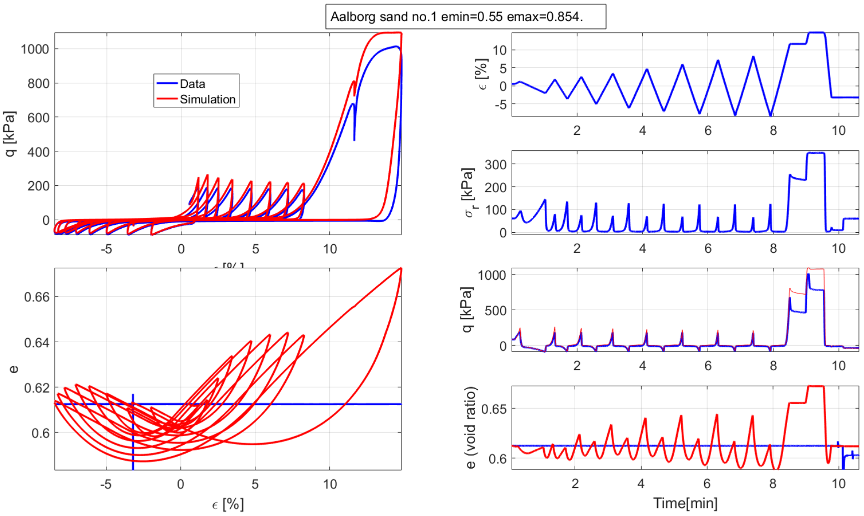

Fig. 3.22: Frederikhaven sand test. Drained, q cycles applied on the specimen (specimen left disturbed after overloading by large ϵs amplitude). The generated $\epsilon(t)$ was used as the input for simulation. The output $q(t)$ (Simulation) was compared with the input $q(t)$ (Data).

Therefore, a conclusion can be made, that half of the solution correct - to predict real time stress state η and σ_r need to be predicted. Performance of η is modeled correctly, but undrained σ_r cannot be modeled until e and water stiffness properties are understood to a higher degree. Research of principles governing σ_r behavior are left for future work.

The way e is modeled at the moment is not adequate for simulating σ_r, but the predicted e response revels some hints for future work. Notice the peaks of $e(\epsilon)$ reach similar height during liquefaction - and so do values of Pp. Thus, it seems plausible to multiply ϵ_v with some stiffness coefficient which would make the peaks fit the Pp. Also, when peak undrained strength is measured, the e history predicts continuing dilation after water stiffness is lost (cavitation). Thus, the way e is treated in BSM is compatible with general patters observed in real-life testing.

While comparing simulation with test results, notice the novelty is not only the model. The testing procedure itself is new. Tests where undrained strength is tested after full liquefaction, and the specimen is then pulled back to initial length, only to be drained and continued to test - such triaxial tests are a novelty, which does not have direct application in the industry. The test procedure is interesting because it raises new questions, new observations, which reveal sand behavior in circumstances beyond the reach of conventional solutions. The fact such procedures are plausible provides opportunities for other researchers to make pioneering research - to look for unknown

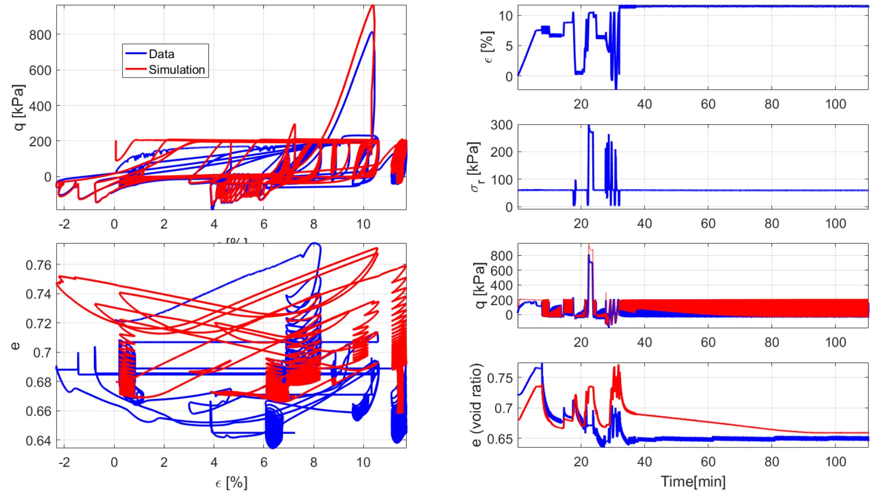

Fig. 3.23: Frederikhaven sand tests. The most complex multi and aggressive multi stage test executed using the frictionless triaxial apparatus.

unknowns, within a new testing scope. Loading scenarios of extreme complexity and aggression can be executed (see Fig.3.23).

The loading history in Fig.3.23, is a challenge to both: generate experimentally and a model numerically. The sequence contains 9 stages of testing. Detailed explanation of each stage was published in journals and conferences (see Appendixes A, B, C). The key points to notice in Fig.3.23:

- drained deformation cycles form stiffness triangles and the model recalibrates itself in those instances.
- undrained stiffness paths are fitted very well since $\eta \approx \phi$ and σ_r is borrowed from measurements.
- Simulation results and experiment measurements converge towards each other in the end.

The level of fitting achieved by one ϵ_y envelope is remarkable. The rules governing ϵ_y are extremely simple, but capture the essential features common to both drained and undrained loading, loss and recovery of stiffness. The model even re-calibrates itself each time cycles of constant ϵ amplitude are encountered - the more loading cycles, the more precise the prediction becomes. Similar behavior was observed in other cohesionless soils as well. BSM calibrated for Frederikhaven was challenged to predict behavior of Aalborg University sand No.1, and silty sand (see Fig.3.24).

The fine silty sand test was executed drained, and σ_r was switched between 2 different values during testing. Near 2 minutes into the test the

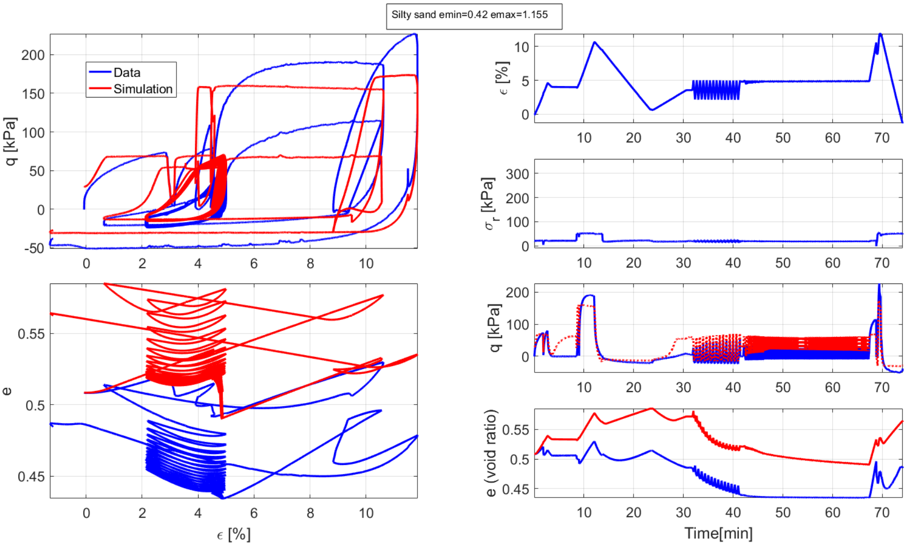

Fig. 3.24: Test executed on a silt specimen. The silt was very sensitive to liquefaction and stable σ_r was hard to sustain. Very slow loading rates had to be used.

hydraulic piston of the triaxial apparatus malfunctioned - started vibrating at very small deformation amplitude, thus causing partial liquefaction, thus - some extra loss of density. This U-PID malfunction caused measurement and simulation to diverge into two different paths in $e(t)$ plot (Fig.3.24), as the vibration amplitude and frequency were too high, thus not present in inputs provided to BSM during simulation.

2.8 Constitutive formulation (ϵ-space plasticity)

The simple implementation of ϵ_y envelope in BSM model shows promising results: irregular stiffness response patterns are predicted, combining both drained and undrained response. As a bonus - volumetric response is predicted to some degree as well. Given the robustness of ϵ_y envelope, it is curious how rarely (if ever) strain-space envelopes are mentioned in contemporary geotechnical paradigm. Nevertheless, a compatible formulation was published in the 80's by P.J.Yoder [44]: strain-space formulation for cohesionless soils. Existence of strain-space plasticity was unknown to the author of this thesis, until simulation were finished. Alas, in unlikely turn of events, P.J.Yoder explicitly asked for "experimental rationale addressing the strain space problem". It seems the new scope of triaxial testing provides access to measurement P.J.Yoder requested 37 years ago. By pure coincidence, results of experiment confirm the theory.

P.J.Yoder had no access to "experimental rationale". His motivation to

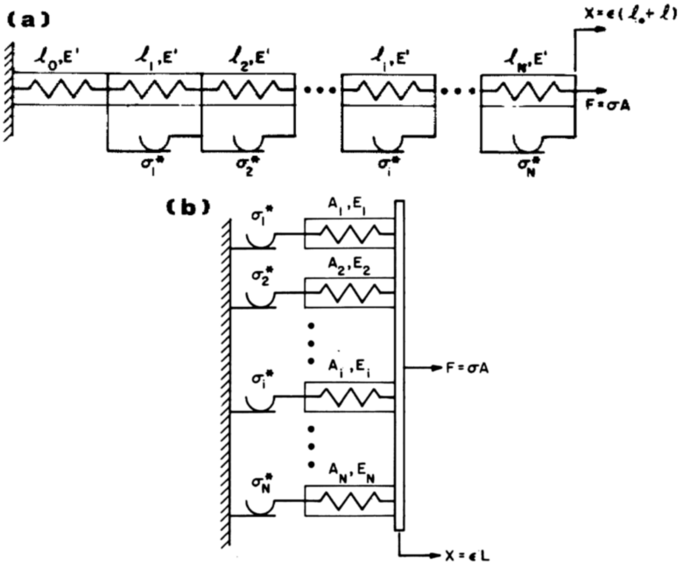

Fig. 3.25: a) The series-parallel model. b) The parallel-series model. [44]

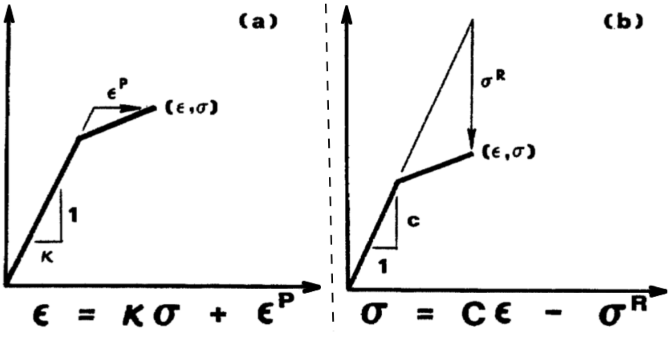

Fig. 3.26: One-dimensional bilinear system, describing the material state at some point along the curve a) the traditional scheme (stress-space); b) the strain-space alternative (using relaxation stress instead of plastic strain); [44]

explore strain-space plasticity was driven by computation benefits:

1. ϵ-space formulation is a parallel spring system, not a series spring system (see Fig.3.25). Thus, there is no need to inverse the global stiffness matrix at every loading step. One matrix inversion could be enough to simulate infinite loading steps (demonstrated later, using p-y curves). Matrix inversion is computation costly, thus avoiding it is a big benefit.

2. Exact relaxation stress is known for every ϵ [44, p. 33, 42] (see Fig.3.26,b). This means iterative return mapping is not necessary. This removes further matrix inversion steps, unavoidable in stress-space solution methods.

Stress-space envelopes move proportional to plastic strain increments. Stress envelope is a function of plastic strain, and plastic strain is a function of the envelope. The two are itterated back and forth, until an equilibrium is found. Alas, the equilibrium is not always available, thus making the titter tatter between stress and strain space prone to errors and instabilities. On the other hand, strain-space envelopes have an exact solution at all times, as both the strain increment and the strain envelope are both in the same coordinate system. Thus, removing the need for iterative solving for envelope position: "The best way to handle the return mapping problem may be to circumvent it - by working in strain space" [44, p .48]. P.J.Yoder provides detailed derivation, implementation and simulations done without iterative return mapping. He compares it with "radial return", "secant stiffness" and "tangent stiffness - radial return" return mapping methods [44, p .88]. His result conclusively show that, simulations can be successfully run without using return mapping. Moreover - strain envelopes are less sensitive to load step size.

In addition to already existing implementation in geotechnics, the ϵ envelope is used in many material modeling paradigms outside geotechnics [13] [31]. This branch of models is advantageous for materials with rapid peak strength loss (such as cracking concrete or fracturing bone). Also, ϵ envelope was used in metallurgy (6061-T6 aluminum [44]) for simulating cyclic loading effects. Thus, the branch of strain-space models has plenty of examples to follow, plenty of unexplored potential for improved computation efficiency, and a new collection of experimental evidence supporting the strain-space principle.

Up to this point, sand stiffness (and volumetric response) were analyzed and modeled in extremely simplified conditions. Isotropic (linear) stress / strain field, in a specimen tested using the frictionless triaxial apparatus. Alas, the conclusions are applicable in a system of nonlinear springs, p-y curves. Next, an example of using deformation envelopes to simulate behavior of a cyclic loaded offshore foundation is given. Moving from problem (j)

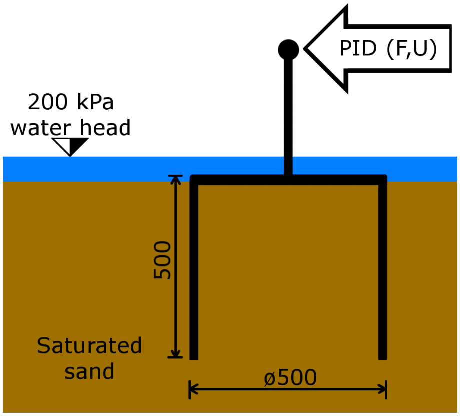

Fig. 3.27: Schematic of the mono bucket prototype, simplified to match case specific testing. PID controlled F or U input can be applied on the top node. While one is applied - the other one is measured. Water head pressure is important during rapid loading, as pore pressure significantly effects the peak strength (the boot effect [29] [45]).

to solution 11 in flowchart Fig.3.1.

3 Mono bucket prototype - testing and modeling

Observations made using triaxial testing should be applicable in foundation design. Thus, deformation dependencies were tested on a foundation as well. A mono bucket foundation prototype was subjected to lateral (overturning) deformation cycles in attempt to generate stable stiffness hysteresis loops. Once again, deformation was the input, and reaction force - the output. Following the principles of BSM, position of "min" and "max" points was monitored, and stiffness patterns were normalized between the points (more details in Appendix D).

3.1 Stable states in offshore foundation prototype

The mono-bucket prototype used at AAU laboratory is fitted with more measuring devices than are required for measuring stiffness alone. There are pore pressure transducers along the height of the skirt and multiple deformation transducers attached to the lid (see Fig.2.4, [25]). However, for the intended purpose of measuring stiffness variation alone, it is enough to have access to reaction force (F) and displacement (U) measured (and applied) at the top of the shaft, as shown in the simplified schematic in Fig.3.27. If U is used as the input - F is measured as the output, and vice versa.

Notice the water head pressure is increased to $200kP$ (see Fig.2.4). The

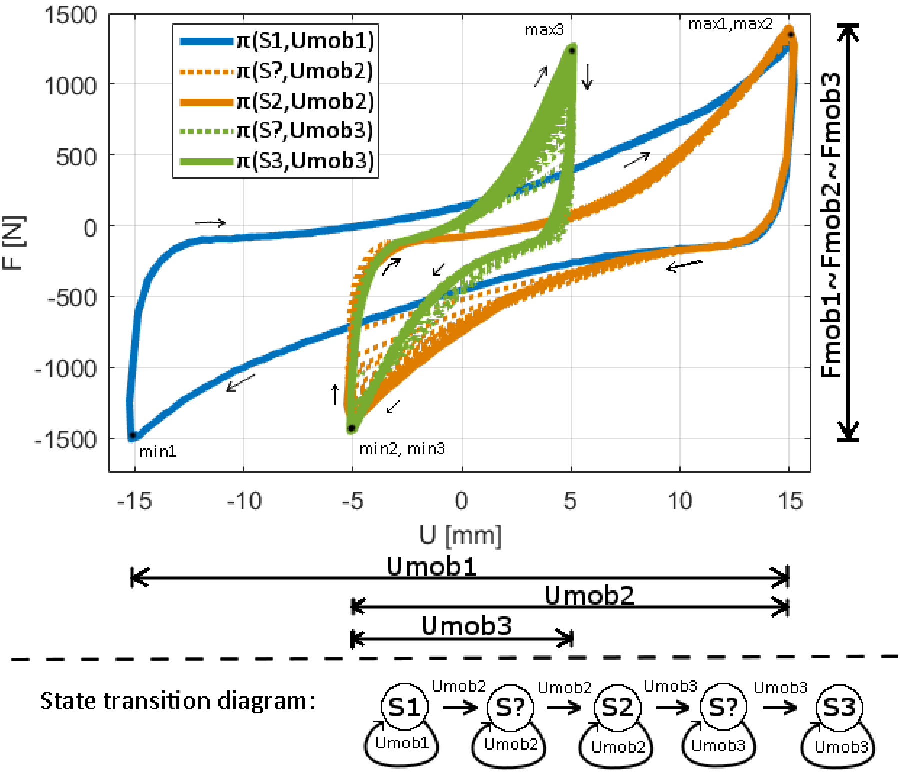

Fig. 3.28: Observing adaptation process generated by progressively smaller Umob amplitude. Points "min" and "max" are gradually shrinking along U axis, but retain very similar amplitude along F axis. A unique stable stiffness path converges for every U amplitude.

higher the water head - the more undrained strength is generated during rapid (impact) loading, due to undrained dilative sand response. The Pp needs to drop down to near $-100kPa$, before undrained peak strength is reached. Thus, when the initial water head is $200kPa$, the undrained response adds a total of $300kPa$ of effective confining pressure. This effect has been demonstrated experimentally by [29] and [45]. However, the phenomenon is a novelty, it is not part of contemporary design standards. Nevertheless, it has the potential to significantly reduce offshore foundation costs.

Following testing procedures developed in triaxial testing, deformation cycles of constant amplitude (Umob) were applied at the top node of the mono bucked. This produced converging stiffness hysteresis loops, within the applied "min" and "max" limits, as visible in Fig's.3.28, 3.29. However, unlike during triaxial testing, the hysteresis loops generated by a mono bucket (at $0.1Hz$ loading frequency) are symmetrical (not triangular), and somewhat concave. Nevertheless, the general behavior remains very similar, and plau-

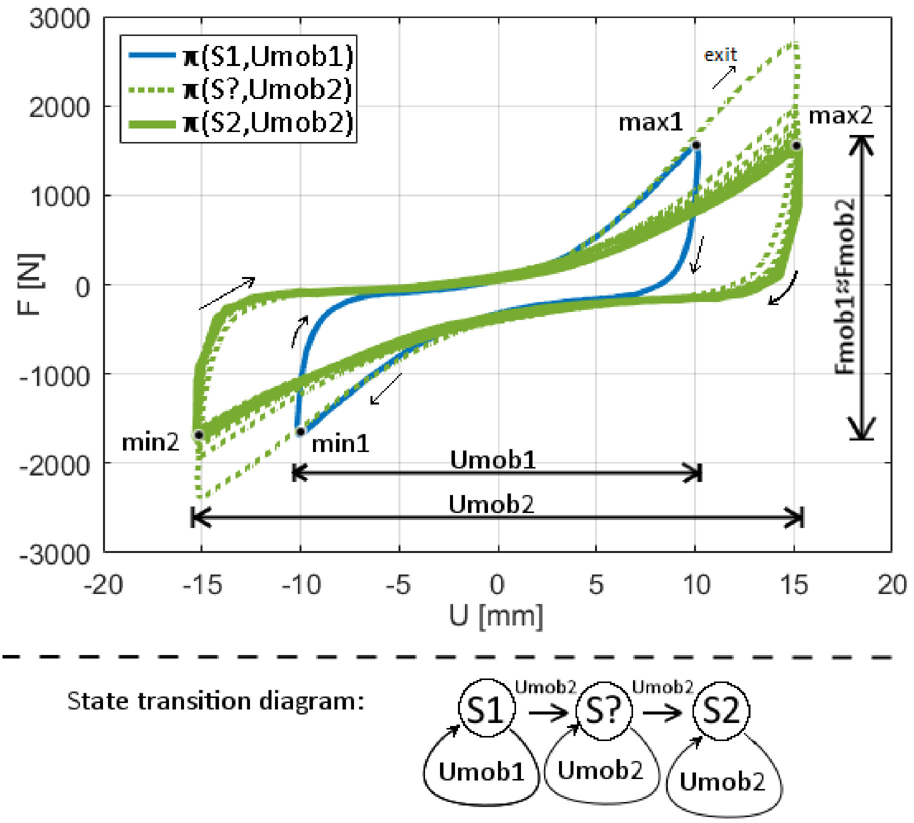

Fig. 3.29: Observing adaptation process generated by progressively bigger Umob amplitude. Points "min" and "max" are pushed apart along U axis, but converge to very similar F limits. A unique stable stiffness path converges for every U amplitude.

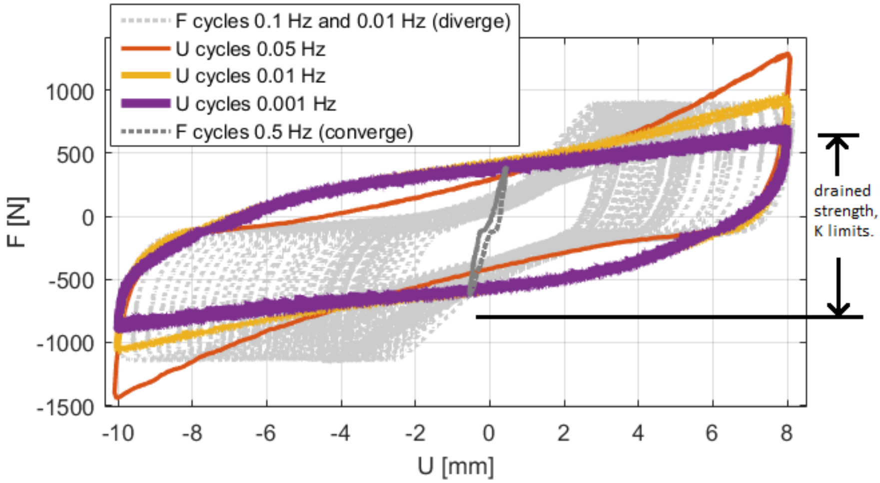

Fig. 3.30: As loading cycles become slower $\Delta U \rightarrow 0$, thus C component can be switched off, and quasi static stiffness curve K can be isolated to analyze individual components within the nonlinear, state dependent equation of motion (Eq.2.1).

sible to describe using a deformation envelope, using the BSM principles.

When a transition from larger Umob to smaller Umob amplitude is made, the "min" and "max" points gradually shrink closer to Umob peaks (see Fig.3.28). However, unlike triaxial testing, exiting towards larger Umob causes gradual "min" and "max" adaptation (see Fig.**??**. In triaxial tests, exit to bigger amplitude caused instantaneous adaptation, but this time adaptation is gradual in both cases (yielding and stabilizing).

In Fig's 3.28 and 3.29 Umob cycles were applied at $0.1Hz$ frequency. Smaller loading frequency produces less pore pressure fluctuation, as more time is given for pore water seepage. To check for drained (quasi static) stiffness hysteresis loop, constant Umob amplitude cycles were applied at decreasing loading frequencies (shown in Fig.3.30). The resultant quasi static stiffness hysteresis loop was observed to follow a familiar convex curvature compatible with Bezier stiffness principle. Thus, BSM can be implanted in a nonlinear p-y curve, by replacing the stiffness hysteresis loop observed during triaxial testing, with a quasi static stiffness hysteresis loop observed using a small scale foundation.

As was mentioned in introduction, the equation of motion (Eq.2.1) requires nonlinear K, C and M components to model dynamic response of sand. If loading cycles are applied at low enough frequency, quasi static response is reached, and the influence of C component is eliminated - leaving only the stiffness curves caused by quasi static K component. Similarly, faster loading cycles will amplify the effects of C, as visible in Fig.3.30. Thus, by manipulating the frequency of Umob cycles one can switch the C component on and off at will. This is interesting, as such tests could allow to decode nonlinear, state dependent K, C and M behaviors.

Based on principle described in BSM, cycles within the drained K limits should stabilize (yield envelope shrinking), above - diverge (yield envelope expanding). To test this hypothesis, F-PID cycles were applied with F amplitudes reaching slightly above and below the measured quasi static drained K strength limits, as is visible in Fig.3.30. The quasi static strength peaks were shaped at 0.001Hz in Fig.3.30. They were normalized within BSM deformation envelope to be used in p-y curves.

The p-y curves model idealized soil without the C component. Nevertheless, it is interesting to notice how much F-PID loads amplify the C component during real-life testing. Deviation from K, caused by C is visible in Fig.3.30 - hysteresis loops generated using F-PID fall below the quasi static stiffness curve, and raise above the curve during different loading phases. During contraction dominant phase - stiffness curve drops below quasi static (partial liquefaction). During dilation - raise above (the boot effect). This is to be expected, as F-PID allows unrestricted loading rate ($\frac{\delta U}{\delta t}$) to accumulate, which means deviation caused by C will be amplified during F-PID controlled loading. The C component behaves like a nonlinear, state dependent damper.

It is curious that different Umob amplitudes converge to identical hysteresis loop shapes even while C component is active (see Fig's. 3.28 and 3.29). This means both K and C components are directly proportional to deformation amplitude. Thus, it can be deduced that stable state C component is normalizable within a deformation envelope as well as the K. The sum of K and C effects could be combined within one deformation envelope.

Because C is proportional to deformation, stable state reached at smaller deformation will cause more dilation rate (steeper stiffness hysteresis loops, stronger boot effect). To check this prediction, test in Fig.3.31 was executed. The foundation was cyclic loaded to stabilize stable hysteresis loops within three different Umob amplitudes, and the exit paths were generated from each stable state, starting from the same loading phase. As expected, larger Umob provided lower dynamic stiffness, smaller Umob cycles - larger dynamic stiffness. Note "pure undrained" response is not plausible in foundation testing, the word "undrained" here is replaced with "dynamic", as fast loads cause undrained response dominant pore pressure fluctuation, during the action of testing (At).

Once correlation between dynamic stiffness and deformation envelope was confirmed experimentally (Fig.3.31), attempts to manipulate (control, prescribe) disturbed soils states began. Recovery of "initial state" is very interesting for a number of reasons. Firstly, dilating soil has huge undrained strength reserve [29] [45]. The phenomenon governing undrained dilative soil strength is called "the boot effect" [19] [25] (a boot pulled out of mud 'quickly'

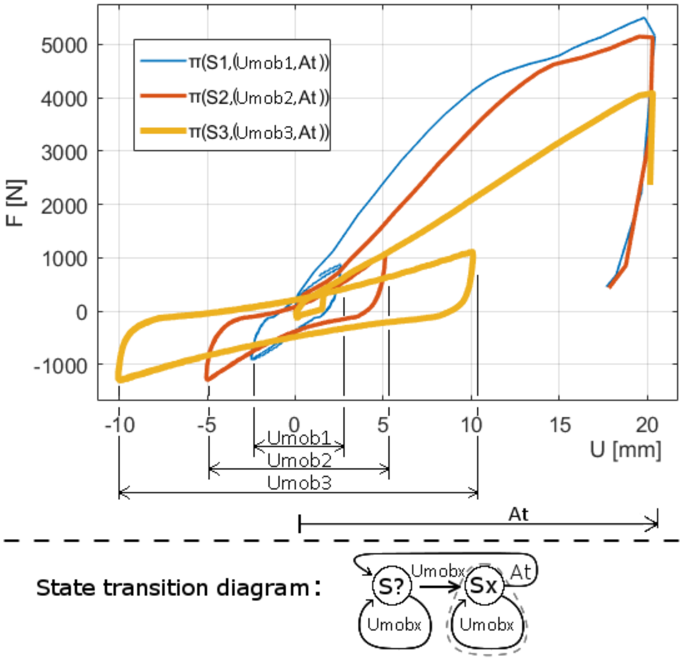

Fig. 3.31: Observing the stiffness path, caused by action of testing (At). After forming a stable state Sx, At is applied. It is noticed that smaller Umob generate recovery of impact resistance. This is likely due to recovery of dilation rate, as the resultant stiffness path extends beyond the drained peak strength limits.

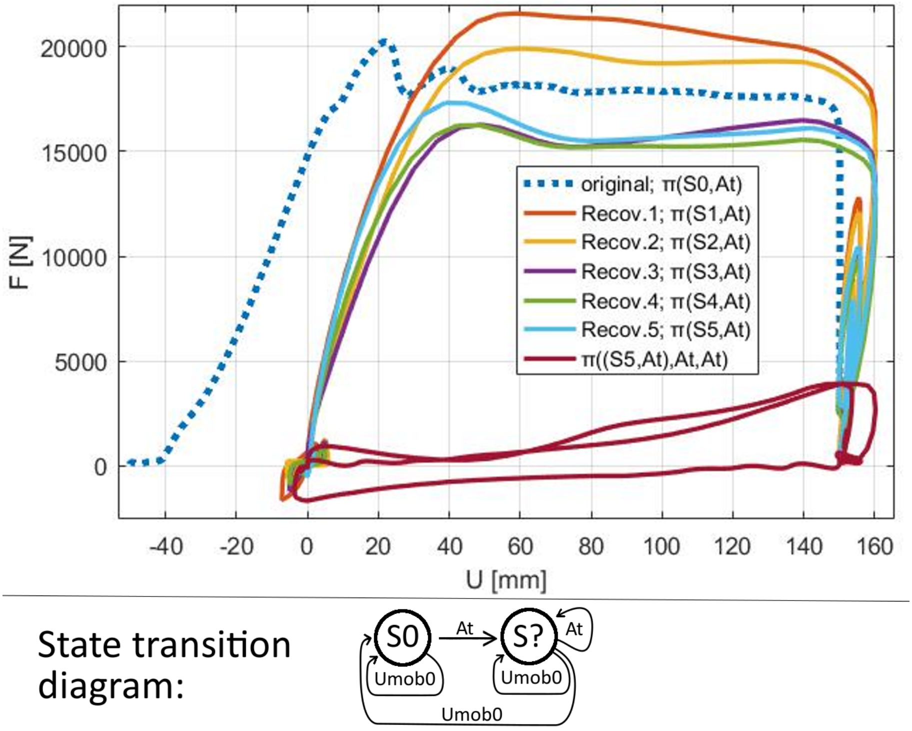

Fig. 3.32: Attempt to recover initial soil state (S0) many times in one loading history, by applying small deformation cycles Umob0. Stabilization back to S0 was plausible to achieve by either manually reducing the size of Umob amplitude, or by applying F cycles within the deformation limits (such F cycles produce Umob amplitudes of gradually smaller amplitude). Notice $\pi((S5, At), (At, At))$ is the only case where At was applied without attempting re-stabilization, and $\pi(S0, At)$ is borrowed from another thesis for reference [25].

generates more resistance than a boot pulled out slowly). This phenomenon is a potential source of higher bearing capacity. However, the benefits can not be used in engineering practice until both loss and recovery from disturbed soil states is modeled correctly. The boot effect is lost after soil is disturbed, as showed by $pi((S5, At), At, at)$ in Fig.3.32). Alas, if the principles governing recovery of the boot effect are understood, the principle could be used in the future, for more efficient foundation designs.

Before a model can be applied in the industry, it has to perform well in controlled laboratory environment. And the fact boot effect was disturbed and recovered 5 times in one testing history (shown in Fig.3.32) is the ultimate proof of concept for BSM principle - it has the descriptive, predictive and prescriptive power, adequate to de-facto describe, predict and control the stiffness path combining both K and C components in a foundation prototype. A similar pattern of episodic loss and recovery of stiffness in full scale foundations is known to occur as well [27] [9].

The observations could lead to improved solutions in offshore engineering industry, but before reaching commercial application the new found soil properties can be used to improve testing procedure efficiency within the laboratory itself. To illustrate this statement, the "original" stiffness path, obtained by S.D.Nielsen [25], is plotted in Fig.3.32. The "original" was obtained while following conventional testing protocols which take between 1 or 2 working days to generate the stiffness path. This is because the prototype has to be physically removed, and the sand box has to be "reset" by applying a gradient, then vibrated using industrial vibrators, then a CPT test is done to ensure the soil was vibrated uniformly, then the foundation is reinstalled. The test itself (generating the dynamic stiffness path) takes just a few minutes, but the preparation time takes a full working day or two. The new findings allow to "reset" initial state within minutes - a dynamic stiffness curve equivalent to "original" was recovered and tested 5 times in less than 2 hours. If this method is used to reset the foundation in the making for cyclic stress response charts (see Fig.2.7), the chart could be filled with measurement points much faster.

As our understanding of disturbed soil states is improved, we will find new applications. It is a new tool, which can find unusual applications. For instance: automating the testing procedure. If it is plausible to recover the initial state of a foundation prototype, a robot could generate entire charts of data fully autonomously. Then again, it could lead to solutions which make stress cyclic charts obsolete in the decades to come. Methodology adequate to control a phenomenon could be adequate to model it.

3.2 p-y springs modeling disturbed soil states

Quasi-static stable stiffness loop converges within deformation cycles of constant amplitude. Thus, p-y curves using drained stiffness hysteresis loop can be normalized within a deformation envelope using BSM principle. Note, the consequent simulations of a flexible beam in sand are not used to fit experimental data, but rather to explore the potential use of p-y curves combined with BSM principle. Nonlinear springs (p-y curves) attached to a beam, could provide insights how disturbed soil layers evolve during dynamic loading. Layers which do not stabilize will be more sensitive to liquefaction (as were disturbed triaxial tested specimens), and layers which do stabilize - can be predicted to recover the boot effect (resistance to impact loading).

BSM used in triaxial testing can be simplified for use with p-y curves. The stiffness path in foundation responses is symmetric, thus there is no need to preserve triangular hysteresis shape. The drained (quasi-static) hysteresis loop in Fig.3.30 can be generated by Bezier stiffness without using guiding lines, thus keeping only the radius R(x) variable from Eq.3.9, and replacing the eta_{min} and eta_{max} with constants of -1 and 1. Similar to scaling η_{norm} towards ϕ, the lateral resistance of a soil layer is scaled by $Fnorm$ (see Fig.3.33), proportional to overburden soil pressure. In simulations analyzed here lateral resistance is linear proportional to depth $Fmax = -Fmin = Depth$. This should suffice to mimic the effects of overburden pressure, for the intended purpose of observing the general behavior patterns of a parallel system of p-y springs with deformation envelopes (BSM model).

Unlike BSM calibrated for a a triaxial tested specimen, simulation of over restrained elastic beam requires to find static equilibrium at each loading step. The algorithm is shown in Fig.3.34. Notice how the spring uses relaxation stress (internal forces $Fint$) directly, without converting it to plastic strain. Exact position of the envelope is known at every step increment, there are no return mapping iterations (exact Δ is known instantly, at every U). Alas, convergence towards static equilibrium slows down when Δ increments become small, as $\Delta \to 0$ when dealing with log shaped f(U) function. Convergence rate can be improved by introducing PID coefficients: $Fint = Fint + kP \cdot \Delta + kI \cdot \int \Delta + kD \cdot \delta\Delta$. Using kP (proportional), kI (integral), kD (derivative) coefficients is a method borrowed from computer control systems. Notice stiffness K is constant in the p-y spring in Fig.3.34. Thus calibrating the PID coefficients is a one time procedure, and obtaining K^{-1} needs to be executed only once. Thus, the stiffness matrix can be inverted once, and used to solve for infinite loading steps, as long as the boundary conditions are not changed. Therefore - one stiffness matrix inversion for an simulation of infinite loading steps.

The soil is modeled using 10 p-y springs "below the soil surface", as seen in Fig's.3.35-3.37. One invisible p-y spring is attached to every node, along

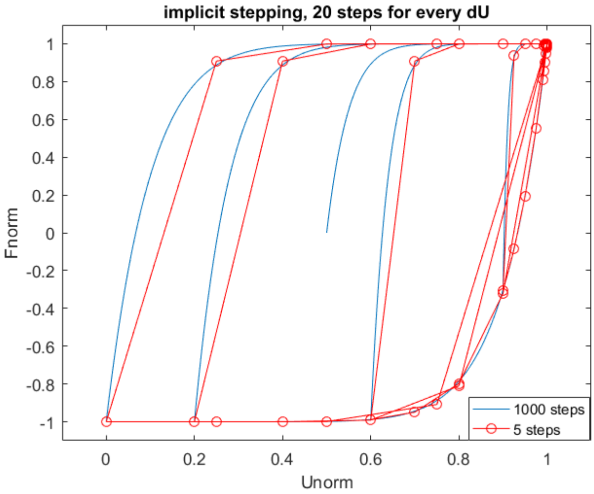

Fig. 3.33: Hysteresis curve imitating drained stiffness loop observed during slow loading cycles. Implicit stepping added for p-y simulations. Each step of Bezier stiffness now subdivides ΔU into 20 implicit steps. Consequently, the curves become very robust. Solution is almost independent of input step size.

the horizontal degree of freedom. The circles near the beam in Fig's.3.35-3.37 show the position of the deformation envelope ("min and max" points), visible on both sides the node. The length of the springs plays no role, as the envelope functions in absolute distance rather than strain.

The elastic beam is made of pure elastic beams with 2 degress of freedom - rotation and shear (horizontal degree of freedom). The axial load (vertical displacement) is ignored in the simulation and the beam has no mass.

The C and M component is ignored both in beam and the soil p-y springs. Such solution could be regarded as excessively conservative, as the C component increases peak strength during dynamic loads.

A loading force or a prescribed displacement ($Fext$ or $Ubdof$ in Fig.3.34) can be applied on the top node of the beam. Two versions of K matrix will be used: one for applying $Fext$ and one for $Ubdof$. $Fext$ is applied when the tip of the beam is unrestricted. $Ubdof$ is applied by assigning a boundary with a prescribed lateral displacement. Thus, the two matrices differ by 1 degree of freedom. Both versions of K^{-1} can be computed once and saved. Thus, to switch from applying Ubdof to Fext loading is as simple as switching between the stiffness matrices. Therefore, a very complex dynamic loading history of infinite loading steps can be made without additional stiffness matrix inversions.

The first two simulations observe deformation envelope behavior during F cycles. The tip of the beam is free to move, and F cycles are applied on

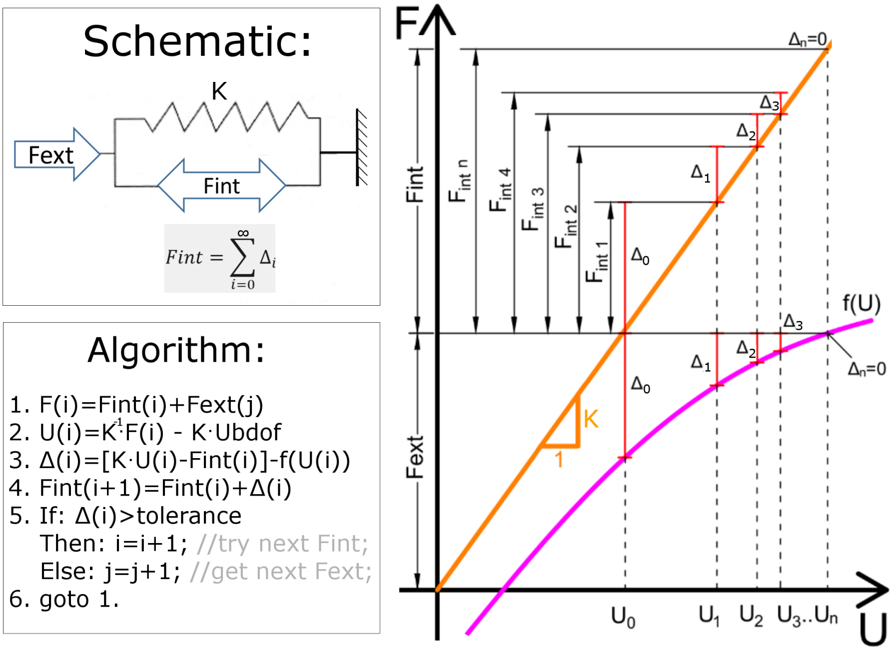

$$Fint = \sum_{i=0}^{\infty} \Delta_i$$

```
1. F(i)=Fint(i)+Fext(j)
2. U(i)=$K^{-1}$·F(i) - K·Ubdof
3. Δ(i)=[K·U(i)-Fint(i)]-f(U(i))
4. Fint(i+1)=Fint(i)+Δ(i)
5. If: Δ(i)>tolerance
   Then: i=i+1; //try next Fint;
   Else: j=j+1; //get next Fext;
6. goto 1.
```

Fig. 3.34: p-y spring schematic, algorithm and demonstration of the principle in action. The error Δ is added directly onto linear spring (stiffness K). Forcing the spring to elongate to a point where external force Fext=f(U). The rate of converging can be improved by using proportional integral derivative (PID) coefficients.

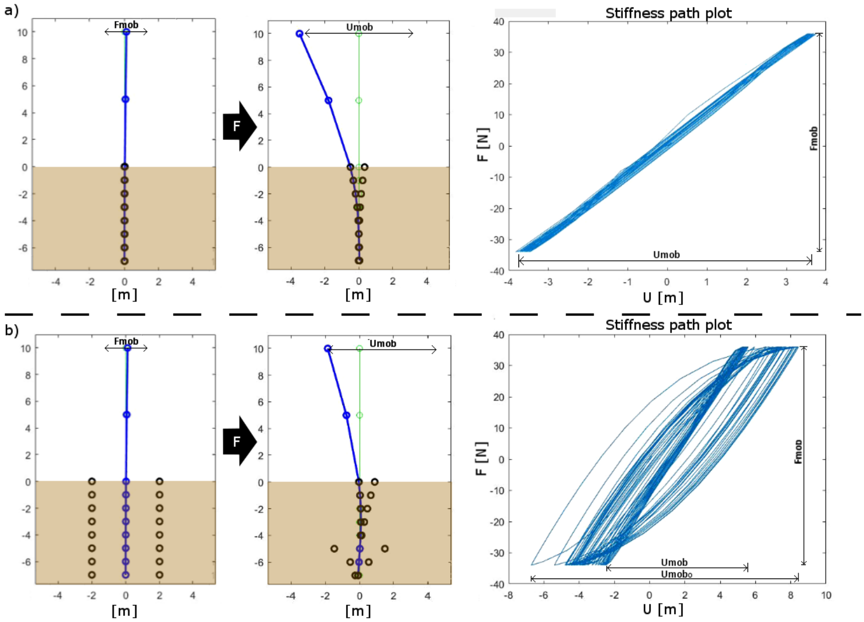

Fig. 3.35: Same force amplitude (Fmob) applied starting with different disturbed soil profiles. Both cases converge to near identical deformation amplitude Umob, however, some disturbed soil profile layers remains with lowered stiffness. Also worth noticing is how upper soil layers can get overloaded (disturbed) more than deeper ones.

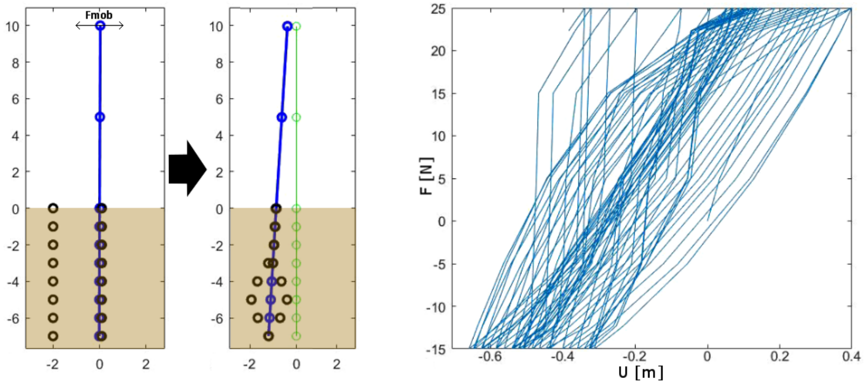

Fig. 3.36: Asymmetrically disturbed soil state (deformation envelopes pushed to the left). The beam "walks" to the left, shifting it's center of mass towards the disturbed envelopes. The applied Fmob was too small (or the beam was too stiff) to disturb upper layers of soil, thus the disturbed soil profile stabilized towards a case different from those observed in cases portrayed in Fig.3.35).

it. Simulation a) in Fig.3.35 is started with a stable soil profile (deformation envelopes very close to the beam). Within the first loading cycles a stable state soil profile is formed - a V shaped profile, where top layers are disturbed, while deep layers remain unchained. While yielding, the top layers lose some stiffness while being fully drained. This behavior could explain phenomenon observed in full scale foundations, where the foundations lose stiffness temporarily after exposure to large loads ([27]). Also, this means top layers could create thin regions of soft soil - where small deformations generate large strains, near the structure.

Simulation b) in Fig.3.35 is started with a disturbed soil state: deformation envelopes are positioned at some distance from the beam. Such disturbed soil profile could be expected after fresh installation of a foundation, as the skirt deforms a thin region of soil while penetrating. Both (a and b) simulation show that upper soil layers stabilize towards a similar V shaped disturbed soil profile. However, in b) case the deeper layers of soil do not stabilize, as deformations are too small around the point of rotation. This could indicate that somewhere along the depth of foundation liquefaction sensitive soil layers could form. This could be interesting for designing of structures in seismic zones.

The third simulation is done to observe what effects asymmetrically disturbed initial soil state has. In addition to asymmetric soil profile, the stiffness of the beam is increased to check how it affects the V shaped soil profile observed previously. The level of asymmetry applied in Fig.3.36 is not likely to be common in nature. It would require the beam to be pushed horizontally (thus pushing all deformation envelopes to one side). Perhaps this could be a case encountered after an underground explosion or a shock-wave produced by an earthquake. Regardless of practical application, simulation of this scenario reveals and interesting behavior predicted by the model. The whole beam "walks" leftward. The center of mass shifts towards the middle of disturbed envelopes. In doing so, some deformation increments are generated in deeper soil layers, where symmetric soil state produced none. Thus, a different deep layers profile is shaped. Alas, a bubble of disturbed (soft and liquefaction sensitive) layers is visible. Also worth noticing is the upper layer condition - the beam is stiffer, thus upper layers are not disturbed into the previously seen V shape.

All three simulations predict a novel explanation of the phenomenon, where a foundation embedded in sand loses stiffness. Both loss and recovery occur in drained mode, without liquefaction. The three simulations could be viewed as loading cases within serviceability limit state (SLS), as the ultimate bearing capacity was not exceeded. If an F load beyond ultimate bearing capacity was applied, the simulation would crash, as the tip of the beam would reach towards infinite displacements. Therefore, to test ultimate limit states (ULS), the beam has to be pushed sideways using prescribed displacement $Ubdof$. In the next simulation, a beam with slightly disturbed initial state is loaded with asymmetric F cycles, before a prescribed displacement $Ubdof$ is applied to check ultimate bearing capacity limit and disturb the stable profile. This is a loading sequence similar to what could be expected in real life scenarios - asymmetric small waves stabilize the soil profile, before a large breaking wave hits it. Similar testing steps are used in existing laboratory tests [24] [14] [25]. Results of the simulation are shown in Fig.3.37. Note, the simulation can be continued indefinitely - infinite loading steps can be applied, while switching between force and displacement applied at the tip of the beam. The method is computation efficient, and parallel processing friendly (springs can be solved in parallel).

At this point the end of the flowchart in Fig.3.1 is reached. The tests had stopped prematurely, before the behaviors predicted by models could be tested experimentally. The geotechnical laboratory was closed to be moved to a new location. Therefore, the testing equipment had to be disassembled for transportation. Thus, further research was postponed to future work.

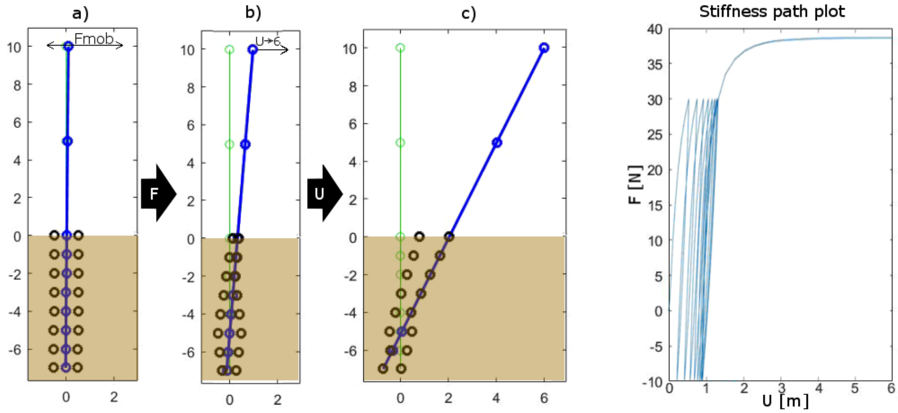

Fig. 3.37: Different loading modes are used in lone loading history. Firs, Fext history is applied. Then, Ubdof history is applied. The simulation was done using only 2 stiffness matrices, each inverted only once, ahead of running the simulation. Convergence rates were on average around 14 iterations per load step, with a few problematic steps (near the peaks of a loading cycle) which required up to 1000 iterations. It is too early to objectively evaluate the robustness and efficiency of the p-y curves, but the principle appears to be stable and therefore functional.

Chapter 4

Conclusion

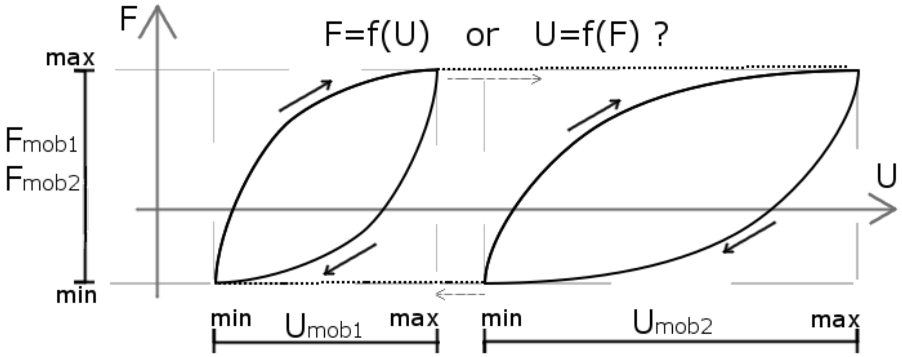

Fig. 4.1: A thought experiment illustrating the conclusion.

The main conclusion is: sand has some exclusively deformation dependent properties, compatible with a deformation (strain) envelope (see Fig. 4.1).

The conclusion does not falsify the utility of stress-space solutions for standard geotechnical problems. However, existing convention does not predict some anomalies and paradoxes observed experimentally - such as lower sand stiffness at higher density. When facing anomalies, paradoxes and unsolved problems, the conventional models need to evolve. Either some missing variables are added on top of existing solutions, or an alternative path of interpreting test results is provided. In this thesis both, a new model and new variables were introduced, in attempt to explain anomalies and paradoxes observed experimentally.

What can be controlled by deformation in testing practice, could be modeled as a function of deformation in theory. Theory must evolve to become more descriptive, predictive and prescriptive of real life phenomenon. Theory evolves through research - generating new facts and reaching new conclusions:

1. New testing scope of frictionless triaxial apparatus was discovered and used in practice:
    - Observing post-liquefaction undrained strength, post-liquefaction disturbed soil states.
    - Multi stage testing (combining drained and undrained stages).
    - Recovery of initial stiffness path (demonstrating predictive and prescriptive power of a strain envelope).
    - Stable state stiffness paths can be controlled - resized and repositioned (quantifying disturbed soil states, parameterizing BSM).
2. New testing scope of small scale foundation testing was noticed and used in practice:
    - Stable state stiffness paths resized and repositioned (demonstrating predictive and prescriptive power of deformation envelopes).
    - A method fo isolate individual components within nonlinear, state dependent equation of motion (isolating K, C and M components).
    - Initial stiffness of a foundation can be recovered (control - proof of BSM prescriptive power).
    - Mechanisms governing loss and recovery of dilative strength demonstrated (the boot effect disturbed and re-stabilized)
3. Original modeling methods proposed:
    - Strain envelope to model triaxial tested sand specimens (BSM):
        - Compatible with both drained and undrained loading cycles.
        - One calibration remains compatible with different sands.
        - Self calibrating when deformation of constant amplitude is encountered
    - Deformation envelope (BSM) in p-y curves
        - Patterns combining loss and recovery of stiffness simulated.
        - Evolution of disturbed soil layers simulated.
        - Formation of stable disturbed soil profiles simulated.

The new facts and conclusions, while numerous, are by no means final. Without doubt the answers are simplistic, alas - functional, as demonstrated experimentally. The BSM model is not complex, but it is counter intuitive.

This is a case where pre-existing options and confirmation bias are the main obstacle. Currently, geotechnical paradigm uses effective stress envelopes, thus research is designed to look for effective stress properties. Alas, some features of sand behave in proportion exclusively to deformation history.

It is important to ask "how" the specimen behaves, rather than "what" the existing models require. Equipment (old and new) must be used to execute tests with unknown outcomes - to observe new facts, reach new conclusions. To expose anomalies and paradoxes. It takes courage to propose something different, for novelty is the thing which contradicts what is known, trusted and comfortable. Nevertheless, a guess is not false until falsified experimentally. Truth is observable and non-falsifiable [4].

1 Future work and limitations

Current application of the new findings is limited to controlled laboratory environment. Phenomenon are researched, their very existence is discovered. To move closer to practical engineering solutions - further more research is necessary. Various geotechnical engineering problems need to be attempted to model and test using deformation envelopes. Similar deformation envelopes as used in BSM, as they provide great descriptive and predictive power within a controlled environment. They novelty has the potential to solve modern geotechnical engineering problems: predicting behavior of disturbed soil states left after/during an earthquake, impact loads. Scaling laws for scaling from small scale to large scale structures. Dynamic simulations for irregular loaded offshore foundations. Predictive power of models allows to model how structures behave exposed to natural elements. Prescriptive power allows to manipulate soil properties - cyclic disturbed soil properties could be used to improve efficiency in construction processes, such as cyclic compaction injected grouting [46].

There is a difference between research and engineering practice. For engineering - models are calibrated. For research - models are questioned. In tests done for research purposes, it is crucial to generated observations which show something new (inductive power), or contradict something known (deductive power). Therefore, testing limits of the equipment must be improved to reach for a new scopes of testing. Specimen durability must be improved and used to extrapolate into more aggressive, more challenging testing sequences. Precision of the equipment must be improved as well. Equipment must reach for new observations, paradoxes and anomalies, which then can be used to improve effectiveness of theory.

Limitations of practical testing scope are inherited by consequent theoretical models. Tests shown in this thesis apply deformation along 1 axis (both triaxial testing and foundation prototype). The 1D limitation is part of all observations. Thus, deriving conclusions towards sand behavior in 2D or 3D stress or strain fields should be done with caution (see E.10). Existing 3D and 2D models can be simplified down to 1 axis problem, and then deductively questioned by comparing with novel test results. But if 2D and 3D models are made from interpretation of 1D data, the resulting concept is nothing more than a "refined guess". Nevertheless, it is important to create competing models - as they raise new questions which inspire further new testing procedures. Without making a theoretical guess (inductive reasoning), an experiment has nothing to contradict (deductive test). Without testing for new patterns, anomalies, paradoxes (inductive testing), theory theory cannot be trimmed (deductive reasoning).

closing remark

To continue research presented, small scale foundations can be tested along 6 degrees of freedom using a Stewart platform to apply the loads. To test 3D sand models in principle strain (or stress) space the true triaxial apparatus can be used. At the moment, it is not certain what shape the 3D strain envelope has, or how deformation properties vary in 2D and 3D space. Nevertheless, the principle of Bezier stiffness is unconditionally stable as long as a finite stress limit is given. Luckily, an effective stress vector projected on the π plane (a plane perpendicular to hydrostatic axis) is always pointing towards a finite stress limit (the edge of a stress envelope, crossed by the π plane): "we can always map from deflection to load but not always from load to deflection" - D.M.Wood.

References

[1] Trial installation: Uk north sea. [Online]. Available: http://universal-foundation.com/case-studies/trial-installation-campaign/

[2] K. H. Andersen and T. Berre, “Behaviour of a dense sand under monotonic and cyclic loading comportement d’un sable dense sous chargement monotonique et cyclique,” in *Geotechnical Engineering for Transportation Infrastructure: Theory and Practice, Planning and Design, Construction and Maintenance: Proceedings of the Twelfth European Conference on Soil Mechanics and Geotechnical Engineering, Amsterdam, Netherlands, 7-10 June 1999*, vol. 2. CRC Press, 1999, p. 667.

[3] D. N. V. AS, “Design of offshore wind turbine structures,” Internet Requests for Comments, DET NORSKE VERITAS AS, OFFSHORE STANDARD DNV-OS-j101, May 2014. [Online]. Available: ttp://www.dnv.com

[4] A. Bird, "Thomas kuhn," in *The Stanford Encyclopedia of Philosophy*, fall 2013 ed., E. N. Zalta, Ed., 2013.

[5] A. W. Bishop and G. E. Green, "The influence of end restraint on the compression strength of a cohesionless soil," *Geotechnique*, vol. 15, no. 3, pp. 243–266, 1965.

[6] M. Budhu, "Soil mechanics and foundations, (with cd)," 2008.

[7] C. R. I. CLAYTON, M. STEINHAGEN, H. M. STEINHAGEN, W. POWRIE, K. TERZAGHI, and A. W. SKEMPTON, "Terzaghi's theory of consolidation, and the discovery of effective stress. (compiled from the work of k. terzaghi and a.w. skempton)." *Proceedings of the Institution of Civil Engineers - Geotechnical Engineering*, vol. 113, no. 4, pp. 191–205, 1995. [Online]. Available: http://www.icevirtuallibrary.com/doi/abs/10.1680/igeng.1995.28015

[8] C. A. Coulomb, *Essai sur une application des règles de maximis & minimis à quelques problèmes de statique, relatifs à l'architecture*. De l'Imprimerie Royale, 1776.

[9] M. Damgaard, L. Andersen, L. Ibsen, H. Toft, and J. Sørensen, "A probabilistic analysis of the dynamic response of monopile foundations: Soil variability and its consequences," *Probabilistic Engineering Mechanics*, vol. 41, p. 46–59, 2015.

[10] C. G. Di Prisco and D. M. Wood, *Mechanical Behaviour of Soils Under Environmentallly-Induced Cyclic Loads*. Springer Science & Business Media, 2012, vol. 534.

[11] R. Dobry and T. Abdoun, "Cyclic shear strain needed for liquefaction triggering and assessment of overburden pressure factor k σ," *Journal of Geotechnical and Geoenvironmental Engineering*, p. 04015047, 2015.

[12] ——, "An investigation into why liquefaction charts work: A necessary step toward integrating the states of art and practice," in *Proc., 5th Int. Conf. on Earthquake Geotechnical Engineering*. Chilean Geotechnical Society Santiago, Chile, 2011, pp. 13–44.

[13] A. M. Farahat, M. Kawakami, and M. Ohtsu, "Strain-space plasticity model for the compressive hardening-softening behaviour of concrete," *Construction and Building Materials*, vol. 9, no. 1, pp. 45 – 59, 1995. [Online]. Available: http://www.sciencedirect.com/science/article/pii/095006189592860J

[14] A. Foglia, "Bucket foundations under lateral cyclic loading: Submitted for the degree of doctor of philosophy," Ph.D. dissertation, Denmark, 2015.

[15] Z. Gao and J. Zhao, "Strain localization and fabric evolution in sand," *International Journal of Solids and Structures*, vol. 50, no. 22, pp. 3634–3648, 2013.

[16] G. W. E. C. (GWEC). (2017) Market forecast for 2017-2021. [Online]. Available: http://www.gwec.net/global-figures/market-forecast-2012-2016/

[17] S. Iai, Y. Matsunaga, and T. Kameoka, "Strain space plasticity model for cyclic mobility," *Soils and Foundations*, vol. 32, no. 2, pp. 1–15, 1992.

[18] L. B. Ibsen, "The stable state in cyclic triaxial testing on sand," *Soil Dynamics and Earthquake Engineering*, no. 13, pp. 63–72, 1994.

[19] L. Ibsen, *The Static and Dynamic Strength of Sand*. Geotechnical Engineering Group, 1995, pDF for print: 11 pp. Published in: Proceedings of the Eleventh European Conference on Soil Mechanics and Foundation Engineering, Copenhagen, 1995 : XI ECSMFE : DGF-bulletin 11, Vol. 6, pp. 69-76.

[20] W. Kirkpatrick, "Influence of end restraint on strain distributions in the triaxial compression test," in *Proc. Geotechnical Conf. Oslo*, vol. 2, 1967.

[21] B. S. Knudsen, M. U. Østergaard, and L. B. Ibsen, "Small-scale testing of bucket foundations in sand," Department of Civil Engineering, Aalborg University, Tech. Rep., 2013.

[22] M. Mohkam, "Contribution à l'étude expérimentale et théorique du comportement des sables sous chargements cycliques," Ph.D. dissertation, 1983.

[23] J. Moust, *A new triaxial apparatus*. Copenhagen, Geoteknisk Institut, 1970, vol. 27.

[24] G. Nicolai and L. Ibsen, *Response of monopiles under cyclic lateral loading in sand*. EWEA, 2015.

[25] S. D. Nielsen, "Transient monotonic and cyclic load effects on mono bucket foundations," Ph.D. dissertation, Aalborg Universitetsforlag, 2016.

[26] S. K. Nielsen, A. Shajarati, K. W. Sørensen, and L. B. Ibsen, "Behaviour of dense frederikshavn sand during cyclic loading," Department of Civil Engineering, Aalborg University, Tech. Rep., 2012.

[27] S. Nielsen, L. Ibsen, and S. Gres, "Cost-effective mass production of mono bucket foundations," 2015, pO: 242.

[28] S. Nielsen and L. Ibsen, "The offshore bucket trail installation," 2015.

[29] S. Nielsen, L. Ibsen, and B. Nielsen, *Dynamic behaviour of mono bucket foundations subjected to combined transient loading*. C R C Press LLC, 2015, vol. 1, pp. 313–318, 978-1-138-02848-7 (set of two volumes hardback + CD-Rom) 978-1-138-02850-0 (Volume1+ CD-Rom) 978-1-138-02852-4 (Volume 2) 978-1-315-67551-0 (ebook PDF).

[30] R. E. Olson and J. Lai, "Apparatus details for triaxial testing," Chaoyang University of Technology, Tech. Rep., 2004.

[31] P. Pankaj and F. E. Donaldson, "Algorithms for a strain-based plasticity criterion for bone," *International journal for numerical methods in biomedical engineering*, vol. 29, no. 1, pp. 40–61, 2013.

[32] U. Praastrup, K. Jakobsen, and L. B. Ibsen, "On the choise of strain measures in geomechanics," Geotechnical Engineering Group, Tech. Rep., 1998.

[33] P. Rowe and L. Barden, "Importance of free ends in triaxial testing," *Journal of the Soil Mechanics and Foundations Division*, vol. 90, no. 1, pp. 1–28, 1964.

[34] T. Sabaliauskas, A. T. Diaz, L. B. Ibsen, and S. D. Nielsen, "Observations during static and cyclic undrained loading of dense aalborg university sand no. 1," Aalborg University, DCE Technical Memorandum, Tech. Rep., 2014.

[35] T. Sabaliauskas and L. Ibsen, *Cyclic Triaxial Loading of Cohesionless Silty Sand*. International Society of Offshore and Polar Engineers, 2015, pp. 821–826.

[36] T. Sabaliauskas, L. B. Ibsen *et al.*, "Triaxial testing beyond yielding," in *The 27th International Ocean and Polar Engineering Conference*. International Society of Offshore and Polar Engineers, 2017.

[37] A. N. Schofield, *Disturbed soil properties and geotechnical design*. Thomas Telford, 2005.

[38] D. Sheng, B. Westerberg, H. Mattsson, and K. Axelsson, "Effects of end restraint and strain rate in triaxial tests," *Computers and Geotechnics*, vol. 21, no. 3, pp. 163–182, 1997.

[39] W. Shockley and R. Ahlvin, "Nonuniform conditions in triaxial test specimens," in *Research Conference on Shear Strength of Cohesive Soils, ASCE, Boulder, Colo*, 1960, pp. 341–357.

[40] I. Stroescu and P. Frigaard, *Scour properties of mono bucket foundation*. C R C Press LLC, 2016, pp. 335–341.

[41] S. Tomas and I. Lars, Bo, "The new scope of frictionless triaxial apparatus – disturbed sand testing," *Geotechnical testing journal*, vol. 42, no. 1, 2019.

[42] I. I. Vardoulakis, "Bifurcation analysis of the triaxial test on sand samples," *Acta Mechanica*, vol. 32, no. 1-3, pp. 35–54, 1979.

[43] D. M. Wood, *Geotechnical modelling*. CRC Press, 2003, vol. 1.

[44] P. J. Yoder, "A strain-space plasticity theory and numerical implementation," no. EERL 80-07, August 1980, a Report on Research Concluded Under Grants from National Science Foundation. [Online]. Available: http://authors.library.caltech.edu/26358/1/8007.pdf

[45] J.-H. S. Yun Wook Choo, Tae-Woo Kang, "Centrifuge study on undrained and drained behaviors of a laterally loaded bucket foundation in a silty sand," in *Proceedings of the Twenty-fifth (2015) International Ocean and Polar Engineering Conference*. International Society of Offshore and Polar Engineers (ISOPE), 2015, pO: 963.

[46] K. Zen, M. Hirasawa, T. Shinsaka, and M. Adachi, "Countermeasure for liquefiable ground beneath the existing structure by cpg," in *Proceedings of the Twenty-fifth (2015) International Ocean and Polar Engineering Conference*. International Society of Offshore and Polar Engineers (ISOPE), 2015, pO: 839.

Paper A

Cyclic triaxial loading of cohesionless silty sand

Tomas Sabaliauskas, Lars Bo Ibsen

The paper has been published in the
Proceedings of ISOPE conference Vol. 25, 2015.

Abstract

Growing global demand for energy is pushing energy harvesting structures into off shore, deep water conditions. This paper originates from work done during development of the bucket foundation for wind turbines, in Aalborg University, Denmark.

Cyclic loading and high water pressure influence cohesionless soil performance. Silty sand from Frederikhaven wind turbine farm was tested using single diameter height samples with lubricated, smooth boundary piston heads in a "Danish" triaxial apparatus. Samples were successfully subjected to loading histories of high complexity suggesting feasibility of such tests for observing complicated soil response encountered in off shore foundation design.

KEY WORDS: Undrained; cyclic; liquefaction; shakedown, triaxial; Danish;

1 INTRODUCTION

Offshore a structure continuously interacts with the soil. By doing so it continuously modifies the soil state. During the life time of a structure the affected soil can potentially strengthen or weaken multiple times. Theory sufficient for monotonic loading describes only a small portion of soil properties. Standard models suitable for retaining walls or static slope stability at rest are insufficient for cyclic offshore loading. Models made for predicting earth quake response are not fully compatible with slow, continuous, repetitive wave loads either. The purpose of this paper is to show a range of undrained soil response observed while testing capabilities of an automated, single diameter height samples using, smooth boundary condition triaxial apparatus.

2 EQUIPMENT

Danish triaxial apparatus is a modified version of conventional triaxial apparatus, where the rough, sliding preventing pressure heads are replaced by smooth, lubricated ones (Ibsen, 1994).

Extra attention was given for water tightness during the tests. 2 latex membranes with vacuum gel in between were used. Back pressure tubes were cut to a minimum length for maintaining pore water volume closer to void volume. Stiff nylon tubes for back pressure maintain more water stiffness, extreme sample saturation levels were reached while CO2 flushing. (Troya & Sabaliauskas, 2014)

Single diameter height specimens with lubricated smooth boundary conditions provide uniform stress and strain distribution. Samples do not form a localized shear band in compressive loading. (Ibsen, 1994) (Hettler & Vardoulakis, 1984). This is of key importance for superior sample durability and performance when compared to conventional 2 diameter height triaxial tests.

Resulting stress field can be represented by a single linear gauss point for Finite Element Method (FEM). Thus the testing setup is considered advantageous for use in FEM model fitting. (Ibsen, 1994) In this article both strains and stresses are taken positive in compression using the geotechnical sign convention. The measurements show natural stress and natural strain.

3 TESTING PROCEDURE

All tests were initiated from anisotropic K0 state which is applied drained, mimicking “in situ” soil state. 80% (dry tamping) initial density is used. (Troya & Sabaliauskas, 2014), (Nielsen & Ibsen, 2013).

After the initial anisotropic K0 condition is applied, sample valves are closed and parts A, B and C are all in undrained condition (Fig. A.1)

- Part A consists of cyclic loading applied using force control. This is where strain accumulation is measured due to applied stress loading history.
- Part B is testing for ultimate bearing capacity – displacement is applied until plasticity limit is reached. This is used to investigate the effect of previous stress history on the bearing capacity as stress is allowed to adopt to applied strain.
- Part C is continued testing after the main procedure (A & B). This part is where highly disturbed samples properties are observed. The purpose of this stage is to push the limits of testing equipment and sample durability. At the same time collecting data on further loading history of ever more disturbed sample response.

Part A loading cycles are continued until one of 3 events occurs:

1. A number of 1000 cycles pass (number of cycles during 3 hour storm peak).
2. axial strain ϵ_a reaches beyond 10% (user defined deformation limit, considered as “excessive” strain)
3. The sample loses geometry judging by external observation (shear band forming, bulging, etc. . .) (Fig. A.11).

If the sample did not lose geometry during cyclic loading in phase A then it is compressed by controlling piston displacement in Part B. Compressing is continued until both pure plasticity is induced and 10axial strain is passed. The deformation is usually kept constant at the strain peak to observe stress

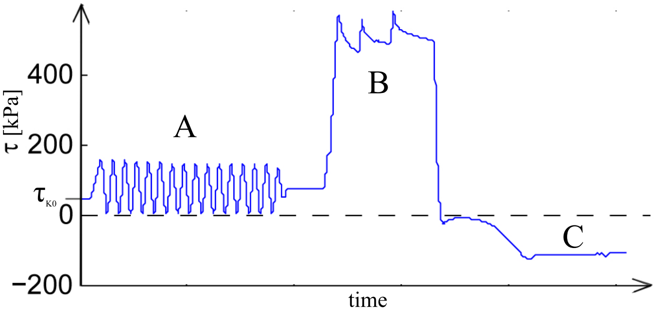

Fig. A.1: Schematic of a loading history.

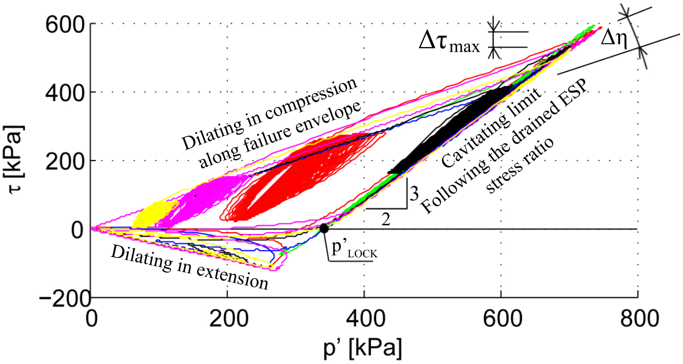

Fig. A.2: Plot of 6 stabilizing loading cyclic tests. A fully defined stress space triangle is visible from raw data.

relaxation. Due to sample geometry no shear band is formed in compression (Hettler & Vardoulakis, 1984). The peak can be tested multiple times, (allowing stress relaxation in between) for consistency. At this point the Main Procedure is finished. At the beginning of stage C all samples are already highly disturbed. It was decided that if a sample has no failure surface and no significant geometrical distortion then it should be tested further. Initially there was no loading plan from this point onward. The first choice was to try and pull a sample to failure.

In Fig. A.1 Schematic of a loading history. Part C goes toward failure in extension, the bottom plate of triaxial apparatus is being pulled down, elongating the sample vertically. It was found that the sample can “remember” the compression deformation previously imposed and sample can be “pulled” back to initial length without signs of physical failure. During the pull sample would exhibit 2 stress peaks, a small instability peak soon after crossing the zero stress line where rapid liquefaction results in pore pressure rebound (Fig. A.3, Fig. A.6), and the second peak at the ultimate bear-

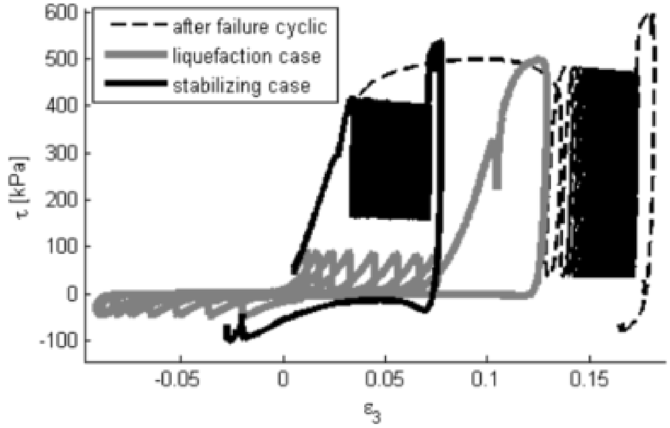

Fig. A.3: Cyclic loading increases undrained bearing capacity in stabilized samples. "After failure cyclic" is plotted as an example virgin load path.

ing capacity, developing with dilation. Majority of samples were found to be testable for ultimate compression and extension numerous times before bulging or failure surface developed. The danger of a shear band formation was present only in extension. The point of failure in extension was found easily predictable (Eq.3)(Fig. A.2)(Ibsen, 1995, Nielsen & Ibsen, 2013).

Before reaching ultimate strength samples always dilate along some stress angle. In monotonic tests the angle is often approximated as a constant, yet in cyclic loading it moves. It repositions closer to the ultimate friction angle with each cycle. To extreme proximity from the failure envelope.

At some point dilation causes sufficient vacuum in pore water to boil the water at room temperature, turning it into steam. This is called cavitation. Due to cavitation water loses its stiffness at -85[kPa] negative pressure (vacuum) (Fig. A.7). The observed plastic response at cavitation is not necessarily a critical state, sample is known to continue dilating up to much greater strains, failure at this point is barely a transition into drained response due to water fluid converting into steam. Ultimate undrained strength is reached due to crossing drained ultimate friction angle, when water turns to gas. (Ibsen, 1995)

4 EFFECTIVE STRESS BOUNDARIES

The boundaries of undrained bearing capacity were found predictable and constrained within a linear triangle in principal stress space. All tests at all times were found to stay inside the triangle visible in Fig. A.2. The dilation path can move so close to failure envelope that raw test data can

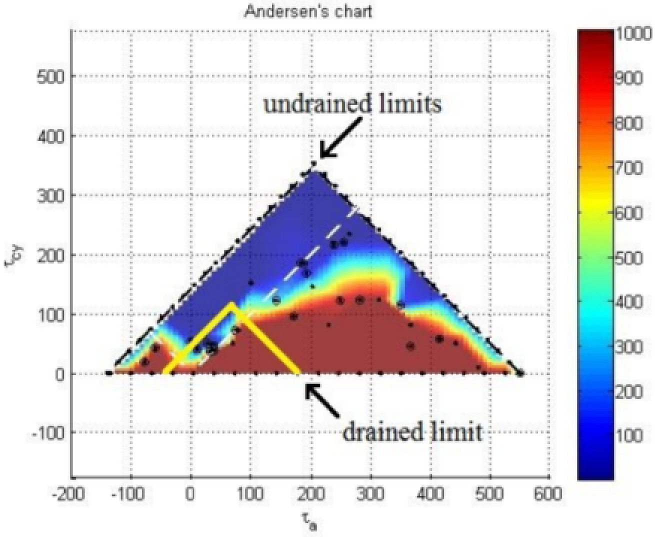

Fig. A.4: Non-normalized Andersen's chart, showing number of cycles until failure (10% strain failure criterion). It can be normalized with undrained τ_{max}

be used to illustrate failure envelope location. The ultimate friction angle is observed to be linear from confining stresses as low as $3[kPa]$ up to near $800[kPa]$. The slight curvature in virgin loading path is found to occur due to increasing dilation rate, caused by exponential growth of dilation rate, especially noticeable in liquefying case Fig. A.7. The angle difference $\Delta\phi$ between virgin dilation path and after cyclic loading is marked in Fig. A.2.

If sample fails after following the virgin dilation stress path then it does so after climbing the cavitation line (climb indicated by $\Delta\tau$ max (Fig. A.2)). Thus the measured friction angle changes slightly due to loading history. Cyclic loading can increase the peak friction angle, slightly. This is perhaps most well described by fabric tensor. (Dafalias, 1985) The cavitation line (Eq.1) is found on p' axis in point p'_{LOCK}. If initial pore pressure $Pp0 = 200[kPa]$, Initial confining stress $p'_0 = 60[kPa]$ and cavitation pressure $P_{cav} = -85[kPa]$ then $p'_{Lock} = 345[kPa]$,

$$p'_{LOCK} = Pp_o + p'_o - P_{cav} \tag{A.1}$$

$$\tau_{max} = -p'_{LOCK} \cdot \frac{sin(\phi)}{sin(\phi) - 1} \tag{A.2}$$

$$\tau_{min} = -p'_{LOCK} \cdot \frac{sin(\phi)}{sin(\phi) + 1} \tag{A.3}$$

If a failure envelope was to be made for undrained response it must con-

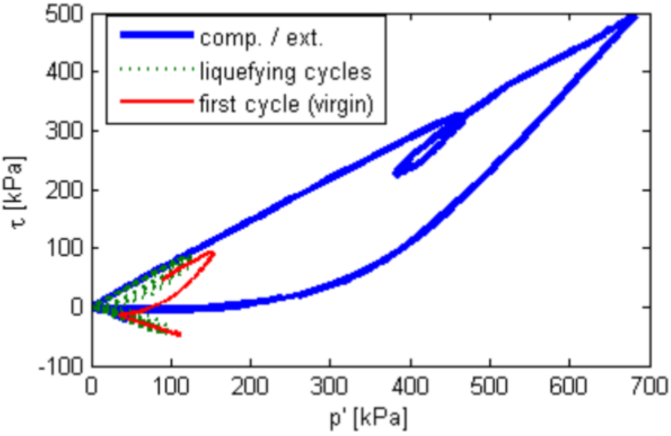

Fig. A.5: Principal stress space, liquefaction loading.

tain the full triangle - Mohr Coulomb envelope, and cavitation limit. In this example the drained strength is near 5 times lower than undrained (Eq 2 & 3) (Fig. A.4). For dense sand in deep water conditions dilation combined with available pore pressure can add significant extra strength.

Approximating the radial strain was impossible with equipment used due to inability to measure undrained volume change during cavitation. Thus plotting is done using axial strain ϵ_a rather than a more commonly used combination of shear strain and stress, γ and τ.

5 ANDERSEN'S CHART

Andersen's chart (Andersen & Berre, 1999) was proposed as a way to visualize soil response. The average sinusoidal load τ_a is on the x axis, the shear cyclic amplitude τ_{cy} is on the y axis, and the number of cycles until "failure" (10% axial strain) is on the z axis. The chart is plotted looking from the top, and the z data is thus displayed color coded. The plot shows how many cycles of a stress amplitude combination will be necessary to induce 10% axial strain.

Due to resulting function surface being very steep, the final result is very good for categorization purpose, separating above and below 1000 cycle resistant stress combinations. Yet the extreme steepness makes it very complicated to measure the exact location of this boundary limit. (Troya & Sabaliauskas, 2014) Some observations from resultant Andersen's chart:

1. soil can liquefy below drained envelope

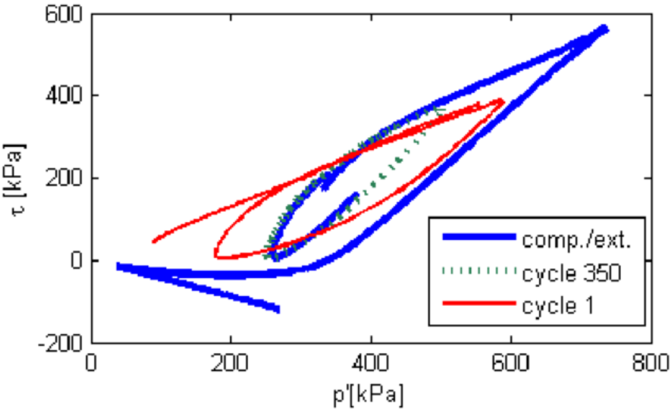

Fig. A.6: Principal stress space, stabilizing, compression cyclic loading case.

2. undrained dense sand can resist loads much greater than drained. Soil is resistant to small amplitude cycles at larger stress states.

Increasing density provides liquefaction resistance. Even though liquefaction can occur at low stress amplitudes draining liquefied soil leads to increase in density. Drained small strain amplitude loading also increases soil density (Richard G. Wan, 2001). For off shore structures the continious exposure to low stress amplitudes will lead to increasing density of soil within active soil mechanisms around the structure. Unlike earthquake caused liquefaction which occurs in rare bursts spreading out over large areas - wind turbine foundations under continious loading can strengthen the soil. And when an a breaking wave does occur - undrained peak strength might use the pore pressure.

6 “EFFICIENCY” OF GRANULAR MATRIX

Undrained cyclic tests clearly show that soil density and confining pressure is insufficient number of parameters to describe the observer cyclic response. Using the term “efficiency” comes from the bold observation that a soil can become more efficient and less efficient at resisting a load.

Variety of rules had been proposed to quantify “efficiency”. The one proposed by Yannis F. Dafalias explains the phenomena through the plastic spin theory and fabric tensor. (Dafalias, 2011, Dafalias, 1985). His findings are supported by extensive Discrete Element Simulations (DEM), observing frozen samples under a microscope and successful simulations of sample preparation influence and loading direction dependence. He came forth with a method to quantify particles rearrangement during loading history, and as “Fabric” changes soil response changes with it. He observed that cohesionless soil can move away from the critical state line on reversal of loading direction. Soil approaches critical state only in very large, continuous, monotonic strains. If the loading direction is changed – soil moves towards higher density and in undrained case this results in liquefaction. After a sufficiently large strain amplitude is induced in reverse dilation will starts once again pushing the soil towards a critical state once again. Some speculate the change in response might be caused by particle crushing. Samples described here were sieve tested after multiple extensive tests, some tests lasting over 12 hours with multiple ultimate bearing capacity tests at densities ranging from high to low. No significant levels of crushing was observed. Density and confining pressure are simply insufficient number of parameters to predict cyclic soil performance. A way to quantify changing soil “efficiency” needs to be added, Fabric tensor and plastic spin theory seem very promising in that regard, even if it means “Challenging the paradigm of critical state soil mechanics” (Y.F.Dafalias, 2012).

7 STABILIZING AND LIQUEFACTION

The type of cyclic loading encountered in wind turbines is rather new. Former exposure to soil liquefaction during earthquakes has somewhat stigmatized cyclic loading as being limited to liquefying and reducing soil strength. But cyclic undrained response can lead to increasing soil stiffness and extra bearing capacity too (Fig. A.4). Stabilizing occurs when deviator stress remains on either positive or negative stress during all cycle length. This is found to increase the friction angle and soil stiffness (Fig. A.3) The loading history in principal stress space indicates that the first cycle is more dilative and contractive than later cycles (Fig. A.6). Dilation path is further from the failure envelope during first cycle and unloading trajectory is not following ESP either. As cycles are applied, but zero stress is not crossed, a sample gradually loses its dilative and contractive properties approaching an equilibrium of dilation and contraction, known as the shakedown state (Richard G. Wan, 2001).

As dilation and contraction stabilize stresses come close to ESP which would be followed in a drained test. The stable state is reached at a position where dilation occurs close to the failure envelope. The stress loop is almost touching the failure envelope (Fig. A.6 cycle 350).

The observed stabilization sequence is slightly different from Stable State Line approaches described in external literature (Ibsen, 1994). Plausibly due to higher amplitude stresses cycles being used here. Liquefying occurs when zero stress line is crossed repeatedly during loading. It can take only one large amplitude zero crossing to fully liquefy a sample, depending on its pre-

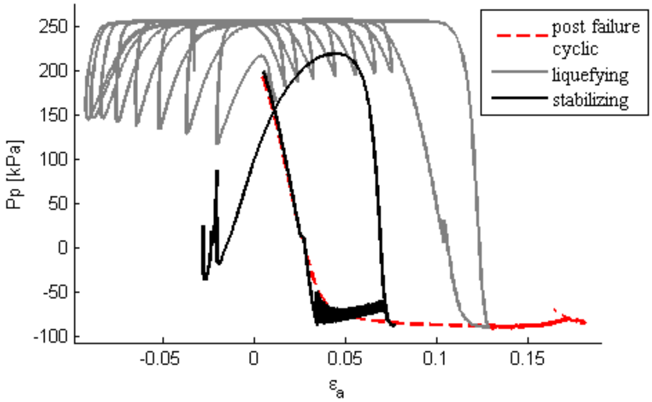

Fig. A.7: Strain and pore pressure plot for stabilizing, liquefying and highly disturbed (failure in first cycle) sample. Same tests as in Fig. A.3

vious loading history. There can be partial liquefaction or full liquefaction. Partial liquefaction occurs when the zero stress line is crossed just slightly. In that case the strain increment never completely stabilizes and strain keeps accumulating forward at a steady pace without increasing the strain amplitude. This leads to incremental collapse. (Nielsen & Ibsen, 2013)

Full liquefaction leads to increasing strain amplitude with each cycle and loss of stiffness. Large gaps of zero stiffness appear within the mobilized strain range (Fig. A.3). This can lead to structural collapse due to excess deformation rather than crossing the strength limits. It was found that soil retains most of its bearing capacity after exposure to liquefying loading, the friction angle does not decrease significantly. But it takes much larger strain amplitudes to reach it. As liquefaction progresses the stress loops in principal stress space tilt sideways adopting to the failure envelope. Dilation and contraction become increasingly more pronounced and dominate the stress path loop, rotate it towards failure envelope angle. (Fig. A.5)

8 CHARACTERISTIC POINTS FOR MODELING

Material models are usually fitted and developed based on available measurements. But test procedures them selves can be adopted to target specific parts of material models, thus checking the validity and stability of used modeling concepts. Observing modeling parameters on top of the data series reveals not only which paramters remain constant or change but gives a better sense of how things are interconnected, what type of interdependance is present in real soil skeleton. Principal stress space – stress angle.

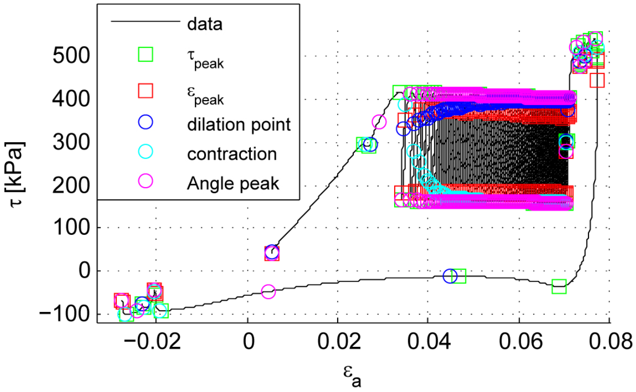

Fig. A.8: Stress angle to strain plot, stabilizing loading case.

One of the most fundamental and consistent properties of all soil is the friction angle. It has remained the heart of both clay and sand models (Schofield, 2005) and is used as inspiration for various parameters in principal stress space. $\eta = \tau/p'$ is a stress ratio, $arctan(\eta)$ gives the stress angle, and it is often used in modeling practice. For instance hardening soil model uses plastic strain attached on stress angle position. Severn Trent softens by correlating soil density with the peaks friction angle (Wood, 2004). The point where hardening transitions into softening in this case would be a stress angle peak and it has been marked in plots Fig. A.8 and Fig. A.9. In undrained liquefaction plastic strains can be seen to develop after peak angles, this is also captured in some multi yeld surface models (Ibsen, et al., 2008).

Another example of stress angle based parameter is Phase transformation line (PTL) (Ibsen, 1994). This line marks where contractive behavior transitions into dilative inside principal stress space. While it is rather fine to model it as a constant during monotonic load, during cyclic loding the line position changes with each cycle. It was decided to show two PTL cases, dilation and contraction. Exact PTL position can only be measured at points where dilative behavior is initiated during a cycle. The mechanism behind its repositioning remains hidden from observation. One can only connect the dots and test theorems on what is the correct way of transitioning from one state to another. Y.F.Dafalias had observed this and chose to model dilation by making dilation angle (ψ) as a function of distance from critical state. Observing dilation rate allowed to scale the relative distance from CSL with a linear coefficient. He introducing a concept of moving "pseudo" critical state lines and captured some of this PTL movement through fabric tensor (Dafalias, 2011). PTL during stabilization and liquefaction In Fig. A.8 and Fig. A.9 axial strain and stress angle are plotted because these two parameters are commonly used to express the volumetric response function.

In stabilizing cases, dilating PTL moves up to high angles. Liquefying PTL moves down. Sample starts dilating near peak loads in a cycle, and starts contracting near the end of unloading in a cycle. Pore pressure amplitude becomes smaller (Fig. A.7), volume of the sample becomes more stable, reaching higher stress angle with each cycle, approaching closer to the ultimate friction angle with each cycle. For liquefying sample dilative PTL moves down and contractive PTL moves up. Sample starts contracting soon after the loading peak is reversed and dilates early after crossing the zero stress, twice in each loading cycle. The sample exhibits large pore pressure amplitudes. Large strain amplitudes develop, increasing with each peak angle crossing. Compressing at this stage was found to lead to near linear dilation path in close proximity to linear ultimate friction angle. An inverse correlation of PTL position development was observed between stabilizing and liquefying case. But stress angle peaks were found to approach the ultimate friction angle in both samples. No sample had ever failed without reaching one of the peak strengths, given in Eq.2 and Eq.3. If the peak is reached in compression a shear band never formed.

Strain volumetric response (pore pressure) Undrained dense cohesionless soil samples reach their peak strength in cavitation mode, when due to volumetric expansion pore pressure drops to near $-100[kPa]$ and cavitates, providing extra confining pressure along the hydrostatic axis. Dilation occurs due to volumetric changes and volumetric strain is described as a function of strain when modeling. Single diameter height, smooth boundary condition triaxial testing allows for large strain amplitudes to be applied during high liquefaction states (Fig. A.7). It is easy to notice that pore pressure tends to rapidly go toward a value of 260[kPa] when the load is reversed, contracting faster than it had dilated. If dilation is caused by approaching the critical state, and critical state is static, then this rapid contraction is caused by going away from the critical state.

During liquefaction increasing strain amplitudes are necessary to recover from each liquefying pore pressure increase. But the soil always starts dilating when the mobilized strain limit is reached, and continue dilating until ultimate limit stress is reached. During stabilization, where loads are not reversed – the pore pressure stabilizes below cavitation pressure. Stable volumetric state in induced at a different volume than initial sample had. The volume becomes increasingly more stable and stiff, to the point where the stress path approaches a drained ESP stress path (Fig. A.6 at 350 th cycle). Yet if a large strain is to pull the sample back it will not hesitate to liquefy, but it will do so with 2 peaks in extension (Fig. A.3).

There are a couple of schools of thought on how to model this. Fabric tensor introduces the concept of keeping the critical state principle and introducing an equivalent of a moving critical state line, where the moving critical state line always moves toward the unique, static critical state line

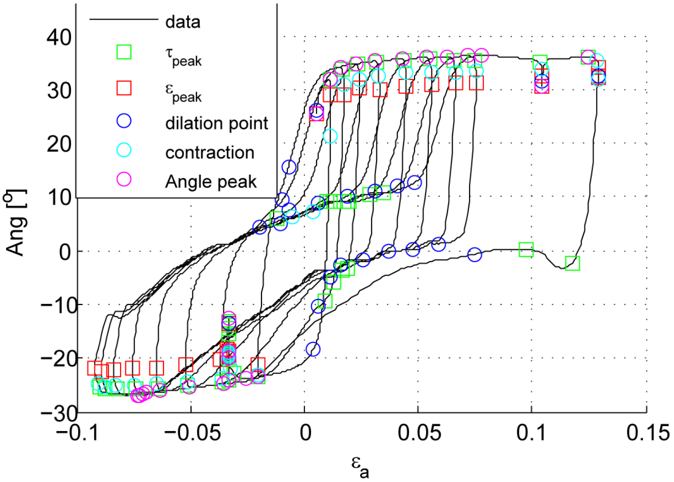

Fig. A.9: Stress angle to strain plot, liquefying loading case.

during large monotonic loading, but away from the monotonic position during reversal of strain direction. (Dafalias, 2011) Alternatively the observations had been captured empirically by using mobilized strain, considering it as a mechanical process described in strain space, where mobilized strain grows during liquefaction – thus providing the large transitioning gaps of pure plasticity. As in Prevost model. (Cerfontaine, 2013).

High levels of liquefaction make samples voulnearable to distortion of geometry. Yeat it was found manageable to reach strain amplitudes of 20% axial strain while retaining vertical walls with no excessive bulging in highly liquefied samples using the single diameter height sample geometry with smooth, lubricated boundry conditions at the end plates. (Hettler & Vardoulakis, 1984) (Ibsen, 1995)

9 EXTENDED OBSERVATIONS

The C part of loading procedure (Fig. A.1) proved very productive in generating new observations, learning to use the equipment, to “feel” and respect the sample limit states and to develop new scripts for computer controlled loading algorithms.

In the beginning it was thought that a sample will be cyclic loaded by stress amplitudes, compressed and thrown away at this point. But the sample did not show any signs if failure or any other observable forms of collapsing. It was decided to test further. Pulling the sample back to its initial length was the first step. Then it was allowed to drain in hope of restoring the initial properties, as the sample was pulled back to initial length while preserving

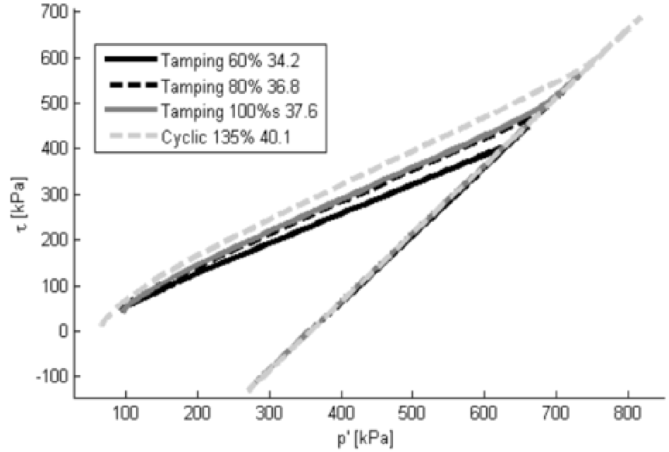

Fig. A.10: Multiple densities; 80% and 135% reached with a single sample. The % density is in relative dry tamping density, with the approximated friction angle next to it.

the initial density to a position on the drained ESP where it was locked in position displacement controlled. After draining the sample was released to 0 stress and loaded toward initial anisotropic K0 condition. Here it was observed, that the sample response had changed a lot, even though density and geometry were preserved (Fig. A.12).

The resultant samples were found a lot more contractive and of lower stiffness. After the anisotropic K0 loading was applied and undrained conditions were imposed the samples were found to "remember" the previous strain loading amplitudes. Draining did not restore any of the initial soil properties, yet many student and engineers had expected it would.

Some stress cycles were applied and sample geometry was visually inspected, then the sample was crushed again, undrained, and pulled back to initial length, undrained. At this point it was found plausible to approximate the peak friction angle at multiple densities, for both compression and extension using one sample (Fig. A.10, Fig. A.11). It can be argued that the resulting lines are merely a dilation path, but it's up to the reader to decide how far away from the ultimate friction angle the stress path is at this point. It had been shown that the PTL moves as the sample is disturbed and when done properly it moves at extreme proximity of the ultimate friction angle. (Fig. A.10) The void ratios limits of dry tamping are found to be e min =0.64 e max =1.05. Relative dry tamping density is described through Eq.4.

$$ID = \frac{e_{max} - e}{e_{max} - e_{min}} \tag{A.4}$$

When ID = 100% it means the standard dry tamping test reached this density and this was set as the "limit" density. It does not mean other methods are incapable of reaching higher densities. But the same tamping method is used to calibrate all soil tests in Aalborg University. The resulting 100% density soil was still liquefiable, even though considered very dense. Draining the sample while it is in a liquefied state would increase the soil density. Draining the sample while it was in dilating state would decrease the density. Undrained loading was found capable of controlling sample density up and down.

Testing the limits of density for this method a density of 156e=0.43 was reached. At this point the sample was purely dilative – at no point in the loading amplitude, no matter how big or small, did it develop pore pressure above the initial 200[kPa]. It was purely dilative. It is interesting to notice that reaching this density did not require high confining pressures, and small stress amplitudes were found mandatory to push the last couple of water drops during the final increments. The resulting friction angle was approximated at 42.1^o. Drained cyclic loading can plausibly lead to similar densities at small strains too. This was observed in Ottawa sand. (Richard G. Wan, 2001)

10 FUTURE WORK

In natural circumstances soil will undergo repetitive loading cycles of various intensity. This is likely to modify the soil parameters. Restoring the initial 80% dry tamping density was found impossible, yet undisturbed sea floor was measured to be around this density. The question is if soil will maintain undisturbed properties throughout a structures life time and during extreme events. There already are full scale measurements indicating changes in dynamic response after and during extreme events.

The next step will be testing drained cyclic response. Preliminary testing of drained samples shows compressing beyond 10% axial strain and pulling back to initial length for over 5 cycles, in fully drained mode is plausible using the same triaxial test setup.

11 CONCLUSION

Significant effect of loading history was observed in undrained cyclic behavior of cohesionless soil. Single diameter test height tests with smooth boundary conditions were found stable and suitable for applying complex loading histories.

Undrained cyclic response is not limited to liquefaction. Undrained ultimate bearing capacity increases in accordance with initial pore water pressure. Even in liquefied soil, at sufficient high strains. Liquefying loading case

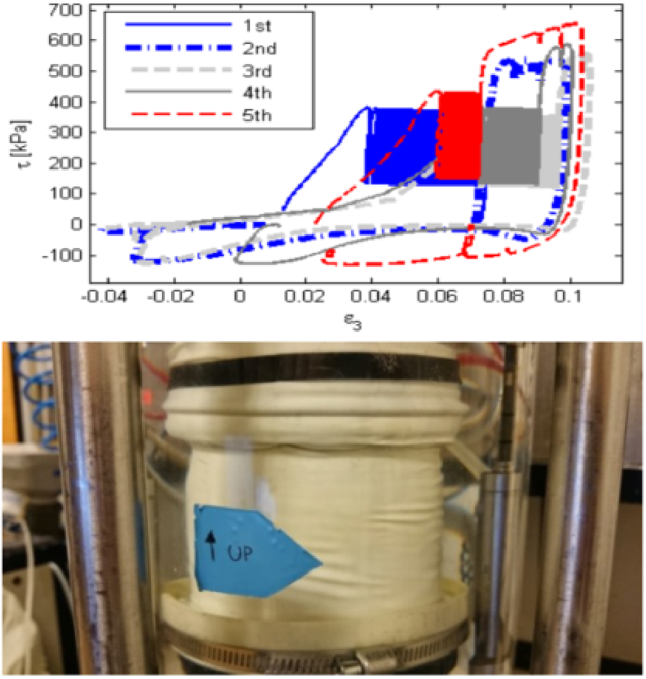

Fig. A.11: sample geometry during compression toward 5^{th} loading case. Static draining was applied after $2^{n}d$ and $3^{r}d$ loading sequence. Small strain cycles in drained mode applied after $4^{t}h$ show signs of restored stiffness. Sample relative densities during stages 1 to 5: 80%, 80%, 93%, 115%, 140%.

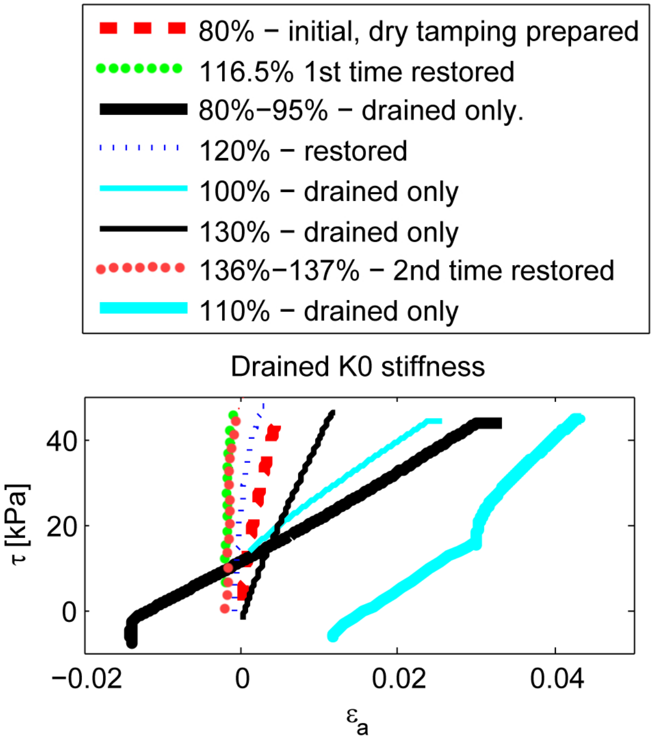

Fig. A.12: Drained stiffness, loading toward K_0 anisotropic state. At higher density soil can be both stiffer and softer, depending on loading history.

was successfully tested for axial strain amplitudes up to 20% followed by an ultimate bearing capacity compression.

Ultimate bearing capacity of samples was found plausible to test multiple times on a single sand sample. A sample can be safely pulled back to initial length after large crushing strains. Draining a sample did not restore its initial properties and left the sample with lower stiffness at higher density. Small, drained strain cycles were found to restore stiffness but increased density even further.

Single diameter height, lubricated smooth boundary triaxial setup was found capable of applying exceptionally long and complex loading scenarios.

12 BIBLIOGRAPHY

Andersen, K. & Berre, . T., 1999. Behaviour of a dense sand under monotonic and cyclic loading comportemen, Amsterdam: European Conference on Soil Mechanics and Geotechnical Engineering.

Cerfontaine, B. R. C. a. F. C., 2013. Possibilities and limitations of the Prevost model for the modelling of cohesionless. Belgium: Proceedings of the 18th International Conference on Soil Mechanics and Geotechnical Engineering.

Dafalias, Y., 2011. Finite Elastic-Plastic Deformations: Beyond the Plastic Spin. Belgrade: Theoretical and Applied Mechanics, Vol. 38, No 4, pp. 321-345.

Dafalias, Y. F., 1985. The plastic spin. s.l.:Journal of Applied Mechanics 52, no. 4 (Hettler, A. & Vardoulakis, I., 1984. Behaviour of dry sand tested in a large triaxial apparatus. s.l.:Geotechnique 34.2 (1984): 183-197..

Ibsen, L. B., 1994. The stable state in cyclic triaxial testing on sand. Aalborg: Soil Dynamics and Earthquake Engineering 13 (1994) 63-72.

Ibsen, L. B., 1995. The Static and Dynamic Strength of Sand. Copenhagen: European Conference on Soil Mechanics and Foundation Engineering.

Ibsen, L. B., Hededal, O. & LeBlanc, O., 2008. A modified critical state two-surface plasticity model for sand - theory and implementation. Aalborg: DCE Technical Memorandum No.8.

Li, Xiang-Song, Yannis F. Dafalias, and Zhi-Liang Wang, 1999. State- dependant dilatancy in critical-state constitutive modelling of sand. s.l.:Canadian Geotechnical Journal 36, no. 4 (1999).

Nielsen, S. D. & Ibsen, L. B., 2013. s.l.:International Society of Offshore and Polar Engineers.

Richard G. Wan, P. J. G., 2001. Drained Cyclic Behavior Of Sand With Fabric Dependance. s.l.:JOURNAL OF ENGINEERING MECHANICS.

Sabaliauskas, T. & Troya, A., 2014. Observations during static and cyclic undrained loading of dense Aalborg University sand no. 1. Aalborg: DCE

Technical Memorandum No. 43.

Schofield, A. N., 2005. Disturbed soil properties and geotechnical design.. s.l.:Thomas Telford.

Troya, A. & Sabaliauskas, T., 2014. Cyclic behaviour of undrained dense Aalborg University sand no. 1. Aalborg: DCE Technical Memorandum. Department of Civil Engineering, Aalborg University,.

Tsegaye, A. B., 2014. On the Mofelling of State-Dilatancy and Mechanical Behavior of Frictional Materials. Trondheim: NTNU. Wood, D. M., 2004. Geotechnical modeling, applied geotechnics volume 1. Oxford: Spon Press.

Y.F.Dafalias, 2012. The 2012 Raymond D. Mindlin Lecture on "Challenging the Paradigm of Critical State Soil Mechanics: The Role of Fabric". New York City: Columbia University.

Paper B

Triaxial testing beyond yielding

Tomas Sabaliauskas, Lars Bo Ibsen

The paper has been published in the
Proceedings of ISOPE conference Vol. 27, 2017.

Abstract

This paper is continuation of work published at ISOPE 2015, where capabilities of undrained triaxial testing were presented. Now, drained loading is emphasized, recovery of disturbed sand properties is observed. After liquefying or yielding, sand becomes disturbed: stiffness and resistance to liquefaction become compromised. However, sand can recover during drained deformation cycles. Specimens can be repeatedly disturbed and recovered using a frictionless triaxial apparatus.

1 INTRODUCTION

Offshore wind turbines are slender structures. Their dynamic response depends on stiffness of soil they stand in. Soil stiffness changes many times during lifetime of a wind turbine. Especially during storm events, as observed by Nielsen et al. (2015a) and Damgaard et al. (2015). This change in soil stiffness is attributed to disturbed soil states; soil supporting the offshore foundation loses stiffness quickly, but recover gradually. In attempt to observe the full cycle, combining loss and recovery of drained sand stiffness, current methodology of testing has to be improved. It is no longer enough to observe ultimate strength of a specimen; the specimen has to be disturbed and re-stabilized multiple times in one continuous loading history.

Standard engineering practice is concerned with ultimate strength. Conventional triaxial apparatus is sufficient for this purpose. Thus, rough end plates and specimens of height to diameter ratio 2:1 are commonly used. However, conventional triaxial apparatus is not suitable for testing disturbed soil properties, for it destroys specimens prematurely. Premature failure is caused by shear rupture and bulging imposed by localized (nonlinear) strain fields. Nonlinearity can be significant enough to force part of a specimen to contracting while other parts are dilating. These effects are described by, Rowe and Barden (1964), Bishop and Green (1965), Kirkpatrick (1967). Occurrence of both dilation and contraction simultaneously is a big problem; it can compromise measurement precision: in drained mode, internal water flow gradients can sabotage measurements of water volume squeeze out or sucked into the specimen; undrained tests suffer as well, as pore pressure measurements are compromised. Further loss of precision in classical apparatus comes from highly localized deformation within the shear zone. Localized strains cannot be reliably measured. Thus, options to observe disturbed soil states beyond yielding are highly limited. Influence of shear rupture can be severe enough to require rejecting measurements done even within the yielding limits, according to Olson and Lai (2004).

Interestingly, the lesser-known "frictionless" triaxial apparatus does not exhibit the same shortcomings. Frictionless triaxial apparatus uses smooth (lubricated) end plates, and a cylindrical specimen of height to diameter ratio 1:1. Frictionless triaxial apparatus is known for improved measurement precision and can reach disturbed soil states without destroying the specimens; Its ability to crush far beyond yielding limits was observed by Vardoulakis (1979), and earlier version of similar apparatus were tested by Jacobsen (1970), and Bishop and Green (1965). It is exciting, that the improved functionality comes together with improved measurement precision. Rowe and Barden (1964) described theoretical feasibility of isotropic stress fields. Vardoulakis (1979) accomplished isotropic yielding in practice, using his "improved" triaxial apparatus. Notice, numerous frictionless triaxial apparatuses exist with unique names assigned to them. "Improved triaxial apparatus", used by Vardoulakis (1979) is one of them. Vardoulakis managed to crush specimens to extreme axial deformation, without provoking shear rupture or bulging. He compressed a specimen axially, to 50strain; there the specimen radius expanded beyond the tips of the end plates. Thus, test was stopped not due to specimen failure, but lack of area on the end plates. Specimens yielded (thus were disturbed), and then disposed of, before bulge or rupture formed. Had there been practical reasons to test disturbed soil properties (such as encountered in modern day offshore foundation design), perhaps Vardoulakis would have attempted to continue testing into deformation cycles similar to those described in this paper. Olson and Lai (2004) also confirm specimens retain cylindrical shape at higher deformation, in frictionless triaxial apparatus. As well as acknowledging improved precision of isotropic yielding. However, Olson and Lai (2004) do not mention any context where this improved durability of specimens could be useful; frictionless triaxial is referred to as a somewhat "higher precision equivalent" of conventional triaxial. Which is not representative, frictionless triaxial apparatus has superior testing scope: it can test disturbed soil states; specimens remain testable after yielding. All while sustaining improved measurement precision, provided by isotropic stress / strain fields.

Ibsen (1994) challenged contemporary triaxial testing methodology by using a frictionless triaxial apparatus to observe cyclic sand properties relevant to offshore engineering. He used "the Danish triaxial apparatus" - a frictionless triaxial apparatus, purpose built in Aalborg Unversity for applying cyclic loads on specimens. Early work of Ibsen (1994) focused on undrained stabilizing in cyclic loaded sand; but his tests stopped short of destroying the specimen as well. Once again, specimens were disturbed, and disposed of while remaining testable. Sabaliauskas and Ibsen (2015) continued investigating cyclic loading procedures relevant to offshore engineering. Undrained strength was tested after undrained cyclic loading. Undrained yielding strength was testable even after liquefying the specimens. Furthermore, a specimen crushed beyond yielding was pulled back to initial length. Undrained specimens, pulled back to initial length, recovered initial geome-

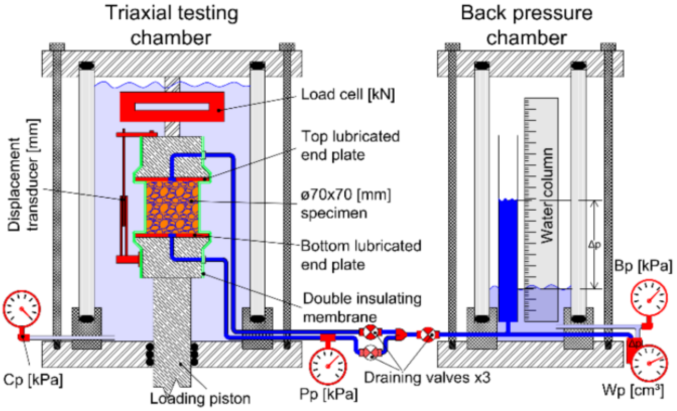

Fig. B.1: Schematic of the Danish triaxial apparatus.

try, but retained disturbed soil states. Contrary to expectation, draining did not restore either initial stiffness or resistance to liquefaction. Thus, work of Sabaliauskas and Ibsen (2015) stopped short of observing recovery of disturbed sand. Specimens pulled back to initial length, once drained, became denser, but remained softer. Lower stiffness at higher density. Nonetheless, one instance of disturbed state reversal was recorded: stiffness recovered gradually, during drained small amplitude deformation cycles. Damgaard et al. (2015) observed similar phenomenon in full-scale offshore wind turbines: foundations lose stiffness rapidly and recover gradually - during small loading cycles. Thus, resonating strongly with unorthodox testing scenarios recently implemented using the Danish triaxial apparatus.

2 EQUIPMENT AND TEST METHODS

Currently, the Danish triaxial apparatus is used exclusively at Aalborg University, geotechnical laboratory, where it became the standard testing method preferred both by local and international clients. The apparatus was initially named "the new triaxial" by Jacobsen (1970) and renamed to "the Danish" by Ibsen (1994). The machine is still being upgraded to this day. Thus, the machine has been in developed for over 40 years, and the third generation of researchers keep modernizing it further (Fig. B.1). Apparatuses similar to the Danish triaxial apparatus have been around since the 60's. These are the "frictionless" triaxial apparatuses with, flat, polished and lubricated end plates. Apparatuses of this type vary by level of automation and positioning of components, but the principle of operation is similar: a specimen, confined by water in testing chamber, is loaded by moving the bottom piston. The top piston is fixed to a load cell. While loading is applied, a computer records readings of digital sensors. Minor differences in construction, can have significant impact on testing capabilities. For instance, the Danish triaxial uses a submerged load cell and displacement transducers, in direct contact with the piston heads (see Fig. B.1). Olson and Lai (2004) describe evolution of triaxial apparatus components in detail. To switch between drained / undrained loading, three draining valves are used (illustrated as x3 valves In Fig. B.1). A digital pressure gauge is connected to bottom drainage tube. If this tube is closed, pore pressure (Pp) present at the bottom of the specimen can be measured. Microscopic volume of water is enough to pressurize the drainage tube, as the tubes are made of extra stiff nylon, thus bulk stiffness of water is preserved. Furthermore, the tubes are cut to minimum length. Thus, water pressure inside the tube becomes representative of Pp present at the bottom of the specimen in real time. Normally, during drained testing all valves are open, and excessively slow loading rate (on the safe side) is applied to avoid Pp buildup. However, in tests presented herein, the bottom drainage tube was closed during drained loading. Specimens - drained only through the top. This is counter intuitive, as using one drainage path will double the drainage time. However, monitoring Pp at the bottom of the specimen allows to observe drainage condition in real time. Back pressure (Bp) applied at the top must be similar to Pp measured at the bottom (Pp $\approx$ Bp). Thus, by observing Pp in real time, one can approximate homogeneity of effective confining pressure (p′) across the specimen height. This allows to adjust loading rates in response to real time soil behavior. Thus, despite slower drainage, faster loading rates were applicable; as loading rate was adjusted to keep Pp at ± 2 kPa from Bp .

Each test procedure began by isotropic consolidating the specimen to initial consolidation state (p′ 0 = Cp – Bp), without axial load. p′ 0 is adjusted by manipulating either Bp or Chamber pressure (Cp) using pressurized air (air pockets at the top of both chambers in Fig. B.1). Both Cp and Bp were held constant during cyclic loading, as they are controlled manually. One must take care to differentiate between p′ 0 and effective confining pressure (p′), for p′0 is point on the p′ axis (Fig. B.4), while p′ changes with respect to deviator stress (q) because p′=p′ 0 +q′/3, or, alternatively, $p' = p'0 + 2/3 * \tau$ given $q = \tau/2$ (see Fig. B.4). Here q′=F/A, where F is reaction force measured by the load cell. Note, true stress and true strain are plotted. Specimen cross-section area $A = \pi R^2$ is updated at each data-point with respect to axial strain ϵ and volumetric strain (ϵ_v). True axial strain (ϵ) is obtained from a pair of displacement transducers, $\epsilon = ln(1\breve{}\Delta H / H_0)$. Whereas ϵ_v is measured by a differential water pressure (Wp), which detects Δ_p in water column (see Fig. B.1). Note, in the real apparatus measurements are done using digital, high resolutions sensors, Fig. B.1 shows mechanical gauges for illustration purposes only. The apparatus has only one moving part - the loading pis-

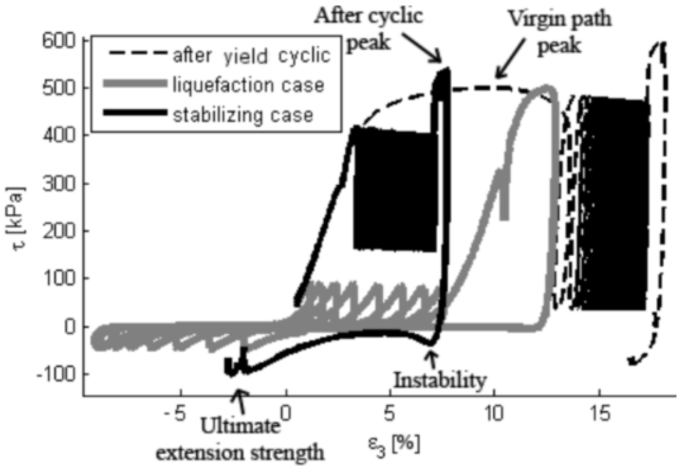

Fig. B.2: Three specimens tested by Sabaliauskas and Ibsen (2015). Undrained τ cycles applied before crushing to yield. Undrained stabilizing, liquefaction and post–yield cyclic loading. Two of the specimens were pulled back to initial length after yield. Note, undrained stabilized specimen nearly liquefied when pulled (see Fig. B.3).

ton, controlled by a high precision, proportional–integral–derivative (PID) controller.

It is worth noting once again, that many implementations of frictionless triaxial apparatuses exist under different names: “the new triaxial apparatus” by Jacobsen (1970), “the improved triaxial apparatus” by Vardoulakis (1979), “the Danish triaxial apparatus” by Ibsen (1994). They all embrace the same principle – the "free end" condition, obtained through frictionless end plates. However, each machine is likely to have its own, unique testing limits. Tests presented in this paper are representative of the Danish triaxial apparatus, in its current configuration.

3 RESULTS AND DISCUSSION

Results presented in this paper are continuation of research presented at ISOPE 2015, by Sabaliauskas and Ibsen (2015), thus a brief reminder of previous work is given before introducing the new results. Summary of testing done by Sabaliauskas and Ibsen (2015):

1. Consolidated undrained (CU) stress cycles applied on undrained specimens. The disturbed specimens were then unconsolidated undrained (UU) compressed beyond yielding, and UU pulled back to initial length (Fig’s 2 & 5).

2. A specimen was fully liquefied to a strain amplitude beyond $\epsilon = 10\%$

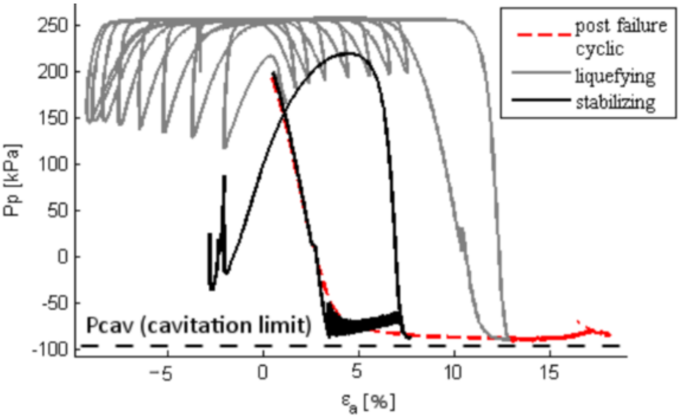

Fig. B.3: Pore pressure response (complementing Fig. B.2) by Sabaliauskas and Ibsen (2015). Undrained yielding occurs with pore pressure near absolute vacuum ($Pcav \approx -100kPa$), when water vaporizes (cavitates), thus losing stiffness. This imposes a physical limit P_0^{max} (see Fig. B.4). Liquefying specimens reach $Pp = 260kPa$, which is equal to Cp held during testing.

then UU compressed to yield (notice, liquefied specimen retained undrained yield strength, visible in Fig. B.2).

3. "Undrained stabilization" takes place during one-way τ cycles. However, upon reversal of loading (pull back to initial length), undrained stabilized specimens show no recovery of resistance to liquefaction (compare Pp Fig. B.3, and stiffness Fig. B.2).

4. Undrained disturbed specimens, pulled back to initial length, were drainable. Thus, cyclic response and yield strength were tested at multiple densities, in one loading history (Fig. B.5).

5. Draining a specimen (pulled back to initial length) was not enough to restore initial stiffness or resistance to liquefaction. Only by adding small amplitude ϵ cycles produced some recovery. This inspired the new testing direction – observation of disturbed sand properties during drained deformation cycles.

In Fig. B.2, plots of three separate specimens are shown. Each specimen was disturbed by undrained τ cycles, and crushed to yielding. These three tests illustrate mechanism governing undrained yield strength. All three specimens yield at the same pore water pressure ($Pcav \approx -100kPa$ in Fig. B.3). Pp cannot decrease below cavitation pressure, as water vaporizes at pressures near absolute zero. This phenomenon governs undrained yield strength in dilative sands (Ibsen, 1994). During undrained triaxial testing, Cp is held constant and Pp cannot drop below $-100kPa$, thus $p_0^{max} < 360kPa$

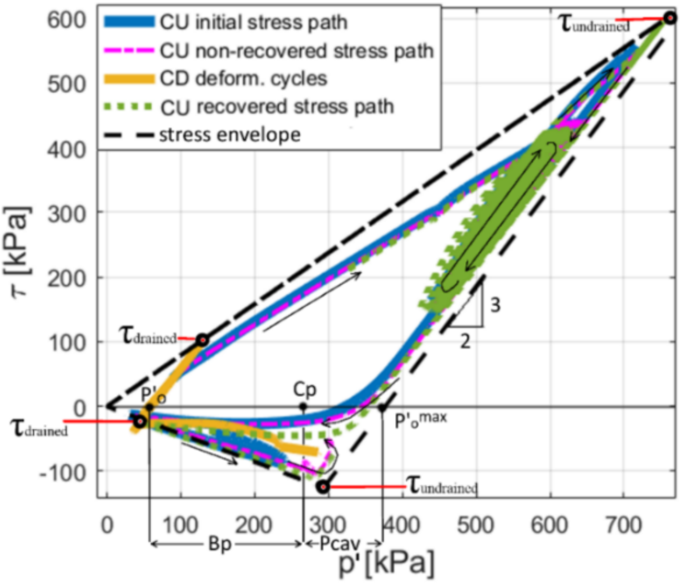

Fig. B.4: Effective stress history of one specimen. Effective stress limits (linear envelopes) of undrained and drained sand are visible. Plotted is effective stress history for Fig. B.5.

(see Fig. B.4 and Eq.2). Thus, effective stresses of undrained sand are limited within thee linear boundaries ("stress envelopes", shown in Fig. B.4):

$$\tau_{min,max} = \frac{p'_o \cdot tan\phi}{\frac{2}{3} \cdot tan\phi \pm 1} \tag{B.1}$$

$$p_o^{max} = p'_o + Bp - Pcav \tag{B.2}$$

Coulomb stress limits (Eq.1) are derived from $\tau = tan(\phi) \cdot p'$, combined with effective stress path (ESP) inclined at 2:3 ratio (Ibsen, 1994), and $p_0 = Cp - Pp$. The p_0^{max} limit is especially relevant for deep-water foundations, as undrained strength grows proportional to overhead water pressure (Bp in Fig. B.4). At 20m water depth, $Bp = 200kPa$. A specimen confined with Cp=260 has $p'_0 = 60kPa$ (saturated soil overburden pressure at $6m$ depth), will undrained yield at $p_0 = p_0^{max} \approx 360kPa$. For comparison, at $Bp = 0kPa$ ($0m$ depth), CU specimen starting at $p'_0 = 60kPa$ would yield at $p_0^{max} \approx 160kPa$ (Eq.2). Undrained yield occurs when stiff water (liquid) becomes vapor (gas). In Fig. B.2 only two specimens are pulled back to initial length, the liquefying specimen crossed initial length more than once. The stabilizing specimen (Fig. B.2) was pulled back to initial length multiple times as well, as shown in Fig. B.5. Specimen was drained multiple times. Surprisingly, no recovery of either stiffness or resistance to liquefaction occurred regardless of

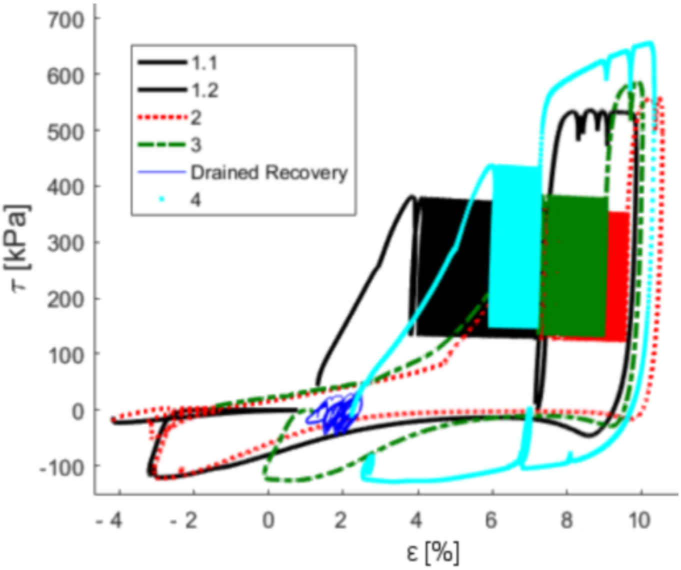

Fig. B.5: Attempts to recover undrained specimen by Sabaliauskas and Ibsen (2015): 1.1 CU τ cycles; 1.2 UU crushed to failure and puled to $\epsilon = -4\%$; 2. Before loading - specimen drained through the top, until Pp = Bp ($p'_0 = 60kPa$). CU τ cycles applied similar to steps 1.1 and 1.2. No recovery of stiffness or liquefaction resistance. 3. Specimen drained consolidated ($p'_0 = 60kPa$) over night. τ cycles similar to 1.1 and 1.2 applied again. No recovery. 4. CD deformation cycles ($p'_0 = 60kPa$) applied. CU τ cycles applied. Recovery of undrained stiffness and resistance to liquefaction noticed. (Note - yield strength increased proportionally to density, but stiffness did not recover until drained ϵ cycles were applied)

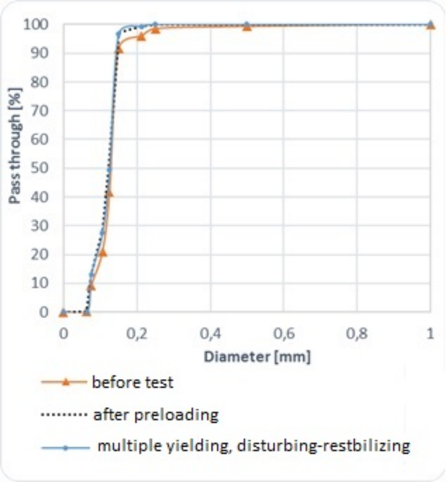

Fig. B.6: Grain diameter pass through obtained by sieving specimens after various testing stages.

draining time: draining for an hour or the whole night made no difference. As long as ϵ was held constant, drainage produced increase in specimen density, without producing recovery.

Undrained sand response during similar τ cycles is compared in Fig. B.5. All four stages were applied on one specimen. Recovery of stiffness and liquefaction resistance was noticed only after draining was combined with ϵ cycles (small cycles < 1% amplitude). Note the four stages had undrained τ cycles applied. Only the drained "recovery" cycles consisted of ϵ cycles. In light of this, Sabaliauskas and Ibsen (2015) proposed deformation dependent sand properties could be governing recovery in disturbed sand states. Dobry and Abdoun (2015), and Dafalias (2011) also propose exclusively deformation dependent soil variables might exist.

Fig. B.4 shows effective stress history of tests from Fig. B.5. It is curious how near identical τ history leads to different ϵ response. Effective stress paths of initial, disturbed and recovered soil state are hardly distinguishable in Fig. B.4. This casts a shadow of doubt on models dependent exclusively on stress envelopes, as the same τ history diverges towards different ϵ outcomes. Alternatively, one can say various ϵ histories converge towards the same τ outcome. This means τ could potentially be normalized in proportion to ϵ. Interestingly, constitutive models using $\epsilon-$ space formulation already exist (Yoder 1980). Furthermore, Yoder (1980) explicitly requested for a testing method capable of observing hardening rules for an ϵ space envelope. By mere coincidence, Yoder's request for experimental proof is addressed 40 years later, during unorthodox frictionless triaxial apparatus testing, presented herein.

Introduction to new test results (drained stabilization) Frederikhavn sand (D50=0.15[mm], emin=0.64, emax=1.05) dry tamped specimens were used for tests shown in Fig's 7-B.13. Initial e value varied slightly: #1 $e_0 = 0.69$; #2 $e_0 \approx 0.7$; #3 $e_0 \approx 0.73$ and #4 $e_0 = 0.72$. Variation in initial density produced unintended variation of yield strength in between specimens during pre-loading. However, initial condition becomes less relevant as specimens are progressively disturbed. Furthermore, outside the scope of this paper, similar re-stabilization patterns were observed on silt, Aalborg university sand no.1 (profile similar to Baskarp no.15 sand), and well graded gravel. Thus, patterns obtained using Frederikhavn sand could be considered representative for a wider range of cohesion-less soils. It is worth noting tests were done at low confining pressures (p' never in excess of 0.8MPa, see Fig. B.4). Thus, crushing can be dismissed as a factor of influence. In addition, some specimens were sacrificed in early stages of testing to sieve – and little to no traces of crushing were detected (see Fig. B.6).

Before drained cycles became the main focus, drained testing capabilities of the Danish triaxial apparatus were not known. It was not clear how large a magnitude deformation can be applied, or how many cycles of deformation can be applied before causing failure of a specimen. Thus, limits of large amplitude drained deformation were tested first, and smaller ϵ cycles applied later. Fig's B.7-B.13 combine both:

1. New testing scope of the Danish triaxial apparatus.
2. Drained recovery (stabilization) patterns of disturbed sand.

By coincidence, while testing limits of the equipment, interesting stiffness pattern was noticed - drained specimens converged towards quasi-static stiffness path named "the stable stiffness triangle". Other researchers (Mohkam, 1983, Fig. B.9) encountered a similar triangular stiffness patterns . However, preexisting studies fail to provide further detail of properties exhibited by this stiffness pattern. In study presented herein, the stable stiffness triangle is scaled and repositioned along the ϵ axis. Properties dependent on τ are separated from those dependent ϵ; yield stress (τ_y) is observed to change with density, while yield strain (ϵ_y) - in proportion to ϵ history.

By controlling both τ and ϵ dependent components, specimen stiffness was regulated. Controlling the cause, gives control of the consequence. Thus, a good model will follow chain of causation observed experimentally. After reaching full control of real specimen stiffness, an empirical model (describing sand specimen behavior) was proposed. (Fig's B.14-B.16). Nonetheless, empirical observations and triaxial testing abilities remain the main focus of this paper. The model serves as a preview of future work, reinforcing practical feasibility of observations.

4 Drained - large deformation amplitude

Three drained cycles of $15\%\epsilon_{mob}$ amplitude were applied on specimen #1 (plot shown in Fig. B.7). After the third cycle, the specimen separated from the top lubricated end plate. A 4^{th} reloading cycle was attempted to reestablish connection with the end plate, but deformation was irreversible. First deformation cycle period was 2 hours (compression and elongation back to initial length), second cycle 25 minutes, third - 10 minutes long. Loading rate was increased while observing Pp build- up at the bottom of the specimen (bottom drainage valve closed, see Fig. B.2). During the test, Cp was kept at constant 260 kPa. Bp at 200 kPa, Pp was allowed to fluctuate within $200 \pm 2kPa$. Since specimen was drained through the top, Bp was applied only through the top. Thus, the bottom end of the specimen was the last to drain. In such configuration Pp is measured at slowest draining point in the specimen. Thus, as long as $Pp \approx Bp$, drained condition is ensured. Still, Pp fluctuated within ±2kPa. Thus, p' was not "perfectly" homogeneous, but sufficient to sustain isotropic yielding for intended testing purposes. Note, point

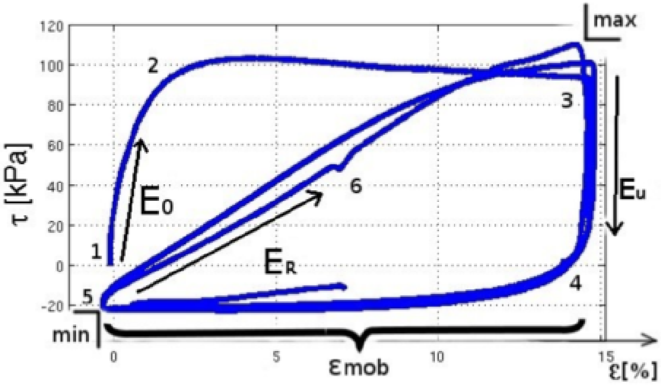

Fig. B.7: Specimen #1, limits of drained testing magnitude. Three cycles of 15% ϵ mob applied. Notice, initial stiffness E 0 re-stabilizes towards E_R during cycle 2 and 3.

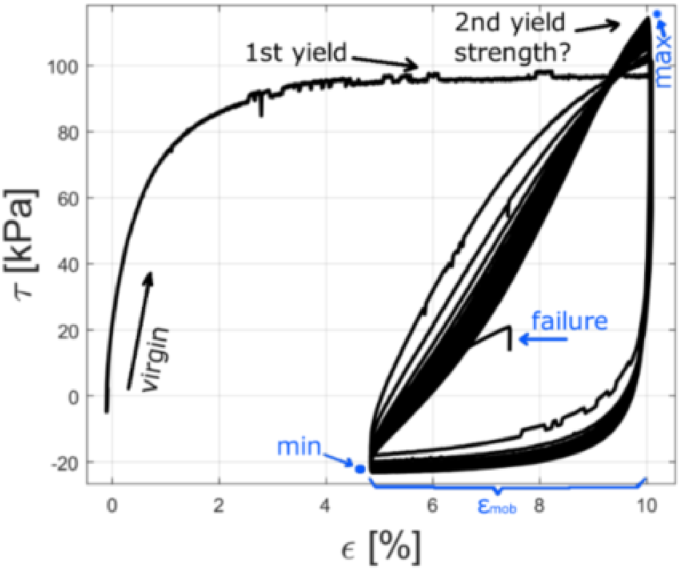

Fig. B.8: Specimen #2. After disturbing to $\epsilon_y = 10\%$, cycles of $\epsilon_{mob} = 5\%$ were applied to failure (22 cycles).

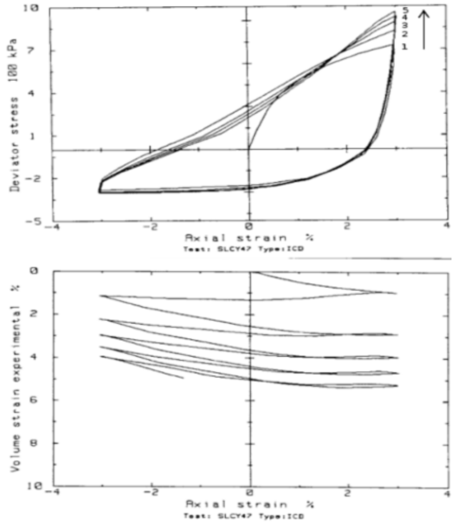

Fig. B.9: Test results by Mohkam (1983). Different sand, similar results.

6 in Fig. B.7. A brief stop for draining was made as Pp developed towards the limit of $\pm 2kPa$. Loading was paused, allowing the Pp to drain-stabilize. A few second pause was enough to allow Pp to stabilize. The triangular stiffness pattern was not disturbed after resuming the load. Some interesting patterns can be illustrated on specimen #1 (Fig. B.7):

1. Similar yield stress (τ_y) is reached during pre-loading (point 2) and after the specimen was disturbed (point 3). τ_y stays constant, only yield strain (ϵ_y) moves. 2. Strength remained, but stiffness changed. Initial compressive stiffness e_0 (cycle 1) shifted to stiffness E_R (cycle 2, 3). 3. Stiffness re-stabilized towards a quasi-stable hysteresis loop connecting yield points "min" and "max". Cycles of constant ϵ_{mob} amplitude caused a stable stiffness triangle to form (claim reinforced during further testing).

Stress peak τ_y relocated from position 2 towards the edges of ϵ mob (position 3 in Fig. B.7). This adaptation pattern will reoccur each time ϵ mob of constant amplitude is applied. A stable stiffness triangle will form within the ϵ mob limits. Thus, drained reloading stiffness can be predicted by observing the "min" and "max" points shown in Fig. B.5. Both "min" and "max" have a unique τ_y and ϵ_y coordinates. The stables stiffness triangle is normalized within a rectangle, set by two τ_y limits two ϵ_y limits . Stiffness curves connect points "min" and "max". The curve is direction dependent. Two unique stiffness curves exist, one for compression (reloading), it points towards "max" point; and one in extension (unloading), it curves towards "min" point. These two distinct stiffness paths shape the stable stiffness triangle. Mohkam (1983) generated a similar stiffness triangle (shown in Fig. B.9), but volumetric re-

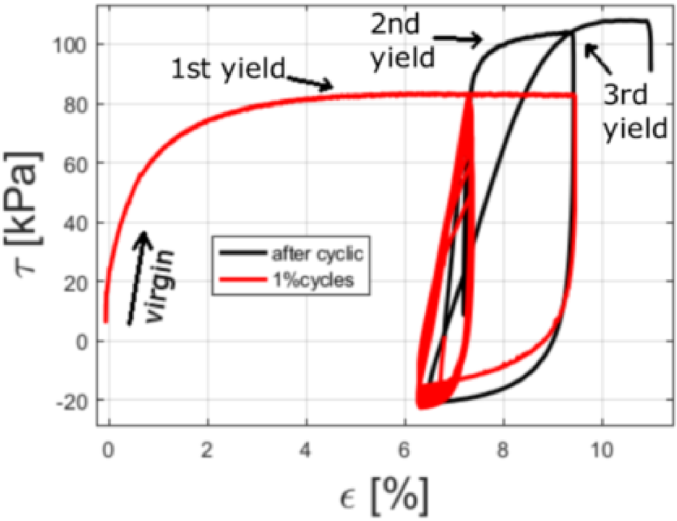

Fig. B.10: Specimen #3. After disturbed to $\epsilon = 10\%_y$ielding, 44 cycles of $\epsilon_{mob} = 1\%$, followed by compression to yield, unloading, and reloading to yield again.

sponse was Mohkam's primary focus. Thus, properties of the triangular pattern were not investigated. Nonetheless, he did record an instance of the stable stiffness triangle fitting description illustrated in Fig. B.7. Note, τ_y in point "max" is moving up as specimen density is increasing (friction angle increases with density, thus pushing τ_y upwards). Triangle in Fig. B.9 was generated at similar amplitude as Fig. B.8 (Fredrikhavn sand). Together, Fig's B.7-B.9 prove existence and repeatability of the stable stiffness triangle. However, these three tests show stabilization towards stiffness lower than initial. Nonetheless, in all cases the stiffness remains directly proportional to deformation amplitude ϵ mob . Thus, if ϵ mob amplitude was reduced, stiffness should increase (recover). Moreover, Sabaliauskas and Ibsen (2015) were not aware of this converging triangular pattern, but similar triangles appear to be developing in Fig. B.5, during small drained deformation cycles. It is plausible, that accidental stabilization of stable stiffness triangles led to recovery of undrained stiffness and resistance to liquefaction.

5 Drained - small deformation amplitude

Previous section described drained testing at large deformation amplitudes. Large deformations produce stable stiffness triangles of lower reloading stiffness. If the observed pattern holds true, cycles of smaller ϵ will cause stabilization towards higher stiffness, as ϵ_y move closer, while τ_y are nearly con-

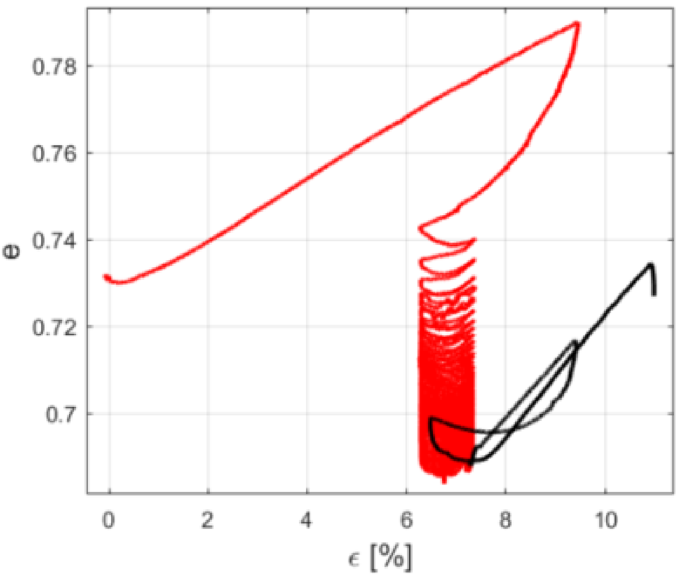

Fig. B.11: Specimen #3 volumetric response of. Density increasing during deformation cycles. Approaching and stabilizing towards $e_{min} = 0.64$. Confining pressure $p'_0 = 60kPa$ at all times.

stant. Specimen #1 was tested at ϵ mob =15(Fig. B.7), Specimen #2: $\epsilon_{mob} = 5\%$ (Fig. B.8), Specimen #3: $\epsilon_{mob} = 1\%$ (Fig. B.10). Specimens #4 shows a more complex loading scenario, where drained stabilization towards small ϵ amplitudes is mixed with drained and undrained disturbing loads (Fig. B.12).

All 4 Frederikhavn specimens were preloaded (disturbed) by large ϵ, causing drained yielding. This pre-loading is meant to push the "max" points forward, leaving the "min" point behind. Thus re-locating and expand the stable stiffness triangle along the ϵ axis. Preloading is part of attempt to control position and size of the stable stiffness triangle. Specimen #1 was pulled beck to initial length after pushing the "max" point forward. Specimen #2 was pulled half way to initial length, before reloading. In both tests position of the "max" point was pushed forward and kept at the chosen peak position during further cyclic loading. Test #3 is different, as reloading does not reach the "max" point set during preload. Instead, the "max" point is forced to creep back, towards 2 nd yield position (see Fig. B.10). The 2nd yield occurred at greater density (see Fig. B.11), thus the 2 nd τ_y position is beyond the preloading yield strength.

Specimen #3 was loaded with 44 cycles of ϵ mob =1% amplitude (Fig. B.10). The first 16 cycles had 10 minute period, each. Then, cycles 16 44 took 1 minute per cycle. Again, Pp accumulation was monitored to ensure proper drained condition is sustained. Reducing the cycle period to 1 minute was plausible because during stabilization of the stiffness triangle volumetric response stabilized as well. Specimen #3 did not collapse during 1% cycles, thus the specimen could be crushed beyond yielding repeatedly after stable stiffness triangle stabilized (yielding three times in total). Stabilization slowed down significantly within the first 16 cycles. Since no further stabilization was visible during 44th cycle, stabilizing cycles were stopped. Plausibly, cycles stopped prematurely as τ_y was mobilized slightly ahead of expected ϵ_y position. Nevertheless, offshore wind turbine foundations, temporarily disturbed by extreme events, encounter similar processes. Loss of soil stiffness (preloading), followed by gradual recovery during cycles, and repeated loss of stiffness (after 2nd yield) is similar to episodic extreme events disturbing offshore wind turbine foundations (Damgaard et al. (2015)).

Specimen #3 was crushed towards 2 nd yield (1 st yield induced during pre- loading), then unloaded and reloaded to yield for the 3 rd time (see Fig. B.10). Speculation that ϵ_y is pushed forward instantly during yielding was confirmed; ϵ_y recovery is not "symmetrical" to disturbing. Distance between points "min" and "max" expands instantly during yielding, but shrinks gradually during ϵ mob cycles short of reaching "min" and "max" point position; also, points "min" and "max" move independently of each other. They both try to envelope recent ϵ mob cycle limits. It is curious, that recovery process is observed only in drained loading conditions. Undrained specimens do not recover stiffness or resistance to liquefaction during small ϵ amplitude cycles. This could be explained by incompressibility of the pore water, which prevents even small increments of volumetric contraction in undrained specimens. Thus "contractive work" is restrained, whereas dilation of undrained specimens is not as restricted, because dilating specimens can literally pull water apart, forcing it to vaporize (see Fig. B.3). However, this brings a new contradiction: stiffness was observed to be independent of density, lower stiffness, at higher density is common. Thus, how can recovery of stiffness depend on specimen volume?

It holds true, that stiffness recovers during contractive increments, but never in direct proportion to absolute density (observed in Figs. B.9-B.13). It could be that recovery of stiffness is dependent on the increment of volumetric work instead of absolute density. A small increment of contraction, can reposition ϵ_y coordinates a great distance apart or closer together, regardless of real time value of absolute density. It is interesting to note, that during 3 rd reloading (Fig. B.10), not only a larger triangle appeared but the volumetric response loop was of larger amplitude as well (Fig. B.11). If size of the triangle is proportional to amplitude of volumetric response, then recovery of undrained properties observed by Sabaliauskas and Ibsen (2015) is explained. Thus, both drained and undrained stiffness appear to recover following the same mechanism, which exhibits converging patterns during deformation cycles. This is interesting, as properties shared by both drained and undrained sand are rare. There is no unifying, "universal" model of sand. Thus, drained- undrained coupling is very interesting. The new found understanding of the stable stiffness triangle allows some interesting testing options to be implemented into further testing procedures as well:

1. Specimen stiffness and sensitivity to liquefaction can be manipulated by stabilizing the specimen towards a stable stiffness triangle within a chosen ϵ amplitude.
2. Density can be manipulated by iterating between drained and undrained loading cycles.
3. A specimen can be tested beyond yielding multiple times, at different densities, all in one loading sequence. The new found sand properties used during testing of specimen #4.

Combining drained and undrained sand, specimen #4 It is of great interest to observe transitioning between drained and undrained cycles, combining disturbed and recovered specimen states. This sequence of events can be encountered at the most crucial moments by offshore wind turbines. An extreme event - a breaking wave - can slam into the supporting structure. The impact load is too fast for pore water to dissipate, thus, undrained loading will be provoked, leaving disturbed soil states. There onward the structure will function within intricate equilibrium of recovery and becoming further disturbed. Eventually, after the peak of the storm, drained soil state will take over and recovery will take place. A typical wind turbine has a lifetime of 20 years; one or two major storms per year; and deformation accumulated by the foundation structure must not exceed 0.25^o degrees inclination. To make matter worse, soil will never behave purely drained or purely undrained; a dominant component will be on one side or the other; and then, loads will be tremendously irregular. Still, tests observing purely drained / undrained condition during semi-regular cycles can help interpolate towards the "partially drained" solution, as patterns valid for both drained and undrained sand are likely to be valid in between as well. Soil can be disturbed even during the very process of installation. Small scale foundations exhibit recovery of stiffness during loading cycles soon after installation (Foglia (2015), Nielsen et al. (2015b)). Thus, a foundation of an offshore structure is likely to begin its life cycle within disturbed soil states. Due to this continuous presence of disturbed sand states, complex loading scenarios must be attempted to observe. The longer and more complex a loading history can be tested – the better.

While testing the limits of triaxial apparatus on Frederikhavn sand specimen #4, 9 loading sequences were applied (see Fig's.B.12,B.13). Iterations between drained and undrained loading were mixed. Amplitude of ϵ cycles

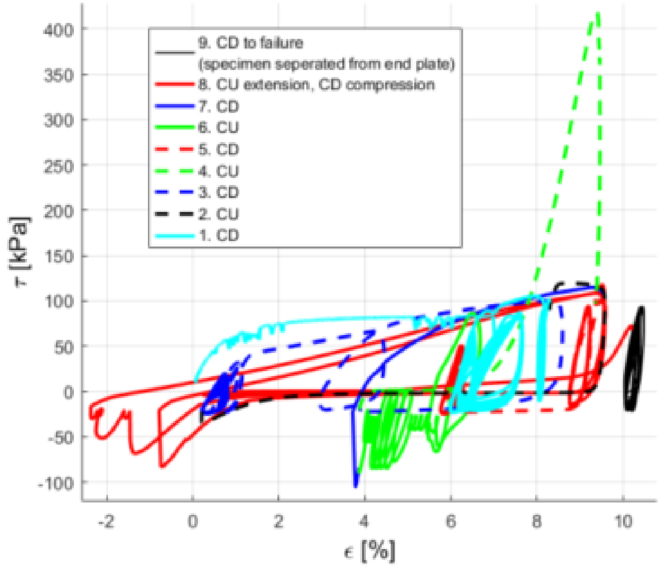

Fig. B.12: Specimen #4. Stress / strain loading history. 9 stages iterating between drained and undrained loading cycles.

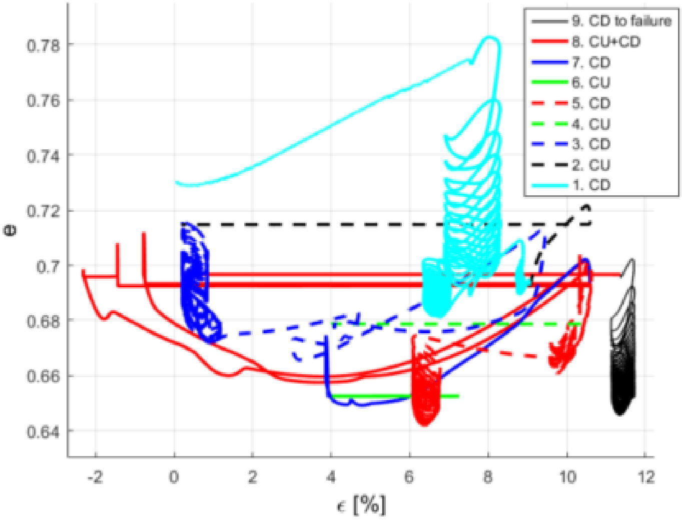

Fig. B.13: Specimen #4. void ratio / strain loading history. 9 stages iterating between drained and undrained loading cycles.

was changes from one group to the other. This way a wide range of disturbed soil response was tested – stabilizing and destabilizing, during both drained and undrained. During the test specimen density varied significantly – contracting towards purely dilative density, and dilating back towards liquefiable soil states. The stable stiffness triangle was a robust and reliable tool to re-stabilize and recover a specimen at any phase during the procedure. Note, $p'_0 = 60kPa$ in all drained stages, and never exceeds p'^{max}_0 in undrained (see Fig. B.4). Description of the complex loading sequence applied on specimen #4:

1. Consolidated drained (CD) cycles at $p'_0 = 60kPa$. Three cycle groups of 3 different ϵ amplitudes applied.
2. Consolidated undrained (CU) pull back to initial length (undrained specimens are less prone to lose contact with the piston head, or shear during extension. And undrained specimen yielding onset is easier to notice, as they yield at a predictable Pp value near -100kPa).
3. CD sequence of 2 cycle groups. First group - ϵ cycles, second group - τ cycles. With a large, monotonic compression applied afterwards.
4. CU compression towards ϵ peak of previous stage.
5. CD unloading, reloading, pull and ϵ cycles.
6. CU τ cycles of various amplitude in extension (undrained stabilization at τ < 0 kPa).
7. CD compression.
8. A mix of CU pull and CD compression. Undrained pulling is combined with small cycles to re-liquefy the specimen during the pull, thus preventing premature shear rupture in extension. CD compression was applied slow enough to avoid Pp accumulation. Specimen lost connection with the top end plate during the last cycle (FAILURE)
9. After specimens cylindrical shape was compromised, isotropic stress distribution could no longer be assumed. But CD cycles of constant ϵ amplitude were applied still. The failed specimen was not leaking, thus volume change could be observed further. Frederikhavn sand density increased to near $e = 0.64$, which matches dry tamping limit $e_{min} = 0.64$.

This loading sequence might seem confusing and chaotic to a human observer, but it is representative of soil states an offshore wind turbine foundation can encounter during a brief episode in a storm. Observation of such

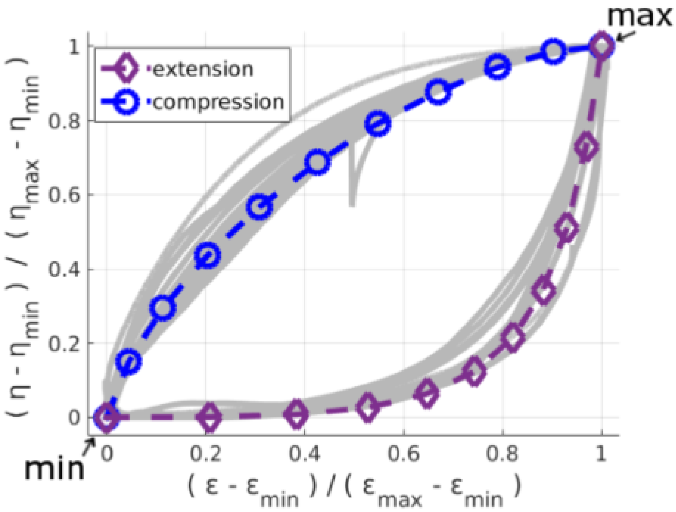

Fig. B.14: A common hardening curve, shared by stabilized stiffness triangles during cycles of various deformation amplitude (Including triangles formed on specimens #1≈3).

"messy" loading cases is necessary; there is no other way to notice predominant patters and regularities governing such chaotic scenarios. Interestingly, the stable stiffness triangle is converging, stable and reoccurring. Furthermore, volumetric response seems to be proportional to size of stabilized triangle. As if transitioning between soil states was equivalent to transitioning between stable stiffness triangles. Using the stable stiffness triangle, combined with undrained stress limits of sand - complex loading scenarios were executed. This is in not a conventional testing procedure. The new scope of testing challenges conventional testing methods. Coincidently, challenging conventional numerical models. Specimens in frictionless triaxial apparatus were loaded using deformation history, and the new found deformation dependent properties seem to require and ϵ envelope. Thus, the prospect of using ϵ envelope in modeling practice is explored in the next section.

6 Empirical model of a specimen, using ϵ envelopes

Before going into details of the model, it should be explicitly noted - this is not an attempt to disgrace stress space plasticity models. It is merely an attempt to fit experimental data by following patterns and regularities observed in disturbed sand specimens. This is an early version of an empirical model, describing specimen response, implementing normalized stable stiffness triangles. Stable stiffness triangles were normalized with respect to ϵ, within "min" and "max" limits. Each triangle τ history was expressed with

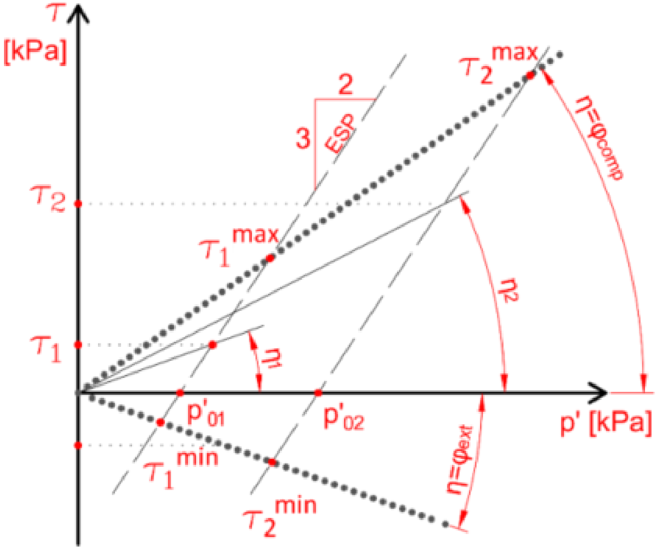

Fig. B.15: Schematic illustrating the empirical model used to simulate τ. Each η is obtained by interpolating ϵ within normalized curves given in Fig. B.14, and scaling the normalized η values between ϕ_{comp} , ϕ_{ext}

stress ratio $\eta = \tau/p'$. Triangles from multiple tests were normalized, and plotted together in $\eta - \epsilon$ plot shown in Fig. B.14. Once plotted, the pattern was manually fitted with two second order polynomial curves.

Similar hardening curves are used in conventional hardening soil models, which use stress envelopes. However, in this case the stress envelope would have to be very narrow and purely kinematic, as unloading and reloading have individual hardening curves; every increment must be pure plastic; furthermore, it is not clear how to express experimentally observed ϵ envelope limits towards τ envelope formulation. Yoder (1980) proposed an interesting alternative. He converted τ envelope of coulomb sand into an $\epsilon-$ space envelope. Conveniently, the normalized hardening curve fits within this ϵ envelope. Strain space formulation by Yoder (1980) has numerous computation benefits as well, as it converts series spring model, into a parallel spring system. This provides addition comfort for calibrating the model as volumetric response and stiffness response, can be fitted independently of each other.

In the empirical model, stress angle ($\eta = \tau/p'$), is expressed as function of normalized strain $\eta = f(\epsilon_{norm})$, where ϵ_{norm} has values between 0 and 1 interpolated within the ϵ envelope, with points "min" an "max" at the boundary of the envelope (Fig. B.14). Note, in Fig. B.14 both η and ϵ are normalized between 0 and 1. When scaled up, $\phi_{comp} \geq \eta \geq \phi_{ext}$ at all times. Thus, no "stress envelope" is necessary; τ satisfies the Coulomb stress limit because

η is always interpolated within ϕ_{comp} and ϕ_{ext} . The principle is illustrated in Fig. B.15, where various values of τ are obtained using various $\eta(\epsilon)$ and p'_0 combinations. Simulation of specimen #4 is shown in Fig. B.16. Measurement and simulation are plotted on top of each other. The fit appears to be surprisingly good, given the loading history contains both drained and undrained loading, as well as irregular loading history. Position of stiffness loss and recovery is predicted correctly (albeit rate of recovery is not captured precisely); unloading reloading cycles overlap with measurements in many positions, both during drained and undrained loading cycles. The empirical model uses 2 inputs, 1 output, 3 constants, and 2 variables. Inputs are ϵ and p′ 0 (from measurements, $p'_0(t) = Pp(t) - Cp(t)$). Output is $\tau(t)$; The ϵ envelope is governed by constants: friction angle (ϕ), kinematic (κ), and isotropic (ι) hardening coefficients; and two variables $\epsilon_{min}(t), \epsilon_{max}(t)$ - envelope coordinates:

1. Input $\epsilon(t)$ and $p'_0(t)$ are provided from real test measurements
2. envelope (“min” “max”) is allowed to shrink, proportional to $\Delta\epsilon(t) = \epsilon(t) - \epsilon(t - \Delta t)$: $\epsilon_{min}(t) = \epsilon_{min}(t - \Delta t) + \iota \cdot |\Delta\epsilon(t)| + \kappa \cdot \Delta\epsilon(t)$ $\epsilon_{max}(t) = \epsilon_{max}(t - \Delta t) - \iota \cdot |\Delta\epsilon(t)| + \kappa \cdot \Delta\epsilon(t)$
3. envelope is checked for yielding, and updated: If $\epsilon(t) > \epsilon_{max}(t)$ then $\epsilon_{max}(t) = \epsilon(t)$; If $\epsilon(t) < \epsilon_{min}(t)$ then $\epsilon_{min}(t) = \epsilon(t)$;
4. $\eta(t)$ is interpolated between $\epsilon_{min}(t), \epsilon_{max}(t)$, depending on loading direction (Fig. B.14)
5. $p_0(t)$ and $\eta(t)$ are known, thus Eq.1. can be used to find $\tau(t)$, by replacing ϕ with $\eta(t)$ (see Fig. B.15).

Again, this is an early version of an empirical model. It ignores the role of volumetric response, thus τ_y values can be expected to misalign. Also, transitioning from one normalized curve to the other one is jumpy, smooth transitioning rules need to be implemented. Further research of hardening rates and in-depth dependencies need to be observed. Nonetheless, even in its crude version, the model can predict specimen stiffness loss and recovery with surprising precision (Fig. B.16). An interesting property of the empirical model is its inherent stability. Each time a stable stiffness triangle stabilizes in real specimens, the model re-calibrates itself to match the triangle. Thus, the model re- calibrates itself automatically.

Notice, undrained cycles were treated the same as drained in simulation shown in Fig. B.16. In reality, the ϵ envelope was never observed to "shrink" during undrained loading, whereas in shrinking was not restricted during undrained episodes. Still, even at this imperfect, early version, the model delivers a promise to unify drained and undrained response. If Pp values were

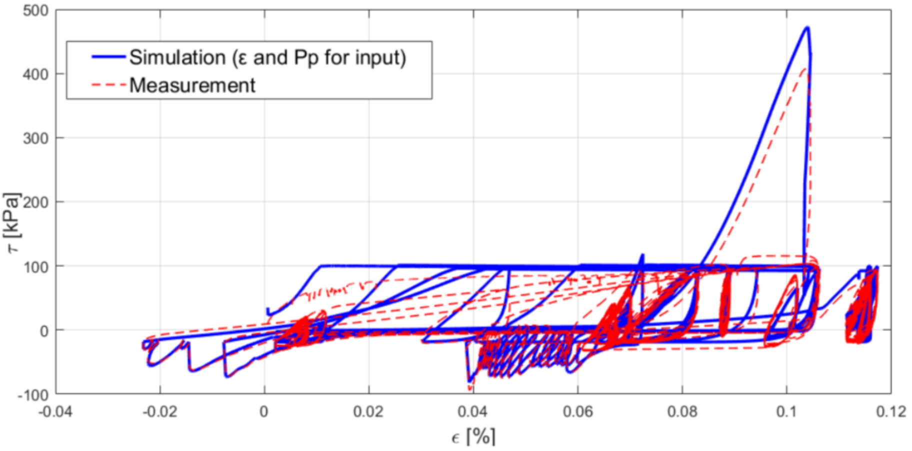

Fig. B.16: Simulation of Specimen #4, using empirical model of a specimen (based on ϵ-space formulation by Yoder, 1980).

simulated instead of borrowing the real life recoded values, this crude empirical model would already be sufficient to combine drained and undrained soil response. However, to simulate Pp history, improved understanding of volumetric response is required. Then, after drained volumetric response is understood, the question of modelling nonlinear stiffness of pore water during cavitation remains. Furthermore, if the model is to be implemented in 3D space, the question of Lode angle remains. The frictionless triaxial can apply loads along fixed lode angle – 0^o and 60^o. Thus, a reliable 3D implementation would take testing which is even more complicated. Nonetheless, it is interesting what shape the 1D ϵ envelope would take in 2D or 3D space. A true triaxial apparatus could plausibly address this question.

7 CONCLUSION

The frictionless triaxial apparatus has exceptional testing potential. Drained and undrained deformation cycles of large amplitude are applicable without causing specimen failure; disturbed specimens can be re-stabilized and re-disturbed many times in one loading sequence.

Sand properties are governed by re-interlocking of grain particles (emphasized by Schofield, 2005). In triaxial tested specimens, the process of re-interlocking appears to be governed by stable stiffness triangles, which stabilize during cycles of constant ϵ amplitude. A stable stiffness triangle, expressed through hardening curves, normalized within an ϵ envelope, captures stiffness loss and recovery surprisingly well, using simple hardening rules. Currently, volumetric response is not modeled (only η was simulated), but frictionless triaxial apparatus is sufficient for further research of volumetric response.

Nevertheless, testing capabilities of frictionless triaxial apparatus are limited: effects dependent on Lode angle cannot be observed. Further research of deformation dependent stiffness patterns could benefit from testing options offered by true triaxial apparatus, as it allows to control all three principle stresses individually. It is interesting how stable stiffness paths change depending on: Lode angle, distance from the hydrostatic axis, and if the shape and hardening rules of a 3D $\epsilon_y$ield envelope can be established (Note, constitutive formulation for implementing such envelope already exists, derived by Yoder, 1980).

In summary, tests presented herein question both: testing and modelling methods. Anomalies, such as lower stiffness at higher density, were addressed by unorthodox tests, which lead to unorthodox model. Nevertheless, sand is the perfect model of itself, and a yield strain envelope is applicable for controlling stiffness in real life specimens. Thus, empowering the experimentalist, yet, unsettling the theoretician.

8 REFERENCES

Bishop, AW, Green, GE (1965). The influence of end restraint on the compression strength of a cohesionless soil. Geotechnique, 243–66.

Dafalias, YF (2011). Finite elastic-plastic deformations: beyond the plastic spin. Theoretical and Applied Mechanics, 321-45.

Damgaard, M, Andersen, L, Ibsen, L, Toft, H, Srensen, J (2015). A probabilistic analysis of the dynamic response of monopile foundations: Soil variability and its consequences. Probabilistic Engineering Mechanics; doi:101016/j.probengmech

Dobry, R, Abdoun, T, (2015). Cyclic shear strain needed for liquefaction triggering and assessment of overburden pressure factor k σ. Journal of Geotechnical and Geoenvironmental Engineering.

Foglia, A (2015). Bucket foundations under lateral cyclic loading, Ph.D. thesis; Denmark.

Ibsen, L (1995). The Static and Dynamic Strength of Sand. Geotechnical Engineering Group. Proceedings of the Eleventh European Conference on Soil Mechanics and Foundation Engineering, Copenhagen, 1995 : XI ECSMFE : DGF-bulletin 11, Vol. 6, 69-76.

Ibsen, LB (1994). The stable state in cyclic triaxial testing on sand. Soil Dynamics and Earthquake Engineering (13), 63-72.

Jacobsen, M (1970). A new triaxial apparatus. Bulletin / Geoteknisk Institut no 27 DGI Bulletin.

Kirkpatrick, W (1967). Influence of end restraint on strain distributions in the triaxial compression test. Geotechnical Conf. Oslo. volume 2.

Mohkam, M (1983). Contribution à letude experimentale et theorique du comportementdes sables sous chargements cycliques. Ph.D. thesis.

Nielsen, S, Ibsen, LB, Gres, S (2015a). Cost-effective mass production of mono bucket foundations, PO: 242.

Nielsen, S, Ibsen, L, Nielsen, B (2015b). Dynamic behaviour of mono bucket foundations subjected to combined transient loading; C R C Press LLC; volume 1, 313-8.

Olson, RE, Lai, J (2004). Apparatus Details For Triaxial Testing. Technical Report;Chaoyang University of Technology.

Rowe, P, Barden, L (2005). Importance of free ends in triaxial testing. Journal of the Soil Mechanics and Foundations Division, 90(1), 1-28. Sabaliauskas, T, Ibsen, LB (2015). Cyclic Triaxial Loading of Cohesionless Silty Sand, International Society of Offshore and Polar Engineers, 821–826.

Schofield, AN (2005). Disturbed soil properties and geotechnical design. Thomas Telford.

Vardoulakis, II (1979). Bifurcation analysis of the triaxial test on sand samples. Acta Mechanica, 32 (1-3), 35-54.

Wood, DM (2003). Geotechnical modelling. volume 1. CRC Press;

Yoder, PJ (1980). A strain-space plasticity theory and numerical implementation, http://authors.library.caltech.edu/26358/1/8007.pdf, Report on Research Concluded Under Grants from National Science Foundation.

Paper C

The new testing scope of the old frictionless triaxial apparatus

Tomas Sabaliauskas, Lars Bo Ibsen

Accepted in the
Geotechnical testing journal, 2017.

Abstract

Offshore wind turbine foundations episodically lose and recover stiffness, as the soil gets disturbed during extreme events. Such sand behavior is not accounted for during standard testing procedures. Therefore, a novel dynamic triaxial testing procedure is explored: specimens are loaded past their peak strength, then they are pulled back to initial length, where attempts to recover their initial stiffness are made by applying further loading cycles. This fundamentally changes how we view our specimens – they are no longer "fragile and brittle". Instead, specimens can be axially compressed and pulled back to initial length many times, as long as shear rupture and bulging are circumvented.

The novel testing procedures were attempted using a frictionless triaxial apparatus. Frictionless triaxial is not a new concept itself, but the novel procedures reveal previously undocumented testing capabilities: (1) Multi stage testing - sand specimens can be liquefied (undrained), drained and re-liquefied (undrained again) many times, in one sequence, on one specimen; (2) Specimens can be compressed to large axial strain (15% strain or more), and pulled back to initial length - more than once. In the process, peak yield strength can be measured more than once, at more than one density – all using one specimen.

.

1 Introduction

When sand is disturbed, its strength and stiffness can change significantly. This is important in various circumstances: in seismic zones, sand can be disturbed during earthquakes; in construction sites, vibration, excavation, transportation, deposition and other processes can produce disturb sand states as well. More recently, episodically reoccurring disturbed states were observed in offshore wind turbine foundations (Damgaard et al., 2015, Gres et al. 2016). The offshore foundation encounter disturbed soil states during most critical of moments: peaks of storms. This presents a challenge, which requires expanding known methodology of both modelling and testing. Tests must account for a new worst-case scenario:

1. Offshore foundation is installed, seafloor is disturbed during installation;
2. Disturbed soil stabilizes (recovers initial stiffness, strength and dilativity) during relative calm loading cycles;
3. A storm event begins:
    (a) Waves of gradually increasing size disturbing soil before the extreme event;

   (b) The extreme wave hits the structure. Structure survives, but the soil supporting the foundation is disturbed even further;
   (c) Storm continues, waves produce accumulating deformation increments;
   (d) As storm calms down, soil begins to stabilize. Soil stiffness, strength and resistance to liquefaction gradually recover;

4. Point 3 is repeated for every storm encountered during a 20 years design life.

The loads are irregular, soil states - changing, and the foundation of a wind turbine must accumulate less than 0.5^o inclination during its 20-year design life (according to DNV-OS-J101 design standard, 2014). Currently, wind turbine foundation design process relies heavily on large safety coefficients, probabilistic estimates, and empirical measurements of full scale and small-scale foundations. Numerical simulations are of limited use, as existing soil models do not capture the full scope of loss and recovery of cyclic preloaded (disturbed) soil fabric (Di Prisco and Wood, 2012). Therefore, disturbed soil properties need to be researched beyond the scope of conventional methods. Thus, unconventional triaxial testing procedures were attempted.

2 Methodology

Conventional tests do not emphasize preservation of disturbed sand specimens. While testing peak strength, conventional triaxial apparatus provokes localized shear rupture. The ruptured specimen is compromised and the test cannot continue. However, that is not the case with frictionless triaxial apparatus. Unlike conventional setup, the frictionless apparatus can measure peak yield strength without producing localized shear rupture. Thus, a test can continue after the peak strength was measured. In fact, peak strength can be measured at multiple densities, using one specimen. Some authors fail to recognize significance of avoiding shear rupture. They refer to the frictionless triaxial apparatus as a "more precise" but "harder to use" equivalent of conventional triaxial (Olson and Lai, 2004), which is misleading. While true that the two apparatuses measure comparable values of peak yield strength (friction angle estimates within ±2.5%), soil has more than one property, and the frictionless apparatus has superior precision for measuring stiffness and volumetric response. In addition to better precision, frictionless apparatus can stabilize disturbed specimens, thus giving access to a completely new category of testing procedures. Therefore, frictionless triaxial apparatus should be considered as a completely different subcategory of triaxial testing, one where a specimen can be repeatedly yielded without causing failure:

- Failure (of a specimen) – irreversible plastic deformation. Stress or strain field becomes distorted by either shear rupture or bulging. These distortions generate localized deformations and stresses which cannot be averaged or measured.
- Yielding (of a specimen) – reversible plastic deformation. If rupture and bulging are circumvented, this fundamentally changes how we view our specimen: it is no longer "fragile and brittle". Instead, it can be squeezed and pulled back to initial length many times – because axial compression can be 'reversed' by plastic elongation increments.

A perfect frictionless triaxial apparatus would allow yielding a specimen indefinitely – any deformation amplitude, for any number of cycles. Thus, one could potentially recreate evolution of disturbed soil states encountered throughout the whole design life of an offshore wind turbine. Unfortunately, no apparatus is perfect and specimens have limited durability. Nonetheless, there seems to be a pattern of researchers stopping a frictionless triaxial test after yielding, prior to failure of a specimen. Vardoulakis (1979) compressed a specimen to axial strain of 50%. He concluded larger strain could be applied with end plates of larger diameter, since his specimen radius enlarged beyond the edge of the end plates. His unsaturated specimens yielded in compression without forming localized shear rupture or otherwise losing cylindrical geometry. This rupture free yield mechanism can be referred to as isotropic yielding: a failure mechanism where the whole volume of a specimen deforms isotopically, producing uniform amounts of dilation and axial deformation, without localized strains or stresses. This can be viewed as infinite number of failure planes competing, yet, due to isotropic condition, neither one becomes dominant – they all yield in parallel, isotopically.

Another storyline where tests stopped after yielding prior to failure, begins with Ibsen (1994; 1995), who used a frictionless apparatus to apply undrained stress cycles on saturated sand. He observed stable state within undrained specimens. Balance between liquefaction and stable state was later elaborated by Sabaliauskas et al. (2014), who expanded work of Ibsen, by adding peak undrained strength tests on top of undrained cyclic preloading. Cyclic preloaded specimens were axially compressed into regions of 20-25% axial strain – yielding without a trace of shear rupture or bulging. Sabaliauskas and Ibsen (2015) noticed the specimens can be tested even further, therefore they expanded the procedure a step further: they pulled undrained compressed specimens back to initial length. After this procedure, the specimen recovered initial geometry, but retained a disturbed soil state – lower stiffness and increased sensitivity to liquefaction. Even after being pulled back to initial length, specimens remained cylindrical, therefore, procedures for stabilizing (recovering stiffness and resistance to liquefaction) were plausible to attempt.

3 Equipment and material

Rowe and Barden (1964) discussed the importance of free end in triaxial testing. Bishop and Green (1965), pioneers of triaxial testing, introduced the frictionless triaxial apparatus as an improved alternative to conventional triaxial apparatus. Thus, the "frictionless" concept was known from the early days of triaxial testing. Two key differences set conventional and frictionless apparatus apart:

1. Specimens of 1:1 height to diameter ratio (instead of conventional 2:1).
2. Frictionless end plates (polished glass, with layers of greased latex). Instead of conventional (high friction, large diameter) porous filter.

It would be an error to assume identical testing capabilities between different types of apparatus. Even within their subcategories, individual apparatuses will have minor performance differences. Thus, while attributing testing capabilities to a particular design, it is worth noticing unique names assigned to individual apparatuses,:

• "Lubricated triaxial apparatus" by Bishop and Green (1965) • "New triaxial apparatus" by Jacobsen (1970) • "Improved triaxial apparatus" by Vardoulakis (1979) • "The Danish triaxial apparatus" by Ibsen (1994).

In tests presented herein, the "dynamic" version of "the Danish triaxial apparatus" was used. Development of this particular frictionless triaxial apparatus began at Aalborg University (AAU), when Jacobsen (1970) introduced the "new triaxial apparatus", inspired by work of Bishop (1965). The "new" was upgraded to "the Danish" by Ibsen (1994), by introducing digital sensors and automated loading controls for clay testing. More recently, a "dynamic" version of the Danish triaxial apparatus was devised, for testing dynamic loaded sand properties. The dynamic apparatus uses a high precision hydraulic oil piston, controlled by a proportional integral derivative (PID) controller. Sabaliauskas et.al. (2015) adjusted the dynamic apparatus by making the drainage tubes (made from extra stiff nylon) shorter, to preserve more pore water stiffness in undrained sand specimens. A second latex sleeve was added on sand specimens, to prevent diffusion of water molecules through the specimen walls (making specimens watertight to a point where less than 10 kPa pore pressure is lost in 2 days' time). Such minor adjustments produce measurable improvement in testing precision. Thus, development of the Danish triaxial apparatus is still ongoing today, nearly 50 years after Jacobsen introduced it at AAU.

It is worth noting the impact of software development for the apparatus. Ibsen (1994) implemented autonomous stress space trajectory controllers, to test effects of stress space paths in clay. More recently, a purpose made algorithm was developed for testing liquefying sand specimens. The algorithm combines PID control with a deformation envelope –deformation amplitude

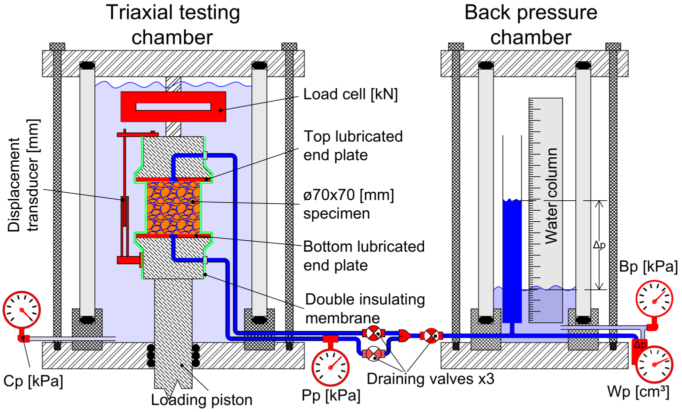

Fig. C.1: Schematic drawing of the Danish triaxial apparatus (frictionless triaxial apparatus).

reached by previous loading cycle is used to extrapolate loading rate required for the next loading cycle. This greatly improves durability of a liquefying specimens. IN addition, the model is challenged to match real time soil states as they evolve.

Currently, the Danish triaxial apparatus is the standard method of testing at AAU, Denmark; used in collaboration with both academic and industrial partners. The Danish triaxial apparatus normally uses a cylindrical specimen of ø70 x 70 mm (1:1) placed between lubricated end plates (ø80mm). A ø5 mm draining hole, with a filter, is located in the center of each polished end plate. If for any reason a specimen of conventional height to diameter ratio (2:1) was necessary, the bottom piston can be lowered, and a specimen of ø70 x 140 mm (or similar) can be inserted. The polished glass end plates are interchangeable with large diameter filter stone. Thus, the Danish triaxial apparatus can easily be reversed to conventional configuration. Notice, this means conventional triaxial apparatuses are just as easily convertible to frictionless configuration.

The Danish triaxial apparatus has a load cell submerged within testing chamber (see Fig.C.1). Thus, the load cell is measuring reaction force acting directly on top of the specimen. However, this makes the load cell sensitive to changing chamber pressure (Cp), but the Force (F) caused by changing Cp can be removed from measurements during data processing. Moreover, normally, during a test, Cp is held constant, after zeroing down the F reading.

Top and bottom lubricated end plates have smooth, polished glass. A sandwich of two thin latex sleeves, lubricated with high vacuum grease is added on each end plate to further lubricate the polished surfaces (note, a small hole is left in the center of a latex circle, for drainage). Olson and Lai (2004) describe problems caused by grease being squeezed out from the end plates. However, no such problems were noticed while operating the

Danish triaxial apparatus. This could be due to properly selected vacuum grease viscosity, or relatively low axial loads encountered during testing. Two displacement transducers are bolted onto the end plates (only one is shown in Fig.C.1). Note, due to low friction at the end plates, the specimen will slide sideways given the slightest misalignment of frictionless surfaces. Thus the endplates must remain near perfectly parallel during testing. This threat of a specimen sliding sideways is the only "complication" encountered while comparing operation if frictionless vs conventional setup.

Drainage tubes of the Danish triaxial apparatus are made from extra stiff nylon. Stiff tubes are necessary to preserve water stiffness in undrained triaxial tests, as undrained water is only as stiff as the tube holding it. In addition, drainage tube length was cut to minimum length, by attaching drainage valves at close proximity to the specimen. If tubes are long, volume of water inside the tubes becomes excessive and lowers sensitivity to volumetric strain generated by the specimen. Eliminating the drainage tubes all together, by placing valves within the piston head would be optimal. However, external drainage valves are easier to install and operate (See Fig.C.1). Note, when drainage valves are open, the water is drained into the water column – a buret type device described in detail by Lade (2016). The water column allows to measure volume of water drained from the specimen. Water volume (Wv) is measured by Δ_p within a water column of chosen diameter (the Danish triaxial apparatus allows to choose from an array water columns permanently installed within the back pressure chamber. A $85cm3$ water column was normally sufficient to avoid overflow during testing towards extreme specimen densities)

Notice positioning of back pressure (Bp) and pore pressure (u) gauges (Fig.C.1). $Bp = u$, if all drainage valves are open; But $u \neq Bp$ if all valves are closed. In undrained mode, u response is proportional to volumetric response of the soil skeleton and water stiffness. A useful technique for testing drained specimens is to keep bottom drainage tube valve closed, while leaving the top drainage path open. Such "partially drained" configuration allows to monitor u buildup at the bottom, while draining only through the top. In a specimen drained through the top, the bottom will be the last part to drain. Thus, if $u \approx Bp$, while the bottom drainage path is closed, the specimen is guaranteed to be drained. This method of monitoring drained condition in real time can be especially useful during dynamic loading, when rates of volumetric response change between cycles, and loading rates can be speedup after stabilization of volumetric response, without compromising pure drained response.

4 Results and discussion

Disturbed sand triaxial testing can be divided into three stages:

1. Specimen preparation.
    (a) Selecting initial density (for maximum durability)
    (b) Deposition (Wet vs. Dry)
    (c) Initial stress state
2. Disturbing the specimen.
3. Stabilizing the specimen.
    (a) Using drained deformation cycles.
    (b) Combined drained and undrained loading cycles.

4.1 Specimen preparation

Any load, during or after deposition, permanently alters the soil fabric, in a way that is unique to that particular loading condition (Budhu (2008), Schofield (2005), Di Prisco and Wood (2015)). Thus, for testing disturbed sand properties, the initial state (stress state, density, etc.) has relatively little importance. The objective of disturbed soil testing is to erase all "memory" of initial soil state – changing stiffness, strength and dilativity as far away from initial state as plausible – before attempting to recover it. That is, unless disturbed soil specimens tend to stabilize towards a stable state different from initial. Either way, specimen durability is the key criterion if repeated loss and recovery of stiffness, strength and dilativity is to be observed.

Selecting specimen density

One factor affecting triaxial tested specimen durability is density. Cohesionless specimens were noticed to shrink significantly during cyclic loading. As a specimen shrinks, the latex sleeve can wrinkle; especially during liquefaction, when specimens become soft (see Fig.C.2a). Appropriate initial density was observed through trial and error, by intentionally densifying specimens prepared with different initial densities. To drain maximum plausible amount of water, at low confining pressures, the specimens were repeatedly liquefied and drained until purely dilative density was reached. Purely dilative means – no excess pore pressure is generated at any phase of a loading cycle. Prior to reaching pure dilative density, a small fraction of excess pore pressure can be detected during a deformation cycle. If deformation is paused at that phase – the tiny, microscopic quantile of excess pore water

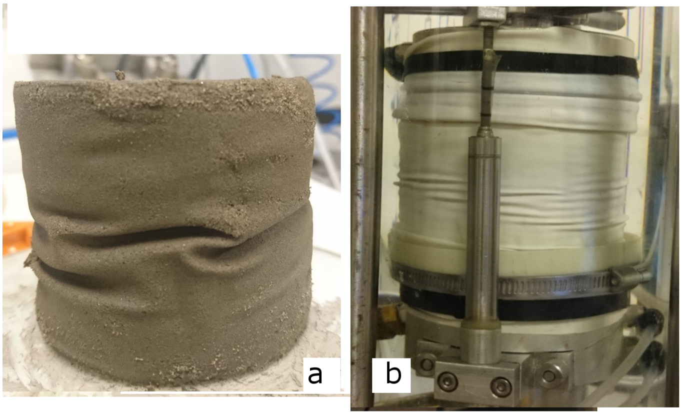

Fig. C.2: a) A silt specimen liquefied and drained many times lost beyond 10% volume. The consequent wrinkles were imprinted during liquefied states. To preserve imprinted pattern, the specimen was drained stabilized (it remained liquefiable at the time of extraction). b) Sand specimen during 4th loading stage shown in Fig.C.5. The specimen was cyclic loaded, compressed and pulled back to initial length 4 times – no excess wrinkles present.

can allowed to drain away. This is an experimental technique, and a very interesting to attempt. It requires very sensitive, well calibrated equipment. Water has stiffness near 4GPa, thus even microscopic volumetric strains are detectable in undrained mode – given the equipment is built and calibrated for the task.

Interestingly, pure dilative state happened to match maximum relative (dry tamping) density IR=100%, where IR=(emax-e)/(emax-emin)*100%. Through trial and error, specimens prepared to IR=80% and IR=90% were noticed to reach purely dilative density without forming excessive wrinkles. The 80-90% range was a good starting point for silt, sand, and well graded gravel (soil profiles tested for stabilization thus far).

Depositing the specimen

Having selected initial density, the required mass of dry (sieved) material can be weighted and shaped into a cylindrical specimen. Preparation procedure depended on soil permeability:

- Permeable material was dry tamped inside a cylindrical mold, with a thin latex sleeve. Measuring each layer height, to ensure uniform density distribution. The dry tamped specimen was held together by vacuum, while the testing chamber was assembled. Then, the specimen was confined by Cp (see Fig.C.1), releasing the vacuum. Thereafter, specimens were flushed with 40 liters of CO2 gas and saturated with de-aired water.

- Low permeability material (silt) was wet deposited. The mold was filled with water before adding soil. The specimen was then stirred using a spoon to force air bubbles out. Once no more bubbles were visible, silt was allowed to settle. Once settled, the mold was gently tapped – liquefying and draining as many times as it takes to reach initial specimen density. The top end plate was then added, with the drainage tubes already filled with de-aired water. Fully saturated specimen was held together by vacuum while the testing chamber was assembled. Once Cp was applied, vacuum is released and Bp is connected.

Notice, both preparation methods left the specimens at condition $Cp > u$, and $Bp = u = 0kPa$. The specimen is confined to $\sigma_r' = Cp$. The dry tamping method is somewhat more reliable, as air is replaced with CO2, then CO2 is pushed out by water. If some bubbles of CO2 are trapped, they dissolve once u pressure is raised. Whereas wet deposition has the danger of trapping air bubbles. Nonetheless, high saturation levels are attainable using either one of the two methods. The typical Skempton B value reaches beyond 0.9, once u is increased to 200 kPa.

Applying initial stress state

The "initial stress state" was chosen to resemble 20 meter water head ($u = 200kPa$), and an overburden pressure of 6 meters under the seafloor ($\sigma_r' = 60kPa$, as saturated soil has unit weight $\gamma \approx 10kN/m$). Such initial state was inspired by Mono Bucket foundations – an innovative offshore foundation type, designed specifically for offshore wind turbines (Houlsby at el., 2005). In addition, such stress state is convenient for observing both liquefaction and dilative response in effective stress space, because the loops and patterns, once plotted, have good resolution, can be followed by a human observer conveniently. For reasons given, initial stress state condition $Cp = 260kPa$, $u = Bp = 200kPa$ is applied.

To increase u from $0kPa$ to $200kPa$, two methods can be used: drained or undrained. In drained case, the bottom drainage path is closed (see Fig.C.1), and Bp is increased slightly, being careful to keep $Cp - Bp > 10kPa$ (otherwise the membrane, holding the specimen, can get inflated like a balloon). Once Bp is increased, u needs time to catch up (as bottom drainage path is closed, Bp has to seep through the whole height of the specimen). The time it takes u to catch up depends on specimen permeability. Sand takes less than a minute – silt takes an hour or longer. Once $u \approx Bp$, Cp can be increased. Preferably, keeping $Cp - Bp < 60kPa$ at all times, to prevent uneven confining of the specimen. Thus, Bp and Cp are increased in a step-wise manner, allowing u to catch up in between steps. Notice $\sigma_r' = Cp - u$ at the bottom (undrained mode), and $\sigma_r' = Cp - Bp$ at the top of a specimen (in drained mode). Since the whole specimen is described by one σ_r' value during post processing, it is crucial to keep $Bp \approx u$ during drained testing, thus condition of $Bp = u \pm 1kPa$ was ensured during testing.

Notice, u takes a long time to catch up with Bp in specimens of low permeability. Such specimens were preloaded using undrained method, by leveraging high Skempton B values ($B = \Delta_u/\Delta Cp$). Due to high saturation: $B \approx 1$. Thus, σ'_r is near constant, if Cp is increased while all drainage valves are closed. However, $B \approx 1$ only at higher pressures. At $u \approx 0kPa$, B can be as low as 0.6. Thus, a drained pause might still be necessary. Nonetheless, one pause is better than 6 pauses with an hour of waiting in between. Undrained preloading starts at $Cp = 20kPa$, $u = 0kPa$. While gradually increasing Cp, u is allowed to gradually lag behind. The gap between Cp and u increases slowly. If at some point $Cp - u > 50kPa$, the procedure is paused, Cp held constant. While valves are still closed, Bp is set to $Bp = u + 20kPa$, and the top drainage path is opened, thus allowing u to raise towards Bp during the "drained pause". After $Bp = u$, valves are closed and Cp increased again. Notice, once $Cp = 260kPa$, the resulting $u \neq 200kPa$. The specimen needs to be left in drained mode, keeping $Bp = 200kPa$, allowing u to settle down to $200kPa$. Consequently, regardless of drained or undrained preloading - the specimen is left isotopically confined to $\sigma'_r = 60kPa$, in drained mode. $Cp = 260kPa$, $Bp = u = 200kPa$. No axial force F is applied yet, thus deviator stress $q = F/A = 0kPa$.

On a side note: Skempton B values were noticed to be sensitive to drainage tube stiffness. This makes sense (see Fig.C.1), as Cp acts both on the specimen and the drainage tubes. Moreover, if the tubes are pulled further out of the apparatus, measured B values decrease. To reduce these effects, the Danish triaxial apparatus uses drainage tubes made of extra stiff nylon, cut down to 20-30cm length. There could be apparatuses which do not account for this effect, B values measured on apparatuses with soft tubing can be misleading. Pore water is only as stiff as the drainage tube in contact with it.

4.2 Disturbing the specimen.

To "disturb" a specimen, means to induce the type of yielding which leads to loss of stiffness and resistance to liquefaction. While disturbing specimens, true axial strain $\epsilon = ln(1\breve{}\Delta H/H_0)$ was measured. Logarithmic correction is necessary at $\epsilon > 10\%$ (Praastrup et al., 1998). In addition, large ϵ imposes large changes in specimen radius. Thus, deviator stress q has to be updated to account for changing cross-section area (A). The A has to be corrected with respect to both volumetric and axial strain. By doing so, measurements of true stress and true strain are plotted in all graphs. Note, for triaxial testing, shear stress $\tau = q/2$. However, it was not plausible to use shear strain, because during undrained peak yielding the pore water can vaporize (cavitate). Since it is not plausible to measure undrained volume change with the setup used, measurement of axial strain is used instead. In addition, q and ϵ work together like a linear spring – both acting on the same axis.

Two control methods can be used to axially load a specimen: force and displacement control. During Force control, the PID controller automatically adjusts bottom piston position to match reaction force F measured by the load cell, with real time force requested by the user. This way deformation is observed as a function of F (researching ϵ as a function of stress). This is useful when measuring accumulated deformation in response to applied force (stress) amplitude.

However, force control can collapse during pure plastic response, when infinite displacements are generated while reaching for implausible F values. Thus, in plastic regions displacement control must be used (when there is a threat to cross peak yield strength, or in the middle of a cycle in liquefied states). While displacement control is active, the PID controller positions the bottom endplate to a displacement specified by the user. Thus, researching stress as a function of ϵ.

On a side note: it is interesting to note that displacement control provides full control of position, velocity and acceleration. Thus, allowing to isolate individual components within equation of motion: stiffness, viscosity and inertia. When measuring nonlinear static stiffness curves in sand, loading rates must be slow enough to retain quasi-static response. This can be ensured only by controlling displacement rate (velocity). Beware, F controlled PID does not shy away from increasing displacement rates excessively, if stiffness is lost.

Fig.C.3 shows four specimens, disturbed following different stiffness paths, using frictionless triaxial apparatus. The loading cases demonstrate large deformation amplitudes are applicable in drained and undrained modes. Notice, peak undrained strength remains testable even after fully liquefying a specimen – a recent achievement in triaxial testing. Undrained sand exhibits significantly higher strength than drained sand, even after liquefaction. The extra undrained strength is attributed to pore water stiffness resisting dilation (Ibsen, 1995): water is extremely stiff - u drops as water is pulled apart by volumetric strain of the soil skeleton. As water is pulled apart, σ'_r climbs up the hydrostatic axis. There is a strict limit to how low u can drop, as near absolute vacuum ($\approx -100kPa$) water turns into gas, losing all stiffness. Thus, undrained strength of sand is governed by water cavitation, and $\sigma'_r < \sigma'_{r,max}$ (see Fig.C.4). Undrained specimen with initial u=200 kPa, and Cp=260 kPa, will yield near u=-100 kPa, thus $\sigma'_{r,max} \approx 360kPa$. Cavitation limit serves as a third linear boundary, which, together with Coulomb effective stress limits, shape a closed, triangular, effective stress area within q/p space. The effective stress limits are marked on top of measurement data plotted in q/p space, in Fig.C.4. Note, both drained and undrained specimens yield by crossing the same Coulomb stress envelope, but undrained specimens cross it higher up

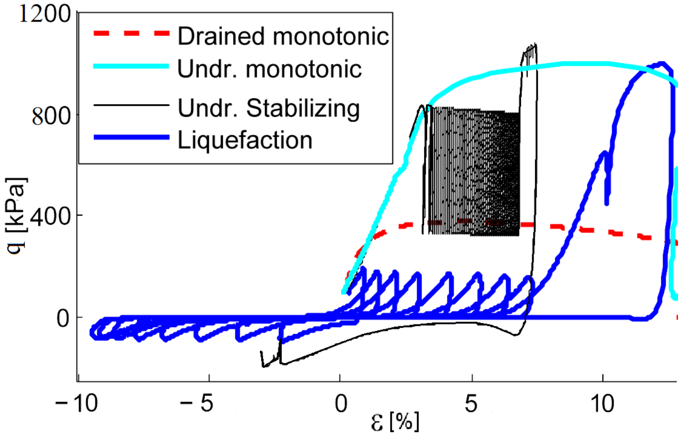

Fig. C.3: (1st-4th specimens) Showing drained and undrained monotonic loading, and one-way, two-way undrained stress cyclic loading. One way loading brings stable state. Two way loading – liquefaction. Note, undrained stable state liquefies instantly if load is reversed (Sabaliauskas and Ibsen (2015)).

the hydrostatic axis after pore water cavitates (Ibsen, 1995).

Figs.C.4-A.5 show a long, multi stage loading history, applied and measured using one specimen (the 5th specimen). Each of the 4 sequences contains the following procedure:

1. 1000 Force controlled of fixed amplitude are applied (1000 is approximately the number of waves encountered during 3 hours of a storm peak in North Sea).
2. After switching to deformation control – specimen axially compressed beyond peak strength and pulled back to initial length.
3. After being pulled back to initial length, specimen is drained consolidated, before re-initiating undrained condition.

In between the stages, attempts were made to "reset" the specimen. Amount of recovery was judged by comparing the stiffness paths generated at each stage. Before sequence 2, specimen was drained for 10 minutes, which is about 20 times longer than u took to catch up to Bp. Before sequence 3, specimen was drained consolidated over night. Before sequence 4, isotropic draining was combined with drained deformation cycles. These 4 sequences were the first attempt to recover a disturbed sand specimen, after noticing a sand specimen is plausible to pull back to initial length, using the frictionless triaxial apparatus. It is important to note, that the very attempt to pull a specimen back to initial length, without producing shear rupture or bulging – is unconventional. Yet, plausible.

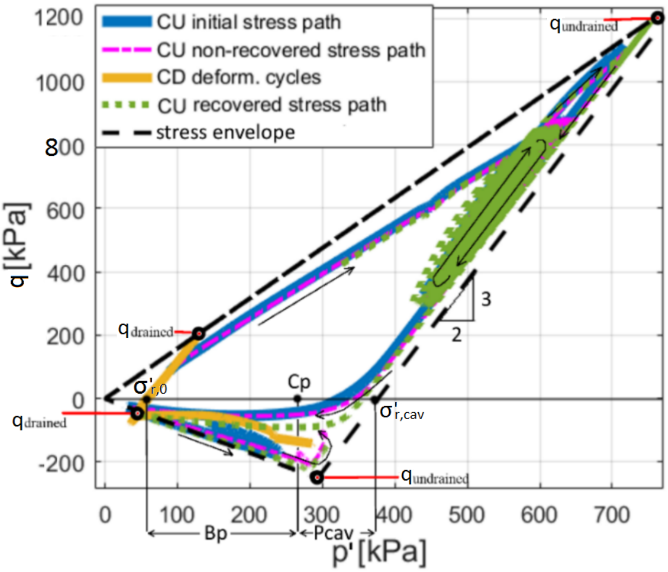

Fig. C.4: (5th specimen) Effective stress history of stages 1, 3, 4 and Drained recovery from Fig.C.5 are plotted. Notice that various ϵ history (Fig.C.5) converges towards similar, overlapping stress paths. Effective stress boundaries, containing Coulomb envelopes and cavitation limit, are shown as well.

Initially, some recovery of undrained sand stiffness was expected after merely draining the specimen, isotopic consolidation. However, drained isotropic consolidation alone did not produce recovery of stiffness or resistance to liquefaction - neither after confining for 10 minutes, nor for 24 hours. Only after some drained deformation cycles were applied, prior to sequence 4 (Fig.C.5), stiffness and resistance to liquefaction were recovered. Deformation cycles stabilized the specimen in 1 hour to a greater degree than 24 hours of drained consolidation. Thus, the role of drained deformation cycles caught attention.

Furthermore, it is curious that each ϵ amplitude creates converging stress paths. Thus, it would make sense to attempt normalizing stress history within a deformation envelope. This could be an interesting branch of testing - deformation dependent disturbed sand properties (as requested by Yoder, 1980).

Stabilizing the specimen

Once undrained sand specimen stiffness recovery was noticed to occur in response to drained deformation cycles, drained testing capabilities of the Danish triaxial apparatus were explored. Cycles of $\epsilon = 15\%$ were found ap-

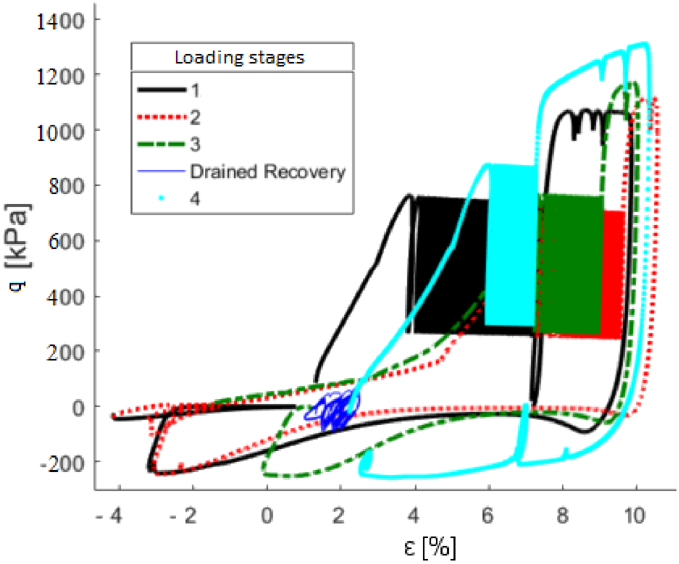

Fig. C.5: (5th specimen) Stiffness history of one specimen, loaded through 4 undrained stages. Specimen was undrained cyclic loaded, compressed and pulled back to initial length 4 times. With drained consolidation before each stage. Notice, stiffness recovery took place only after drained deformation cycle were applied prior to 4th stage (effective stress history given in Fig.C.4, and specimen shape, during 4th testing stage, is shown in Fig.C.2b).

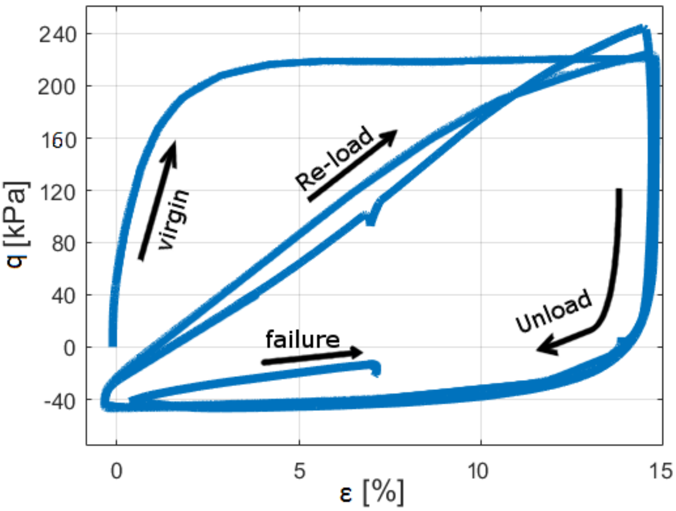

Fig. C.6: (6th specimen). Three drained cycles of 15% deformation amplitude. Notice how re-loading stiffness adapts to deformation amplitude, forming a stiffness triangle.

plicable on drained specimen three times (see Fig.C.6), before specimen lost contact with the top endplate. A triangular stiffness pattern emerged in the process, during unloading / re-loading (cycle 2 and 3). The next (7th) specimen was used to check if similar triangular stiffness pattern would reemerge proportional to a smaller deformation amplitude as well.

The 7th specimen withstood 22 drained cycles of 5% strain. Near constant stiffness was present while density was increasing. Once again, failure was caused by separation of specimen from the top end plate, during pulling. Note, extensions is vividly called "pulling", but the expression "pull" should be understood as: lowering the bottom end plate slowly, slow enough to allow radial stress to squeeze the specimen radially, forcing axial elongation, thus – staying in contact with the end plate being pulled down, slowly. Separation from the end plate can be prevented by slowing down the pull, or even reversing the loading direction if early signs of separation onset are detected by visually inspecting the specimen during real-time testing.

Notice 7th specimen (Fig.C.7) is the first case with volumetric response plotted. It is interesting, how the triangular stiffness pattern retains near constant reloading stiffness while density is increasing. The virgin stiffness path is steeper than the disturbed reloading stiffness, regardless of how dense the disturbed specimen became. Counter intuitively, lower stiffness at higher density is present. Lack of correlation between density and stiffness is perhaps best seen during liquefaction, where a specimen loses stiffness rapidly despite near constant density (as seen in Fig.C.3). Stable stiffness triangle,

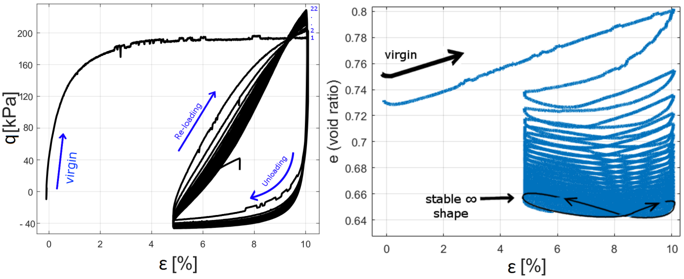

Fig. C.7: (7th specimen). Drained triaxial test of 5% amplitude reaching 22 cycles. Notice stiffness is near constant and converges towards a triangle, while density is increasing. Only strength remains proportional to absolute density.

similar to that observed in Fig.C.7, was detected by Mohkam (1983), but there seem to be no cases of observing properties of the stable stiffness triangle after generating it. The new, unorthodox triaxial tests were designed to scale/reposition, disturb/re-stabilize the stiffness triangle.

The 8th specimen (Fig.C.8) shows 44 cycles of 1% amplitude, followed by compression into 2nd yield, unloading by 3%, and reloading into the 3rd yield. Again, constant stiffness at different densities was observed while comparing stiffness paths leading to 1st and 2nd yield instance. In addition to different stiffness at similar density, while comparing stiffness path leading towards 3rd and 2nd yield. It is surprising how little correlation is present, between stiffness and absolute density. However, correlation between peak strength and density remains strong. Increasing density increases peak yield strength, but not stiffness. This is noticeable in drained and undrained tests alike. Fig 3 shows that the undrained strength is similar in all 3 tests, regardless of stiffness variations caused by cyclic preloading. In Fig 5 the undrained peak strength gradually increased due to the specimen being draining in-between undrained sequences (increasing in density, with each draining instance). Thus, it seems stiffness and strength are not correlated. The two sand properties behave mutually independent. Strength (friction angle) remains proportional to absolute density. Whereas stiffness – to deformation history, and volumetric work increment.

Iterating between stabilizing and disturbing, drained and undrained.

To question disturbed sand stabilization principles observed thus far, attempts were made to manipulate - scale, reposition, disturb and re-stabilize - the stable stiffness triangle more aggressively. The 9th specimen, see (Fig.C.9), was stabilized to three different deformation amplitudes. Notice the sequence of triangle stabilization: triangle A was stabilized first, then triangle B, then C. Thus pushing the triangle back and forth along the ϵ axis. Triangle

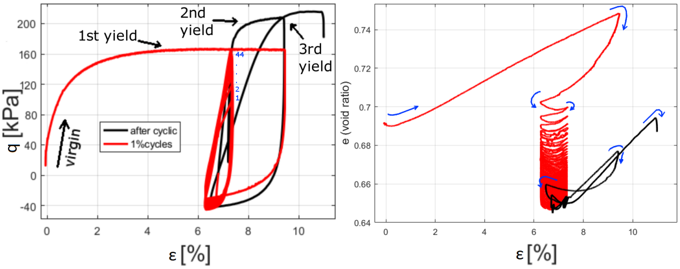

Fig. C.8: (8th specimen). Drained triaxial test, 44 cycles of 1% deformation, continuing into yielding and unloading reloading of 3% deformation amplitude. Notice lower stiffness at higher density is present, before 3rd yield compared to 1st yield.

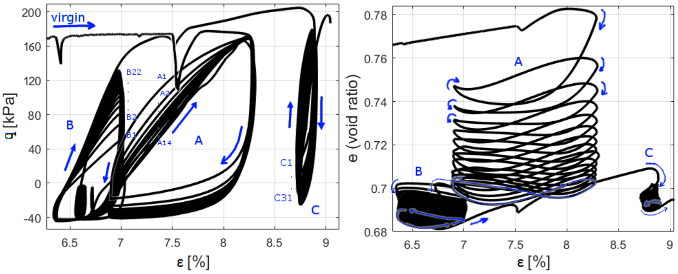

Fig. C.9: (9th specimen) 3 groups of deformation cycles was applied to the specimen. Notice the stiffness triangle develops at each deformation amplitude. In addition, higher reloading stiffness at lower density (and vice versa) can be observed.

A was shaped by 14 cycles, B by 22 cycles, C by 31 cycle. Once again the lack of correlation between absolute density and stiffness can be observed. Note, triangle C looks near elastic, but that is an illusion caused by the triangle developing within narrow deformation amplitude. Moreover, after exiting stage C, the 9th specimen had not failed, and the test continued further. However, later stages become excessively complex very rapidly. Thus, 10th specimen is shown first, to familiarize the reader with an additional procedure, before revealing the conclusive continuation of 9th specimen loading history.

Test sequence executed on the 10th specimen was designed to separate deformation dependent sand properties from stress dependent ones. Stiffness triangle height and length changed proportionally to varying ϵ amplitude and σ_r'values. Thus, the hysteresis loop was plausible to enlarge/shrink (scaled) along ϵ and q axis (one axis at a time). And the hysteresis loop was plausible to reposition left and right on the ϵ axis. Results of 10th specimen testing are shown in Fig.C.10, and results can be summarized as:

- First triangle (reloading stiffness E1) was fully stabilized, and deformation cycle was stopped in the middle of reloading cycle. While holding

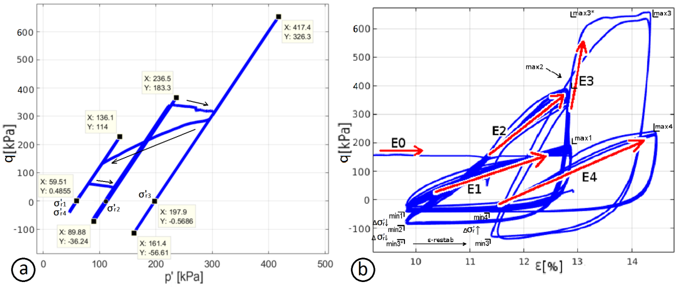

Fig. C.10: (10th specimen) Vector E marks reloading stiffness of 4 stable stiffness triangles. a) Effective stress history applied in the test. b) Stress/strain history. The vector E marks the reloading stiffness of the four stable stiffness triangles shown.

deformation constant, $\sigma'_r, 1$ was increased to $\sigma'_r, 2$ (see Fig.C.10a), and deformation cycles started again. A stable stiffness triangle appeared instantly, fully stabilized towards E2 after first loading cycle.

- Before exiting second stiffness triangle, deformation cycle was stopped at the peak position near point max2 (see Fig.C.10b). While holding ϵ constant, $\sigma'_r, 2$ was increased to $\sigma'_r, 3$. Then, the specimen was compressed, applying ϵ from point max2 to max3.

- Yielding, during compression, disturbed the stiffness triangle. One deformation cycles was applied to probe for reloading stiffness curve of disturbed triangle. The deformation cycle was stopped near point max2. While holding ϵ constant, $\sigma'_r, 3$ was lowered to $\sigma'_r, 4$ (note $\sigma'_r, 4 = \sigma'_r, 1$, Fig.C.10a). Upon resuming deformation cycles, the disturbed triangle continued stabilizing, and converged towards a stable state stiffness $E4$, where $E4 \approx E1$.

In the outcome, during testing of 10th specimen, a stiffness triangle was scaled and repositioned successfully. Disturbed/stable triangle state was not affected by changing σ'_r. Changing σ'_rappears to enlarge/shrink the stiffness triangle instantaneously along the q axis, without altering disturbed soil state produced by deformation history. Notice the points min and max in Fig.C.10b. Each point has two coordinates – q_y and ϵ_y. The yield stress (q_y) is reliably predicted by Coulomb stress limits. Curiously, the yield strain (ϵ_y) coordinate behaves like a strain envelope, enveloping recent deformation history. Request for experimental methods capable of observing ϵ_y was left by Yoder (1980). In his thesis, Yoder derived constitutive formulation of strain-space (ϵ-space) plasticity for cohesionless soils. He noted methods for observing isotropic and kinematic hardening rules for ϵ_y are missing. Note, the triaxial tests were executed without per-exposure to Yoder's work. Thus,

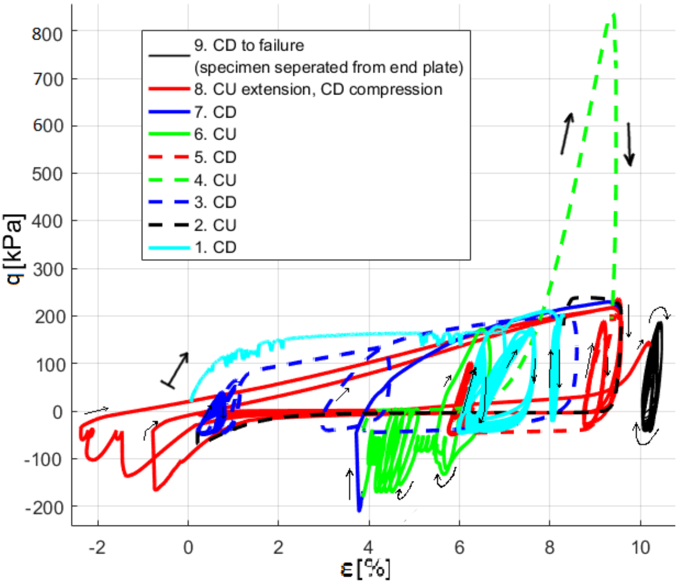

Fig. C.11: Stress/strain loading history of the 9th specimen. Testing sequence of nine stages was applied. Irregular loading was applied using frictionless triaxial apparatus.

Yoder's request was addressed by coincident. Nonetheless, experimental results seem to be best represented by a ϵ_y envelope, defined in ϵ-space.

Using deformation dependent sand properties, specimen durability can be improved. Thus, allowing to execute testing sequences of immense complexity, such as shown in Fig.C.11. It was mentioned earlier, that the 9th specimen survived the three iterations of drained stabilizing. The three triangles visible in Fig.C.9 are the 1st stage in test sequence shown in Figs.C.11-A.12. The 9th specimen was tested through a chaotic mix of consolidated drained (CD) and consolidated undrained (CU) loading stages. The 9 sequences contain the following:

1. CD cyclic loading, three different cycle groups applied (groups A, B and C, from Fig.C.9).
2. CU pull towards the initial length of the sample. u was kept away from cavitation by introducing small liquefaction cycles each time u dropped below 0 kPa (to rise u towards 260 kPa). Cp was held at constant 260 kPa in all stages, during this test.
3. CD stabilizing deformation cycles. Followed by Force controlled stabilizing and displacement controlled compression beyond yielding.
4. CU peak strength test followed by liquefaction.

5. CD cycles – recovering soil stiffness, increasing soil density to non-liquefy-able density.
6. CU force cycles within none-liquefy-able density, near pure dilative state.
7. CD loading, provoking dilation towards liquefiable density.
8. Mixed loading cycle – CU pulling (using liquefaction to preserve specimen during pull), CD compression. The top 1 cm of the specimen began to bulge inwards.
9. CD cycles applied on now deformed specimen. At this point stiffness measurement precision is debatable, but the membranes are intact, specimen remains watertight, thus density change is observed. Reaching non-liquefy-able density once again.

Notice reoccurrence of stiffness triangles in Fig.C.11, and the magnitude of volumetric change in Fig.C.12. Sand was densified towards "non-liquefy-able" soil state, and dilated back to liquefiable density – more than once, in one, continuous loading sequence. Deformation amplitudes beyond 12% were applied repeatedly, in the process. This demonstrates robustness of frictionless triaxial testing. Such complex loading sequence is but a small glimpse at complexity of soil response which can be encountered by an offshore foundation during a storm. Nevertheless, patterns and regularities governing evolution of disturbed sand response, are accessible and can be researched using a frictionless triaxial apparatus.

5 Conclusion

It is worth noting specimens were sieved before and after the tests. No traces of crushing were present (see Fig.C.13), as can be expected with effective confining pressures below $0.9MPa$. Crushing was the first concern raised while presenting the frictionless triaxial testing results in workshops, courses and conferences.

Frictionless triaxial apparatus has unique testing capabilities. Shear rupture is replaced by isotropic yielding, which not only improves measurement precision but specimen durability as well. Therefore, the frictionless triaxial apparatus can explore regions of disturbed soil states inaccessible using conventional equipment. This puts the frictionless triaxial apparatus into a whole new category of testing equipment compatible with complex, irregular, aggressive, long loading sequences – required to research disturbed soil states.

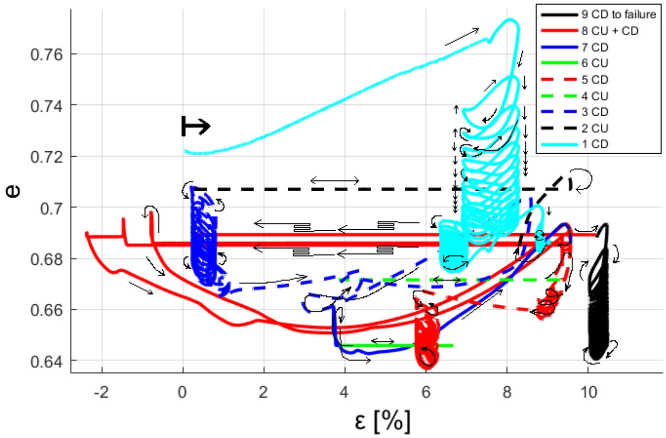

Fig. C.12: Volumetric response history of the 9th specimen. Testing sequence of nine stages was applied. Irregular loading was applied using frictionless triaxial apparatus.

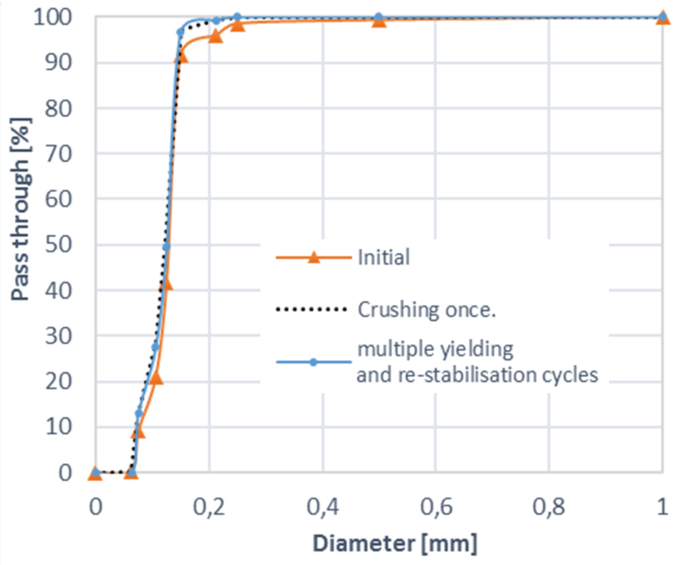

Fig. C.13: Sieving results – even after most aggressive procedures changes in grain diameter were insignificant. Therefore, crushing is not likely to be the cause of mechanical soil properties observed using dynamic frictionless triaxial testing.

A frictionless triaxial apparatus can pull a specimen back to initial length, after measuring peak strength. The disturbed specimen can then be stabilized and re-yielded countless times, all while iterating between drained and undrained loading stages – in one, continuous loading history. This opens a whole new scope of testing. One where sand is not treated as "brittle", "sliding" or "rupturing", but "interlocking" from one disturbed soil state to another (as emphasized by Schofield, 2005). The new scope of testing is potent with new observations, new questions and answers - new knowledge.

At relatively low confining pressures, the specimen were densified to non-liquefiable density, forced to dilate into liquefiable range and re-densified once again. All by using deformation dependent properties. In addition, each drained deformation amplitude has a unique stiffness triangle, but all triangle have similar stress amplitudes. Thus, there seems to be no way of differentiating between triangles by their stress amplitude, they are unique only with respect to deformation amplitude – deformation history.

The reappearing stable stiffness triangle can be normalized conveniently within a strain envelope, such as used in strain-space plasticity formulation derived by Yoder (1980). The unorthodox formulation is fully compatible with Coulomb stress limits. It merely interpolates stresses by using a strain envelope. The strain-space plasticity formulation is not widely known. Thus, it is vital to mention work of Yoder (1980) next to empirical evidence supporting it.

Methodology required for stabilizing a sand specimen is outrageously simple: drained deformation cycles of constant amplitude. A similar stiffness triangle converges within any deformation amplitude. Smaller deformation amplitudes produce triangles with higher stiffness. Larger amplitudes – lower stiffness. Thus, by controlling deformation amplitude, the stiffness triangle can be controlled - resized and repositioned along the ϵ axis. By Varying p' the triangle was scaled along the q axis, isotopically, without affecting disturbed soil state. Therefore, for predicting changes in disturbed soil states, only strain (deformation) history was required.

It is surprising that material as common as sand remains somewhat mysterious to this day. In addition, the testing equipment is old, only the procedure was changed ever so slightly – observing sand as a deformation dependent, rather than stress dependent. Applying deformation cycles rather than stress cycles. The frictionless triaxial apparatus was introduced half a century ago by Bishop and Green (1965). The inventors proposed it as a superior alternative to conventional testing. And still, 50 years later, something new remains to be tested in geotechnics, besides more and more precise measurement.

6 References

Budhu, M. Soil mechanics and foundations, (with cd) 2008.

Damgaard, M., Andersen, L., Ibsen, L.B., Toft, H., Srensen, J., A probabilistic analysis of the dynamic response of monopile foundations: Soil variability and its consequences, Probabilistic Engineering Mechanics 41 (2015)

DiDi Prisco, C.G., Wood, D. M., Mechanical Behaviour of Soils Under Environmentallly-Induced Cyclic Loads, Vol. 534, Springer Science & Business Media, 2012.

Gres S, Fejerskov M, Ibsen LB, Damkilde L. Experimental damping assessment of a full scale offshore mono bucket foundation. Proceedings of Isma2016. 2016

Houlsby GT, Ibsen LB, Byrne BW. Suction caissons for wind turbines. Frontiers in Offshore Geotechnics: ISFOG, Perth, WA, Australia. 2005 Jan 1:75-93.

Ibsen, L.B., “The stable state in cyclic triaxial testing on sand.” Soil Dynamics and Earthquake Engineering, 1994, (13):63–72.

Ibsen, L.B., “The Static and Dynamic Strength of Sand,” presented at the Eleventh European Conference on Soil Mechanics and Foundation Engineering, Copenhagen, 1995 : XI ECSMFE : DGF-bulletin 11, Vol. 6, pp. 69-76.

Jacobsen, M., “A new triaxial apparatus,” Geoteknisk Institut no 27 DGI Bulletin, 1970.

Lade PV. Triaxial testing of soils. John Wiley & Sons; 2016.

Mohkam M. Contribution à letude experimentale et theorique du comportement des sables sous chargements cycliques. Ph.D. thesis; 1983.

Olson RE, Lai J. Apparatus Details For Triaxial Testing. Technical Report; Chaoyang University of Technology; 2004.

Praastrup, U., Jakobsen, K, Ibsen, L.B. On the Choise of Strain Measures in Geomechanics. Technical Report; Geotechnical Engineering Group; 1998.

Rowe, P., Barden, L., “Importance of free ends in triaxial testing,” Journal of the Soil Mechanics and Foundations Division, 1964, 90(1):1–28.

Sabaliauskas, T, Diaz, A.T., Ibsen, L.B., Nielsen, S.D., “Observations during static and cyclic undrained loading of dense Aalborg University sand no. 1.”, Aalborg University, DCE Technical Memorandum, 2014.

Sabaliauskas, T., Ibsen, L.B., “Cyclic Triaxial Loading of Cohesionless Silty Sand,” International Society of Offshore and Polar Engineers, 2015, p. 821–6.

Schofield, A.N., Disturbed soil properties and geotechnical design. Thomas Telford, 2005.

Vardoulakis, I.I., “Bifurcation analysis of the triaxial test on sand samples,” Acta Mechanica, 1979, 32(1-3):35–54.

Yoder, PJ, “A strain-space plasticity theory and numerical implementation”, 1980, EERL 80-07, http://authors.library.caltech.edu/26358/21/8007.pdf,

a Report on Research Concluded Under Grants from National Science Foundation.

Paper D

Deterministic finite-state analysis of disturbed foundation stiffness

Tomas Sabaliauskas, Lars Bo Ibsen

The paper has been submitted to the
Canadian Geotechnical Journal Vol. XX(X), pp. XXX–XXX, 201X.

Abstract

Offshore wind turbines are slender structures, dynamic response of which depends on foundation stiffness. Unfortunately, foundations embedded in sand can become disturbed, their stiffness can increase and decrease episodically. To investigate the phenomenon governing loss and recovery of stiffness, an original testing program was implemented. A prototype of an offshore foundation was repeatedly disturbed and re-stabilized: the stiffness curve generated while testing peak strength was disturbed and reset back to initial state, multiple times, in one loading sequence.

The ability to reset the "initial stiffness path" was achieved after observing a new physical phenomenon: converging Stiffness hysteresis loops. During cycles of constant deformation amplitude, stiffness hysteresis loop were observed to converge in proportion to applied deformation amplitude. Thus, by controlling position and amplitude of deformation cycles, the stiffness hysteresis loops can be "stretched" and "repositioned" along the deformation axis. Therefore, allowing to de-facto control cyclic stiffness of a foundation - to disturb and reset the initial soil state. The observations provide new factual evidence, which suggests some features of cyclic stiffness in sand could be governed exclusively by deformation history. Furthermore, inputs adequate to control a phenomenon in practice, could be adequate to model the phenomenon in theory. Thus, the new observations could be a precursor to a new generation of numerical models.

1 Introduction

Episodic loss and recovery of stiffness is observed in full-scale offshore foundations [27], [9]. Offshore wind turbines are slender structures, resonant frequency of which relies heavily on foundation stiffness. Unfortunately, properties of cyclic loaded sand (therefore foundations embedded in sand) are not well understood [10]. Sand has notoriously non-linear, counter intuitive properties, which arise from the very nature of this material: sand is made of individual grains, that re-arrange and re-interlock, forming complex networks of force chains [37], [6].

The grains of soil do not rearrange if deformation is not present. Deformation is essential for rearranging the grains. It is a common practice to model deformation (U) as a function of Force (F). However, a stiffness curve can be interpreted from two perspectives. U can be seen as a function of F, thus U(F). On the other hand, F can be interpreted as a function of U, thus F(U). Which perspective is correct should be judged by the level of control it provides. If a phenomenon can be controlled by manipulating U input, it would make sense to described it as a F(U) system. The statement is illustrated in Fig.D.1.

To view sand as a deformation dependent material is not a new idea. Liq-

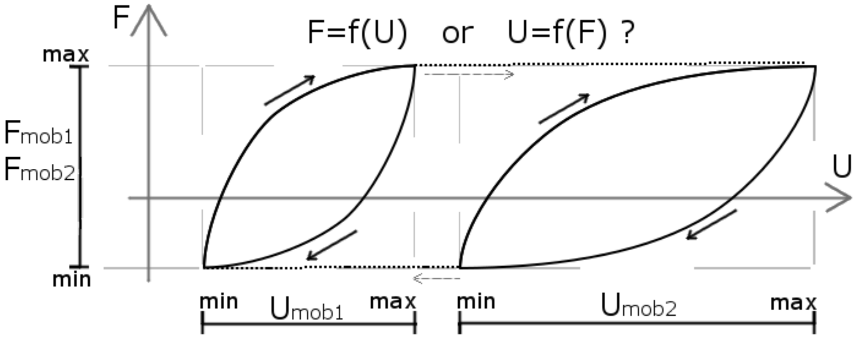

Fig. D.1: A thought experiment, illustrating experimentally observed sand stiffness hysteresis loop behavior. The system can only be uniquely defined as an $F(U)$ system, not $U(F)$. The same *Fmob* is shared by all hysteresis loops, thus it is not plausible to predict which loop is generated if *Fmob* is applied. However, each hysteresis loop has a unique *Umob*, therefore it is plausible to describe, predict and control the hysteresis loop as a function of U, thus supporting the $F(U)$ perspective.

uefaction charts normalized by strain amplitude fit measured data across a larger range and with higher precision than stress normalized charts [2] [12] [11] [34]. However, stress normalized charts are more commonly used, as they are compatible with conventional path of thinking, where loads (stresses) are measured or applied during testing. Many engineering problems are not concerned with post-liquefaction behavior, where strain normalized liquefaction charts are most advantageous. Thus, in cases where it is adequate to merely avoid liquefaction, stress normalized charts can be sufficient. However, offshore wind turbine foundations require to combine both loss and recovery of stiffness, in both drained and undrained loading, as dynamic loads can potentially be rapid enough to cause undrained response or deform thin layers of soil in close proximity to the foundation wall.

It is not common to observe (model or test) sand stiffness as a function of deformation. Only dilation (volumetric response) is normally modeled (and thus tested) as a function of deformation. Liquefaction, in essence, is a phenomenon caused by volumetric contraction, when water is not allowed to drain from the voids. If deformation amplitudes are applied on a drained specimen, then results shown in Fig.D.2 are obtained. The original author of test shown in Fig.D.2 was attempting to quantify volumetric response of a cohesionless soil specimen, while ignoring the stiffness hysteresis loops. However, it is very interesting that, the first stiffness path is curved differently than the or fifth one. While the 2^{nd} and 5^{th} stiffness hysteresis follow a similar looking triangular pattern. Only the peak of the triangle increases as the density increases. Thus, interesting stiffness behavior patterns can be generated using a triaxial apparatus.

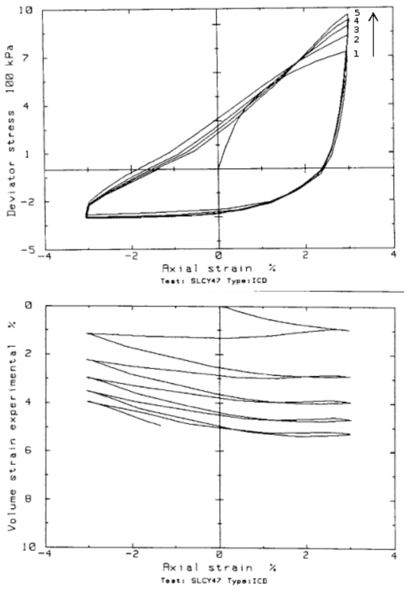

Fig. D.2: Stiffness triangle generated while testing volumetric response [22]

The converging "stable stiffness triangle" (stiffness hysteresis loop in Fig.D.2) was recreated and investigated to a deeper degree recently [35] [36] [41], using a frictionless triaxial apparatus. The recent findings observed causation governing the phenomenon. The new knowledge allows to control stiffness hysteresis loops in sand specimens to an extreme degree. The stiffness hysteresis loop can be pushed left and right along the strain axis. The triangle can be "stretched" and "squeeze" horizontally. The user has full control and can selectively chose the position and inclination of the slope of the stiffness hysteresis loop. Thus, in triaxial testing, a method to de-facto control sand stiffness is already known. Now, a similar procedure is attempted on a prototype of a foundation, embedded is sand. It is interesting how the complex, nonlinear stress and strain fields develop within the soil continuum when deformation cycles are applied on a structure. It can be predicted that, to some degree, during cycles of constant deformation amplitude a foundation prototype should converge towards stable stiffness hysteresis loops similarly as a sand specimen does during triaxial testing. Alas, before executing the tests, it was not clear what stiffness hysteresis loops will be generated by a foundation prototype, and if the properties of these hysteresis loops will be comparable to patterns observed using a frictionless triaxial apparatus.

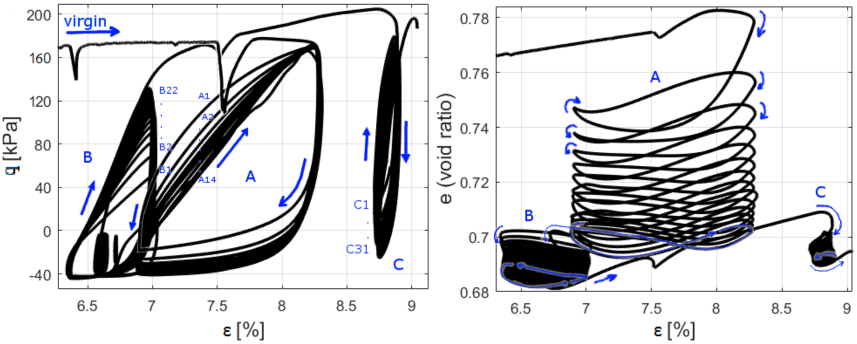

Fig. D.3: Controlling stiffness hysteresis loops during drained frictionless triaxial testing. Three stiffness triangles are allowed to converge at three different deformation amplitudes [41]

2 Equipment

Aalborg University (AAU) geotechnical laboratory has a long history of R&D in geotechnical testing equipment. From frictionless triaxial and consolidation apparatuses [23], to sand boxes recreating water pressures found at the sea floor [25], for testing prototypes of foundations. The sand boxes are used for testing innovative offshore foundation concepts, such as the mono-bucket foundation - an offshore wind turbine foundation, designed to compete with mono-piles. The mono-bucket uses less steel and is installed faster than a mono-pile. Also, installation of the mono-bucket is quiet (no noise mitigation cost), and it can be decommissioned without leaving a footprint (removed by reversing the suction pump, thus pushing the suction caisson out of the sea floor). Research of the mono-bucket is part of M.Sc. and Ph.D. theses at AAU [29] [25]. Consequently, a small scale mono-bucket was readily available for the case study presented in this paper. Schematics of the testing rig and the mono-bucket used are given in Fig's.D.4 and D.5.

The testing rig (Fig.D.4) contains a sand box inside a pressure chamber. The pressure chamber allows to generate pore water pressures found at the sea floor. $200kPa$ pressure is used to imitate $20m$ water head. Pressurizing the water is important for undrained soil response, encountered during rapid (impact) loading. If sand is deformed fast, the pore water cannot escape, thus the volume of voids becomes "locked" by pore water stiffness in undrained mode. This makes dilative sand (and structures embedded in it) much stronger and resistant to impact loads [45], [29]. The benefit of increased peak strength is counter balanced by the potential of losing stiffness due to liquefaction. Especially during two-way cyclic loads [34], [35]). The additional undrained strength component is called "the boot effect" [25]. The name illustrates the fact that, to pull a boot out of mud one has to pull slowly

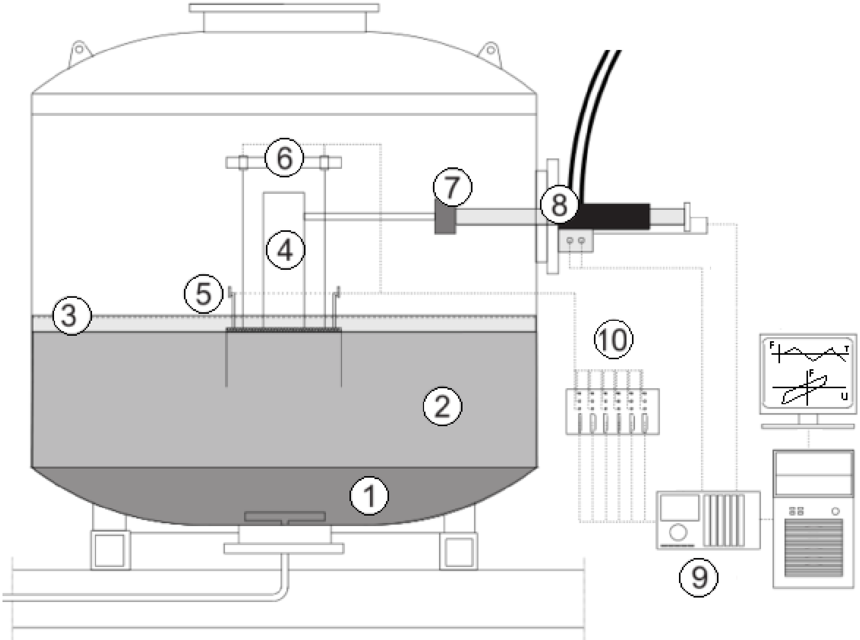

Fig. D.4: The testing-rig. A sand box within a pressure chamber, for small scale foundation testing. 1) Bottom layer of soil is gravel. It acts as a filter for drainage tubes. 2) Aalborg University sand No.1. 3) Water head above soil level. The soil is fully saturated at all times. 4) The monobucket, attached to a shaft. 5) Valves and warer pressure transducers, measuring water pressure along the skirt, and below the lid. 6) Displacement transducers. A total of three displacement are measured. 7) A load cell, measuring focre. 8) A high pressure, digital walve controolled piston. 9) MOOG controller / data logger, with automated load control and realt ime data plotting options. 10) MGC plus data acquisition box [29]

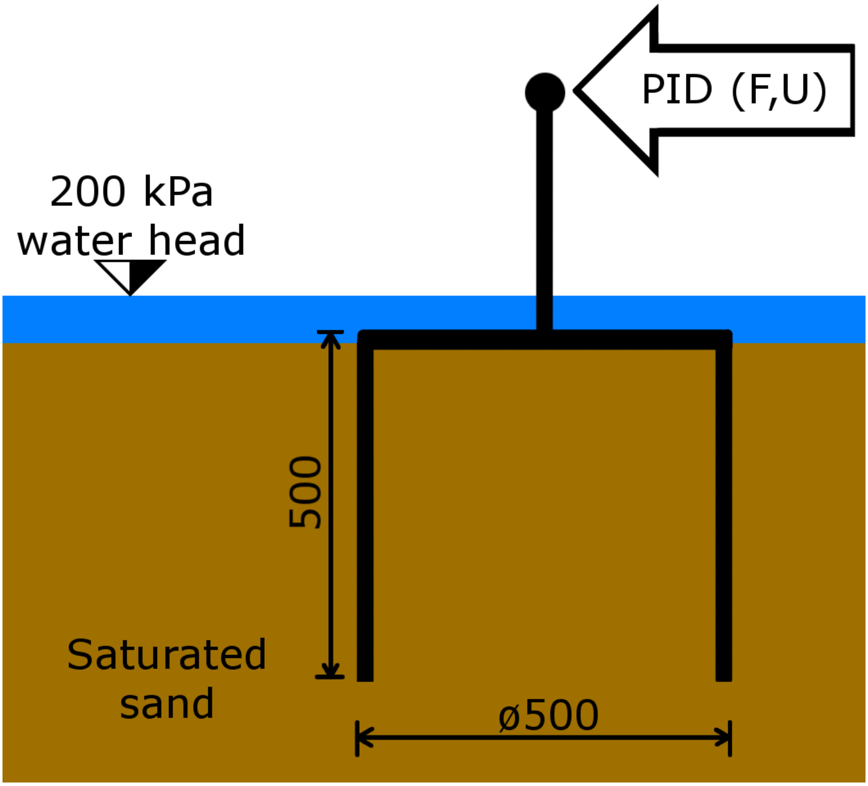

Fig. D.5: The small scale mono bucket foundation is inserted in fully saturated sand. Either force or displacement can be applied horizontally on the top tip of the shaft. The testing rig is placed within a pressurized chamber, where 200 kPa pressure is applied to imitate 20 m water depth. The extra pore pressure is important for increasing dynamic peak strength [29], [45], [19]

.

- fast loads generate additional pore water pressures, which add resistance. In deep water the high water pressure amplifies the boot effect, thus the boot effect is especially relevant for deep water foundations [21] [45]. For this reason, the test shown here were executed with $200kPa$ overhead pressure. In the case study presented in this paper, the boot effect is part of the dynamic stiffness hysteresis loops which are repeatedly disturbed and recovered.

In the testing rig (Fig:D.4) a mono-bucket prototype embedded in sand is shown. A simplified schematic of the test is given in Fig.D.5. The foundation has a large diameter lid, with a skirt along the periphery. The large diameter skirt provides leverage, which makes skirt friction more efficient at resisting overturn moment. While the lid provides a large surface for distributing the vertical load (static weight of a wind turbine). Thus, the mono bucket combines the benefits of both gravity and skirted foundation, by distributing the vertical load across a large surface area, while the skirt is optimized to resist overturning. Together, the two components form a water tight caisson, which traps a large mass of soil and water. Thus adding mass and stability. In addition, there is no need for scour protection, as the lid itself protects against scour [40]. The prototype in Fig.D.5 is Ø500 mm in diameter, and 500 mm in height. The skirt is 6 mm thick. There is one horizontal hydraulic piston attached at the top of the shaft (the shaft is 300mm long). The hydraulic piston is controlled by proportional-integral-derivative (PID) controller, with a load cell and a displacement transducer attached to the piston.

when compared to pile foundations, the mono-bucket is cheaper (less metal consumption), faster to install, easier to decommission (potentially reusable), and there are no added costs associated with noise mitigation or scour protection. Alas, despite the benefits, the mono-bucket is a novel concept, which means higher risk factors for potential investors. The uncertainty comes largely because dynamic loaded sand properties are not well understood [10], and performance of the mono bucket depends on a complex array of phenomenon combining drained, undrained and partially drained soil response. The novel testing procedures described in this paper are part of effort to remove uncertainties associated with novelty.

3 Methods

The testing equipment is rather simple - a hydraulic piston pushing / pulling a foundation at the tip of the shaft. The hydraulic piston applies the "inputs" applied, while the foundation generates the "outputs" measured. The equipment is simple in construction, but the prototype generates complex, nonlinear outputs. To reduce complexity of analysis, the problem is reduced to a minimum number of variables - stiffness is observed by plotting F output generated while applying U input, at the tip of the shaft. This is different from done by previous researchers [28] [29] [25] [45] , as conventionally the opposite path of control is assumed (normally F is the input, U - the output). Here, however, instead of measuring U accumulated in response to F cycles, an attempt is made to observe and control stiffness hysteresis loops as functions of U history. This is an attempt to look for stiffness properties dependent on U history, to control F history as a function of U history.

As mentioned in introduction, the idea of using U as the input was inspired by recent success of controlling stiffness hysteresis loops in triaxial testing. Alas, additional theoretical justification can be given. Equation of motions says $F = K \cdot U + C \cdot \frac{\delta U}{\delta t} + M \cdot \frac{\delta^2 U}{\delta t^2}$. Thus, by applying F three nonlinear components are provoked - nonlinear $K \cdot U$, nonlinear $C \cdot \frac{\delta U}{\delta t}$, and nonlinear $M \cdot \frac{\delta^2 U}{\delta t^2}$. This means that, by using F as the input, the output is encrypted under three layers of nonlinear functions, which makes it hard to decipher the equation of motion. If F was used as the input, $K = U^{-1} \cdot [F - \frac{\delta U}{\delta t} \cdot C - \frac{\delta^2 U}{\delta t^2} \cdot M]$ would have to be solved, but at the beginning all three: K, C and M are unknown, nonlinear functions.

On the other hand, when U is the input, it is applied while controlling $\frac{\delta U}{\delta t}$ and $\frac{\delta^2 U}{\delta t^2}$. Therefore, $\frac{\delta U}{\delta t} \rightarrow 0$ can be applied, thus canceling $C \cdot \frac{\delta U}{\delta t} \approx 0$. Also $\frac{\delta U}{\delta t}$ input can be set to a speed where $\frac{\delta^2 U}{\delta t^2} \approx 0$. Thus, allowing to isolate $F = U \cdot K$, which allows to analyze state dependencies of quasi-static $K = \frac{F}{U}$. Then, if quasi-static K is understood, the loading rate could be increased to $C \cdot \frac{\delta U}{\delta t} \not\approx 0$, thus $C = \frac{\delta t}{\delta U}[F - K \cdot U]$ could be observed. Therefore, using U as the input has the potential to observe one nonlinear component at a time, and decode the entire nonlinear equation of motion. For reasons given, U is interesting to use as the input, while treating F as the output.

While applying deformation cycles in triaxial testing, a new phenomenon was observed - the "stable stiffness triangle" [35] [36] [41]. The phenomenon allows to describe, predict and prescribe the size and position of converging stiffness hysteresis loops. The novel method of executing a test attempts to observe and test the fundamental features governing shape and position of stiffness hysteresis loops. It was noticed that, if *Umob* amplitude or position is changed, the stable stiffness hysteresis loop readopts to fit within the new *Umob* amplitude. Thus, stiffness hysteresis loops can be quantified, predicted and controlled by controlling the amplitude and position of *Umob*. Now, the principle is attempted to apply on a foundation prototype. *U* cycles of amplitude *Umob* are applied at the tip of the shaft, and patterns governing stiffness hysteresis loops are observed (see Fig's. D.6, D.7).

4 Results

It is interesting that stiffness hysteresis loops converge towards the same *Fmob* amplitude, when *Umob* amplitude is changed (illustrated in Fig.D.1). This is an interesting property, it allows to make a deductive conclusion: *Umob* is not predictable as a function of *Fmob* (observing *Fmob* is inadequate to predict *Umob*). Hysteresis loops can be uniquely quantified, predicted and controlled only if *Fmob* is treated as a function of *Umob*. This conclusion is proved experimentally by tests shown in Fig's. D.6 and D.7.

If *Umob* amplitude is made smaller, the *Fmob* limits gradually recover within the smaller *Umob* amplitude (see Fig.D.6). Similarly, if *Umob* amplitude is increased, the *Fmob* gradually drops towards previous *Fmob* limits (see Fig.D.7). In both cases, the hysteresis loops converge towards the same *Fmob* limits "min" and "max", but given smaller *Umob* amplitude the hysteresis loop is steeper (higher stiffness), while larger *Umob* amplitudes produce a hysteresis loop stretched across a larger deformation amplitude, thus re-

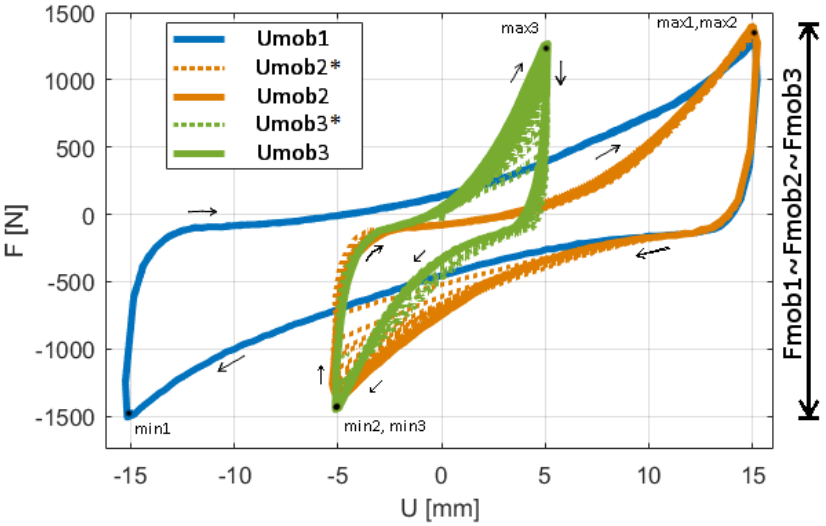

Fig. D.6: Deformation cycles transitioning from bigger to smaller *Umob*. Notice, all *Umob* converge to similar *Fmob* amplitudes.

ducing overall stiffness. Therefore, stiffness of cyclic hysteresis loops can be controlled by controlling *Umob* amplitude.

Furthermore, after the stiffness hysteresis loop converges, the exit path follows a tangent trajectory. This is visible in Fig.D.7, where the stiffness path exiting point *max*1 is marked "exit". Judging by this observations, stiffness hysteresis loops stabilized using smaller *Umob* will have a steeper exit path. To test this hypothesis, three stable states were generated at different *Umob* amplitudes. The stable states were then paused at the same phase of a deformation cycle, and the "exit" paths were tested. As expected, the smaller the *Umob* the steeper the exit path.

If the "exit" stiffness path depends on amplitude of *Umob*, then the initial stiffness path could be recovered by applying gradually smaller *Umob*, until the "initial" stiffness fully recovers. This assumption was tested, and the result is plotted in Fig.D.9. The "initial stiffness path" was reset 5 times in one loading history. The result is compared with preexisting research of mono-bucket foundation (the "original" path in in Fig.D.9 [25], [29]). It is interesting to compare "reset" stiffness paths with the "original" for two reasons. Firstly, this proves validity of assumptions derived from observations. Both stiffness and strength of dynamic loaded foundation are recovered in comparison to pre-existing results. Secondly, because the "original" and "reset" foundation behave somewhat equivalent, the new method of could be used to improve the "original" test preparation procedure.

In Fig.D.9 the "original" stiffness path was generated by following a la-

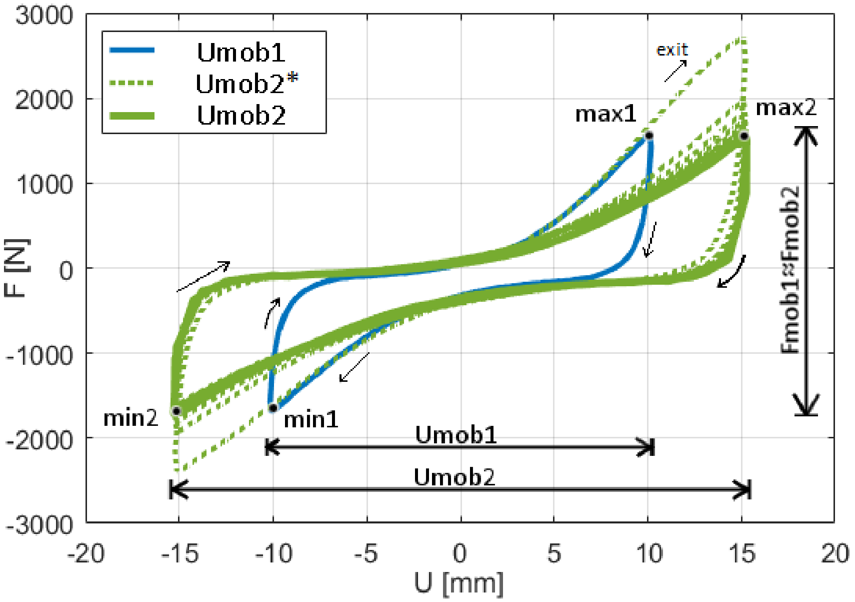

Fig. D.7: Deformation cycles transitioning from smaller to bigger $Umob$. Notice, both $Umob$ converge to similar $Fmob$. Upon exiting $Umob1$, the tangent stiffness path shoots above the $max1$. But F at $max2$ stabilizes equivalent to F at $max1$.

bor intensive procedure, where the foundation prototype is removed using a crane, then a vertical water pressure gradient is applied loosen up the soil. Then the soil is vibrated using an industrial vibrator and CPT tested to check if CPT results are uniform across the entire sand box. The foundation prototype is then pushed back into the sand, cyclic loaded with small force amplitudes to emulate stabilization caused by small waves. And then the peak strength is tested. Thus, the "original" stiffness path takes 2 days of preparation, but the test itself takes just a few seconds. The new method of "reseting" could allow to test peak strength five times in less than two hours, thus greatly improving efficiency of gathering data. Furthermore, by eliminating manual labor, the testing procedure could be made fully autonomous. An algorithm can monitor formation of stable stiffness hysteresis loops, and execute pre-programmed loading sequences which reset the foundation prototype in between testing cyclic response. Thus, the new findings have great potential for direct application in research and development.

The converging hysteresis loops shown thus far were all generated at $\omega = 0.1Hz$ deformation frequency (using triangular sawtooth wave as U input). The triangular sawtooth wave has a constant $\frac{\delta U}{\delta t}$ between the peaks. Thus, when $\omega \rightarrow 0Hz$, then $\frac{\delta U}{\delta t} \rightarrow 0$. In methodology section, U was declared as input for this very reason - U can be applied increasingly slower, to a point

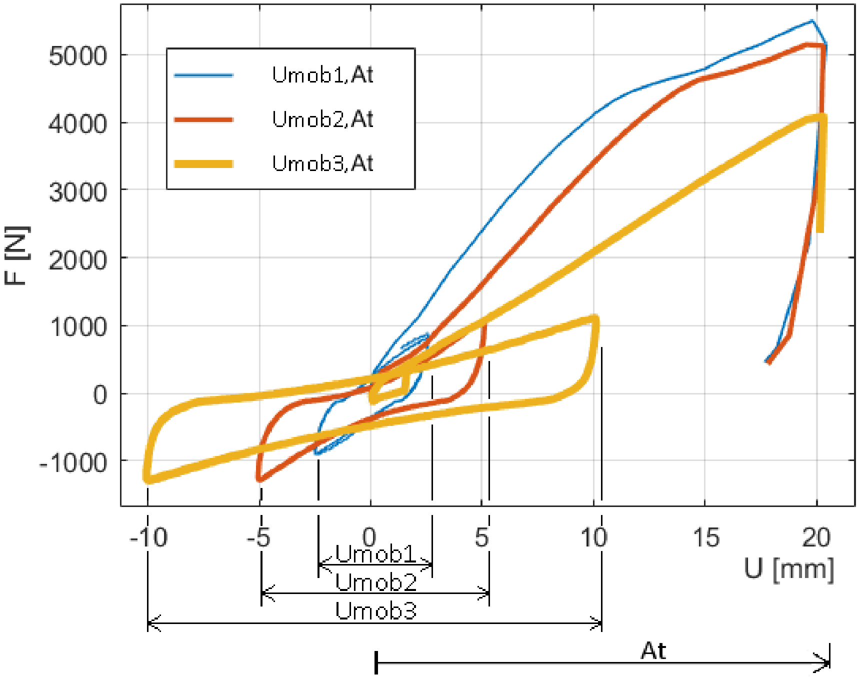

Fig. D.8: Three exit paths, measured after stabilizing three different stable states, at three different *Umob*. Note, *At* amplitude here is reduced to 20 mm. The state transition diagram is deduced to represent the general case.

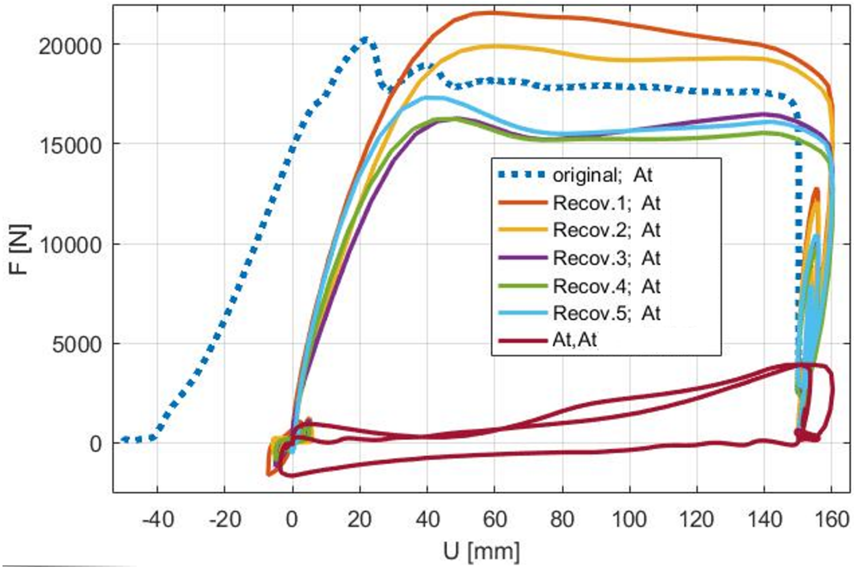

Fig. D.9: A test showing recovery of initial stiffness path (thus initial soil state *So*). The initial stiffness path was recovered 5 times in one loading history. Test result is compared with the "original" stiffness path published in preceding research [29].

where $\frac{\delta U}{\delta t} \approx 0$, thus canceling $C \cdot \frac{\delta U}{\delta t}$ effects from equation of motion. If the assumption holds true, there should be a loading rate where quasi static K is detected. Once $\frac{\delta U}{\delta t} \approx 0$, further reduction of $\frac{\delta U}{\delta t}$ will not produce detectable changes in cyclic stiffness hysteresis loop. The test in Fig.D.10 confirms the assumption.

As expected, by slowing down ω the converging stiffness hysteresis loop converge towards a quasi-static pattern. After $\omega < 0.001Hz$, further reduction did not produce change in the stiffness hysteresis loop. Therefore, deviation from hysteresis loop observed at $\omega > 0.001Hz$ can be attributed to $C \cdot \frac{\delta U}{\delta t}$ effects, potentially caused by pore water pressure gradients (partial liquefaction, and boot effect). Exposed to deformation, sand expands and contracts - the faster the deformation, the less time for water to drain, thus pore water pressure gradients are generated. Because these effects depend on the loading rate, they can be attributed to the C component in the equation of motion.

The quasi-static K stiffness path, observed at $\omega < 0.001Hz$ is very interesting, as it behaves like the back bone of soil fabric. The C component merely causes deviation from the quasi-static hysteresis loop. Comparing the stiffness paths in Fig.D.10 it is visible that hysteresis loops at $\omega > 0.001Hz$ can push the curve above and below the quasi-static K equilibrium. When the stiffness path moves towards $F = 0$, the deviation can be attributed to con-

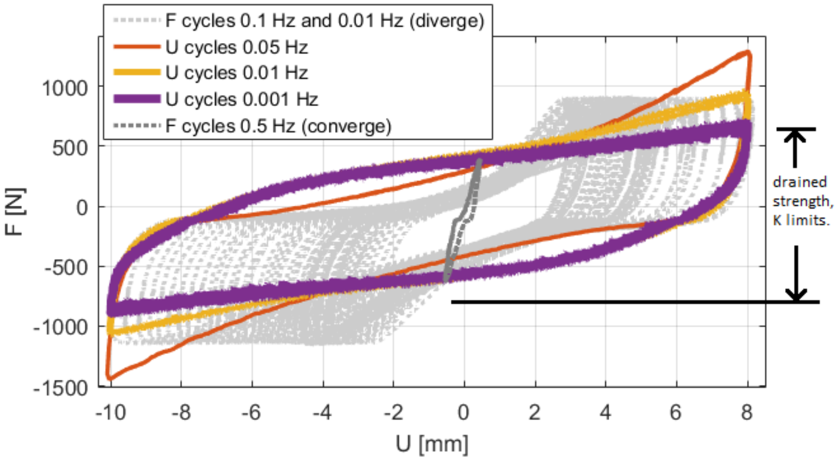

Fig. D.10: Stable state stiffness hysteresis loops, generated at varying loading frequencies. triangular sawtooth wave creates constant $\frac{\delta U}{\delta t}$ when U is the input. When F amplitude is input, $\frac{\delta U}{\delta t}$ is not controlled, hence C dependent deviation from static K is amplified.

traction (partial liquefaction, loss of stiffness). The part of the path reaching beyond quasi static hysteresis loop, can be attributed to dilation (boot effect, increase in peak strength and stiffness). Thus, providing new insights in the workings of nonlinear K and C functions describing a mono-bucket foundation.

At this point it is evident, that some stiffness patterns are governed exclusively by $Umob$. The input allows to scale and reposition converging stiffness hysteresis loops generated by a cyclic loaded foundation prototype. Alas, the patterns generated using $Umob$ provide new insights for calibrating F based solutions as well. If $Fmob$ is applied as the input, within the quasi-static "drained strength K limits", the resulting $Umob$ output converge towards $Umob \approx 1mm$ amplitude. Thus, there is a $Umob$ amplitude towards which $Fmob$ cycles converge, within the constraints of quasi-static K hysteresis loop. The pattern converges regardless of relatively fast deformation frequency (0.5Hz in Fig.D.10).

On the other hand, $Fmob$ cycles reaching beyond quasi-static drained strength K limits are not stable (see Fig.D.10). When $Fmob$ amplitude reaches beyond quasi static hysteresis loop, $Umob$ diverges towards infinite. Curiously, the slower the loading cycles, the faster the deformation accumulates. $Fmob$ cycles applied at 0.1Hz accumulate $Umob$ in smaller increments than than 0.01Hz cycles do. This supports the assumption that C component is caused by pore water gradient, the boot effect relies on negative pore pressure generated in dilating state. Because the system is partially drained, slow loading frequencies provide more time for water seepage. Thus, the system behaves like a linear damper - providing less resistance at lower loading frequencies.

Finally, notice how the stiffness hysteresis loops generated by *Fmob* (Fig.D.10) are notably more curved than those shaped during *Umob* cycles. This is because $\frac{\delta U}{\delta t}$ is not limited while *Fmob* is applied. At times of low stiffness, large $\frac{\delta U}{\delta t}$ velocity accumulates, thus amplifying the effects of the $C \cdot \frac{\delta U}{\delta t}$ component, consequently amplifying the curved deviation from quasi-static K loop.

5 Discussion and conclusion

Using *Umob* (or U) as the input, converging stiffness hysteresis loops were scaled and repositioned. Methods adequate to control a phenomenon, could be adaquate to model it. Thus, the mono-bucket foundation could benefit from being modeled as an $F(U)$ system. Stable state hysteresis loops preserve their overall shape by stretching and squeezed within *Umob* amplitude. This type of behavior can be accounted for by using a deformation envelope. Just like stress (or force) envelopes, deformation (or strain) envelopes can be used in modeling. A potentially compatible constitutive formulation for strain-space plasticity is readily available [44]. Strain-space formulation is interesting not only for its new found compatibility with experimental evidence, but it has substantial computation benefits as well: fewer matrix inversions, reduced return mapping computation cost. Albeit principles of strain-space plasticity are not widely used in geotechnical paradigm, there are ample examples of strain-space (stress relaxation) models outside the geotechnical paradigm. For example: behavior of cracking concrete [13], human bone fractures [31] and aeronautic aluminum [44] had been successfully modeled by using strain-space (stress relaxation) envelopes.

In dynamic simulations of offshore wind turbines, the entire equation of motion has to be accounted for. It is not enough to solve for static equilibrium. Damping effects are crucial for preserving stability of the slender structures [9]. Thus, the entire equation of motion - static, viscous and inertia component - need to be accounted for. For foundations embedded in sand, each component within the equation of motion behaves like a nonlinear function: quasi-static stiffness hysteresis loops move and stretch, dilation / contraction rates change, and mass (density) of sand keeps changing as well. Experimental evidence given in this paper provides practical guidelines on how to isolate each component within the nonlinear equation of motion. The existence of quasi static stiffness hysteresis loop K is shown, which allows to isolate and observe properties the C component as the next step. This opens a new branch of testing procedures which can potentially lead to a new generation of models.

The findings do not follow convention, bu the proof is demonstrated experimentally. Inputs adequate to control a phenomenon in practice, should be adequate to model in theory. What is understood - is controlled. The authors demonstrate how to selectively chose the position and inclination of stiffness hysteresis loops. The initial stiffness path is recovered by manipulating the "memory" of the soil grain structure. A stiffness path equivalent to initial stiffness path was disturbed and recovered 5 times in one loading sequence. This conclusively demonstrates the descriptive, predictive and prescriptive power delivered by the new facts and conclusions described in this paper.

References

[1] Trial installation: Uk north sea. [Online]. Available: http://universal-foundation.com/case-studies/trial-installation-campaign/

[2] K. H. Andersen and T. Berre, “Behaviour of a dense sand under monotonic and cyclic loading comportement d’un sable dense sous chargement monotonique et cyclique,” in *Geotechnical Engineering for Transportation Infrastructure: Theory and Practice, Planning and Design, Construction and Maintenance: Proceedings of the Twelfth European Conference on Soil Mechanics and Geotechnical Engineering, Amsterdam, Netherlands, 7-10 June 1999*, vol. 2. CRC Press, 1999, p. 667.

[3] D. N. V. AS, “Design of offshore wind turbine structures,” Internet Requests for Comments, DET NORSKE VERITAS AS, OFFSHORE STANDARD DNV-OS-j101, May 2014. [Online]. Available: ttp://www.dnv.com

[4] A. Bird, “Thomas kuhn,” in *The Stanford Encyclopedia of Philosophy*, fall 2013 ed., E. N. Zalta, Ed., 2013.

[5] A. W. Bishop and G. E. Green, “The influence of end restraint on the compression strength of a cohesionless soil,” *Geotechnique*, vol. 15, no. 3, pp. 243–266, 1965.

[6] M. Budhu, “Soil mechanics and foundations, (with cd),” 2008.

[7] C. R. I. CLAYTON, M. STEINHAGEN, H. M. STEINHAGEN, W. POWRIE, K. TERZAGHI, and A. W. SKEMPTON, “Terzaghi’s theory of consolidation, and the discovery of effective stress. (compiled from the work of k. terzaghi and a.w. skempton).” *Proceedings of the Institution of Civil Engineers - Geotechnical Engineering*, vol. 113, no. 4, pp. 191–205, 1995. [Online]. Available: http://www.icevirtuallibrary.com/doi/abs/10.1680/igeng.1995.28015

[8] C. A. Coulomb, *Essai sur une application des règles de maximis & minimis à quelques problèmes de statique, relatifs à l'architecture*. De l'Imprimerie Royale, 1776.

[9] M. Damgaard, L. Andersen, L. Ibsen, H. Toft, and J. Sørensen, "A probabilistic analysis of the dynamic response of monopile foundations: Soil variability and its consequences," *Probabilistic Engineering Mechanics*, vol. 41, p. 46–59, 2015.

[10] C. G. Di Prisco and D. M. Wood, *Mechanical Behaviour of Soils Under Environmentallly-Induced Cyclic Loads*. Springer Science & Business Media, 2012, vol. 534.

[11] R. Dobry and T. Abdoun, "Cyclic shear strain needed for liquefaction triggering and assessment of overburden pressure factor k σ," *Journal of Geotechnical and Geoenvironmental Engineering*, p. 04015047, 2015.

[12] ——, "An investigation into why liquefaction charts work: A necessary step toward integrating the states of art and practice," in *Proc., 5th Int. Conf. on Earthquake Geotechnical Engineering*. Chilean Geotechnical Society Santiago, Chile, 2011, pp. 13–44.

[13] A. M. Farahat, M. Kawakami, and M. Ohtsu, "Strain-space plasticity model for the compressive hardening-softening behaviour of concrete," *Construction and Building Materials*, vol. 9, no. 1, pp. 45 – 59, 1995. [Online]. Available: http://www.sciencedirect.com/science/article/pii/095006189592860J

[14] A. Foglia, "Bucket foundations under lateral cyclic loading: Submitted for the degree of doctor of philosophy," Ph.D. dissertation, Denmark, 2015.

[15] Z. Gao and J. Zhao, "Strain localization and fabric evolution in sand," *International Journal of Solids and Structures*, vol. 50, no. 22, pp. 3634–3648, 2013.

[16] G. W. E. C. (GWEC). (2017) Market forecast for 2017-2021. [Online]. Available: http://www.gwec.net/global-figures/market-forecast-2012-2016/

[17] S. Iai, Y. Matsunaga, and T. Kameoka, "Strain space plasticity model for cyclic mobility," *Soils and Foundations*, vol. 32, no. 2, pp. 1–15, 1992.

[18] L. B. Ibsen, "The stable state in cyclic triaxial testing on sand," *Soil Dynamics and Earthquake Engineering*, no. 13, pp. 63–72, 1994.

[19] L. Ibsen, *The Static and Dynamic Strength of Sand*. Geotechnical Engineering Group, 1995, pDF for print: 11 pp. Published in: Proceedings of the Eleventh European Conference on Soil Mechanics and Foundation Engineering, Copenhagen, 1995 : XI ECSMFE : DGF-bulletin 11, Vol. 6, pp. 69-76.

[20] W. Kirkpatrick, "Influence of end restraint on strain distributions in the triaxial compression test," in *Proc. Geotechnical Conf. Oslo*, vol. 2, 1967.

[21] B. S. Knudsen, M. U. Østergaard, and L. B. Ibsen, "Small-scale testing of bucket foundations in sand," Department of Civil Engineering, Aalborg University, Tech. Rep., 2013.

[22] M. Mohkam, "Contribution à l'étude expérimentale et théorique du comportement des sables sous chargements cycliques," Ph.D. dissertation, 1983.

[23] J. Moust, *A new triaxial apparatus*. Copenhagen, Geoteknisk Institut, 1970, vol. 27.

[24] G. Nicolai and L. Ibsen, *Response of monopiles under cyclic lateral loading in sand*. EWEA, 2015.

[25] S. D. Nielsen, "Transient monotonic and cyclic load effects on mono bucket foundations," Ph.D. dissertation, Aalborg Universitetsforlag, 2016.

[26] S. K. Nielsen, A. Shajarati, K. W. Sørensen, and L. B. Ibsen, "Behaviour of dense frederikshavn sand during cyclic loading," Department of Civil Engineering, Aalborg University, Tech. Rep., 2012.

[27] S. Nielsen, L. Ibsen, and S. Gres, "Cost-effective mass production of mono bucket foundations," 2015, pO: 242.

[28] S. Nielsen and L. Ibsen, "The offshore bucket trail installation," 2015.

[29] S. Nielsen, L. Ibsen, and B. Nielsen, *Dynamic behaviour of mono bucket foundations subjected to combined transient loading*. C R C Press LLC, 2015, vol. 1, pp. 313–318, 978-1-138-02848-7 (set of two volumes hardback + CD-Rom) 978-1-138-02850-0 (Volume1+ CD-Rom) 978-1-138-02852-4 (Volume 2) 978-1-315-67551-0 (ebook PDF).

[30] R. E. Olson and J. Lai, "Apparatus details for triaxial testing," Chaoyang University of Technology, Tech. Rep., 2004.

[31] P. Pankaj and F. E. Donaldson, "Algorithms for a strain-based plasticity criterion for bone," *International journal for numerical methods in biomedical engineering*, vol. 29, no. 1, pp. 40–61, 2013.

[32] U. Praastrup, K. Jakobsen, and L. B. Ibsen, "On the choise of strain measures in geomechanics," Geotechnical Engineering Group, Tech. Rep., 1998.

[33] P. Rowe and L. Barden, "Importance of free ends in triaxial testing," *Journal of the Soil Mechanics and Foundations Division*, vol. 90, no. 1, pp. 1–28, 1964.

[34] T. Sabaliauskas, A. T. Diaz, L. B. Ibsen, and S. D. Nielsen, "Observations during static and cyclic undrained loading of dense aalborg university sand no. 1," Aalborg University, DCE Technical Memorandum, Tech. Rep., 2014.

[35] T. Sabaliauskas and L. Ibsen, *Cyclic Triaxial Loading of Cohesionless Silty Sand*. International Society of Offshore and Polar Engineers, 2015, pp. 821–826.

[36] T. Sabaliauskas, L. B. Ibsen *et al.*, "Triaxial testing beyond yielding," in *The 27th International Ocean and Polar Engineering Conference*. International Society of Offshore and Polar Engineers, 2017.

[37] A. N. Schofield, *Disturbed soil properties and geotechnical design*. Thomas Telford, 2005.

[38] D. Sheng, B. Westerberg, H. Mattsson, and K. Axelsson, "Effects of end restraint and strain rate in triaxial tests," *Computers and Geotechnics*, vol. 21, no. 3, pp. 163–182, 1997.

[39] W. Shockley and R. Ahlvin, "Nonuniform conditions in triaxial test specimens," in *Research Conference on Shear Strength of Cohesive Soils, ASCE, Boulder, Colo*, 1960, pp. 341–357.

[40] I. Stroescu and P. Frigaard, *Scour properties of mono bucket foundation*. C R C Press LLC, 2016, pp. 335–341.

[41] S. Tomas and I. Lars, Bo, "The new scope of frictionless triaxial apparatus – disturbed sand testing," *Geotechnical testing journal*, vol. 42, no. 1, 2019.

[42] I. I. Vardoulakis, "Bifurcation analysis of the triaxial test on sand samples," *Acta Mechanica*, vol. 32, no. 1-3, pp. 35–54, 1979.

[43] D. M. Wood, *Geotechnical modelling*. CRC Press, 2003, vol. 1.

[44] P. J. Yoder, "A strain-space plasticity theory and numerical implementation," no. EERL 80-07, August 1980, a Report on Research Concluded Under Grants from National Science Foundation. [Online]. Available: http://authors.library.caltech.edu/26358/1/8007.pdf

[45] J.-H. S. Yun Wook Choo, Tae-Woo Kang, "Centrifuge study on undrained and drained behaviors of a laterally loaded bucket foundation in a silty sand," in *Proceedings of the Twenty-fifth (2015) International Ocean and Polar Engineering Conference*. International Society of Offshore and Polar Engineers (ISOPE), 2015, pO: 963.

[46] K. Zen, M. Hirasawa, T. Shinsaka, and M. Adachi, "Countermeasure for liquefiable ground beneath the existing structure by cpg," in *Proceedings of the Twenty-fifth (2015) International Ocean and Polar Engineering Conference*. International Society of Offshore and Polar Engineers (ISOPE), 2015, pO: 839.

Paper E

A deformation (strain) envelope for cyclic disturbed sand

Tomas Sabaliauskas, Lars Bo Ibsen

The paper has been submitted to the
Soils and Foundations Vol. XX(X), pp. XXX–XXX, 2018.

Abstract

A new phenomenon was recently discovered. During deformation cycles, sand stiffness hysteresis loops converge in proportion to deformation amplitude. Behavior of the novel phenomenon has been investigated using a frictionless triaxial apparatus. The new knowledge is now summarized in an original concept called the Bezier stiffness model (BSM).

BSM summarizes findings shaped during years of unconventional triaxial testing. It delivers a set of rules which combine loss and recovery of sand stiffness, during drained and undrained loading, given irregular loading cycles. BSM does not follow convention, but is remarkably functional during real-life frictionless triaxial testing.

Curiously, the BSM remains stable during irregular loading cycles, transitioning both drained and undrained loading. Remarkably, the concept predicts a paradox - lower stiffness at higher density. The paradox is predicted by BSM, and confirmed to exist experimentally afterwards.

The novelty raises awareness of counter intuitive soil properties, which are not part of contemporary geotechnics. This paper raises the assumption that, some properties of sand could be exclusively deformation dependent, and thus can benefit from being modeled using a deformation (strain) envelope.

1 Introduction

Offshore wind turbines are slender structures, sensitive to variation in soil stiffness. The natural frequency of a wind turbine must lie within a narrow window to avoid dynamic amplification (resonance). Thus, even slight change in soil stiffness can cause oscillation beyond design limits [9] [27] [10]. This calls for a soil model combining both loss and recovery of sand stiffness. Unfortunately, such model is not part of existing convention.

In attempt to find new insights, unconventional triaxial tests were conducted. A frictionless triaxial apparatus was used to manipulate stiffness of sand. Attempts were made to combine both loss and recovery of sand stiffness in one loading sequence. In the outcome, a new phenomenon was discovered, and methods of controlling the stiffness hysteresis loops were established. The tests results are published in journals and conferences [41] [35] [36]. In this paper, the Bezier stiffness model (BSM) is developed based on knowledge derived from the recently published test results. Consequently, practical experiment is heavily emphasized, while making very few references to literature or theory.

The unconventional testing procedures discovered new testing options accessible using the frictionless triaxial apparatus: a specimen can be axially deformed beyond peak strength, without causing shear rupture. Because shear rupture is avoided - the test can continue. The specimen can be "pulled" back

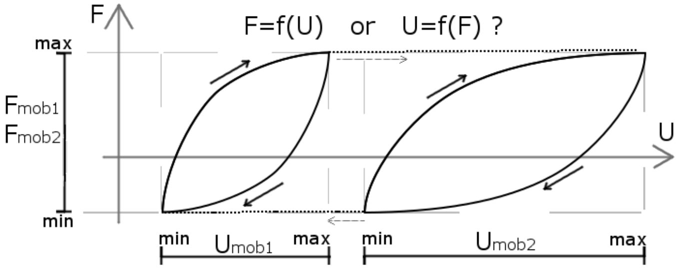

Fig. E.1: A graphical visualization of conclusions derived from recent experimental evidence [35] [36]. During deformation cycles of constant amplitude, stiffness hysteresis loops stabilize to fit within the deformation amplitude. Each hysteresis loop can be uniquely defined within a $Umob$ amplitude, as an $F = f(U)$ function. However, a unique solution based for $Fmob$ amplitude does not exist (all loops share the same force amplitude).

to initial length, and the (now) disturbed specimen can be compressed towards peak strength repeatedly. Thus, peak strength can be tested more than once, at more than one density, using one specimen. Further new testing options were detected later: a specimen was liquefied, axially deformed to reach undrained peak strength, "pulled" back to initial length, and allowed to drain. At this point, post-liquefaction recovery of drained stiffness was observed, during drained deformation cycles [41] [35] [36] [34]. In latest stages of testing, extremely complex loading sequences were executed: sequences combining drained and undrained phases, during irregular deformation cycles. Some of the original test results are given together with BSM simulation results in Fig's E.6 - E.8.

During the original tests [41] [35] [36], on which the BSM is built, randomized inputs were applied on sand specimens, to observe how the stiffness hysteresis loops respond. If stiffness hysteresis loops became gradually steeper, this was taken as a sign of stiffness recovery, and the inputs were analyzed for potential causal factors. If hysteresis loops were observed to became less steep, this was taken as a sign of stiffness loss (randomized inputs analyzed for causal factors). Eventually, rules governing stiffness loss and recovery were established. The rules allow to manipulate "sand memory". The "memory" can be rewritten (disturbed) and reset (stabilized) many times, by manipulating deformation history. Smaller deformation amplitudes create hysteresis loops of higher stiffness (see Fig.E.1). Larger deformation amplitudes - lower stiffness. Thus, stiffness hysteresis loops can be controlled (stretched, scaled, repositioned) by controlling the applied deformation (strain) amplitude. What is adequate to control a phenomenon, should be adequate to model it. Following this assumption, the idea of using a deformation envelope for modeling stiffness hysteresis loops was born.

The topic of stiffness loss and recovery having deformation dependencies is only remotely touched by a few researchers [12], [11]. Thus, the hypothesis can be considered a novelty. In testing practice, stiffness loops transition from one stable stiffness hysteresis loop to another. Thus, in theory, they could be modeled following the same causality. The principle is illustrated in Fig.E.1, where both stiffness hysteresis loops have unique deformation amplitudes, but share the same stress (Force) limits. It is not plausible to predict which hysteresis loop will be activated if F cycles are applied. To control which hysteresis loop is activated, deformation amplitude has to be controlled. Therefore, effects of deformation history must be preserved - as can be done by using a deformation (strain) envelope ϵ_y.

In its current form, the BSM is limited to fitting frictionless triaxial test results. The BSM describes behavior of a specimen, and caution should be taken when extrapolating towards more fundamental constitutive assumptions. Simulations describe behavior of a cylindrical specimen (height to diameter ratio 1:1, 70x70mm), placed between two lubricated end platen [32] [5] [42] [30]. The specimen is contained within a soft latex sleeve, to separate internal and external water pressure. Radial effective stress (σ_r) is generated by the water pressure difference (specimen saturated with vacuum boiled water). Axial effective stress (σ_a) has the additional component of reaction force generated by the specimen pushing against the load cell (see Fig.E.2, and Eq.E.2). Both σ_r and σ_a are effective stresses [7]. This should be a familiar starting point to all readers to whom modeling of advanced dynamic triaxial tests results is relevant (to learn more about unique testing options provided by frictionless triaxial apparatus see references: [35], [36], [34], [19], [32], [42], [30]).

Despite limited scope of application, BSM raises awareness of an important factor: deformation dependent sand properties. The key objective of this paper is to raise awareness of two facts: sand stiffness has features which are deformation history dependent, and a deformation (strain) envelope can be used to quantify, model and control them. Outside the scope of this publication, the BSM principle has been tested on various cohesionless soils (silty sand, coarse sand, gravel). Thus, BSM is not limited to Frederikshavn sand. Alas, all measured data plots shown in this paper were generated using Frederikshavn sand, which has $D_{50} = 0.1mm$. Sand used for specimens was sieved before and after testing, no crushing of grains was detected (as can be expected for confining pressure below $0.9MPa$). Further details about the equipment and the material can be found in numerous publications [41] [35] [36] [34] [19] [23].

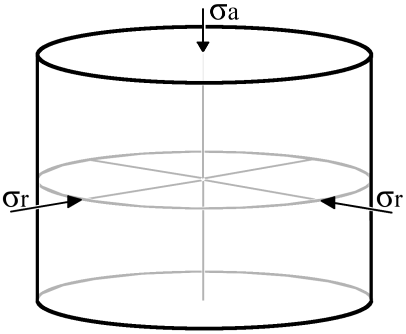

Fig. E.2: Illustration of effective stresses acting on a specimen tested using frictionless triaxial apparatus. Radial stress σ_r is generated by difference between external (cell) and internal (pore) pressure. Axial stress σ_a has the additional stress component, measured by a load cell. The reaction force is distributed on the flat surface.

2 Stress-space parameters

During frictionless triaxial testing, the confining pressure (p, Eq.E.1) and deviator stress (q, Eq.E.2) are generated by a combination of σ_r and σ_a. In drained mode σ_r is constant (selected by user). In undrained mode, σ_r variates. The variation occurs because undrained specimen tries to contract and expand while water is locked within voids. Volumetric contraction is a complicated nonlinear phenomenon, and there is no reliable way to model it, yet. Therefore, σ_r generated by the specimen is used as an input, only σ_a will be simulated. Alas, σ_r is constant during drained loading, thus could be treated as constant during simulation of drained loading cycles.

$$p = \frac{\sigma_a + 2 \cdot \sigma_r}{3} \tag{E.1}$$

$$q = \sigma_a - \sigma_r \tag{E.2}$$

$$\eta = q/p \tag{E.3}$$

$$q_{max} = -\frac{3 \cdot \sigma_r \cdot tan(\phi)}{tan(\phi) - 1} \tag{E.4}$$

$$q_{min} = -\frac{3 \cdot \sigma_r \cdot tan(\phi)}{tan(\phi) + 1} \tag{E.5}$$

Data plotted in p-q space should look familiar to most readers, as the Coulomb envelope becomes visible there [8] (see Fig.E.3). Given that $q = 2 \cdot \tau$, the linear stress boundary can be captured by $q = 2 \cdot p \cdot tan(\phi)$. Note, the friction angle ϕ here is not meant to be compatible with Coulomb envelopes used in conventional models. The "Coulomb" notation is BSM borrowed to fit a linear stress boundary observed during practical experiment.

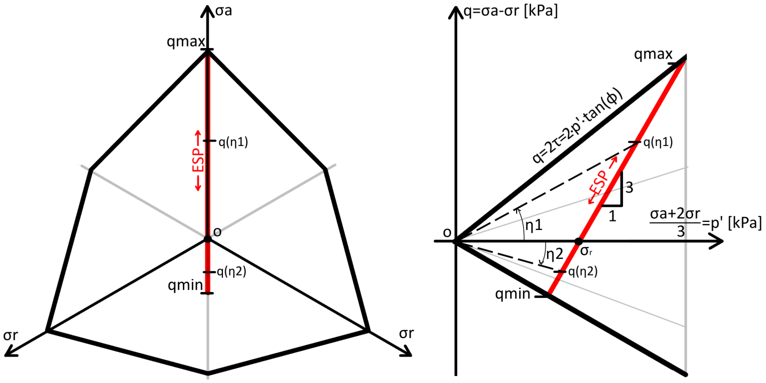

Fig. E.3: Stress space (q-p space) boundaries, defined by linear Coulomb stress envelope. The effective stress path (ESP), generated during a triaxial test, does not exceed the stress limit. Notice, ESP path can be expressed either using Cartesian coordinates (q and p) or polar (η and σ_r). Both coordinate systems satisfy q_{min}, q_{max} limits equally well.

When a drained specimen is axially loaded, a tilted effective stress path (ESP) is created. This is because $\sigma_3 = const$ during drained loading, thus causing $p \propto \frac{1}{3}q$ inclination of ESP line. To predict where ESP line collides with the Coulomb envelope, q_{min} and q_{max} points can be expressed as shown in Eq's.E.4, E.5. This is adequate to preserve the stress limits encountered during triaxial testing practice.

The characteristic points q_{max} and q_{min} can be expressed as a polar coordinate system, by using angle (η) and radius (σ_r). This allows to interpolate points along the ESP line, within ϵ_y envelope. As long as $\phi_{max} \geq \eta \geq \phi_{min}$ the linear Coulomb limits are satisfied. The stress angle η can also be referred to as "stress ratio", as given in Eq. E.3. Hardening curves parameterizing η will be normalized within the ϵ_y envelope, while position of ESP will move along the p axis under influence of σ_r. Thus, interpolating stresses on ESP line within the Coulomb limits.

The need to normalize η within ϵ_y envelope was observed experimentally. Stable stiffness hysteresis loops were generated at different ϵ amplitudes. The measured hysteresis loops were then normalized within case specific ϵ amplitude (amplitude used to generate case specific hysteresis loops). Remarkably, after normalizing, the hysteresis loops were observed to follow a common hardening curve (see Fig.E.4) [35] [36]. Such common feature can serve as a reliable anchoring point for interpolating η within ϵ_y limits. The normalized curves were fitted using Bezier spline, and expressed in Eq.E.6.

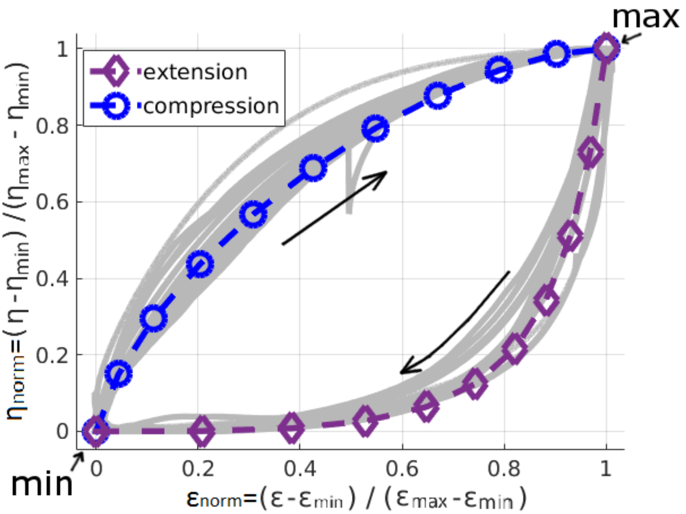

Fig. E.4: When stable stiffness triangles generated at different σ_r and different ϵ amplitudes are normalized with respect to ϵ amplitude and η - a common pattern is visible. All stable stiffness triangles converge towards very similar normalized stiffness curves [36].

$$\eta_{norm}(x) = \begin{cases} -((9-8x)^{\frac{1}{2}}-3)^{\frac{3}{8}} & \text{, extension } (\eta_{min}) \\ \frac{3(40x+9)^{(\frac{1}{2})}}{8} - \left(\frac{5(\frac{2x}{5}+\frac{9}{100})^{\frac{1}{2}}}{2} - \frac{3}{4}\right)^{\frac{3}{2}} - \frac{9}{8} & \text{, compression } (\eta_{max}) \end{cases} \tag{E.6}$$

3 Strain-space boundaries

When modeling a triaxially tested specimen, deformation is applied along one axis. Thus, it is a 1D problem, which can be modeled without following a complex constitutive formulation. ϵ_y can be described as a circle, with a radius (ϵ_R) and a center (ϵ_o) coordinate (see Eq. E.7). To control the envelope, isotropic / kinematic hardening coefficients can be used (see Eq's. E.8, E.9). The envelope has to move and change size in proportion to deformation increments $\Delta\epsilon$. This can be achieved using two pairs of hardening coefficients - one for expanding (yielding or "disturbing" the stiffness), and one pair for shrinking the envelope (stabilizing or "recovering" the stiffness). At every $\Delta\epsilon$ iteration increments the envelope shrinks. Then, if resulting ϵ is crossing the ϵ_y limits, the ϵ_y expands enough to contain real time *epsilon* within the envelope. Thus, envelope is shrinking gradually but expanding (yielding) instantly.

Strain increments during $f_\epsilon < 0$ cause stabilizing (shrinking of ϵ_y). Stabilizing is gradual, $\kappa_{k,2} + \kappa_{i,2} < 1$ (see Eq.E.6). Therefore, ϵ_y diameter shrinks towards ϵ slowly. Because the envelope shrinks slowly, but expands instantly - cycles of deformation force it to stay at a diameter closely matching the applied deformation amplitude. The edges of the envelope converge towards the peaks of applied deformation cycles. In simulations values $\kappa_{k,2} + \kappa_{i,2} \approx 0.15$ appear to work rather well for a wide range of tests and even among different soil profiles - from coarse to fine sands. Nonetheless, selecting κ_k and κ_i as linear coefficients (constants) is not ideal. This must be emphasized - fixed coefficients are merely for proof of concept in early development of the BSM. Further observations (more frictionless triaxial tests) are needed to gain deeper understanding of proportion governing ϵ_y behavior [41] [35] [36].

$$f_\epsilon = \epsilon_R - abs(\epsilon - \epsilon_o) \tag{E.7}$$

$$\Delta\epsilon_R = \begin{cases} \kappa_{i,1} \cdot abs(\Delta\epsilon), & \text{if } f_\epsilon < 0 \\ -\kappa_{i,2} \cdot abs(\Delta\epsilon), & \text{otherwise} \end{cases} \tag{E.8}$$

$$\Delta\epsilon_o = \begin{cases} \kappa_{k,1} \cdot \Delta\epsilon, & \text{if } f_\epsilon < 0 \\ \kappa_{k,2} \cdot \Delta\epsilon, & \text{otherwise} \end{cases} \tag{E.9}$$

4 Bezier stiffness

In Fig.E.4, two normalized hardening curves are given. Imagine starting at point "max" and moving down the extension curve. If the loading stops in the middle, and loading direction is reversed, the η_{norm} will "teleport" from extension to compression line. It is desirable to have a method to transition from one normalized hardening curve to the other gradually, rather than "teleporting". To generate a curved transition, a recursive function inspired by Bezier spline was formulated. The principle is illustrated in Fig.E.5, and the parameters are given in Eq's. E.10 - E.12. Curves η_{min} and η_{max} shown in Fig.E.4 are used as "guides", and Bezier stiffness principle allows to interpolate between the normalized hardening curves.

The $R(x)$ variable (Eq.E.12) is used to keep stiffness curves within ϵ_y limits. As $R(x) \to 0$, the stiffness curve becomes more vertical. Thus, ensuring increasingly more vertical stiffness path near the edge of the ϵ_y envelope. Notice the 10^{-4} in Eq.E.12 - the number creates finite stiffness limit, the stiffness path never becomes pure vertical (thus avoiding the "teleportation" problem). This adds stability during simulations.

It is worth noticing that, the Bezier stiffness principle is unconditionally stable. As long as there is a finite stress value (provided by normalized

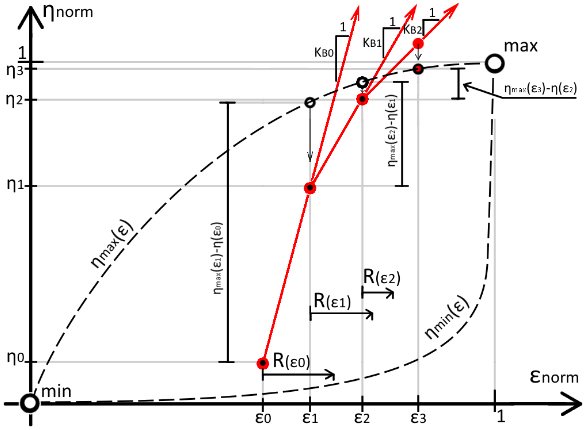

Fig. E.5: A recursive function to interpolate within normalized hardening curves (inspired by Bezier spline). The curvature becomes steeper as the R parameter changes. The solution is unconditionally stable: as long as finite "max" (or "min") limit is given, a curved-tangent transition occurs.

curve), the Bezier stiffness curve will converge towards it, following a curved, tangent trajectory (see Fig.E.5). Alas, the Bezier stiffness principle is still a subject to further research, the formulation given is adequate to recreate simulation results shown later.

$$K_b(i) = \frac{\eta_{max}(\epsilon(i+1)) - \eta(i)}{R(\epsilon(i))} \tag{E.10}$$

$$\eta(i+1) = \eta(i) + K_B(i)\Delta\epsilon \tag{E.11}$$

$$R(x) = \frac{1-(1-2x)^2}{10} + 10^{-4} \tag{E.12}$$

5 Volumetric response

Modeling of specimen stiffness hysteresis loops, stiffness paths - stiffness, is the primary focus of this paper. However, empirical tests used for analyzing stiffness reveal some interesting patterns in volumetric response as well. Stiffness and volumetric response can be modeled in parallel, as two (mostly) independent properties. Stiffness was controlled in practice, thus is modeled in theory, while ignoring volumetric response. Nevertheless, volumetric response patterns were observed to have deformation dependencies potentially compatible with an ϵ_y envelope [41] [35] [36] . Therefore, an attempt to add them into the BSM is made.

Lack of correlation between stiffness and density can be demonstrated experimentally, by creating a disturbed soil state where stiffness is lower, but density is higher. To demonstrate this paradox, one has to start with small deformation amplitudes to generate a stable hysteresis loop of high stiffness. Then, deformation amplitude is increased. The specimen continues to contract (becoming denser), but because deformation amplitude is increased, the stiffness hysteresis loop is stretched "flat", and the consequent stiffness hysteresis loop has lower overall stiffness. Thus, creating a disturbed soil state of lower stiffness at higher density [41] [35] [36]. Similarly, while liquefying, an undrained specimen becomes less stiff without significant change in absolute density. Thus, again, showing change of stiffness, while density is near constant.

While correlation between stiffness and absolute density is questioned, the peak strength and absolute density remain correlated. ϕ is modeled as a function of e. Alas, change in ϕ merely moves the Coulomb envelope, which is interpolated by $0 \geq \eta_{norm} \geq 1$. Therefore, strength and stiffness are modeled in parallel, as two (nearly) independent parameters. This is an interesting conundrum: peak strength and stiffness behave independently. Liquefied specimens lose stiffness, but preserve peak undrained strength. Disturbed soil states with higher strength at lower stiffness were demonstrated empirically in numerous publications [41] [35] [36] [34]. This is a very counter intuitive property of cohesionless soil (sand), but the phenomenon follows simple causation, correctness of which is proved empirically.

The BSM uses two coefficients to capture volumetric response: dilation angle, and contraction angle: ψ_{cont} (Eq.E.13) and ψ_{dil} (Eq.E.14). Tangent of these is multiplied by $\Delta\epsilon$ increment, and the result is summed to generate the total volume change increment Δe (Eq.E.15). Dilation and contraction is calculated separately (and summed afterwards), as this allows to scale dilative / contractive component according to absolute density limits e_{min} and e_{max}. Thus, ensuring the simulation stays within realistic absolute density limits.

$$\psi_{cont} = \begin{cases} k_{cont} \cdot (1 - \epsilon_{norm})^{\frac{(emax-e)}{(emax-emin)\cdot log(\epsilon_R \cdot k_R + 1)}} & \text{, in compresion} \\ k_{cont} \cdot (\epsilon_{norm})^{\frac{(emax-e)}{(emax-emin)\cdot log(\epsilon_R \cdot k_R + 1)}} & \text{, in extension} \end{cases} \tag{E.13}$$

$$\psi_{dil} = \begin{cases} k_{dil} \cdot \epsilon_{norm}^{\frac{(emax-e)}{(emax-emin)}} & \text{, in compresion} \\ k_{dil} \cdot (1 - \epsilon_{norm})^{\frac{(emax-e)}{2(emax-emin)}} & \text{, in extension} \end{cases} \tag{E.14}$$

$$\Delta\epsilon_V = |\Delta epsilon| \cdot (tan(\psi_{cont}) - tan(\psi_{dil})) \tag{E.15}$$

6 Performance of the model

Finally, simulations can be attempted by combining the parametric equations into one algorithm. The inputs are ϵ and σ_r. Both inputs are taken directly from measurement, thus inputs used in testing are identical to inputs used in simulation. Later, the outputs of the real specimen are compared with the outputs of numerical simulation.

1. INPUT ϵ, σ_r.
2. Update ϵ_R, ϵ_o, in proportion to $f_\epsilon(\epsilon)$ (Eq's. E.8, E.9)
3. Update ϵ_{mob} within ϵ_y limits.
4. OUTPUT $e = f(e, \psi(\epsilon_{norm}), \Delta\epsilon)$ (Eq. E.15)
5. Update $\phi = f(e)$ (optional)
6. Update $\eta_{norm} = f(\eta_{norm}, \epsilon_{norm}, \Delta\epsilon_{norm})$ (Bezier stiffness)
7. Update $\eta = \eta_{norm} \cdot ((\phi_{comp} - \phi_{ext}) - \phi_{ext})$
8. OUTPUT $q = f(\eta, \sigma_r)$

The outputs are q and e. For undrained tests e should be held constant, but simulation of a parallel system allow to generate e history without distorting stiffness. Thus, e is plotted drained at all times - this provides additional information about the behavior of the BSM. In future, improved model should use e to generate pore pressure response. Thus, e would be responsible for p (or σ_r) variation during undrained testing. But for the time being, σ_r is borrowed as input from measurement, thus e serves no role in stress plots.

The two outputs (q and e) are plotted on top of empirically measured data in Fig's E.6-E.8. Each figure shows 6 data plots. The primary objective is to model sand stiffness, thus the $q(\epsilon)$ plot is given first. Under the stiffness plot, $e(\epsilon)$ is given. The two main plots have many overlapping hysteresis loops, thus are hard to follow. To make comparison easier, the time histories of ϵ, σ_r, q and e are given on the right side of Fig's E.6-E.8. Notice q and e are the outputs, thus simulation results are plotted on top of the measured data, while ϵ and σ_r are the inputs, thus there are no simulation to plot there.

While looking at the data plots, one can see imperfections - noise in inputs borrowed from tests. It is interesting to keep the imperfections as an extra challenge for the model. Note all the simulations were run with the same calibration, the same coefficients. This demonstrates robustness of the BSM. The same calibration performs relatively well during drained and undrained loading sequences, through irregular cycles, given noisy inputs. The simulations overlap with measured data quite well. Baring in mind the original

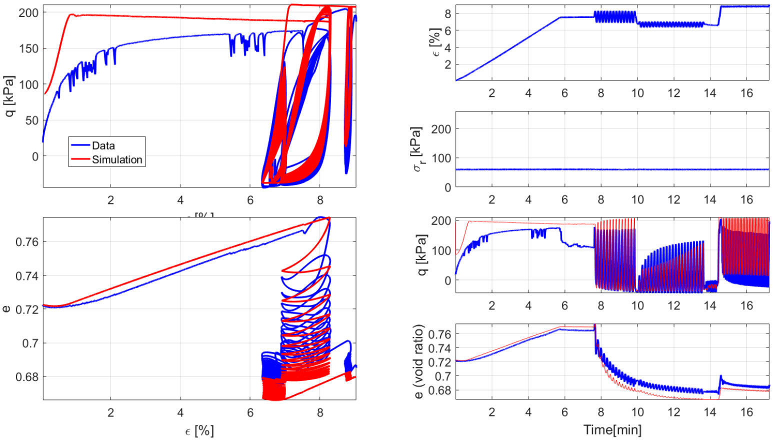

Fig. E.6: A plot of measured data and simulation. A drained sand specimen was exposed to 3 different ϵ amplitudes, while σ_r was held constant.

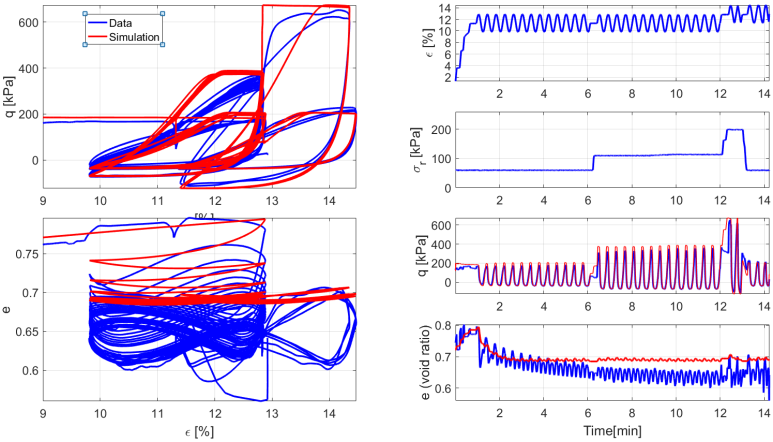

Fig. E.7: A plot of measured data and simulation. A drained sand specimen was exposed to similar ϵ amplitudes, at different σ_r values.

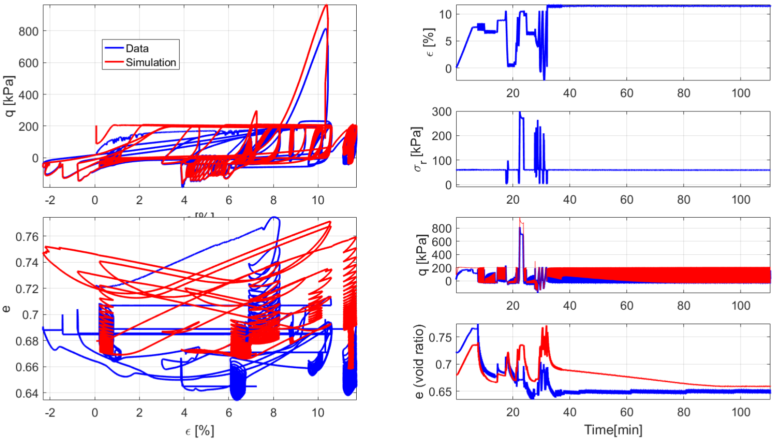

Fig. E.8: A plot of measured data and simulation. A sand specimen was exposed to various ϵ amplitudes, at different σ_r values. Both drained and undrained loading is present. Notice, σ_r has to be borrowed from measurements during undrained loading, only η is modeled at all times. Note, during undrained loading, measured e is constant, but the model continues to behave drained. It is known that undrained specimen do not recover stiffness during small amplitude ϵ cycles, thus fitting could be improved if undrained ϵ_R was not allowed to contract during undrained cycles [35] [36].

objective was to capture stiffness hysteresis loops in their final "stable state" it is remarkable that the model captures some of the transition process as well.

It is interesting that the novel approach is inherently stable. Hysteresis loops predicted by the model converge towards hysteresis loops generated by the specimen. This means the model re-calibrates itself when ϵ cycles of constant amplitude are applied. The more loading cycles applied - the more precise the prediction. Notice how the simulation and data converge towards each other each time ϵ cycles of constant amplitude are encountered. The fact volumetric response is fitted to some degree - is a lucky coincidence as well. Alas, this indicates that some of the assumptions raised during development of the BSM could be worth researching further.

7 Discussion and conclusion

Here, the decision to use a deformation envelope was made exclusively from observations gathered during unconventional triaxial testing [35] [36] [41]. The original tests began as a randomized trial and error, in attempt to find patterns and features missing in conventional methodology. A way to control specimen stiffness in testing practice was established, and only then the intuitive rules of thumb were attempted to implement into an BSM. Now, the original BSM shows promising results. While the model cannot be applied to anything outside of modeling a specimen, it delivers new ideas on how to interpret cyclic loaded sand response. New principles, a new perspective, where irregular loaded sand is interpreted using a strain-envelope, instead of a stress-envelope.

By coincidence, a somewhat compatible constitutive formulation was noticed to exist after developing the BSM: strain-space plasticity formulation for cohesionless soils, by P.J.Yoder [44]. Unlike authors of this paper, Yoder had no access to experimental results. He investigated the concept exclusively for potential computation benefits. A remarkable feature of strain-space plasticity is that it behaves like a parallel spring system (rather than series, as stress-space plasticity does). Strain envelopes converge in one iteration - there is no need to titter tater between plastic corrector and stress envelope position (strain increment and strain envelope are in the same space). Moreover, simulations of complex time history can be executed by inverting the stiffness matrix only once (see Fig.E.9). The spring stiffness (K) in Fig.E.9 is constant, thus can be inversed once for infinite loading steps. Error Δ is directly summed into internal forces vector F_{int}, without converting to plastic strain - thus avoiding implicit matrix inversions, which are unavoidable in stress-space plasticity (used in flow rule). Therefore, strain-space and stress-space plasticity formulations could be viewed as competitive branches of models. Given the new experimental evidence, and performance of the BSM strain envelope, the principles of strain-space plasticity could be worth exploring deeper. In addition, strain-space plasticity is rather common in other branches of material sciences, outside geotechnics. Models of bone fracture [31] and cracking concrete [13] use it, because strain envelopes provide stable solutions during rapid changes in peak strength.

The BSM is proof of concept. The principle brings forth the idea that unknown deformation dependent sand properties may exist. It is plausible that stress envelopes alone will not solve all geotechnical problems. Maybe stress and strain envelopes can coexist, at least for certain advanced applications, such as design of offshore wind turbine foundations in seismic zones. Thus, the main contribution of the BSM are the open questions. The model cannot be used by the industry, but it can be used by researchers: to raise new questions, to attempt new testing procedures, new inspire novel solutions. To look at old problems from a different perspective.

The model was derived based exclusively on empirical evidence, generated during unconventional testing procedures, made available by the frictionless triaxial apparatus. The frictionless triaxial apparatus is not a new device, it was introduced in the 60's [5] as a higher precision alternative to classical triaxial apparatus [30]. Alas, the frictionless triaxial apparatus offers more than improved precision, it has a unique testing scope of its own, provided by the fact specimens are not "destroyed" (no shear rupture) when peak strength is reached [42] [19] [35] [36] [34]. The frictionless triaxial apparatus

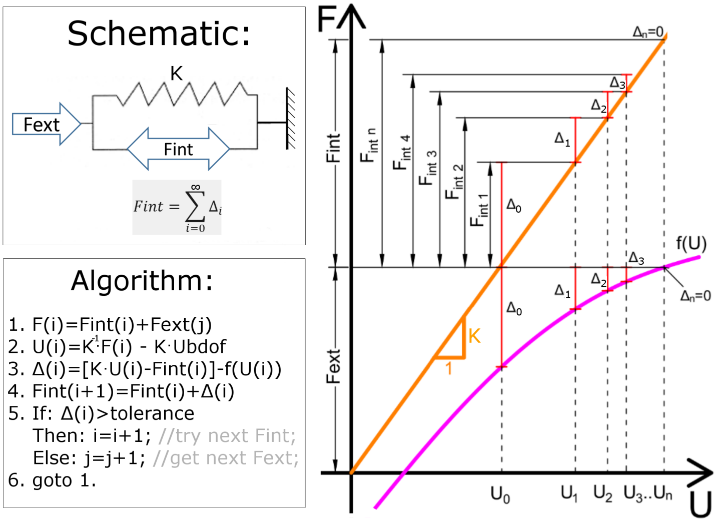

```
1. F(i)=Fint(i)+Fext(j)
2. U(i)=K^-1·F(i) - K·Ubdof
3. Δ(i)=[K·U(i)-Fint(i)]-f(U(i))
4. Fint(i+1)=Fint(i)+Δ(i)
5. If: Δ(i)>tolerance
   Then: i=i+1; //try next Fint;
   Else: j=j+1; //get next Fext;
6. goto 1.
```

Fig. E.9: The principle of using deformation envelopes (relaxation stress).

has the potential to deliver further new knowledge, as long as theoretical testing limits are questioned, and practical, real-life capabilities are followed. Alas, the frictionless triaxial apparatus has one fundamental limitation: loading path is limited to stress / strain paths following lode angle $\theta = 0$. Thus, observations are limited to 1D (axial) loading, which is inadequate for researching the ϵ_y envelope in 2D or 3D. The weakness of dataset is inherited by the BSM. It is not safe to extrapolate beyond 1D loading. The problem is illustrated in Fig.E.10: there is more than 1 way to interpolate stress within a 2D strain envelope. The correct way cannot be known, until further tests are done. Alas, a true triaxial apparatus exists, and could be used for testing deformation dependent properties in 2D and 3D.

It is crucial to recognize that some geotechnical problems are not solved efficiently by existing convention. Sand behavior can be extremely counter intuitive. Thus, convention and "common sense" can be misleading. A model is only as good as its ability to match real life measurements. And the improvised, intuitively formulated BSM delivers a remarkable capability to capture the "general trends" encountered during irregular loading cycles, combining drained and undrained loading in one continuous sequence.

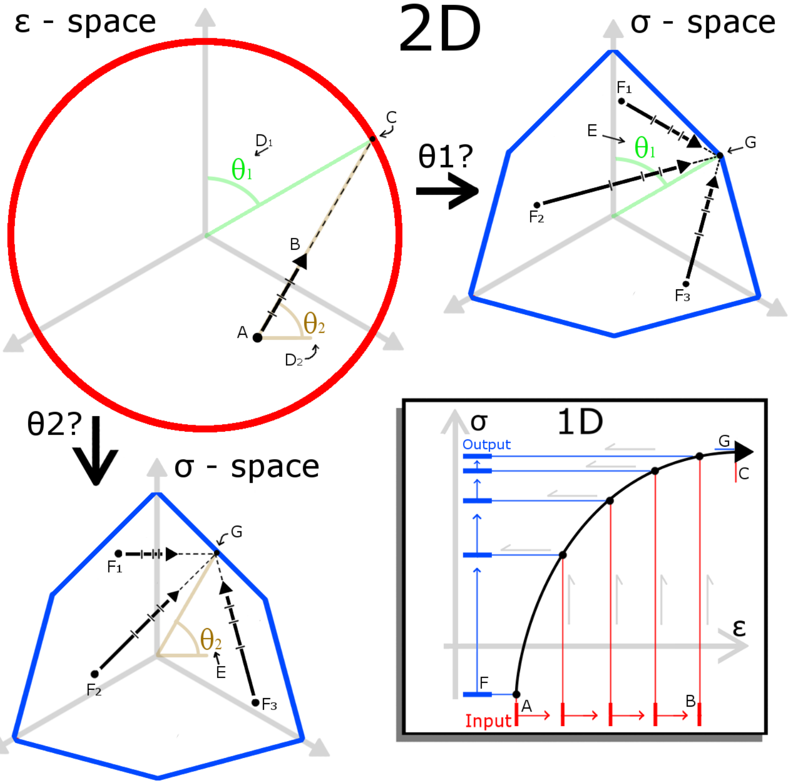

Fig. E.10: Data is a Inadaquate to conclusively define rules governing a 2D (or 3D) model. To illustrate the point, notice how ϵ-space vector AB is pointing to point C on the 2D ϵ_y envelope. $\theta_1 \neq \theta_2$, thus it is not certain which (if either) should be used for interpolating in σ-space.

Paper F

Improved PID control for triaxial testing liquefied specimen

Tomas Sabaliauskas, Lars Bo Ibsen

The paper has been published in the
DCE technical memorandum, 2017.

The layout has been revised.

Abstract

Using a frictionless triaxial apparatus, sand specimens can be tested at relatively high axial strains, even while liquefying. However, liquefying specimens have extremely nonlinear stiffness, thus standard PID control does not perform well. To maintain control over applied loads, the PID controller was modified to adapt to disturbed soil states. The proposed methods expand the scope of testing towards options which are otherwise inaccessible by triaxial testing.

1 INTRODUCTION

A single diameter height specimen tested using frictionless triaxial apparatus is very durable. It can be compressed beyond yielding and pulled back to initial length – both drained and undrained. Such specimens yield isotopically, without forming a dominant shear rupture (in contrast to conventional triaxial apparatus). If no water is added, unsaturated specimens can develop multiple failure planes simultaneously (Fig. 1). Whereas saturated specimens – do not form shear rupture at all when compressed.

Due to isotropic strain (and stress) distribution, specimen durability increases dramatically. A fully saturated sample can be crushed beyond 10% axial strain without forming a shear band or bulging. And the deformation remains reversible, the sample can be pulled back to initial length, liquefied, drained and repeatedly cyclic tested in one, long, aggressive sequence. A sample liquefied and drained 6 times is shown in Fig. 2. The extreme scope of testing is obtained using two factors. First – mechanical properties of the frictionless apparatus, which preserves the specimen shape and durability. Second – load control methods, which adapt to changing specimen stiffness and strength, thus ensuring the end plates will stay in contact with the specimen being tested.

Triaxial apparatus is rather simple in construction. At the bottom a piston moves up and down, moving the bottom end plate with it. At the top, and end plate is fixed to a load cell (Ibsen, L. B., 1995). A proportional integral distance (PID) controller can move the bottom piston to a user defined target position (U) or force (F), where F is measured by the load cell. Thus, a PID controlled can operate either in displacement mode or force mode (U or F mode).

In standard tests target U or target F can be specified manually, or set to follow a pre-defined wave shape (sinusoidal, saw tooth, square wave, etc.). These options are available by default in the software used to control the (dynamic) Danish triaxial apparatus. Each wave shape has unique benefits and limitations.

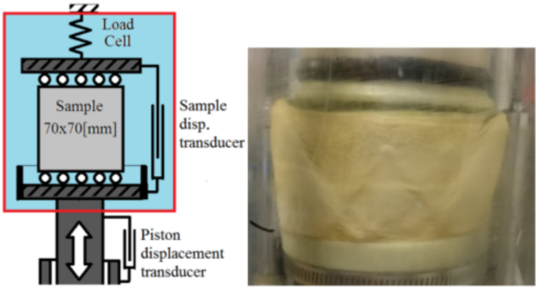

Fig. F.1: Schematic of test setup and axially compressed (20% strain) dry, unsaturated Aalborg no.1 sand, resulting in 6 overlapping shear bands.

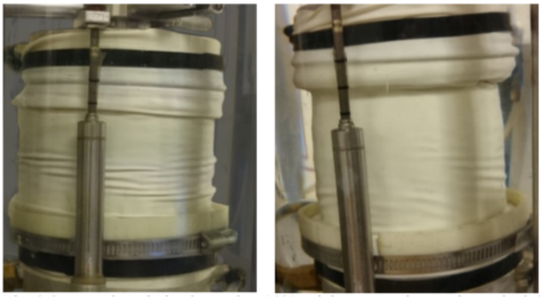

Fig. F.2: Saturated, undrained samples. 10% axial compression strain on the left. On the right - 6 times compressed to failure, pulled to initial length and drained with cyclic testing in between. Geometry remained satisfactory.

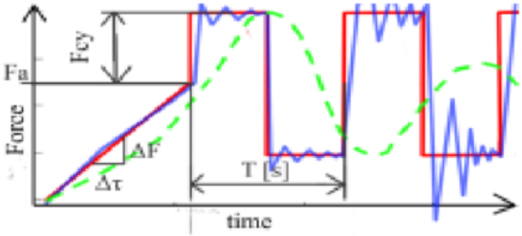

Fig. F.3: Square wave loading with 2 cases of bad tuning illustrated on top.

1.1 Linear ramp loading

The most basic type of loading is linear ramp. The load is applied at a constant rate, either $\Delta F/\Delta t$ or $\Delta U/\Delta t$, towards the target F or U. Cyclic loading tests start with linear ramp "preloading" towards the average Force (Fa). A linear loading path can be seen going towards Fa in Figs. 3-6. The produced loading path looks like a line, but the PID controller is adjusting piston position a thousand times per second – to keep the real time value of F or U "on target".

One must recognize that the PID controller is predicting how many "injections of oil" need to be supplied to the piston, in effort to keep the measured F (or U) "on target". The number of injections is calibrated by three coefficients – P, I and D. The coefficients are found through trial and error and as long as F (or U) response remains somewhat linear the PID calibration performs well. The PID controller works especially well with U control. Hydraulic fluid is extremely stiff, thus the same number of oil injections will produce the same amount of displacement regardless of how stiff or soft the specimen becomes.

F controlled loading is different. Number of oil injections necessary to keep F "on target" vary with specimen stiffness. If a system was near linear elastic, there would be no problem, but stiffness can change a lot in sand specimens, thus F-PID control can fail. PID controller calibrated "too stiff" can resonate – oscillate out of control (see Fig.3). Whereas relaxed values cause F-PID to lag behind the F target. This makes applying F cycles on liquefying specimens very complicated. Standard PID controllers are simply not robust enough.

1.2 Square wave loading

Square wave (Fig.3) has very steep transition from one peak to another. This makes it great for tuning the PID controller, as square waves expose resonance or overdamping. PID control has 3 coefficients – position, integral and derivative. These three determine how aggressively the piston reaches for the

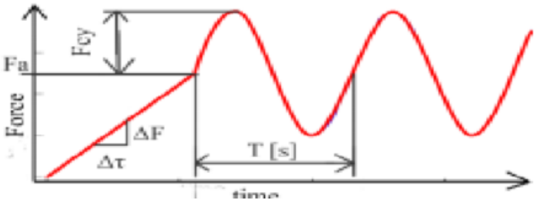

Fig. F.4: Sinusoidal loading shape.

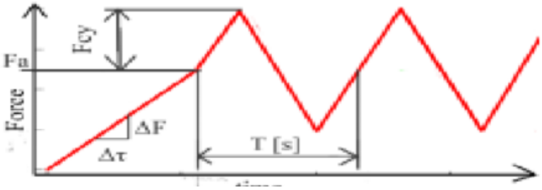

Fig. F.5: Saw tooth (triangular) loading.

target. The three are normally calibrated through trial and error, while the test is running.

In F mode, PID coefficients depend on specimen stiffness. The number of oils injections required to reach target F changes with specimen stiffness. Thus, different parameters of F-PID are necessary at different stiffness. However, no such problems are present during U-PID calibration: hydraulic piston is grossly overpowered, thus the correlation between U and oil injections remains the same, regardless of the specimen stiffness. Which makes U-PID calibration stable at all times.

1.3 Sinusoidal loading

Sinusoid wave (Fig.4) has smooth curves, making it easier for F-PID to catch up with real time measurements at the peaks. This wave shape is stable over a wider range of specimen stiffness, as the smooth shape reduces the danger of resonating and/or under/over-loading a specimen. But during liquefaction it was found impossible to maintain a stable sinusoidal shape using F-PID control (shown in Fig.7).

1.4 Saw tooth loading

Cycles of linear ramp unloading/reloading can be combined into a saw-tooth pattern (Fig. 6). This is advantageous for testing deformation cycles. The loading rate (du) is constant during such loading cycles, this allows to isolate individual components within equation of motion:

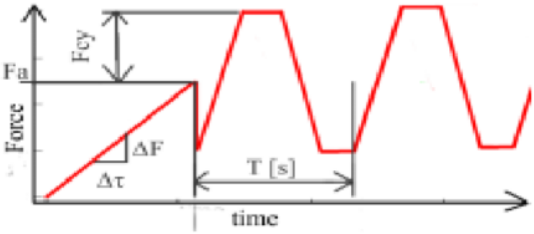

Fig. 3 Trapezoid loading

Fig. F.6: Trapezoid loading (notice the sudden drop after Fa preloading. The drop is generated by MOOG controller, and can cause problems if left unnoticed)

$$F = K \cdot u + C \cdot du + M \cdot ddu \tag{F.1}$$

Where u is displacement, $du = \Delta U / \Delta t$ (first derivative, loading rate), ddu – second derivative (acceleration). And K, C and M are stiffness, damping and mass components. To model dynamic sand response, the K, C and M need to be treated as nonlinear functions. Therefore it is crucial to isolate them one at a time. If U cycles are applied at increasingly slower du, a quasi-static K will emerge. Once K curvature is quasi-static, further reduction in du will not produce changes in measurement. But if du is increased (cycle frequency increased), the quasi-static stiffness path will start changing, and the deviation will be caused by C component. Thus, U-PID saw-tooth loads allow to separate K from C, from M, all behaving like nonlinear state defendants.

1.5 Trapezoid loading

If saw-tooth peaks are paused for a brief moment – trapezoidal wave is shaped (Fig.6). The flat peaks can be used for observing stress relaxation (U-PID) and strain creep (F-PID) with each cycle. Allowing specimens to stabilizer at the peaks can ensure quasi-static response is being measured.

2 STRAIN AND STRESS VS U AND F

The default control methods are limited to F and U control. Yet, specimens are tested for stress and strain. Thus, it would be good if U and F could be applied in ways which target stress and strain. This is where standard PID is modified to meet triaxial testing. Converting piston U to specimen strain takes some compromises. Piston displacement does not match specimen deformation "exactly". As Fig.1 shows, piston displacement is redistributed between the specimen and the load cell (load cell deforms like a spring too).

However, the load cell is a very stiff spring. Even more so during liquefaction, when the specimen becomes soft, and in a series spring system, the softest spring absorbs largest proportion of deformation (in this case, the specimen absorbs most of the deformation). Thus, even though PID control has no access to real specimen deformation, the piston position can be used as a close substitute. Especially during liquefaction.

Given these observations, true strain can be obtained as:

$$\epsilon = ln(1 - \frac{\Delta U}{H_0}) \tag{F.2}$$

Where H0 is initial specimen height. In addition, undrained specimens have constant volume – thus, predictable cross-section to obtain stresses from. True (absolute) stress can be obtained as:

$$\tau = \frac{q}{2} = (F/A_0) \cdot (1 + \epsilon) \tag{F.3}$$

Where A0 is the initial cross-section area of a specimen, and $(1 + \epsilon)$ accounts for change in cross-section during loading. Note, here the stress measured is "absolute", not "effective". Absolute (undrained) stress limits are predictable. Firstly, undrained yielding always occurs when pore pressure drops to near $-100kPa$, thus undrained yielding can be predicted by monitoring real time pore pressure. Secondly, undrained yielding strength can be approximated with equation:

$$\tau_{min,max} = \frac{(Cp + 100) \cdot tan(\phi)}{\frac{2}{3} \cdot tan(\phi) \pm 1} \tag{F.4}$$

where Cp and ϕ are the chamber pressure and the friction angle, respectively. The constant of $100kPa$, representing cavitation limit. The theoretical limit for cavitation is $100kPa$ (absolute vacuum), but in tests, cavitation of de-aired specimens occurred near $-85kPa$ Thus, using 85 (or slightly less) instead of 100 could be an option providing more realistic estimates.

3 LIQUEFACTION

The challenge of measuring liquefaction in cyclic loaded specimens, using the Danish triaxial apparatus was attempted by Nielsen & Ibsen, 2013. Two way loaded sinusoidal F-PID cycles were applied, and the PID controlled produced "overshooting" peaks (visible in bottom picture of Fig.7).

Overshoot occurs because of rapidly changing stiffness of liquefied specimens. There is a "pure plastic gap" when crossing q=0 axis, thus changes in stiffness are tremendous when loading direction is reversed (see Fig.9). In pure plastic zone F-PID will produce acceleration which will accumulate into

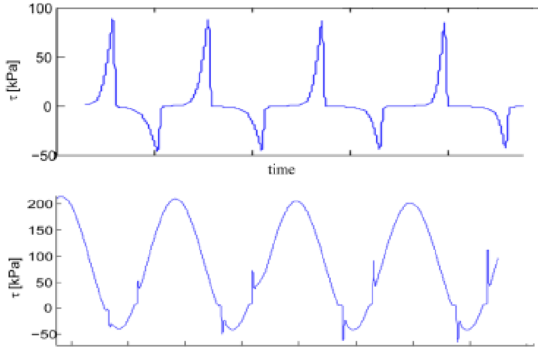

Fig. F.7: Performance of script loading (top) compared with to F-PID controlled sinusoidal loading (bottom), acting on liquefying specimen.

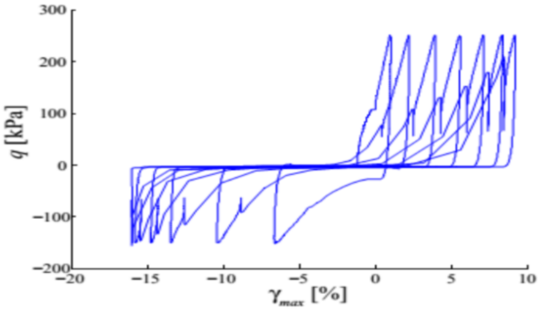

Fig. F.8: Force controlled liquefaction response (Nielsen & Ibsen, 2013). If loaded further the “double peaks” will shoot beyond the maximum stress level.

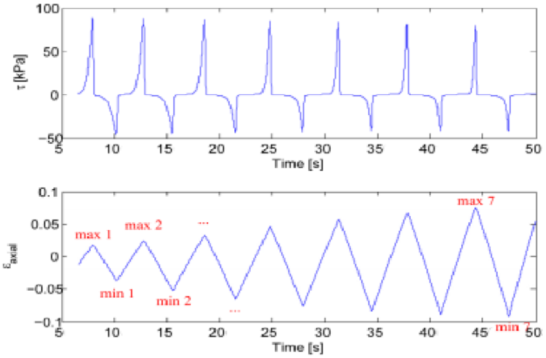

Fig. F.9: Adopting strain controlled liquefaction loading. Stress time series on top. Strain time series in the bottom.

large loading velocity (du component). F-PID accelerates and de-accelerates with a minor delay, thus, it will not be able to stop once the target F is reached. And to make matters worse, after F-PID exceeds the target F it will attempt to unload assuming linear stiffness. But unloading stiffness is much steeper in sand, thus the "overshoot" will be followed by "undershoot". This F-PID behavior cannot be prevented using the PID coefficients. Make the piston more aggressive and it will oscillate out of control around the target F value. Relax the settings – and overloading/under-loading will get worse. However, U-PID has no such problems. U-PID is unconditionally stable. The only problem is targeting F values using U-PID for input.

4 Targeting F using U-PID

The problem with using U-PID is that F plays no role in U-PID algorithm. One has to specify the targeted U and the U-PID will control oil injections required to reach the U target. Thus, to target F instead, it is necessary to monitor real time F values, and change the targeted U value once the F limits are reached. Luckily, the MOOG station allows to monitor real time F using scripts (Troya & Sabaliauskas, 2014). Furthermore, not only F limits can be observed, but F can be converted into τ within the script using Eq's (2,3).

A script can take measurement of F a few thousand times per second. Measurements can be converted to τ within the same millisecond, and du direction is reversed once τ peak was reached. The principle is very simple, each time τ peak is triggered, loading direction is reversed (see Fig. 9). However, it

is not enough to merely reverse displacement direction, the loading period needs to be preserved. The distance between peak U positions is increasing with each loading cycles, thus the du value has to be updated after every peak – to cover the next distance faster (or slower) depending on how the peak position evolves during the test.

Notice how ϵ distance is smaller between $max1 - min1$ compared to $max7 - min7$ in Fig.9. The "gap" between the peaks is increasing as specimens liquefy. This is easy to account for if du component (loading rate) is updated after each peak crossing. Distance between min1 to $min2$ needs to be crossed with: $du = (max1 - min1)/T$, and distance between $max7$ to $min7$ is crossed with $du = (max7 - min6)/T$. This allows to update du with respect to previous loading cycle. This does not provide the exact solution, as loading rate is slightly too slow, but in Fig.9 one can see the period is rather stable, and close to $T = 11$.

5 Limitations

It must be noted, that F-PID is problematic only at high plasticity, and during periods of unstable stiffness. Otherwise, when stiffness is near linear, F-PID performs really well. At times when stiffness is very steep, F-PID is the only real option. At high stiffness, U-PID scripts becomes unstable, as small deformation creates large F fluctuations. Therefore, care must be taken to select the correct setting:

1. U-PID for testing nonlinear, pure plastic behavior 2. F-PID for testing linear, elastic behavior.

6 FUTRE WORK

Using U-PID loading, specimens survive through aggressive liquefaction. Thus, post liquefaction soil states can be researched. This is interesting for researching soil states left after earthquakes. As well as disturbed soil states encountered by offshore wind turbines.

The new testing scope allows to iterate between liquefaction and draining, which allows reach very high densities, which could not be accessed using alternative preparation methods. The specimens can be densified to the point of purely dilative state. Such "exotic" soil state (pure dilative) could be very interesting to research as a fundamental boundary limit of sand. Foundations of structures built offshore must function in cyclic loaded environment. Thus, liquefaction and drained postliquefaction recovery are both important. The control algorithms developed thus far are sufficient to safely liquefy, drain and reliquefy specimens. Thus, evolution full complexity of disturbed sand stiffness can be observed.

7 Introducing new capabilities

Besides new testing capabilities already available, the equipment is not perfect. Some modifications can be implemented to improve it further. At the moment, two computers are connected to the (dynamic) Danish triaxial apparatus. One of them is dedicated to data acquisition. The second one – PID controller. The two computers do not communicate with each other. The PID controlled has no access to data describing the specimen itself. If the two computers were upgraded to share a common database, a whole new level of automation would become plausible: Scripts could be written to target specific densities of a specimen. Specimens could be "reset" to initial stiffness, to make data tables autonomously. Pore pressure measurements would allow to prevent undrained specimens from yielding more efficiently. In the most farfetched scenario machine learning algorithms could be implemented for data mining. Sand has extremely nonlinear stiffness, complexity of which quickly overwhelms a human observer. Given how durable and stable the specimens are, it could be plausible to generate state space maps and decision tress (such as Markov decision process) by allowing a machine learning algorithm to explore the patterns autonomously.

8 CONCUSION

The new found capability to test liquefied sand is stable and reliable. A specimen can be liquefied, and continued to test thereafter. As specimen durability is improved, it becomes plausible to increase complexity and aggressiveness of testing, which in turn provide access to new observations – new knowledge.

Some remaining limitations of the equipment cannot be surpassed without partial reconstruction of equipment – such as combining the separate computers into one unit. But it seems new testing scope can be reached by merely changing the software, rather than upgrading the hardware. The testing capabilities of frictionless triaxial apparatus are not exhausted yet, the equipment can reach observations far beyond conventional testing limits.

9 BIBLIOGRAPHY

Hettler, A. & Vardoulakis, I., 1984. Behaviour of dry sand tested in a large triaxial apparatus. s.l.:Geotechnique 34.2 (1984): 183-197.

Nielsen, S. D. & Ibsen, L. B., 2013. s.l.:International Society of Offshore and Polar Engineers.

Praastrup, U., Jakobsen, K. P. & Ibsen, L. B., 1999. Two Theoretically Consistent Methods for Analysing Triaxial Tests. Aalborg: Computers and Geotechnics. Vol. 25(1999), pp. 157- 170.

Sabaliauskas, T. & Troya, A., 2014. Observations during static and cyclic undrained loading of dense Aalborg University sand no. 1. Aalborg: DCE Technical Memorandum No. 43.

Shajarati, A., Sørensen, K. W., Dam, S. K. & Ibsen, L. B., 2012. Manual for Cyclic Triaxial Test. Aalborg: DCE Technical Report No. 114.

Troya, A. & Sabaliauskas, T., 2014. Cyclic behaviour of undrained dense Aalborg University sand no. 1. Aalborg: DCE Technical Memorandum. Department of Civil Engineering, Aalborg University,.

Ibsen, L. B., 1995. The Static and Dynamic Strength of Sand. Copenhagen: European Conference on Soil Mechanics and Foundation Engineering

Paper G

The making of Andersen's liquefaction chart

Tomas Sabaliauskas, Lars Bo Ibsen

The paper has been published in the
DCE technical memorandum No.62, 2016.

The layout has been revised.

Abstract

This technical report contains supplementary material describing procedures used in triaxial testing result analysis. The content explains concepts relevant to very specific case study where triaxial test results were analyzed. Andersen's chart (Andersen & Berre, 1999) is a graphical method of observing cyclic soil response. It allows to separate cyclic stable soil states from cyclic unstable. Normally, the chart is obtained by manually fitting experimental measurements into a data plot. Here, steps of automating the procedure and normalizing the chart are provided.

1 INTRODUCTION

Cyclic undrained sand response is used in offshore engineering, to predict soil to structure interaction. Knut H. Andersen introduced a chart which describes undrained cohesionless soil response (Andersen & Berre, 1999). His chart was generated using dynamic, single diameter height, frictionless triaxial apparatus at Aalborg University by Troya, A. & Sabaliauskas, T., (2014). Andersen's method was modified during tests at AAU, improved methods of normalizing the chart, and algorithms which generate the chart atomically, were introduced. This makes generating the chart – more efficient, and after the chart is generated – improved normalizing allows to use it in a wider scope of application.

To obtain the Andersen's chart, undrained cyclic tests were done with varying stress amplitude τ_{cy} and average stress values τ_a (illustration of soil behavior during cyclic loading is given in Fig. G.1). If some particular configuration of amplitude and mean value leads to instability within soil – the Andersen's chart will predict it. Before each test τ_{cy} and τ_a were selected to target a specific position on Andersen's chart – thus higher concentration of measurements could be clustered in critical regions of the chart. As more data points were collected, position of the "failure" limit became more evident – and measurements clustered around the failure line. Automated algorithms, used to generate parts of the chart from incomplete data, allowed to target the failure line more efficiently.

2 SOIL USED

Silty sand taken from a wind turbine farm in Frederichaven, Denmark is used for testing. All samples are tested from initial conditions of pore pressure $\Delta Up = 200[kPa]$, initial confining pressure $p'_0 = 60[kPa]$, anisotropic K0 consolidation is chosen as the initial state reassembling in situ soil state for cohesionless soil with friction angle of approximately $\phi = 39^o$ giving ini-

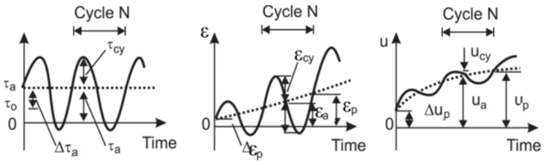

Fig. G.1: Cyclic, average and plastic components of shear stress, strain and pore pressure (Andersen & Berre, 1999)

tial sample state of $\sigma_1 = 161[kPa]$, $\sigma_3 = 60[kPa]$; Samples are dry tamped to 80% relative density (maximum porosity $e_{max} = 1.05$; minimum porosity $e_{min} = 0.64$).

3 UNDRAINED BEARING CAPACITY (NORMALIZING)

If the sample was loaded drained it would follow the Effective Stress Path (ESP line in Fig. G.2). Undrained dilative sand deaviates from the ESP path, and develops up the hidrostatic effective stress axis, until pore water reaches near -100kPa. Thus, both drained and undrained sand cross the same effective stress envelope, but they cross it in different positions – despite identical initial state. When dense sand is compressed to failure undrained, it dilates along some friction angle (points A-C in Fig. G.3). Dilation will force the confining pressure p′ to rise (while pore pressure is dropping). At some point pore pressure will reach near -100[kPa] and turn into gas (cavitate, at room temperature). As the stiffness of pore water is lost, water evaporates, specimen transitions into drained response - and the failure envelope is reached. Yielding is triggered (C-D in Fig. G.3, TSP-Ucav in Fig. G.2). Cavitation plays a definitive role in response of undrained, dense, cohesionless soil. It provides a strict limit which ultimate strength adheres to (Fig. G.2, Fig. G.5) (Ibsen, 1994) (Ibsen, 1995)(Nielsen & Ibsen, 2013) (Troya & Sabaliauskas, 2014). This was not taken into account in original work by Andersen (Fig. G.4). But since the maximum and minimum bearing capacity can be found from equations (2-3), the Andersens chart can be normalized within these limits.

$$P'_{LOCK} = p'_o + U_o - U_{cav} \tag{G.1}$$

$$\tau_{max} = -p'_{LOCK} \cdot \frac{sin(\phi)}{sin(\phi) - 1} \tag{G.2}$$

$$\tau_{min} = -p'_{LOCK} \cdot \frac{sin(\phi)}{sin(\phi) + 1} \tag{G.3}$$

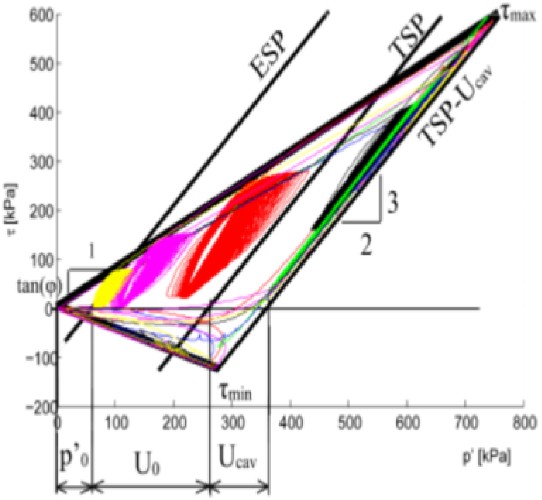

Fig. G.2: Multiple cyclic tests followed by ultimate bearing capacity crushing. Contained in a "triangle" consisting of friction angles and cavitation limit.

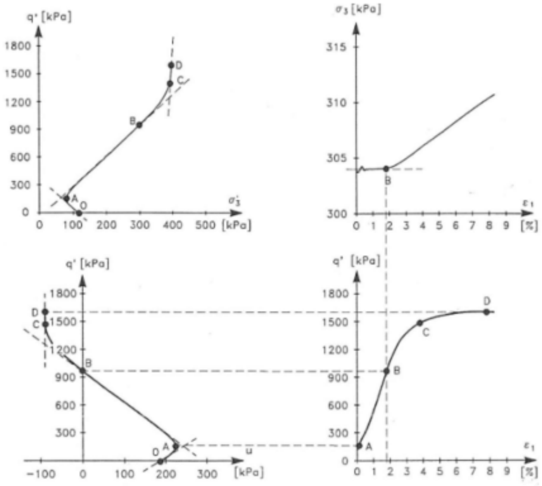

Fig. G.3: Pore pressure and strain of Monotonic CU triaxial on AAU sand 1. (Ibsen, 1995)

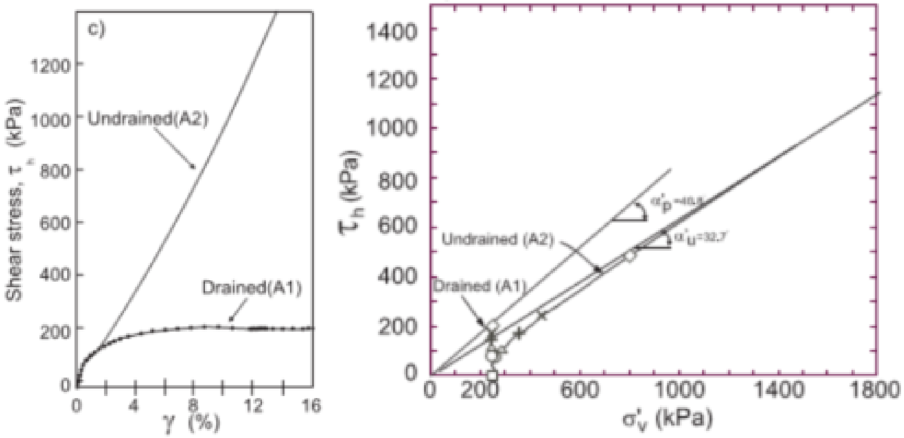

Fig. G.4: Andersen's stress-strain chart and principal stress DSS test – undrained response does not reach plastic failure due to extremely high initial pore pressure available for dilation. (Andersen & Berre, 1999)

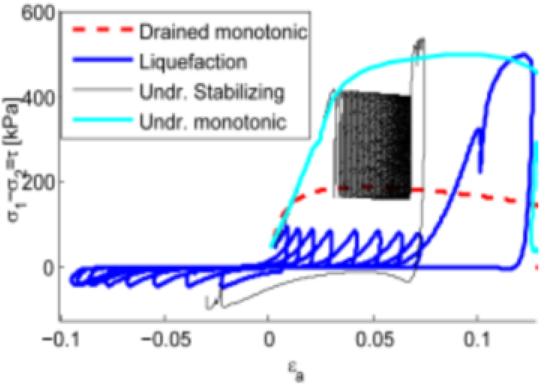

Fig. G.5: Undrained strength testing in various testing cases.

The provided bearing capacity expressions were suggested as a potential choice for normalising the Andersen's chart by Nielsen & Ibsen, (2013).

4 THE ANDERSENS CHART

Each sample starts from anisotropic – K0 state which is loaded over 1 hour of slow, drained loading. Then the valves are closed and a cyclic, sinusoidal shaped load is applied. No additional preloading was applied. Tests revealed 3 distinct zones within the Andersen's chart.

1. Liquefaction failure (two way loaded)
2. Incremental failure (one way loaded case 1)
3. Stabilization (One way loaded case 2)

Stress reversal causes liquefaction, and incremental collapse was encountered if one way loaded cycles were not too far from being two-way loaded. (Fig. G.6). (Ibsen, 1994) (Ibsen, 1995) (Andersen & Berre, 1999) (Nielsen & Ibsen, 2013) (Sabaliauskas & Troya, 2014). Testing was optimized toward finding an isoparametric line which shows stress states reaching 10% axial strain at 1000 th cycle. 1000 cycle limit was chosen because it approximates the number of waves during a 3 hour storm peak in typical storm in North Sea. During testing it was found that 1000 cycles produce a very steep function separating stable response from unstable, thus clustering around this line was essential. To illustrate the need for "targeting the line", a line with similar τ_{cy} is shown in In fig Fig. G.6. Notice, how holding τ_{cy} constant crosses the "failure line" twice. The objective of testing was to find settings as close to the "failure line" as plausible, by modifying τ_a , while τ_{cy} is held constant. Alternatively, if Ta is held constant – τ_{cy} position can be modified. Notice, both τ_a and τ_{cy} are absolute stresses (not effective stress). The original chart, proposed by Andersen, was normalized using drained stress σ'_{vc} (Fig. G.8). Normalizing undrained response with drained strength is not the correct approach. Undrained ultimate strength for dense, cohesionless soil can be reliably quantified as shown previously, by formula 2 and 3. When using the undrained yield strength to normalize undrained Andersen's chart – the axis become contained between -0.3 and 1, as visible in Fig. G.6 (note, the value on the negative side is not fixed to -0.3, the value depends on the friction angle).

5 TRIANGULATING THE ANDERSEN'S CHART

While linear interpolation with constant τ_{cy} or constant τ_a is a valid option, it is not a very efficient way of generating a surface plot. A better approach

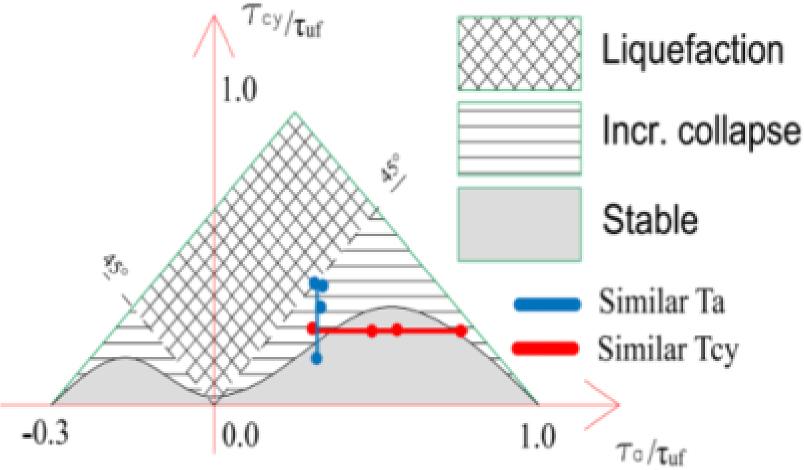

Fig. G.6: Normalized schematic of observed response.

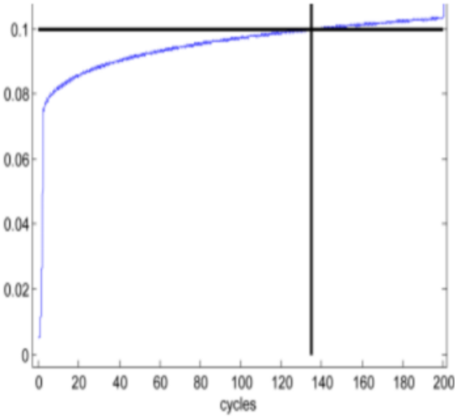

Fig. G.7: Strain development with cycles and Strain peak detection.

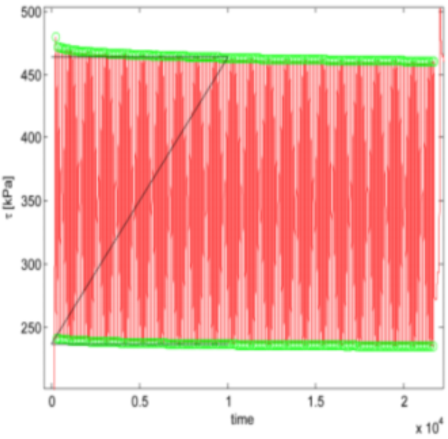

Fig. G.8: Stress peak identification and position of averaged values.

would be to plot what is "visible" at each step, using measurements available before the final version of the chart is known. Then, parts of the picture, which need "improved definition", could be targeted. This was accomplished by meshing the test data with triangular surfaces, and then color plotting the 3d surfaces along the Z axis. With each test the triangulated surface would update itself automatically, and the researcher could choose which part will be refined further during the next test. Each data point has 3 coordinates - τ_a , τ_{cy} and the number of cycles n. The value of n depends on "failure strain limit" defined by the user (as illustrated in Fig. G.7). And number of cycles leading to each strain increment is obtained using two sided peak detection (shown in Fig. G.8).

Collection of 3 coordinates (τ_a , τ_{cy} and n), obtained from testing is used together with collection of points set manually. If the cycle amplitude τ_{cy} =0[kPa], no cyclic loading is applied. This is equivalent to monotonic loading, which does not fail until τ_a reaches the ultimate undrained failure. Thus, for all points where $\tau_{cy} = 0[kPa]$, n=1000 cycles. Similarly, if $(\tau_a + \tau_{cy}) > \tau$ max or $(\tau_a - \tau c y) < \tau_{min}$ the sample will cross the ultimate strength before completing the first cycle. Thus the outer perimeter of the triangle is set to n=0 cycles.

At this point the chart can be interpolated by triangulation. A surface is formed by connecting the nearest points into a triangles (Delaunay triangulation). As more tests are done, definition of the chart is increased. Fig. G.10 shows a chart near its final stages. However, there are some final changes that need to be done - cases where uncertainty is encountered by Delaunay triangulation algorithm. The uncertainty can be solved by either making an additional test, to provide an additional point of τ_a , τ_{cy} and n coordinates.

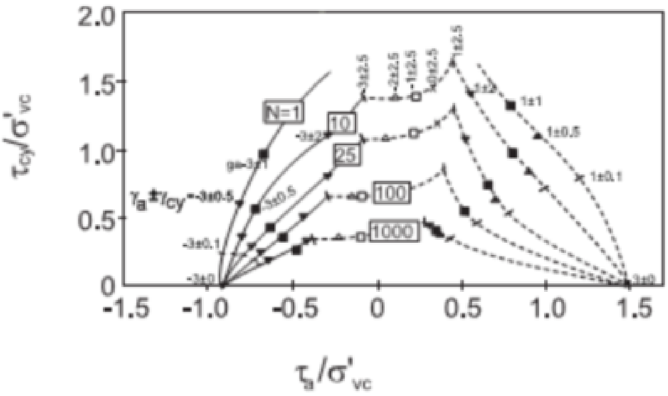

Fig. G.9: Original Andersen's chart for undrained soil response (normalized by drained confining pressure)

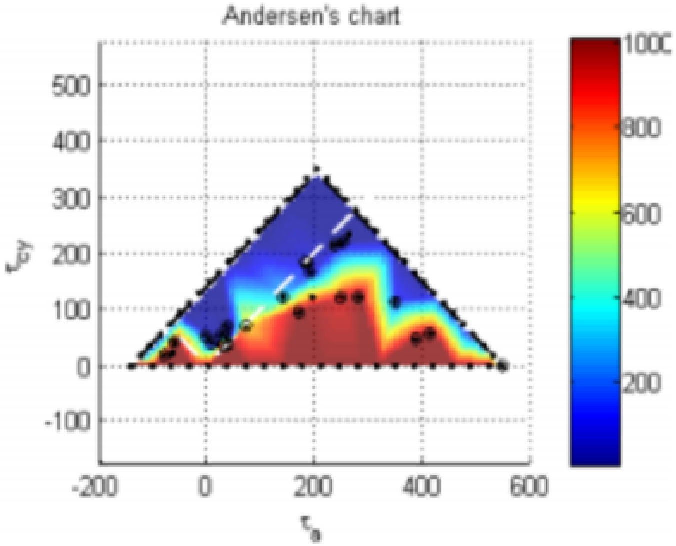

Fig. G.10: Andersen's chart before manual corrections. Dots indicate tested points. Fully autonomous generated by algorithm – some triangulation error present.

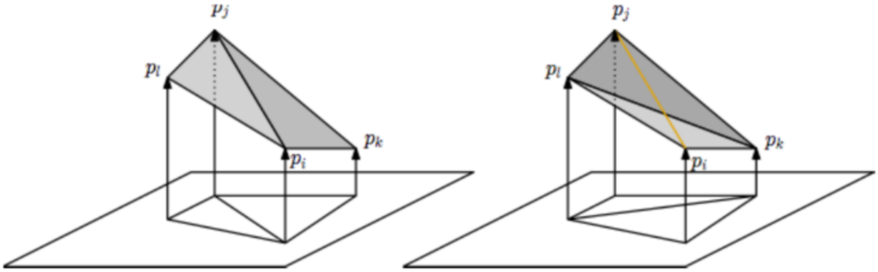

Fig. G.11: “Edge flipping”. There are 2 ways of connecting 4 points into triangles. Manual identification of the correct one might be necessary.

Or, the required values of τ_a , τ_{cy} and n can be linearly interpolated between two measurement points to fine-tune the triangle edges.

6 FINE TUNING TRIANGLE EDGES

Given 4 points, there are 2 ways to connect them into triangles. Both are illustrated in Fig. G.11. If a 5th point is added by interpolating it on one of the 2 plausible lines, the user can "flip" the edge towards the preferred outcome. Thus, the final chart will have 3 sets of τ_a , τ_{cy} and n coordinates:

1. Test results
2. Boundary points
3. Edge flipping interpolation

And the resulting chart is shown in Fig. G.12.

7 BIBLIOGRAPHY

Andersen, K. & Berre, . T., 1999. Behaviour of a dense sand under monotonic and cyclic loading comportemen, Amsterdam: European Conference on Soil Mechanics and Geotechnical Engineering.

Andersen, K. H., 2009. Bearing capacity under cyclic loading — offshore,. Oslo: The 21st Bjerrum. Hettler, A. & Vardoulakis, I., 1984. Behaviour of dry sand tested in a large triaxial apparatus. s.l.:Geotechnique 34.2 (1984): 183-197..

Ibsen, L. B., 1994. The stable state in cyclic triaxial testing on sand. Aalborg: Soil Dynamics and Earthquake Engineering 13 (1994) 63-72 .

Ibsen, L. B., 1995. The Static and Dynamic Strength of Sand. Copenhagen: European Conference on Soil Mechanics and Foundation Engineering.

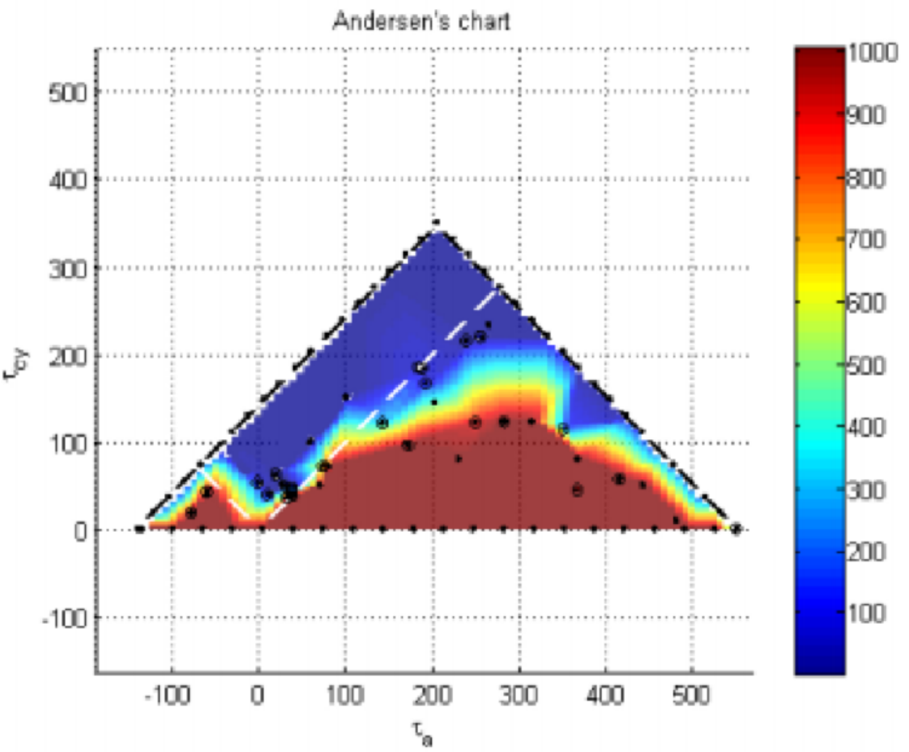

Fig. G.12: Andersen's chart for Frederic haven silty sand – not normalized, raw data for 10% axial strain limit.

Nielsen, S. D. & Ibsen, L. B., 2013. s.l.:International Society of Offshore and Polar Engineers.

Praastrup, U., Jakobsen, K. P. & Ibsen, L. B., 1999. Two Theoretically Consistent Methods for Analysing Triaxial Tests. Aalborg: Computers and Geotechnics. Vol. 25(1999), pp. 157-170.

Sabaliauskas, T. & Troya, A., 2014. Observations during static and cyclic undrained loading of dense Aalborg University sand no. 1. Aalborg: DCE Technical Memorandum No. 43.

Shajarati, A., Sørensen, K. W., Dam, S. K. & Ibsen, L. B., 2012. Manual for Cyclic Triaxial Test. Aalborg: DCE Technical Report No. 114.

Troya, A. & Sabaliauskas, T., 2014. Cyclic behaviour of undrained dense Aalborg University sand no. 1. Aalborg: DCE Technical Memorandum. Department of Civil Engineering, Aalborg University,.

Paper H

The guessing game. Analysis of cyclic loaded foundation as a finite state transition system

Tomas Sabaliauskas, Lars Bo Ibsen

The paper has been published in the
DCE technical memorandum No.249, 2018.

1 Introduction

Episodic loss and recovery of stiffness is observed in full-scale offshore foundations [27], [9]. This phenomenon is especially relevant to offshore wind turbines, as the slender structures rely on foundation stiffness to avoid resonating with cyclic loads. Unfortunately, dynamic loaded sand response (and therefore foundation response) is not well understood [10]. Sand has notoriously non-linear, counter intuitive properties, which arise from the very nature of this material: sand is made of individual grains. The grains rearrange and re-interlock, forming complex networks of force chains [37], [6]. Each time sand is deformed, the soil fabric is disturbed permanently: the grains physically rotate and move to a new arrangement. Consequently, the same loads generate different outcomes, depending on how the grains are arranged (as shown in Fig.H.1).

There are infinite number of unique grain arrangements (soil states S). If the same action of testing (At) is applied starting at different arrangement S, each S generates a unique stiffness path $\pi(S, At)$ (see Fig.H.1). However, some $\pi(S, At)$ look similar. Therefore, can be grouped together: if $\pi(S1, At) \approx \pi(S3, At)$, then $S1 \approx S3$. The opposite is also true: if $\pi(S1, At) \not\approx \pi(S2, At)$, then $S1 \not\approx S2$. Thus, similar (equivalent) soil states can be categorized relative to each other. This allows to discretize an infinite-state problem into a finite-state transition system. Based on this premise, a novel, original testing procedure was formulated.

The original testing procedure introduced here is called "the guessing game". The procedure begins with acknowledging that the "initial state" of soil is not known. This is the case for wind turbine foundations during a storm - the soil is repeatedly disturbed and stabilized, thus the "initial" state is not known,. However, a test starting with unknown soil state $S*$ can be tested by some action of testing At. Thus, generating a reference stiffness path, a "signature" $\pi(S*, At)$. The signature serves as a reference, according to which $\pi(S*, At)$ can be categorized. If at some point the same stiffness path is generated by At, one can say the "initial stiffness path" was reset (meaning, the "initial state" was reset). Such is the ultimate goal of the guessing game - to find a path back to "initial stiffness path".

The guessing game maps soil states into a decision tree, where S are the nodes and A are the links. Sequences of actions preserved in A vectors cause transition from one soil state S to another. The decision tree grows by iterating through sequence $S* \xrightarrow{At} S \xrightarrow{A*} S*$. Each cycle has an inductive phase (reaching for unknown soil state $S*$ by guessing $A*$) and a deductive part (converting unknown $S*$ to known S through applying At to test for the signature). As the causal tree grows, knowledge is preserved: as $S*$ get converted to S, it becomes plausible to deterministically predict which S will be

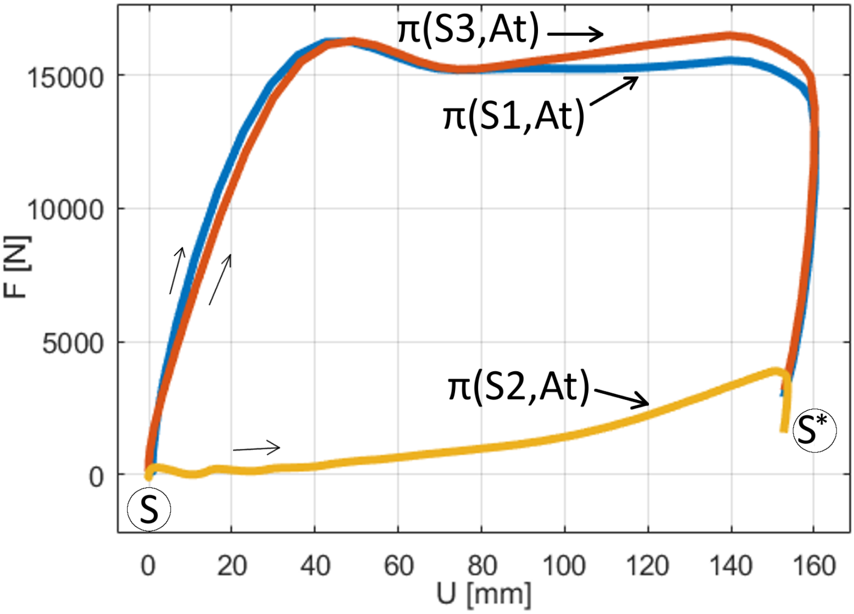

S*=π(S,At); Where At is full speed pull to U=160 [mm]

Fig. H.1: The same action generates different outcomes. Three different stiffness paths $\pi(S, At)$ were generated by the same action At. Different S was present before the At, thus each S, At combo leaves a unique "signature". If equivalent signatures are put into discrete categories $(S1 \approx S3; S2 \not\approx S3)$, infinite-state is deduced to a finite-state problem.

caused by action A. As the game progresses, sequences of actions within A vectors become shorter. When the decision tree converges, vectors A contain purified causation, which allows to move from S to S using the shortest route.

The guessing game was contemplated intuitively from exposure to philosophy of science and principles found in machine learning and computer engineering (state-transition systems). The principle implements ideas inspired by work of Thomas Kuhn [4], where truth is described as both observable (inductively) and non-falsifyable (deductively). Inductive phase embraces "guessing" - extrapolating towards unknown soil states from a known one (observable). Deductive phase embraces removal of irrelevant factors from A links (removing what's falsifiable). The case study presented in this paper uses the guessing game to analyze properties of a cyclic loaded foundation prototype embedded in sand. At first glance it may seem tempting to use conventional geotechnical models for "guessing", but convention collapses at a certain point: loading scenarios combining drained and undrained response during irregular loading cycles, reaching highly disturbed soil states, which are then reversed back to initial state - are beyond the scope of convention. Thus, convention is avoided. When guessing, $A*$ are intentionally randomized and scrambled to explore counter intuitive corners of the finite-state system. The problem is treated like a genuine state-space transition system. The user is given a joystic attached to a hydraulic piston pushing a foundation prototype back and fortH: Then, the "player" is given the task to find a sequence of A which would re-generate the first stiffness path $\pi(S_o, At)$. Thus, essentially disturbing the foundation back to "initial" state. Decisions are made following intuition and real-time decision making, rather than premeditated action sequences. The player is challenged to generate and test ad-hoc mental models and assumptions following real-time feedback from the object being tested.

2 Equipment

Aalborg University (AAU) geotechnical laboratory has a long history of R&D in geotechnical testing equipment. From frictionless triaxial and consolidation apparatuses [23], to sand boxes recreating water pressures found at the sea floor [25]. The sand boxes are used for testing the mono-bucket foundation - an innovative offshore wind turbine foundation, designed to compete with mono-piles. After decades of R&D, the mono-bucket has recently entered offshore wind turbine market. The patented concept is now represented by Universal foundation A/S. The mono-bucket uses less steel and is installed faster than a mono-pile. Also, installation of the mono-bucket is quiet, and it can be decommissioned without leaving a footprint (removed by reversing the suction pump, thus pushing the suction caisson out of the

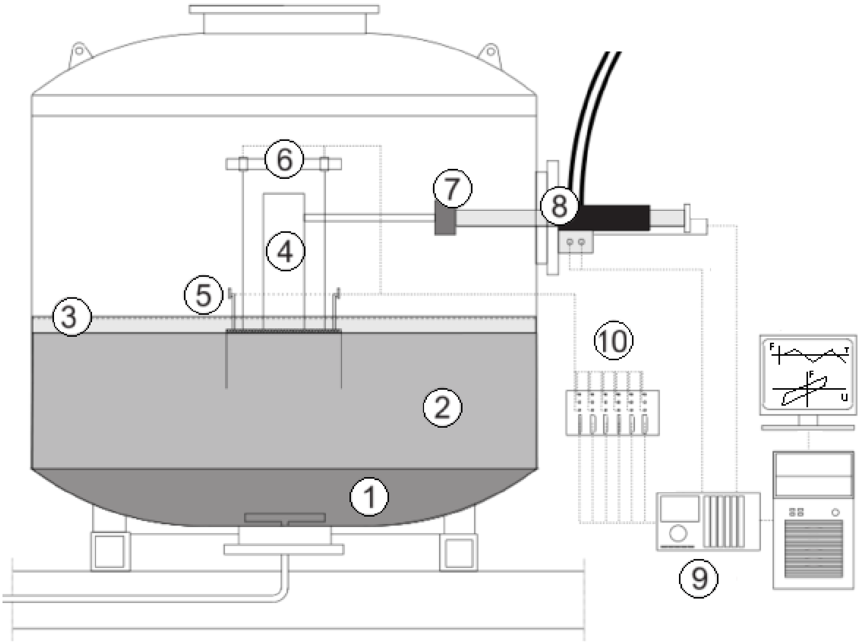

Fig. H.2: The testing-rig. A sand box within a pressure chamber, for small scale foundation testing. 1) Bottom layer of soil is gravel. It acts as a filter for drainage tubes. 2) Aalborg University sand No.1. 3) Water head above soil level. The soil is fully saturated at all times. 4) The monobucket, attached to a shaft. 5) Valves and warer pressure transducers, measuring water pressure along the skirt, and below the lid. 6) Displacement transducers. A total of three displacement are measured. 7) A load cell, measuring focre. 8) A high pressure, digital walve controolled piston. 9) MOOG controller / data logger, with automated load control and realt ime data plotting options. 10) MGC plus data acquisition box [29]

sea floor). Research of the mono-bucket is part of M.Sc. and PH:D. theses at AAU. Consequently, a small scale mono-bucket was readily available for the case study presented in this paper. Schematics of the testing rig and the mono-bucket used are given in Fig.H.2 and Fig.H.3.

The testing rig (Fig.H.2) contains a sand box inside a pressure chamber. The pressure chamber allows to generate pore water pressures found at the sea floor. $200 kPa$ pressure is used to imitate $20 m$ water head. Pressurizing the water is important for undrained soil response, encountered during rapid (impact) loading. If sand is deformed fast, undrained response is generated. The pore water cannot escape, the volume of voids becomes "locked" by pore water stiffness. This makes dilative sand (and structures built in it) much stronger and resistant to impact loads [45], [29]. The benefit of increased peak strength is counter balanced by the potential of losing stiffness due to liquefaction. Especially during two-way cyclic loads [34], [35]). The additional undrained strength component is called "the boot effect" by some

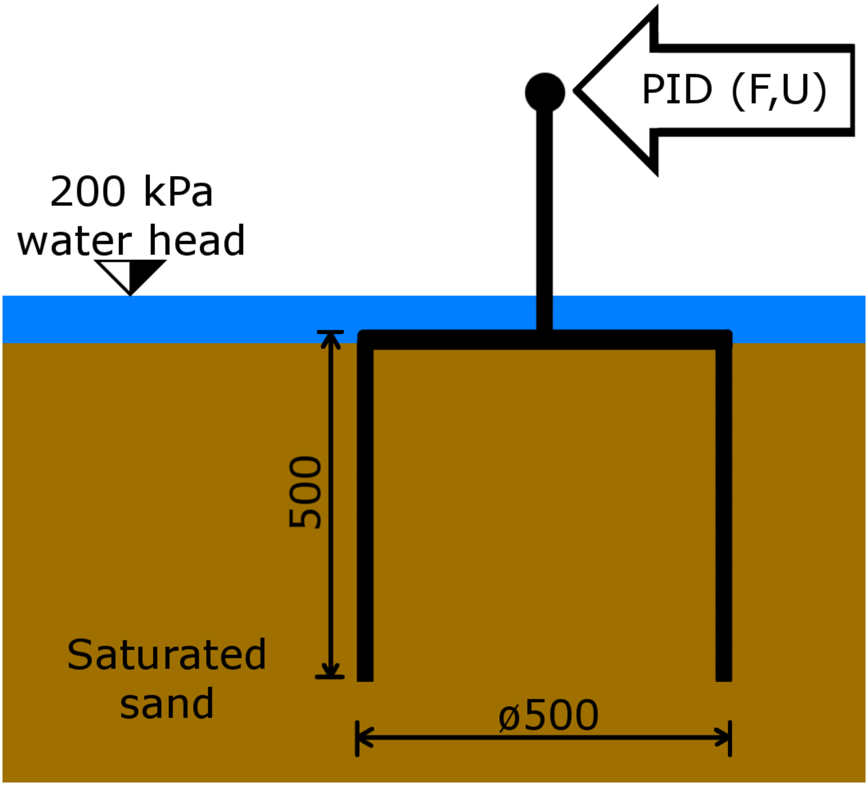

Fig. H.3: The small scale mono bucket foundation is inserted in fully saturated sand. Either force or displacement can be applied horizontally on the top tip of the shaft. The testing rig is placed within a pressurized chamber, where 200 kPa pressure is applied to imitate 20 m water deptH: The extra pore pressure is important for increasing dynamic peak strength [29], [45], [19]

.

authors [25], because to pull a boot out of mud one has to pull slowly - fast loads generate additional pore water pressures, which add resistance. Interestingly, the case study presented here shows the boot effect is lost when stiffness is lost, and recovers when stiffness recovers. Thus, the boot effect is a "state dependent" phenomenon as well, pore pressure effects are part of the stiffness path generated during $\pi(S, At)$. Thus, if the initial soil state is recovered, the boot effect will recover with it. High water pore pressure amplifies the boot effect, thus the boot effect is especially relevant for deep water foundations [21].

In the testing rig (Fig:H.2) a mono-bucket prototype is inserted in sand. A simplified schematic of the test is given in Fig.H.3. The caison foundation has a large diameter lid, with a skirt along the periphery. The large diameter skirt provides large leverage, which makes skirt friction more efficient at resisting overturn moment. In addition, the lid provides a large surface for distributing the vertical load (static weight of a wind turbine). Thus, the mono bucket acts like a gravity foundation, distributing the vertical load across a large surface area, while the skirt is optimized to resist overturning. Together, the two components form a water tight caisson, which traps a large mass of soil and water. Thus adding mass for added stability.

As mentioned earlier, the mono-bucket is meant to rival mono-pile foundations. The purpose of the mono-bucket is to improve current offshore industry standard for intermediate water depth offshore foundations. The mono-bucket is lighter in weight, faster to install [28]. The mono-bucket can also be quickly and cheaply un-installed, without leaving a footprint. In addition, there is no need for scour protection, as the lid itself protects against scour [40]. Thus, the mono-bucket has the advantages of cheaper production, faster installation, easy decommission, and no added costs associated with noise mitigation or scour protection. Despite all the benefits, the mono-bucket is a novel concept, which brings higher risk factors. Potential clients are cautious of novelty largely because dynamic loaded sand properties are not well understood [10], and the mono bucket provokes a complex array of phenomenon combining drained, undrained and partially drained soil response. Thus, tests researching the dynamic properties continue, and the new approach (the guessing game) is attempted to gain new knowledge. The prototype in Fig.H.3 is Ø500 mm in diameter, and 500 mm in height. The skirt is 6 mm thick. There is one, horizontal hydraulic piston attached at the top of the shaft (the shaft is approximately 300mm long). The hydraulic piston if controlled by proportional-integral-derivative (PID) controller, with a load cell and a displacement transducer attached to the piston.

3 Methods

The testing equipment is rather simple - a hydraulic piston pushing / pulling a foundation at the top of the shaft. The hydraulic piston applies the inputs, the foundation generates outputs. The equipment is simple in construction, but the foundation prototype generates complex, nonlinear, state-dependent outputs. To make analysis manageable, the problem is reduced to a minimum number of variables - stiffness is observed by monitoring force (F) and displacement (U) at the tip of the shaft (see Fig.H.3). In this study U is used as the input, F is measured as the output.

U is used as the input because "we can always map to load from displacement, but not always from load to displacement" - David Muir Wood lecture, 2015. Using F for input imposes significant limitations. Firstly, F inputs are only conditionally stable: given F beyond the peak strength U accelerates towards infinite, causing loss of control and endangering the testing equipment. F cycles are plausible to apply only within the limits of peak strengtH: Secondly, even within confines of peak strength limits, F inputs provoke a combination of nonlinear stiffness (K), damping (C) and inertia (M) forces (see equation of motion, Eq.H.1). Thus, applying F provokes three nonlinear components - state dependent $K \cdot U$, state dependent $C \cdot \frac{\delta U}{\delta t}$, and state dependent $M \cdot \frac{\delta^2 U}{\delta t^2}$. This means that, whenever F is applied as the input, the output is encrypted under three layers of nonlinear state functions. Which is very hard to decipher, as the equation $K = U^{-1} \cdot [F - \frac{\delta U}{\delta t} \cdot C - \frac{\delta^2 U}{\delta t^2} \cdot M]$ would have to be solved, while all three: K, C and M are unknowns.

$$F = K \cdot U + C \cdot \frac{\delta U}{\delta t} + M \cdot \frac{\delta^2 U}{\delta t^2}. \tag{H.1}$$

On the other hand, when U is the input, it is applied wile controlling $\frac{\delta U}{\delta t}$ and $\frac{\delta^2 U}{\delta t^2}$. Therefore, attempts can be made to find loading setting where $\frac{\delta U}{\delta t} \to 0$, thus making $C \cdot \frac{\delta U}{\delta t} \approx 0$. Also $\frac{\delta U}{\delta t}$ input can be varied very slowly, making $\frac{\delta^2 U}{\delta t^2} \approx 0$. Thus, allowing to cancel two out of three components in equation of motion, consequently isolating $F = U \cdot K$. This allows to analyze state dependencies of quasi-static $K = \frac{F}{U}$. If (in the future) phenomenon governing K are fully understood, then the loading rate could be increased to where $C \cdot \frac{\delta U}{\delta t} \not\approx 0$, and the effects of C could be isolated by solving $C = \frac{\delta t}{\delta U}[F - K \cdot U]$. Alas, rules governing quasi static K must be discovered beforehand. Nevertheless, using U as the input has the potential to observe one nonlinear (state dependent) component at a time, and potentially decode the entire nonlinear, state dependent equation of motion.

For reasons given, U is defined as the input. The F is plotted (and analyzed) as a function of U (the foundation is treated as an $F(U)$ system). Analysis of resulting data plots is conducted purely graphically: measured data is plotted, stiffness paths $\pi(S, At)$ are visually inspected, and the player makes real time judgment based on charts plotted on the computer screen, during real-life, real-time testing. The goal is to recover the "initial" stiffness path $\pi(S_o, At)$. Because the method to reset the initial state are not known, the researcher has to begin the procedure by blindly guessing the action sequence $A*$, Then, after $A*$ is applied, consequent state $S*$ is tested using At, and the guessing game continues. Once a sequence A leading to S_o is found, the game can continue to improve efficiency of the solution by looking for causal factors within the A sequence. The game ends when the causal factors governing cyclic foundation stiffness are found - the optimal path to S_o is found.

As mentioned in the introduction, the guessing game draws a causation tree, a type of a flowchart. Links are inductively guessed and deductively trimmed. In the process, a finite set of data structures can be encountered. To illustrate them, the links and nodes are divided into subcategories: four

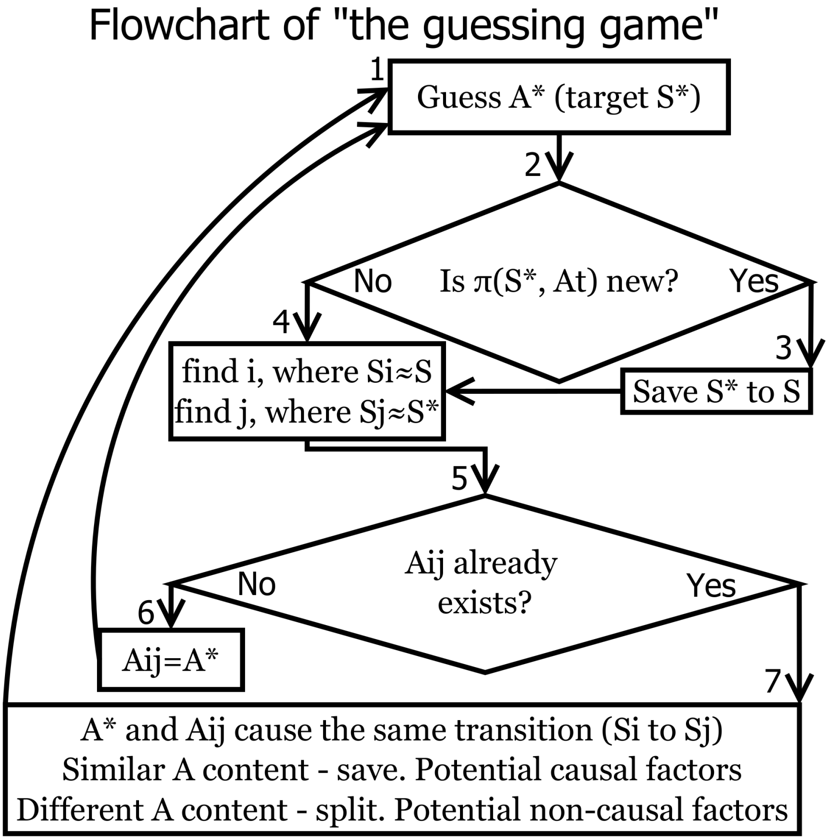

Fig. H.4: The three stages of "the guessing game". Detecting new nodes, detecting links, detecting conflicts between guessed and known links.

1. Nodes - the consequences of applying A.
    - (a) Known (S). States with known signatures, tested by At (marked as $S\overset{At}{\to}$ in diagram Fig.H.5).
    - (b) Predictor (S^*). States with unknown signatures, before applying At.
2. Links (sequence of actions) - the causes of changing S.
    - (a) Predictor (A^*). Scrambled, randomized, guessed action sequence with unknown outcome, creating $S*$.
    - (b) Transition (A_{ij}). Action sequence known to cause transition from S_i to S_j.
    - (c) Self reference (A_{ii}). Action sequence preserving the same S after testing.
    - (d) Causal action (Aj). Action which causes Si to occur regardless what S the Aj is applied from.

Table H.1: Types of nodes and links encountered during the guessing game.

types of links, and two types of nodes (see Table.H.1).

Known node (S): In a deterministic finite-state system, pairs of S are connected with one unique A. Thus each $\pi(S, A)$ has unique outcomes. If applying the same A sequence generates different $\pi(S, A)$, the cause can only be attributed to difference in S.

Predictor node ($S*$): States with unknown $\pi(S*, At)$. The $S*$ can be generated in two ways - by interpolating or extrapolating. Interpolation is plausible, because S changes gradually. Soil grains do not "teleport" from one arrangement to another. Thus, if a known sequence A is paused before completion, the transition $S_i\overset{A_{ij}}{\to}S_j$ is split into $S_i\overset{A_{ik}}{\to}S_k^*\overset{A_{kj}}{\to}S_j$. Thus, S_k^* is predicted (interpolated) between two known states. Similarly, S^* can be extrapolated, by starting from a known S and applying a sequence which has not been applied there: $S\overset{A*}{\to}S*$, where S is known, but the action A^* had never been applied starting at S. Thus, extrapolating into unknown.

Predictor link (A^*): When actions $A*$ are applied for the first time, the consequent $S*$ is unknown. It is not known what $S*$ is created by $A*$ until the signature $\pi(S*, At)$ is tested. The uncertain outcome means $A*$ can either

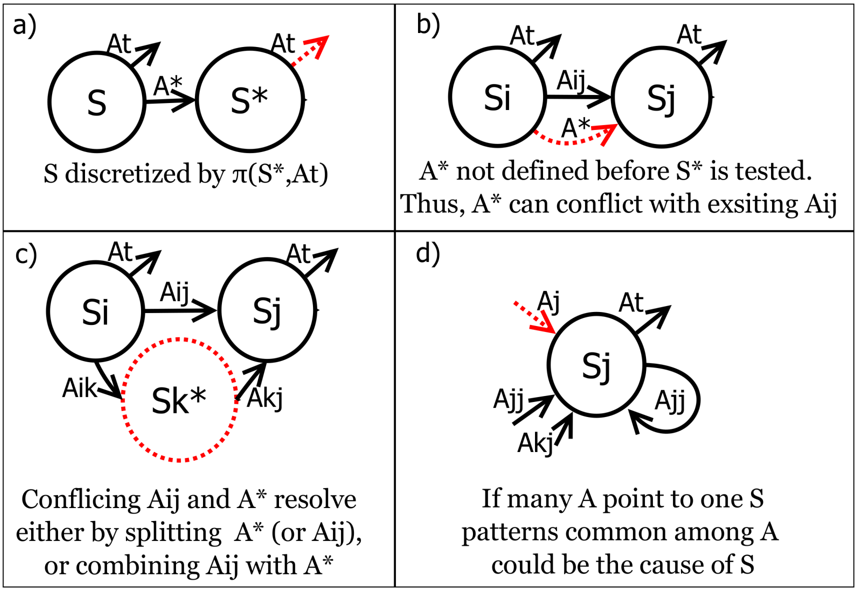

a) S discretized by π(S*,At)

b) A* not defined before S* is tested. Thus, A* can conflict with exsiting Aij

c) Conflicing Aij and A* resolve either by splitting A* (or Aij), or combining Aij with A*

d) If many A point to one S patterns common among A could be the cause of S

Fig. H.5: Key data structures observed during "the guessing game".

detect a new link, or cause a conflict with already known A_{ij}. (see Fig.H.5-a,b)

Transition link (A_{ij}): Actions causing transition from S_i to S_j. Only one A_{ij} can be defined between S_i and S_j. When A_{ij} is observed for the first time, the action sequence will not be optimal. As the game continues, $A*$ will start to conflict with existing A_{ij}, causing the same transition to occur using two different paths (see Fig.H.5,b). The conflict can be resolved in 2 ways: either by splitting A_{ij} and introducing a new node S_k* (Fig.H.5,c), or combining the conflicting A_{ij} and $A*$ deductively (Fig.H.5,d). Similarities between conflicting $A*$ and A_{ij} are potential causal factors. Transition from S_i to S_j is causal, thus if $A*$ and A_{ij} have similarities - those are likely to be a causal factor. Differences in conflicting A_{ij} and $A*$ are non-causal factors, which allows to deductively trim the sequence saved in A_{ij}.

Self reference link (A_{ii}) A special case of A_{ij} is when $i = j$. This means the S_i was either not disturbed at all by actions in Aii, or the Si was both disturbed and reversed during the sequence A_{ii}. The correct case can be diagnosed by splitting $A_{ii} = A_{ij} + A_{ji}$, and interpolating $S*$. In data plots, such structures generate self overlapping hysteresis loops. These are very interesting, as they provide an observable reference point which can be detected without applying At. Thus, self overlapping hysteresis loops can serve as a local convergence point, which helps the user to orient within the decision tree without using At.

Causal link (A_j) A special case of A_{ii} is A_j, which can be deduced after multiple A are noticed to point towards one S (Fig.H.5,d). If Sj has a cause, and the cause is purified, then regardless what S or $S*$ the A_j is applied from, the outcome is always Sj. This case can be written as $Sj = \pi(S*, Aj)$. The objective of the entire game can be defined as looking for Ao, as Ao is the action guaranteed to recover So - the initial stiffness path $\pi(So, At)$. This is only plausible if Ao contains the causal factor governing the "initial state". Thus, by analyzing Ao, the cause could be extracted and implemented in a physical model of the system being analyzed.

When implemented, the subcategories of nodes S and links A allow to propagate knowledge through the causal tree - known sequence At allows to convert unknown $S*$ into known S. Known S are used to convert unknown $A*$ into known A_{ij}. Known A_{ij} start conflicting with $A*$. Through deductive resolve, A_{ij} are trimmed down to A_j, and finally Ao. It is remarkable "knowns" can be used to define "unknowns".

4 Results

While playing the guessing game, a phenomenon was discovered. The phenomenon of converging stiffness hysteresis loops. When deformation cycles of amplitude $Umob$ are applied at the tip of the foundation prototype, stiffness hysteresis loops converge to a stable contour (see Fig's. H.6, H.7). This means the soil structure goes through a sequence of equivalent S states, in a closed loop. A sequence of S becomes locked in a phase dependent, temporally "stable state". In state transition diagram, this is a self referencing structure $S_i \xrightarrow{A_{ii}} S_i$ (see Fig.H.5).

It is interesting to analyze the phenomenon in more detail. The stiffness hysteresis loops shaped during $\pi(S, Umob)$ converge towards the same $Fmob$ amplitude. Every hysteresis loop is parametrized by unique $Umob$, but they all share the same $Fmob$ limits. If $Umob$ amplitude is made smaller (see Fig.H.6), the $Fmob$ limits graduall converge towards a hysteresis loop within the "min" and "max" limits. Similarly, if $Umob$ amplitude is increased (see Fig.H.7), the $Fmob$ gradually adapts as well. In both cases, the same F limits are followed, but given smaller $Umob$ amplitude the hysteresis loop is steeper (higher stiffness), while larger $Umob$ amplitude creates a hysteresis loop stretched across a larger deformation amplitude, thus stiffness is lower. This reveals an interesting feature of the system: it is not plausible to tell which stable state is currently active, by looking at $Fmob$ amplitude (all stable hysteresis loops share the same F limits), but each stable state can be

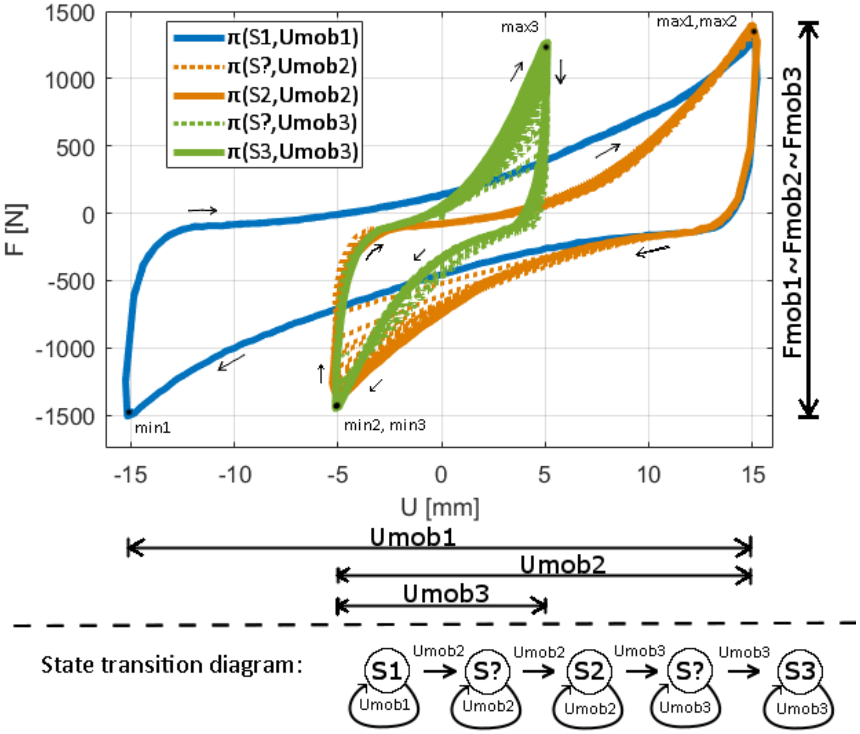

Fig. H.6: Deformation cycles transitioning from bigger to smaller *Umob*. Notice, all *Umob* converge to similar *Fmob* amplitudes.

uniquely described, predicted and controlled by *Umob* (stiffness hysteresis loops are uniquely dependent on *Umob* amplitude). Thus, it is not plausible to predict which hysteresis loop is active by observing *F* amplitude. The hysteresis loops can be uniquely described, predicted and prescribed only by observing / controlling the *Umob* parameter.

The observed *Fmob* and *Umob* relationship allows to deduce a causal pattern: all *Umob* converge towards one *Fmob* (given a constant loading frequency, 0.1 Hz in this case). Thus, *Fmob* can be efficiently expressed as a function of *Umob*. However, the opposite is not true, *Umob* cannot be defined as a function of *Fmob*, as one *Fmob* is shared by infinite *Umob*. This makes sense given the fact that deformation is essential for soil grains to rearrange (soil state *S* to change). Stress cycles can be applied without moving the grains. Whereas deformation forces the grains to move, rotate and re-arrange. If the force is removed, but deformation is applied - soil state changes. Whereas, locking the grains together (removing the deformation) and applying the stress cycles would not change the soil state.

During each deformation cycles, infinite different *S* are transitioned, as

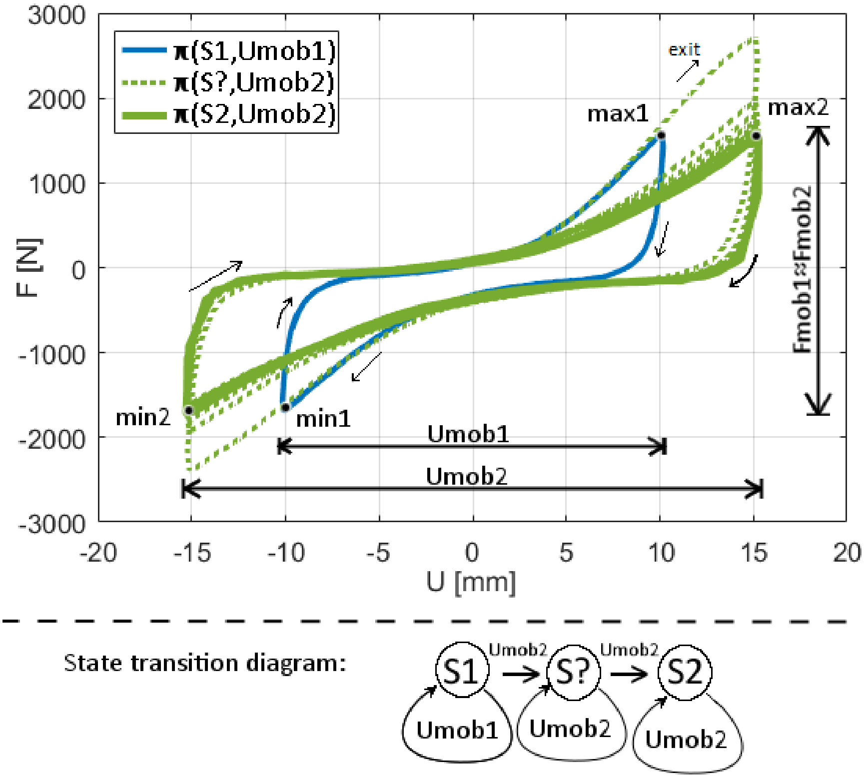

Fig. H.7: Deformation cycles transitioning from smaller to bigger *Umob*. Notice, both *Umob* converge to similar *Fmob*. Upon exiting *Umob*1, the tangent stiffness path shoots above the *max*1. But *F* at *max*2 stabilizes equivalent to *F* at *max*1.

the transition is gradual - grains do not "teleport" from one arrangement to another. (sequence A_{ii})), the S being transitioned overlap in phase with equivalent S sequence generated during the previous loading cycle. Thus equivalent S re-occur in phase with the deformation cycle. A temporal "stable state" is reached, the phase dependent S pattern becomes synchronized, "locked" in a temporal loop (note, the hysteresis loops in Fig's H.7 and H.6 were generated at 0.1Hz frequency).

When exiting the stable state, the exit path follows a tangent trajectory. This is visible in Fig.H.7 while exiting point $max1$. This indicates that stable states generated at smaller $Umob$ will have a steeper exit patH: To test this hypothesis, three stable states were generated at different $Umob$ amplitudes. The stable states were paused at the same deformation phase, to generate comparable exit paths. The result is shown in Fig.H.8. As expected, the smaller the $Umob$ the steeper the exit path (dynamic stiffness, combining K and C component from equation of motion).

At this point some causal assumptions can be made - if the "exit" stiffness path depends on the phase and diameter of $Umob$, then the initial stiffness path could be recovered by applying gradually smaller $Umob$, until the "initial" stiffness fully recovers. This assumption was tested, and the result is plotted in Fig.H.9. To evaluate success of stiffness recovery, stiffness paths generated using the new hypothesis are compared with pre-existing research of mono-bucket foundation. The "original" path is borrowed from preexisting research [25], [29].

In Fig.H.9 the "original" stiffness path was generated by following a labor intensive procedure, where the foundation prototype is removed using a crane, then water is allowed to rise from below the sand - producing an upward seepage gradient which loosens the soil. Then the soil is vibrated using an industrial vibrator and CPT tested in different spots of the testing rig to check if CPT results are consistent. The foundation prototype is then pushed back into the sand, cyclic loaded with small force amplitudes to emulate stabilization caused by small loading cycles prior to a storm. And then the At action is applied. Thus, "the original" stiffness path takes 2 days of preparation to execute one At test lasting just a few seconds.

Two days of preparation for a two second test is not very efficient. Worse yet, the "original" preparation method is both heavy manual labor and struggles to repeat the exact initial state So (manual labor brings human errors). The state transition analysis reveals a novel way to reset the initial state So - by applying gradually smaller $Umob$ amplitudes. Using the new method, At is applied starting with soil states $S1$ to $S5$ in Fig.H.9. Soil states $S1$ to $S5$ can be renamed to So, as they generate stiffness paths comparable with the "original", thus effectively "reseting" the stiffness path within minutes of each other. this allows to repeat the peak strength test 5 times in less than one hour.

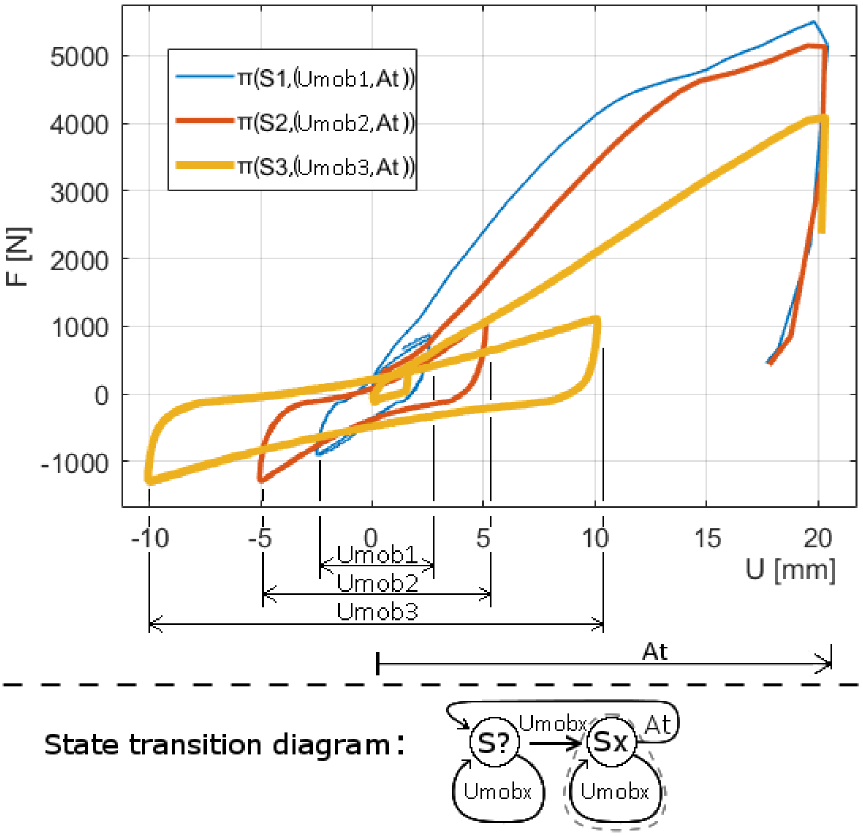

Fig. H.8: Three exit paths, measured after stabilizing three different stable states, at three different *Umob*. Note, *At* amplitude here is reduced to 20 mm. The state transition diagram is deduced to represent the general case.

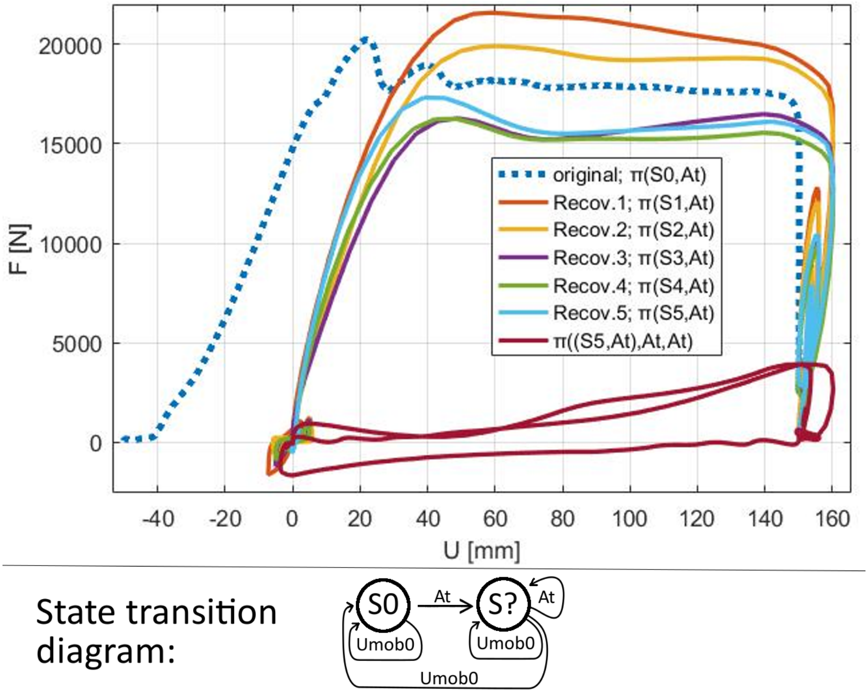

Fig. H.9: A test showing recovery of initial stiffness path (thus initial soil state *So*). The initial stiffness path was recovered 5 times in one loading history. Test result is compared with the "original" stiffness path published in preceding research [29].

If small *Umob* cycles are not applied, the path $\pi((S5, At), At, At)$ in Fig.H.9 is generated. $\pi((S5, At), At, At)$ is the "disturbed" stiffness path left after At. After At foundation stiffness drops very significantly. Interestingly, if At is applied multiple times in a row, if creates a temporal stable hysteresis loop at a large deformation amplitude. Only after stabilizing the hysteresis loop towards a small *Umob* amplitude, the initial stiffness path is recovered. The observations is very simple, but it reveals an important physical property governing stiffness of a foundation embedded in sand - stiffness behaves as functions of deformation.

The stable states shown thus far were all generated at $\omega = 0.1Hz$ deformation frequency (using triangular sawtooth wave as U input). The triangular sawtooth wave has a constant $\frac{\delta U}{\delta t}$ between the peaks. Thus, when $\omega \rightarrow 0Hz$, then $\frac{\delta U}{\delta t} \rightarrow 0$. In methodology section, U was declared as input for this very reason: deformation can be applied slow enough to cause $\frac{\delta U}{\delta t} \approx 0$, thus canceling $C \cdot \frac{\delta U}{\delta t}$ effects. If true, there should be a loading rate where quasi static K is detected. Once $\frac{\delta U}{\delta t} \approx 0$, further reduction of $\frac{\delta U}{\delta t}$ will not produce detectable changes in stable state K stiffness hysteresis loop. The test shown in

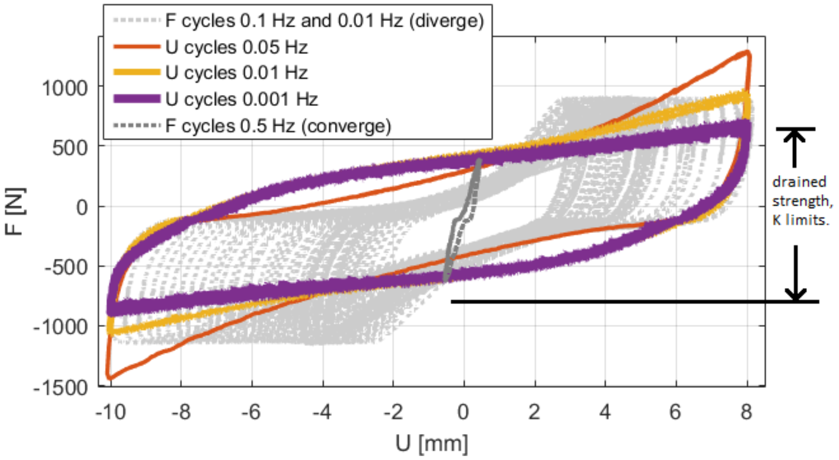

Fig. H.10: Stable state stiffness hysteresis loops, generated at varying loading frequencies. triangular sawtooth wave creates constant $\frac{\delta U}{\delta t}$ when U is the input. When F amplitude is input, $\frac{\delta U}{\delta t}$ is not controlled, hence C dependent deviation from static K is amplified.

Fig.H.10 was run to test this assumption.

As expected, slowing down ω causes converging changes within the hysteresis loop generated at a fixed amplitude. Pore pressure has more time to dissipate, thus deviation from quasi static K loop gradually diminishes. The K hysteresis loop observed at $\omega = 0.001Hz$ has no detectable C effects, and further reduction in ω does not produce further change. Because deviation from quasi-static loop depends on deformation rate, it can be attributed to the C component in equation of motion (Eq.H.1). Exposed to deformation, sand expands and contracts - the faster the volume change, the bigger the pore water pressure gradient. Thus, the C component can be attributed to pore water pressure gradients. If load is applied slow enough, then even tiny pore pressure gradients have enough time to dissipate - drained more. Therefore, the quasi-static stable state K loop can be viewed as purely drained soil response (in this case, at $\omega \leq 0.001Hz$).

The drained quasi static K stiffness path is very interesting, as drained response is effectively the back bone of soil fabric. When sand dilates or contracts, pore pressure varies and pushes the stress path above or below the drained path [35], [36]. Comparing the stiffness paths in Fig.H.10 it is visible that hysteresis loops have both contraction and dilation dominant loading phase. Stiffness loop drop below the drained path can be attributed to contraction dominant phase (partial liquefaction, loss of stiffness). The stiffness path above the drained hysteresis loop can be attributed to dilation (boot effect, increase in peak strength). Thus, giving valuable insights how state dependent K and C function coexist, and can be isolated from each other.

Finally, the drained stiffness hysteresis loop provides valuable reference points for cases where F is used for input (see Fig.H.10). F cycles within the drained K limits converge towards $Umob \approx 1mm$. Thus, there is a $Umob$ amplitude towards which $Fmob$ cycles converge, regardless of relatively fast deformation frequency ($0.5Hz$ in Fig.H.10). On the other hand, F cycles reaching beyond the drained K loop limits are not stable. When F cycles exceed the drained limits, $Umob$ diverges towards infinite. Curiously, slower loading frequency creates larger deformation increments. This makes sense, given the C component acts as a linear damper - the more time is spent beyond the drained limits, the more time there is for deformation to accumulate. F beyond drained limits relies on pore water "locking" the voids at constant volume (resisting deformation). Because the system is partially drained, slow loading frequencies provide more time for water seepage, therefore allowing more water to fill the voids, thus more deformation - required for soil grains to change arrangement. Finally, notice how the stiffness hysteresis loops generated by $Fmob$ are notably more curved than those shaped during $Umob$ cycles. This is because $\frac{\delta U}{\delta t}$ is not limited by while $Fmob$ is applied. Therefore, at times of low stiffness, large $\frac{\delta U}{\delta t}$ accumulates, thus amplifying the $C \cdot \frac{\delta U}{\delta t}$ component, thus amplifying the curvature.

5 Discussion

In engineering practice, loads are collected and applied as F vectors. Engineers need to prevent excess inclination of a structure, thus it is tempting to look for $U(F)$ solutions, where deformation is predicted as a function of F history. However, the foundation behaves as an $F(U)$ system (see Fig.H.11). The F history can be uniquely described, predicted and prescribed as a funtion of U. Solutions using $F(U)$ models could have fundamental limitations when applied to $U(F)$ problems. The new experimental evidence suggests that, there is no unique $Umob$ for every $Fmob$, only a unique $Fmob$ for every $Umob$. Thus, $Fmob$ is uniquely predictable as a function of $Umob$, but not the other way round.

Stable state hysteresis loops preserve their overall shape by stretching and squeezed within $Umob$ amplitude. This type of behavior can be modeled by normalizing the stiffness path within a deformation envelope. Just like stress (or force) envelopes, deformation (or strain) envelopes can be used in modeling. A potential constitutive formulation for strain-space plasticity is readily available [44]. Strain-space formulation is interesting not only for its new found comparability with the new found experimental evidence. Strain-space plasticity has substantial computation benefits as well: fewer matrix inversions, reduced return mapping computation cost. There are ample examples of strain-space (stress relaxation) models in non-geotechnical

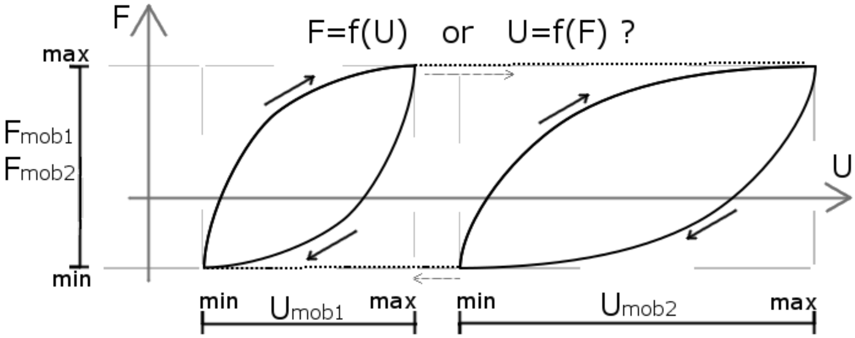

Fig. H.11: A thought experiment, illustrating the observed stiffness hysteresis loop behavior. Only *Fmob* can be uniquely defined by *Umob*, therefore it is an $F = f(U)$ problem.

paradigms of material science: cracking concrete [13], bone fractures [31] and aeronautic aluminum [44] had been successfully modeled by using strain-space (stress relaxation) envelopes. Thus, principles of strain-space plasticity could be borrowed from neighboring branches of material science.

Stiffness is the primary objective in this paper. But during the tests, the mono-bucket prototype was equipped with additional sensors not required for measuring stiffness. For instance, the vertical displacement of the bucket was measured as well (see plots in Fig.H.12). It is interesting to side note, that each time initial stiffness was recovered, the foundation was noticed to lower itself down, towards a repeatable deptH: The wide lid of a mono bucket means the soil under the lid was compacting. Whereas, during peak strength test - the foundation raised itself upward (the soil volume dilated). Thus, the deformation cycles which produced stable state stiffness loops, produced stable state volumetric response as well. It is already known that liquefaction charts are best normalized by deformation (strain) amplitude [12], [11], and increasingly mode deformation dependent sand properties are being discovered in dynamic frictionless triaxial tests as well [35], [36]. Thus, there symptoms that deformation dependent properties of sand is an intriguing topic ripe with opportunities for pioneering researcH: To access these soil properties: new testing protocols, new analysis and new modeling methods may need to be developed. Thus, the main contribution of the new findings are the new questions which open the path to numerous branches of original research - future work.

6 Conclusion

The conclusion is bold: stress-space solutions could be incompatible with the properties governing disturbed sand stiffness behavior. Disturbed sand stiff-

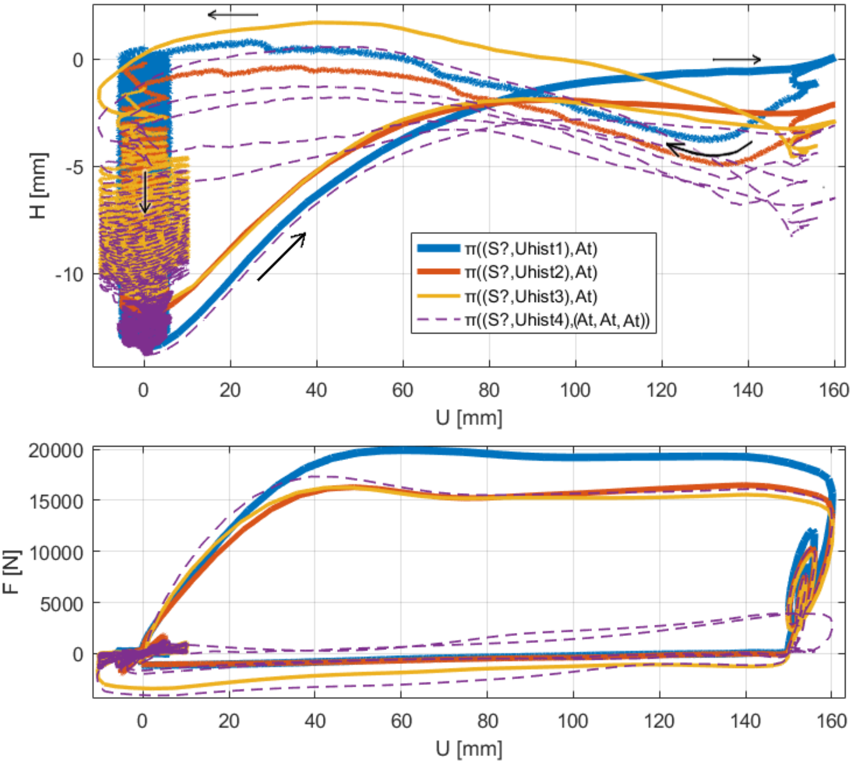

Fig. H.12: Loss and recovery of stiffness, is noticed to occur together with loss and recovery of foundation deptH: Note the foundation has a flat, solid lid, thus the change in depth can occur only if the soil volume is contracting during stabilization, and dilating while being disturbed.

ness behaves as a function of strain (deformation), rather than stress (force). $U(F)$ models may be inadequate for $F(U)$ problems. Alas, a potentially compatible (strain-space plasticity) formulation already exists [44]. It is rarely encountered in geotechnics, but is used in neighboring branches of material science [13], [31]. In addition to being an $F(U)$ model (thus, likely compatible with $F(U)$ problems), strain-space plasticity offers substantial computation benefits: fewer matrix inversions, fewer return mapping iterations.

The conclusion was reached in the outcome of trying a novel analysis method. The guessing game. The original, non-geotechnical perspective analyses the data structure governing the problem (stiffness) itself. Rather than anchoring to pre-existing convention, the guessing game forces to reformulate the problem, and approach it from a different perspective: analyzing disturbed sand as a finite-state transition system. This unconventional methodology has revealed principles which allow to control both loss and recovery of stiffness in real-life, real-time testing. The proof is demonstrated empirically. All $Umob$ share the same $Fmob$ limits, but $Fmob$ limits do not produce unique $Umob$ amplitudes (with the exception of converging towards the minimum amplitude). "We can always map from displacement to load, but not from load to displacement" - David Muir Wood lecture, 2015.

The new found requirements could be ignored when dealing with conventional geotechnical problems, where loads are static. Alas, to solve problems containing dynamic loading, a static equilibrium is not enough - the whole equation of motion has to be accounted for. Not only K is nonlinear, but the C and M components have nonlinear state dependencies. The new findings provide practical means to isolate quasi static K curves and to observe its dependencies by manipulating $Umob$ amplitude and the rate of deformation $\frac{\delta U}{\delta t}$. This allowed to switch the $C \cdot \frac{\delta U}{\delta t}$ component on and off selectively. Thus, the approach might allowing to decipher the full equation of motion - one nonlinear state / phase dependency at a time.

Finally, it is crucial to recognize that the proof is demonstrated ir real-life experiment. A stiffness path equivalent to initial stiffness path was disturbed and recovered at least 5 times in one loading history. Thus, conclusively demonstrating the descriptive, predictive and prescriptive analytic powers delivered by the novel approacH:

References

[1] Trial installation: Uk north sea. [Online]. Available: http://universal-foundation.com/case-studies/trial-installation-campaign/

[2] K. H. Andersen and T. Berre, "Behaviour of a dense sand under monotonic and cyclic loading comportement d'un sable dense sous chargement monotonique et cyclique," in *Geotechnical Engineering for Trans-*

portation Infrastructure: Theory and Practice, Planning and Design, Construction and Maintenance: Proceedings of the Twelfth European Conference on Soil Mechanics and Geotechnical Engineering, Amsterdam, Netherlands, 7-10 June 1999, vol. 2. CRC Press, 1999, p. 667.

[3] D. N. V. AS, "Design of offshore wind turbine structures," Internet Requests for Comments, DET NORSKE VERITAS AS, OFFSHORE STANDARD DNV-OS-j101, May 2014. [Online]. Available: ttp://www.dnv.com

[4] A. Bird, "Thomas kuhn," in *The Stanford Encyclopedia of Philosophy*, fall 2013 ed., E. N. Zalta, Ed., 2013.

[5] A. W. Bishop and G. E. Green, "The influence of end restraint on the compression strength of a cohesionless soil," *Geotechnique*, vol. 15, no. 3, pp. 243–266, 1965.

[6] M. Budhu, "Soil mechanics and foundations, (with cd)," 2008.

[7] C. R. I. CLAYTON, M. STEINHAGEN, H. M. STEINHAGEN, W. POWRIE, K. TERZAGHI, and A. W. SKEMPTON, "Terzaghi's theory of consolidation, and the discovery of effective stress. (compiled from the work of k. terzaghi and a.w. skempton)." *Proceedings of the Institution of Civil Engineers - Geotechnical Engineering*, vol. 113, no. 4, pp. 191–205, 1995. [Online]. Available: http://www.icevirtuallibrary.com/doi/abs/10.1680/igeng.1995.28015

[8] C. A. Coulomb, *Essai sur une application des règles de maximis & minimis à quelques problèmes de statique, relatifs à l'architecture*. De l'Imprimerie Royale, 1776.

[9] M. Damgaard, L. Andersen, L. Ibsen, H. Toft, and J. Sørensen, "A probabilistic analysis of the dynamic response of monopile foundations: Soil variability and its consequences," *Probabilistic Engineering Mechanics*, vol. 41, p. 46–59, 2015.

[10] C. G. Di Prisco and D. M. Wood, *Mechanical Behaviour of Soils Under Environmentallly-Induced Cyclic Loads*. Springer Science & Business Media, 2012, vol. 534.

[11] R. Dobry and T. Abdoun, "Cyclic shear strain needed for liquefaction triggering and assessment of overburden pressure factor k σ," *Journal of Geotechnical and Geoenvironmental Engineering*, p. 04015047, 2015.

[12] ——, "An investigation into why liquefaction charts work: A necessary step toward integrating the states of art and practice," in *Proc., 5th Int. Conf. on Earthquake Geotechnical Engineering*. Chilean Geotechnical Society Santiago, Chile, 2011, pp. 13–44.

[13] A. M. Farahat, M. Kawakami, and M. Ohtsu, "Strain-space plasticity model for the compressive hardening-softening behaviour of concrete," *Construction and Building Materials*, vol. 9, no. 1, pp. 45 – 59, 1995. [Online]. Available: http://www.sciencedirect.com/science/article/pii/095006189592860J

[14] A. Foglia, "Bucket foundations under lateral cyclic loading: Submitted for the degree of doctor of philosophy," Ph.D. dissertation, Denmark, 2015.

[15] Z. Gao and J. Zhao, "Strain localization and fabric evolution in sand," *International Journal of Solids and Structures*, vol. 50, no. 22, pp. 3634–3648, 2013.

[16] G. W. E. C. (GWEC). (2017) Market forecast for 2017-2021. [Online]. Available: http://www.gwec.net/global-figures/market-forecast-2012-2016/

[17] S. Iai, Y. Matsunaga, and T. Kameoka, "Strain space plasticity model for cyclic mobility," *Soils and Foundations*, vol. 32, no. 2, pp. 1–15, 1992.

[18] L. B. Ibsen, "The stable state in cyclic triaxial testing on sand," *Soil Dynamics and Earthquake Engineering*, no. 13, pp. 63–72, 1994.

[19] L. Ibsen, *The Static and Dynamic Strength of Sand*. Geotechnical Engineering Group, 1995, pDF for print: 11 pp. Published in: Proceedings of the Eleventh European Conference on Soil Mechanics and Foundation Engineering, Copenhagen, 1995 : XI ECSMFE : DGF-bulletin 11, Vol. 6, pp. 69-76.

[20] W. Kirkpatrick, "Influence of end restraint on strain distributions in the triaxial compression test," in *Proc. Geotechnical Conf. Oslo*, vol. 2, 1967.

[21] B. S. Knudsen, M. U. Østergaard, and L. B. Ibsen, "Small-scale testing of bucket foundations in sand," Department of Civil Engineering, Aalborg University, Tech. Rep., 2013.

[22] M. Mohkam, "Contribution à l'étude expérimentale et théorique du comportement des sables sous chargements cycliques," Ph.D. dissertation, 1983.

[23] J. Moust, *A new triaxial apparatus*. Copenhagen, Geoteknisk Institut, 1970, vol. 27.

[24] G. Nicolai and L. Ibsen, *Response of monopiles under cyclic lateral loading in sand*. EWEA, 2015.

[25] S. D. Nielsen, “Transient monotonic and cyclic load effects on mono bucket foundations,” Ph.D. dissertation, Aalborg Universitetsforlag, 2016.

[26] S. K. Nielsen, A. Shajarati, K. W. Sørensen, and L. B. Ibsen, “Behaviour of dense frederikshavn sand during cyclic loading,” Department of Civil Engineering, Aalborg University, Tech. Rep., 2012.

[27] S. Nielsen, L. Ibsen, and S. Gres, “Cost-effective mass production of mono bucket foundations,” 2015, pO: 242.

[28] S. Nielsen and L. Ibsen, “The offshore bucket trail installation,” 2015.

[29] S. Nielsen, L. Ibsen, and B. Nielsen, *Dynamic behaviour of mono bucket foundations subjected to combined transient loading*. C R C Press LLC, 2015, vol. 1, pp. 313–318, 978-1-138-02848-7 (set of two volumes hardback + CD-Rom) 978-1-138-02850-0 (Volume1+ CD-Rom) 978-1-138-02852-4 (Volume 2) 978-1-315-67551-0 (ebook PDF).

[30] R. E. Olson and J. Lai, “Apparatus details for triaxial testing,” Chaoyang University of Technology, Tech. Rep., 2004.

[31] P. Pankaj and F. E. Donaldson, “Algorithms for a strain-based plasticity criterion for bone,” *International journal for numerical methods in biomedical engineering*, vol. 29, no. 1, pp. 40–61, 2013.

[32] U. Praastrup, K. Jakobsen, and L. B. Ibsen, “On the choise of strain measures in geomechanics,” Geotechnical Engineering Group, Tech. Rep., 1998.

[33] P. Rowe and L. Barden, “Importance of free ends in triaxial testing,” *Journal of the Soil Mechanics and Foundations Division*, vol. 90, no. 1, pp. 1–28, 1964.

[34] T. Sabaliauskas, A. T. Diaz, L. B. Ibsen, and S. D. Nielsen, “Observations during static and cyclic undrained loading of dense aalborg university sand no. 1,” Aalborg University, DCE Technical Memorandum, Tech. Rep., 2014.

[35] T. Sabaliauskas and L. Ibsen, *Cyclic Triaxial Loading of Cohesionless Silty Sand*. International Society of Offshore and Polar Engineers, 2015, pp. 821–826.

[36] T. Sabaliauskas, L. B. Ibsen *et al.*, “Triaxial testing beyond yielding,” in *The 27th International Ocean and Polar Engineering Conference*. International Society of Offshore and Polar Engineers, 2017.

[37] A. N. Schofield, *Disturbed soil properties and geotechnical design*. Thomas Telford, 2005.

[38] D. Sheng, B. Westerberg, H. Mattsson, and K. Axelsson, "Effects of end restraint and strain rate in triaxial tests," *Computers and Geotechnics*, vol. 21, no. 3, pp. 163–182, 1997.

[39] W. Shockley and R. Ahlvin, "Nonuniform conditions in triaxial test specimens," in *Research Conference on Shear Strength of Cohesive Soils, ASCE, Boulder, Colo*, 1960, pp. 341–357.

[40] I. Stroescu and P. Frigaard, *Scour properties of mono bucket foundation*. C R C Press LLC, 2016, pp. 335–341.

[41] S. Tomas and I. Lars, Bo, "The new scope of frictionless triaxial apparatus – disturbed sand testing," *Geotechnical testing journal*, vol. 42, no. 1, 2019.

[42] I. I. Vardoulakis, "Bifurcation analysis of the triaxial test on sand samples," *Acta Mechanica*, vol. 32, no. 1-3, pp. 35–54, 1979.

[43] D. M. Wood, *Geotechnical modelling*. CRC Press, 2003, vol. 1.

[44] P. J. Yoder, "A strain-space plasticity theory and numerical implementation," no. EERL 80-07, August 1980, a Report on Research Concluded Under Grants from National Science Foundation. [Online]. Available: http://authors.library.caltech.edu/26358/1/8007.pdf

[45] J.-H. S. Yun Wook Choo, Tae-Woo Kang, "Centrifuge study on undrained and drained behaviors of a laterally loaded bucket foundation in a silty sand," in *Proceedings of the Twenty-fifth (2015) International Ocean and Polar Engineering Conference*. International Society of Offshore and Polar Engineers (ISOPE), 2015, pO: 963.

[46] K. Zen, M. Hirasawa, T. Shinsaka, and M. Adachi, "Countermeasure for liquefiable ground beneath the existing structure by cpg," in *Proceedings of the Twenty-fifth (2015) International Ocean and Polar Engineering Conference*. International Society of Offshore and Polar Engineers (ISOPE), 2015, pO: 839.

SUMMARY

Offshore wind turbine are slender structures, performance of which depends on foundation stiffness. Wind turbine foundations embedded in sand episodically lose and recover stiffness due to soil being disturbed by cyclic loads. To understand and model this phenomenon, new methods of testing and modeling of disturbed sand were attempted.

To observe the phenomenon governing disturbed sand states, dynamic tests were conducted using a frictionless triaxial apparatus and a small scale mono-bucket foundation. Experimental observations were then summarized into an original model. While developing the original concept, new paradoxes and anomalies were predicted: soil states of lower stiffness at higher density. The anomalies are confirmed to exist experimentally.

The new knowledge allows to control cyclic stiffness of sand in real-life real-time testing. Methods adequate to control a phenomenon, should be adequate to model it. Because deformation allows to control cyclic stiffness in experiment, deformation envelopes were proposed for modeling. Remarkably, the final result is one set of rules which are applicable in both drained and undrained soil states, combining loss and recovery of stiffness, during irregular cyclic loads.

ISSN (online): 2446-1636
ISBN (online): 978-87-7210-250-4

AALBORG UNIVERSITY PRESS